UNIVERSITY OF SOUTHAMPTON

FACULTY OF ENGINEERING AND APPLIED SCIENCE

INSTITUTE OF SOUND AND VIBRATION RESEARCH

Feedback Control of Vibration with Inertial Actuators

by

Luca Benassi

A thesis submitted for the degree of

Doctor of Philosophy

February 2004

UNIVERSITY OF SOUTHAMPTON

ABSTRACT

FACULTY OF ENGINEERING AND APPLIED SCIENCE
INSTITUTE OF SOUND AND VIBRATION RESEARCH

Doctor of Philosophy

Feedback Control of Vibration with Inertial Actuators

By Luca Benassi

The design of inertial actuators for active vibration control is considered. Unlike reactive actuators, inertial actuators do not need to react off a base structure and can therefore be directly installed on a vibrating structure. In order to guarantee good stability margins with feedback controllers, however, the actuator resonance must have a low natural frequency and it must be well damped. Unfortunately, the need to have an inertial actuator with a low resonance frequency leads to unwanted static deflections of the actuator proof-mass.

The behaviour of an inertial actuator is analysed with different inner feedback control schemes. First, it is shown that a phase-lag controller in the inner loop, based on the measurement of the transmitted force, can be used to significantly improve stability margin and performance of the system using relatively low gains.

The use of integral displacement feedback as an inner loop can provide self-levelling capabilities for the inertial actuator thus overcoming the static deflection problem. A novel device for active vibration control, based on an inertial actuator with a proof-mass displacement sensor and inner PID controller, is described and its performance is demonstrated experimentally. It is found that the effective natural frequency and damping of the actuator can also be changed substantially with such a controller, thus allowing an inertial actuator to be customised for a specific application.

The stability and performance are then analysed for an active isolation system using the modified inertial actuator and an outer velocity feedback control loop. The plant response, from force actuator input to sensor output, is derived in terms of the mechanical mobilities of the equipment structure being isolated and the vibrating base structure, and the mechanical impedance of the intervening mount. The results of an experimental study of active vibration isolation using a modified inertial actuator are then described. Theory and experiments agree well, demonstrating the effectiveness

of the modified inertial actuator in isolating a piece of equipment from a vibrating base.

In the second part of the thesis, strategies for the suppression of plate vibration are investigated by considering the equivalent impedance of power-minimising feedforward vibration controllers. The minimum power, transmitted to infinite and finite plates by a single primary force and a single secondary force, optimised at each frequency, has been compared with the power reduction that can be achieved with passive vibration treatments. The equivalent impedance is defined to be the ratio of the optimised secondary force to the total velocity at the secondary force location, but it is generally non-causal and so cannot be implemented for broadband random excitations. The approximation of the equivalent impedance by lumped parameter systems is considered. In particular, passive controllers, based on springs and dampers, have been analysed, although, in many practical applications, a rigid ground is not available to react these components off.

The results of a theoretical and experimental study of active vibration suppression on a flexible plate using the modified inertial actuator are then described. Theory and experiments agree well, demonstrating the effectiveness of the modified inertial actuator in controlling vibrating panels.

Table of Contents

List of Figures

List of Tables

Acknowledgements

This thesis was born because I was hungry. Let me explain. In the spring of 2001, my first professional creature came to life. It was an aircraft wing. Despite the success of the effort and restless hours of mad studying and work in the sometimes unbearable Mojave desert, I felt that the puzzle was not complete. The sense of accomplishment vanished quickly and quietly. It was then that I realised I needed more answers from that faded orange book I used to reference so often. It was then when I realised that I was hungry for more and deeper knowledge.
A few months later, I flew to Southampton. I was about to start a PhD supervised by one of the authors of that orange book. Thank you Steve for all the guidance and support.

Later at ISVR, the first reviews and comments of my work arrived. A scientific piece of work is like a child. It grows faster and stronger if it is fed and educated appropriately not only by its professional parent, but also by the competent community which the work gets exposed to. Thank you Mike. Thank you Paolo.

A special paragraph of this tale must be reserved to those who helped me keep my sanity. Yes, I tend to work a lot, but I have also been surrounded by people who can sense when it is time to come to rescue me. My friendship especially with Lewis, Torbjörn, James, Jim, Mona, Steve and Olie is a treasure that is simply priceless.

I have three more people to thank. My gratitude to my parents Angela and Germano is as boundless as the Universe, especially in these troubled times for you dear dad. Thank you for your support through good times and bad, and your constant encouragement to achieve. I am like a tree. My branches can be shaken by the winds, but the roots you gave me are solid and firm.
I like tales with happy endings. This thesis is dedicated to Lisa whose love, drive and spirit have been both a guiding light and an inspirational force.

List of Notation

a_a	Inertial actuator proof-mass acceleration
A	First term of the quadratic form of the total power
$\mathbf{A}$	State matrix in a state space model
$\mathbf{A}_{CL}$	Closed loop state matrix in a state space model
b	Second term of the quadratic form of the total power
B	Magnetic flux density
$\mathbf{B}$	Input matrix in a state space model
B_j	Inertial actuator input impedance using the j-th control scheme
c	Last term of the quadratic form of the total power
c_a	Inertial actuator damping
c_B	Wave speed
c_m	Passive mount damping
C	Capacitance
$\mathbf{C}$	Observation matrix in a state space model
$CA(j\omega)$	Charge amplifier transfer function
d	Disturbance
d_j	j-th damping
D	Bending stiffness
$\mathbf{D}$	D matrix in a state space model
$\mathbf{D}_g$	Damping matrix in generalized coordinates
$\mathbf{D}_m$	Damping matrix in modal coordinates
E	Young's modulus
f	Force
$\mathbf{f}$	Force vector
f_a	Actuator force
f_c	Command force
f_i	Inertial force
f_j	Force component of the j-th point

f_p	Primary force
f_s	Secondary force
f_{so}	Optimal secondary force
f_t	Total transmitted force by the inertial actuator
g	Gravity
g_I	Integral displacement feedback gain
g_P	Displacement feedback gain
g_V	Rate feedback gain
G	Plant frequency response
G_d	Disturbance frequency response
h	Plate thickness
h_f	Force feedback gain
h_{if}	Integrated force feedback gain
h_{iv}	Integrated velocity feedback gain
h_{lp}	Low pass filter gain
h_{pl}	Phase-lag compensator feedback gain
h_v	Velocity feedback gain
H	Feedback controller frequency response
$\mathbf{H}$	Output selection matrix in the state space model
H_0^2	Second kind of Hankel function of the 0^{th} order
i	Current
$i_{\max}$	Maximum current to the inertial actuator
I	Moment of inertia
$\mathbf{I}_{ng}$	Identity matrix of order ng
$Int(j\omega)$	Realistic integrator transfer function
J	Cost function
J_0	0^{th} order Bessel function of the 1^{st} kind
k	Bending wave number
k_a	Inertial actuator stiffness

k_j	j-th stiffness
k_m	Passive mount stiffness
$\mathbf{K}$	Solution of the LQR problem
KE	Kinetic Energy
K_0	Second kind of the modified Bessel function of the 0^{th} order
K_b	Magnetic constant
K_f	Force constant
$\mathbf{K}_g$	Stiffness matrix in generalized coordinates
K_E	Electric constant
l	Conductor length
L	Inductance
m	Mass per unit surface
m_a	Inertial actuator proof-mass
m_b	Base mass
m_e	Equipment mass
m_j	j-th mass
$\mathbf{M}_g$	Mass matrix in generalized coordinates
n_g	Number of degrees of freedom
N	Number of conductors in series
P	Frequency averaged power ratio
P_c	Frequency averaged power ratio of the controlled system
P_j	j-th point
P_u	Frequency averaged power ratio of the uncontrolled system
$PA(j\omega)$	Power amplifier transfer function
$\mathbf{Q}$	Observation weight matrix
r	Distance between point i and j
R	Resistance
$\mathbf{R}$	Actuation weight matrix
$\mathbf{S}$	Solution of the Riccati equation
t	Time

t_0	Initial time
t_f	Final time
T	Time delay
T_{aj}	Blocked response of the actuator using the j-th control scheme
u	Plant input
$\mathbf{u}$	Input vector in a state space model
$\mathbf{v}$	Velocity vector
$\mathbf{V}$	Modal eigenvectors matrix
v_j	Velocity component of the j-th point
v_a	Inertial actuator proof-mass velocity
v_b	Base velocity
v_{bj}	Base velocity at the j-th point
v_e	Equipment velocity
v_{ep}	Equipment velocity before the actuator is attached
V	Voltage
V_b	Back EMF
V_c	Voltage drop across the coil
V_l	Inductive voltage drop
$\mathbf{w}$	Vector of the effect of the primary force on the states
x	Inertial actuator displacement
x_j	x coordinate of the j-th point
$x_{\max}$	Inertial actuator stroke
$\mathbf{x}$	State vector in a state space model
y	Plant response
$\mathbf{y}$	Output vector in the state space model
y_j	y coordinate of the j-th point
$\mathbf{Y}$	Mobility matrix
Y_e	Equipment mobility
Y_b	Base mobility

Y_{ij}	Transfer mobility between point i and j
z_j	z coordinate of the j-th point
Z	Impedance
$\mathbf{Z}$	Impedance matrix
Z_a	Mechanical impedance of the inertial actuator
Z_{ij}^a	Inertial actuator impedance between point i and j
Z_{ij}^m	Mount impedance between point i and j
Z_m	Impedance of the passive mount
Z_D	Desired impedance
α	Weight coefficient ratio
ε_{mn}	Normalising factor
γ	Euler's constant
$\boldsymbol{\gamma}$	Displacement vector in generalized coordinates
γ_j	Displacement of the j-th mass
Φ_{mn}	m,n-th natural mode
η	Hysteretic loss factor
$\boldsymbol{\Gamma}$	Actuation selection matrix
δ	Delta function
Δh	Extra thickness
$\boldsymbol{\eta}$	Modal coordinates vector
λ	Self-levelling coefficient
λ_f	Flexural wavelength
λ_i	i-th eigenvalue
μ	Mass ratio
ζ	Damping ratio
ζ_a	Inertial actuator damping ratio
Π	Power
Π_{opt}	Power due to the optimal solution
Π_p	Power due to primary force

Π_s	Power due to secondary force
ρ	Density
υ	Poisson's ratio
$\mathbf{\Psi}$	Observation selection matrix
τ	Inverse of the cut-off frequency
ω	Frequency
ω_a	Inertial actuator resonance frequency
ω_j	j-th resonance frequency
$\mathbf{\Omega}$	Resonance matrix

Chapter 1

Introduction

1.1 Introduction to the thesis

1.1.1 Problem and objectives

Vibration occurs in most machines, structures, and dynamic systems, leading to many undesirable consequences. Vibration often becomes a problem due to "unpleasant" motion, noise and dynamic stresses, which could lead to fatigue and failure of the structure or machine, energy losses, decreased reliability, and degraded performance. Vibration control is aimed at reducing or modifying the vibration level of a mechanical structure.

When a vibration problem needs to be remedied, it is desirable and often necessary to understand its whole nature. This includes, among others, understanding its originating source, the nature and direction of the vibration at the problem location, the path along which the vibrational energy reaches that location, and the frequency content of the vibration. In particular, a problem which arises in several application areas is the isolation of sensitive equipment from vibration of the base structure to which it is attached (Figure 1.1).

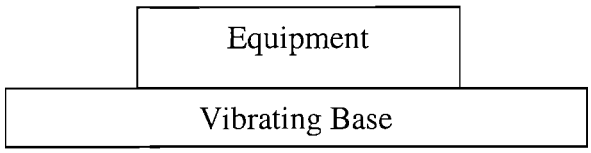

Figure 1.1 *Complete transmission of the vibrations to the equipment if no isolator is applied.*

Before attempting to apply any isolator (Figure 1.2), it is important to know as much as possible about the conditions under which it will be used and the fragility of the equipment to be mounted. This knowledge must be coupled with an understanding of the various types of vibration and shock isolators which might be applied to a given problem. Depending on the type of isolator, the material from which it is made, and the operating conditions, the performance of the isolator and its effectiveness can vary widely. These factors must be considered and the proper accommodations, to arrive at a reasonably accurate estimate of the performance of the isolated system, have to be made.

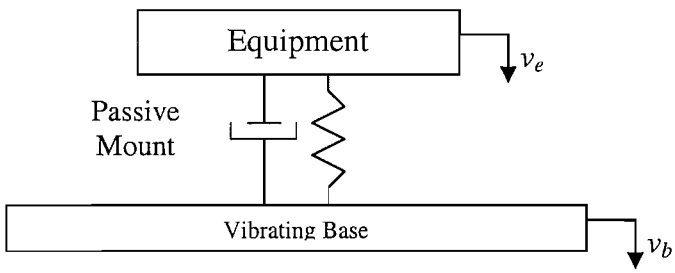

Figure 1.2 *Passive vibration isolation with a passive mount.*

This thesis is specifically concerned with the use of inertial actuators in active vibration control systems. Inertial actuators do not need to react off a base structure, so they can be used as modules that can be directly installed on a vibrating structure. In particular, one application that this thesis addresses is the problem of vibration isolation of a sensitive piece of equipment (Figure 1.3) using inertial actuators.

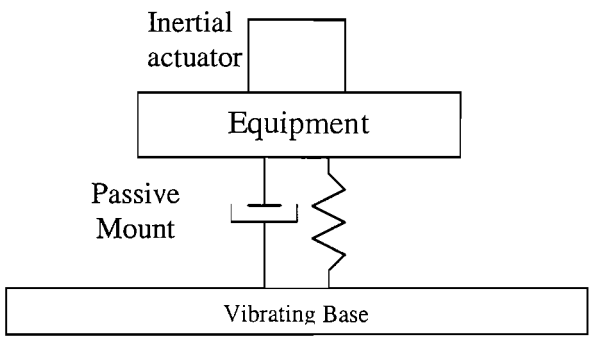

Figure 1.3 *Active vibration isolation using an inertial actuator.*

Vibrating bodies usually generate vibration forces in more than one direction. Typically only the predominant vibrating direction is controlled, whether the mount is passive or active. Multiple axis active vibration isolators to minimize the transmission of vibration along translational and rotational axes have been considered in theory (Ryaboy, 1995, and Su *et al.*, 1996), but there are few reports of experimental work (Spanos *et al.*, 1995, and Horodinca *et al.*, 2002). In this research, single degree of freedom (SDOF) systems are considered.

Before isolation is used to solve a vibration problem, attempts should be made to reduce the disturbance from the source. If this is not possible or impractical, it may be possible to modify the frequency response of the base structure so that it is less excited by the disturbance. The final part of the thesis is concerned with the use of active systems with inertial actuators for this purpose.

1.1.2 Passive vibration control

There are two classes of vibration control: passive vibration control and active vibration control. Passive vibration control involves the modification of the stiffness, mass and damping of a vibrating system to make the system less responsive to its vibratory environment (von Flotow *et al.*, 1990). The modification may take the form of basic structural changes or the addition of passive elements such as masses (which can be chunks of concrete in buildings), springs (such as vibration isolators), fluid dampers or damped rubbers. These elements simply react passively in opposition to the accelerations, deflections or velocities imposed upon them by vibration. None of them require any external assistance to do this, apart from their immediate passive

neighbours or structural components that interact with them. A straightforward solution to many vibration problems is to increase the stiffness within a machine. There is however a practical limit in passively increasing the stiffness of a structure. Furthermore, due to structural design rules, vibrations in high-precision machines are typically badly damped. Introducing additional passive damping into high-precision structures however is complicated, as the stresses and strains to be damped are very small. However, the common and "fail safe" approach to vibration control of structures is still adding damping to the structure (Procopio, 1986). Damping dissipates some of the vibration energy of the structure either by transforming it into heat or by transferring it to a connected structure. Examples of passive damping materials include viscoelastic materials, viscous fluids, high damping alloys, and particle damping. The most common of these are viscoelastic materials. Viscoelastic materials dissipate mechanical energy into heat when they undergo cyclic stresses due to polymer chain interactions. Elastometric mounts (natural rubber for example, see Lord Corporation, 2002) have been used as vibration isolators for many years (Johnson, 1995). More recently, the development of fluid-filled mounts for a variety of applications including automotive (Fang *et al.*, 2001), marine (Althaus and Ulbrich, 1992), and aerospace (Owen *et al.*, 1992) has provided the ability to improve their performance. Passive vibration cancellation can be achieved by appending an underdamped structure (a dynamic absorber) with the natural frequency similar to the disturbing frequency (Sun *et al.*, 1995, and Brennan, 1997). In any event, the majority of these applications based on passive damping use viscoelastic materials for vibration control. Although most passive damping treatments are inexpensive to fabricate, their successful application require a thorough understanding of the vibration problem in hand and the properties of the damping materials (Friswell *et al.*, 1997a).

1.1.3 Passive vibration isolation

In general, the isolation of any vibration-sensitive equipment from base vibration is usually performed on the transmission paths (mounts, Figure 1.2). The fundamental benefit provided by any mount is reduced structural vibration. In many applications, unwanted noise is a direct result of structural vibrations. Therefore, mounts also provide noise reduction benefits (Bies and Hansen, 1996). However, with such passive mounts there is a trade-off between low and high frequency isolation

performances depending on the damping of the mount. In fact, a major challenge is to make the mount as stiff as possible, statically, to better couple and support, and dynamically as soft as possible, to better isolate. This is difficult to accomplish with passive elastometric mounts, as described by Crede and Ruzicka (1996) and Ungar (1992).

"Transmissibility is a measure of the reduction of transmitted force or motion afforded by an isolator" (Crede and Ruzicka, 1996). If the source of vibration is an oscillating motion of the base, transmissibility is the ratio of the vibration amplitude of the equipment to the vibration amplitude of the foundation. The motion of the vibrating base and the equipment may be expressed in any consistent units, such as displacement, velocity, or acceleration, and the same expression for the transmissibility applies in each case (Crede and Ruzicka, 1996). An example of transmissibility of a typical single degree of freedom mass-spring-damper system subject to a base excitation (Figure 1.2) is shown in Figure 1.4 for different values of damping ratio ζ, using fixed values of mass and stiffness. Figure 1.4 shows that a damper with higher damping ratio will limit motion at resonance, but increases transmissibility at higher frequencies. This establishes the trade-off for the linear isolation system.

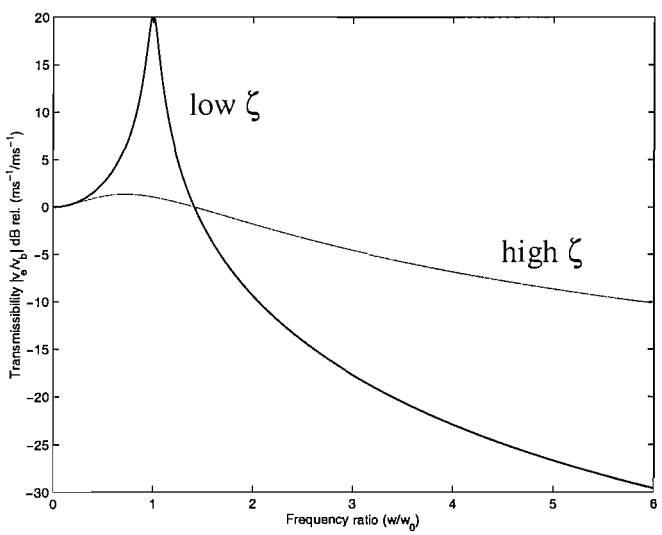

Figure 1.4 *Transmissibility of a simple mass-spring-damper system with base excitation and different damping ratio ζ, as a function of the frequency ratio ω/ω_0, where ω_0 is the resonance frequency of the system.*

In the process of deciding on a vibration isolator for a particular application, there are a number of critical pieces of information which are necessary to define the desired functionality of the isolator. Some items are more critical than others but all should be considered in order to select, or design, the appropriate product. Some of the factors which must be considered are weight, size and centre-of-gravity of the equipment to be isolated. Obviously, the weight of the unit will have a direct bearing on the type and size of the isolator. The size or shape of the equipment can also affect the isolator design since this may dictate the type of attachment and the available space for the isolator. The centre of gravity location is quite important and isolators of different load capacities may be necessary at different points on the equipment due to weight distribution. The locations of the isolators relative to the centre of gravity, for example, could also affect the design of the isolator.

Also, knowledge of the type of dynamic disturbances to be isolated is important. This is basic to the definition of the problem to be addressed by the isolator selection process. In order to make an educated selection or design of a vibration isolator, this type of information must be defined as well as possible. Typically, sinusoidal or random vibration spectra will be defined for the application. In many installations of military electronics equipment, random vibration tests have become commonplace and primary military specifications for the testing of this type of equipment (such as MIL-STD-810) have placed heavy emphasis on random vibration, tailored to the actual application. Other equipment installations, such as in shipping containers, may still require significant amounts of sinusoidal vibration testing.

Shock tests are often required of many types of equipment. Such tests are meant to simulate those operational (for example carrier landing of aircraft) or handling (for example bench handling or drop) conditions which lead to impact loading of the equipment.

In addition to the weight and dynamic loadings which isolators must react, there are some static loads which can impact the selection of the isolator. An example of such loading is that imposed by an aircraft in a high-speed turn. This manoeuvre loading must be reacted by the isolator and can cause, if severe enough, an increase in the isolator size. These loads are often superposed on the dynamic loads. This particular aspect will be focussed in details in Chapter 4.

Allowable system response is another important information needed in order to appropriately choose the correct isolator. The equipment manufacturer or user should

have some knowledge of the fragility of the unit. This fragility, related to the specified dynamic loadings, will allow the selection of an appropriate isolator. This may be expressed in terms of the vibration level versus frequency or the maximum shock loading which the equipment can endure without breaking.

The specification of allowable system response should include the maximum allowable motion of the isolated equipment. This is important to the selection of an isolator since it may define some mechanical, motion limiting feature which must be incorporated into the isolator design. It is fairly common to have an incompatibility between the allowable "sway space" and the motion necessary for the isolator to perform the desired function. In order for the isolator to give a certain level of performance, it is required that a definite amount of motion be allowed. Problems in this area typically arise when isolators are not considered early enough in the process of designing the equipment or the structural location of the equipment.

The environment in which the equipment is to be used is very important to the selection of an isolator, particularly the temperature. Variations in temperature can cause variations in the performance of many typical vibration isolators. Consequently, it is quite important to know the temperatures to which the system will be exposed. The majority of common isolators are elastomeric. Elastomers tend to stiffen and gain damping at low temperatures and to soften and lose damping at elevated temperatures. The amounts of change depend on the type of elastomer selected for a particular installation.

Other environmental effects from humidity, ozone level, atmospheric pressure, altitude, etc., are generally minimal and may be typically ignored. Some external factors that may not be thought of as environmental may impact the selection of an isolator. Fluids (oils, fuels, coolants, etc.), which may be in the area of the isolators, may cause a change in the material selection or the addition of some form of protection of the isolators. Also, light may effect the correct operation of some optical sensors.

The length of time for which an isolator is expected to function effectively is another strong determining factor in the selection or design process. Vibration isolators, like other engineering structures, have finite lives. Those lives depend on the loads imposed on them. The prediction of the life of a vibration isolator depends on the distribution of loads over the typical operating spectrum of the equipment being isolated. Typically, the longer the desired life of the isolator, the larger that isolator

must be for a given set of operating parameters. The definition of the isolator operating conditions is important to any reliable prediction of life.

1.1.4 Semi-active vibration control

"In semi-active vibration control, the stiffness or damping properties are changed to adjust the internal dynamic forces in order to minimise the response" (Brennan, 2003). For example air springs allow a system to change its stiffness, while electro/magneto rheological fluids allow a system to change its damping. Another example of semi-active control is obtained using tunable vibration absorbers, and in particular passive electronic damping using piezoelectric ceramics is a less temperature-sensitive and more tuneable alternative to viscoelastic damping treatments. In this damping technique, the mechanical energy of the structure is converted to electrical energy using piezoelectric materials. The high mechanical stiffness of the piezos enables efficient energy transfer to the piezo damper. The electrical energy is dissipated as heat in an electrical shunt circuit, allowing for specific vibration frequencies to be targeted and damped electronically.

1.1.5 Active vibration control

Active control augments the structure with sensors, actuators and some form of electronic control system, which specifically aims to reduce the measured vibration levels. In contrast to passive vibration control, active vibration control systems do require external assistance. They depend essentially upon a source of power to drive active devices, which may be electromechanical, electrohydraulic or electropneumatic actuators.

Initial investigations into active vibration control were primarily interested in controlling tonal excitations. This is because of the relative simplicity of obtaining an appropriate reference signal, compared to broadband excitation. Discussion of the control of tonal excitation then addresses other subject areas, such as isolation of rotating machinery from supporting structures.

Active vibration control systems are ideally suited for use in the low-frequency range, below approximately 1000 Hz. Although higher frequency active control systems have been built, a number of technical difficulties, both structural and electronic (where higher sampling rates are required), limit their efficiency. At higher frequencies, passive systems also become more cost effective. A complete vibration

control system generally consists of active control for low frequencies and passive control for higher frequencies.

In addition, passive vibration damping and cancellation strategies become ineffective when the dynamics of the system or the frequencies of the disturbance vary with time. Moreover, active systems can provide increased effectiveness in controlling sound and vibration compared to passive approaches. Also, it is not suitable to attach large passive vibration control appendages, such as a tuned mass damper, to some applications. Active damping and cancellation control can address these concerns.

Due to remarkable advances in sensor, actuator, and more importantly computer technologies in recent years, active systems have become cost effective solutions to most sound and vibration control problems. Active damping is sometimes necessary to achieve greater performance, or to produce controlled system properties.

1.1.6 Active vibration isolation

To provide a more favourable static and dynamic stiffness compromise in an active isolation systems, hybrid solutions must be used. These are usually based on mounts and actuators. When an active isolator is designed, two configurations are possible. The secondary actuator can be placed either in series or in parallel (this latter case is shown in Figure 1.5) with the passive mount. Blackwood and von Flotow (1993) investigated the first configuration by coupling a piezoelectric actuator in series with a passive mount.

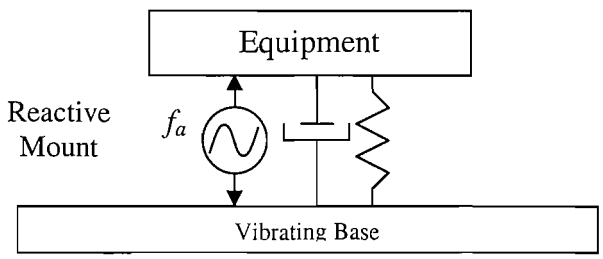

Figure 1.5 *The secondary actuator is in parallel with the passive mount.*

However, the effectiveness of such a mounting design was shown to be heavily dependent upon the high stiffness of the actuators. Due to the small deflection capacity of piezoelectric actuators, the use of such actuation is limited to the isolation of very small amplitude motion of base structure. In many situations, the base

vibration is of the order of millimetres. As a result, an actuator with a longer stroke, such as an electromagnetic shaker, installed in parallel with the passive mount, is required. An experimental study was conducted by Serrand and Elliott (2000) on the active vibration isolation of a rigid equipment structure using two electromagnetic shakers, which were installed in parallel with two passive mounts.

An active isolator can be implemented using various feedback control strategies, among which independent direct velocity feedback control is one of the most popular. The absolute velocities of the equipment structure are measured at each mounting point and directly fed back to the actuators driving that point. Using independent velocity feedback control, Kim *et al.* (1999 and 2001) investigated a four-mount active vibration isolation system with a rigid equipment structure.

The work by Huang *et al.* (2001a,b) investigates a similar four-mount system for active vibration isolation of a flexible equipment structure. Particular emphasis is placed on the isolation of low frequency vibration (0~200Hz), for which the mounts can be assumed to behave as lumped springs and dampers. The main objective was to investigate the control performance and stability issues associated with the four-mount vibration isolation system when the additional flexibility of the equipment structure is introduced. Active isolation experiments were first implemented on a rigid base before moving to the final flexible base, in order to have a full understanding of the control mechanisms. With the rigid base structure, the actuator force that reacts off the base has no effect on the equipment velocity and so the actuator force on the equipment and velocity sensor on the equipment are, in principle, collocated. It was shown that under these conditions the control system is unconditionally stable. When the base structure is not rigid, however, the stability of the control system cannot be guaranteed a priori. Here, the equipment velocity is caused by both the actuator force acting directly on the equipment and the reactive actuator force causing the base to move. However, a careful analysis has demonstrated that good stability properties are still obtained.

1.1.7 Reactive or inertial actuators

Actuators are used in active vibration control to generate a secondary vibrational response, and in practice they can be configured either to react off the base structure or function as an inertial actuator (also called proof-mass actuator). Inertial actuators do not need a "ground" to push against, so they can be used as modules that can be

directly installed on a vibrating structure. This fact makes inertial actuation particularly suitable for stand-alone applications. This was investigated by Elliott *et al.*, (2001a), and Benassi *et al.*, (2002a,b,c,d) and this topic, being the core of this thesis, will be extensively discussed in the next chapters.

1.1.8 Actuator types

The actuation means suggested in the literature vary from servohydraulic devices to using controllable materials, such as piezoelectric devices. Piezoelectric actuators produce an electric charge when mechanically strained; conversely, they produce mechanical strain when an electric field is applied. There are two broad classes of piezoelectric materials used in vibration control: ceramics and polymers. The piezopolymers are mostly used as sensors, because they require high voltages and have a limited control authority. The best-known piezopolymer is poly-vinylidene-fluoride (PVF2). Piezoceramics can be used as actuators and sensors over a wide range of frequencies, including ultrasonic applications. They are well suited for high precision up to the nanometer range. The most common piezoceramic is Lead Zirconate Titanate (PZT). Ceramic piezoelectric actuators are stiff and provide more actuation force than polymers, and they can be stacked for increased actuator displacement (Morgan Electro Ceramics, 2001). A lot of work on vibration control using piezos has been carried out (D'Cruz, 1998), and significant results have been obtained, in particular by Guigou *et al.* (1994), Garcia-Bonito *et al.* (1998), Balakrishnan (1999), Alvarez-Salazar (1999), Brennan *et al.* (1999) and Yousefi-Koma and Vukovich (2000). Although these approaches have been extensively applied to simple structures, such as beams and plates, it has been suggested that their application to more realistic structures is difficult and complicated by the large number of sensors and actuators that are needed to adequately control the structure (Carabelli *et al.*, 2000, Sun *et al.*, 2001, and Wang *et al.*, 2001). The challenge lies in managing all the sensors and actuators that are needed to define and control the complicated modal characteristics of a practical structure. This was illustrated by Blackwood and von Flotow (1993) and Baek and Elliott (2000). Another limitation to more widespread adoption of piezoelectric vibration suppression technology has been the lack of integration of the piezo transducers and the electronics used for power distribution, sensor conditioning and control.

The THUNDER piezoelectric actuator is a newly developed active control device that possesses many advantages compared to other classical piezoelectric actuators. Particularly, its capacity in generating high displacement and its inherent high load capacity make it an ideal candidate in active isolation applications (Marouze' *et al.*, 2001). THUNDER is developed by NASA Langley Research Center, and its high displacement range and high load capacity result from its particular fabrication process.

As was previously explained, an active structure consists of a structure fitted with a set of actuators and sensors coupled by a controller. If the bandwidth of the controller includes some vibration modes of the structure, its dynamic response must be considered. If the set of actuators and sensors are located at discrete points of the structure, they can be treated separately. The distinctive feature of smart structures is that actuators and sensors are often distributed and have a high degree of integration inside the structure, which makes a separate modelling impossible.

From a mechanical point of view, classical structural materials are entirely described by their elastic constants, relating stress and strain, and their thermal expansion coefficient, relating strain to temperature. Smart materials are materials where strain can also be generated by different mechanisms involving temperature, electric field or magnetic field, etc., as a result of some coupling in their constitutive equations.

The most celebrated smart material, beside piezos, is Shape Memory Alloys (SMA, Choi *et al.*, 2000). They can recover large strains and are compact, but have no sensing capabilities. Although two-way applications are possible after education, SMAs are best suited for one-way tasks such as deployment. In any case, they can be used only at low frequency and for low precision applications, mainly because of the difficulty of cooling. Fatigue under thermal cycling is also a problem. SMAs are not used much in vibration control, although an interesting vibration neutralizer is under investigation at ISVR (Brennan, 2003).

Another class of materials for active control is magnetostrictive materials such as Terfenol-D. These have been available for more than one hundred years, and are similar to piezoelectric materials in the sense that they change shape when exposed to a magnetic field (as opposed to an electric field for piezoelectric materials). The main advantage of magnetostrictive materials is that they can produce very high strains relative to piezoelectric materials (von Flotow *et al.*, 1994a,b). They have been applied in many fields, including active isolation of aircraft components (von Flotow,

1988 and 1997, McConnell, 1992, Sutton *et al.*, 1997, and Tzou and Ding, 2001). The maximum response is obtained when the material is subjected to compressive loads. Magnetostrictive actuators have a long lifetime and can be used in high precision applications.

Electrorheological (ER) fluids and magnetorheological (MR) fluids are materials that respond to an applied electric or magnetic field with a dramatic change in rheological behaviour. The essential characteristic of these fluids is their ability to reversely change from free-flowing liquids to semi-solids, having controllable yield strength, in milliseconds when exposed to either an electric or a magnetic field. By contrast with ER fluids, MR fluids have the advantages of having higher yield strength, being insensitive to pollutions, and using low voltage power. Semi-active and active control applications of controllable fluid technology in real-world systems have grown steadily (Meng *et al.*, 2001, and Lord, 2002). Examples include controllable dampers for vehicular suspension systems, real-time rotary brakes that provide force feedback in steer-by-wire systems, rotary and linear dampers, etc. However, high power amplifiers are required and a rather complex magnetic circuit is needed in order to achieve good performance.

1.1.9 Sensing

The range of available devices to measure position, velocity, acceleration, and strain is extremely wide, and there are more to come, particularly in optomechanics. Displacements can be measured with inductive, capacitive and optical means (laser interferometer, Ghoshal *et al.*, 2000); the latter two have a resolution in the nanometer range. Piezoelectric accelerometers are very popular but they cannot measure a DC component. Strain can be measured with strain gauges, piezoceramics, piezopolymers and fiber optics. The latter can be embedded in a structure and give a global average measure of the deformation.

Presently, a large safety factor is used in determining routine maintenance schedules for critical parts, such as replacement of skins for aircraft wings or damage detection in large space structures, because any failure during operation could prove catastrophic (Friswell *et al.*, 1997b, and Friswell and Inman, 1999b). Assuming that the location of the structural damage can be identified at its inception, one could apply active vibration control on the structure as a means of reducing stresses in the damage zone, hence ensuring that the damage does not grow rapidly with time. However, the

probability of having an error sensor at the damage location is small, which indicates that a different approach would be required for implementing the active control. Work is reported (Dunn and Garcia, 1997) aimed at developing an active vibration control system that allows the control to minimize the stress or vibration at any arbitrary point on the vibrating structure, even where there is no error sensor present. This is accomplished by using what are referred to as "virtual sensors". These virtual sensors use information from physical sensors at other locations on the structure to estimate the vibration response at the virtual sensor location. This approach offers the possibility of being able to control the structural vibration at any desired location on the structure. The development of health monitoring systems also include the identification of specific modes. Modal sensors and actuators have been studies in order to reduce the problem of spillover and also reduce the number of transducers (Gawronski, 2000, Friswell, 2001).

1.1.10 Control strategies and issues

The active isolation control system used for vibration isolation purposes can be either feedforward or feedback. When a signal correlated to the disturbance is available, feedforward adaptive filtering constitutes an attractive alternative to feedback for disturbance rejection; it was originally developed for noise control, but it is very efficient for vibration control as well. Its principle is explained in Figure 1.6.

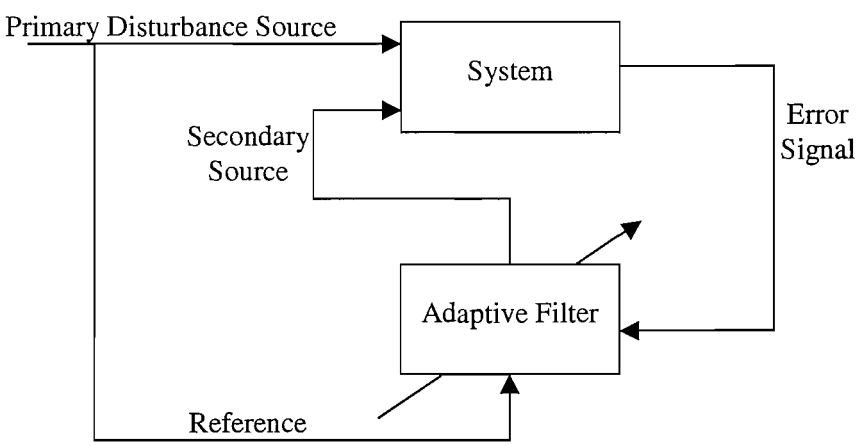

Figure 1.6 *Principle of feedforward control.*

The method relies on the availability of a reference signal correlated to the primary disturbance. This signal is passed through an adaptive filter, the output of which is applied to the system by secondary sources. The filter coefficients are adapted in such a way that the error signal at one or several critical points is minimized. The idea is to produce a secondary disturbance that cancels the effect of the primary disturbance at the location of the error sensor. Of course, there is no guarantee that the global response is also reduced at other locations and, unless the response is dominated by a single mode, there are places where the response can be amplified. The method can therefore be considered a local one, in contrast to feedback control, which is global. Unlike active damping, which can only attenuate the disturbances near the resonances, feedforward works for any frequency and attempts to cancel the disturbance completely by generating a secondary signal of opposite phase.

The method does not need a model of the system, but the adaptation procedure relies on the measured impulse response. The approach works better for narrow-band disturbances, but broadband applications have also been reported. Because it is less sensitive to phase lags than feedback, feedforward control can be used at higher frequency . This is why it has been so successful in acoustics (Grewal *et al.*, 2001).

Feedforward control has also been used extensively in the active machinery vibration isolation involving a time domain Least Mean Square (LMS) adaptive filter (Sommerfeldt *et al.*, 1990, Jenkins, 1993, Jiang *et al.*, 1993, Elliott *et al.*, 1987 and 1994, and Fuller *et al.*, 1996). The use of an LMS controller allows the systems to track the disturbance frequencies as they change, therefore providing optimal isolation in the entire frequency range of interest. The efficiency of this method depends on determining an appropriate reference signal. When this signal cannot be obtained easily, a feedback control has to be used. For example, for known periodic disturbances, feedforward control may indeed be preferable, as shown by Nelson *et al.* (1987), but in many cases vibrations are not periodic in nature and it is not possible to obtain information of the incoming disturbance soon enough for a feedforward control to be effective (El-Beheiry and Karnopp, 1996). Under those circumstances, feedback control is considered the best method.

A typical feedback control system is shown in Figure 1.7, in which $G(j\omega)$ is the frequency response of the plant and $H(j\omega)$ is the frequency response of the feedback

controller. The design problem consists of finding the appropriate compensator $H(j\omega)$ such that the closed-loop system is stable and behaves in the appropriate manner.

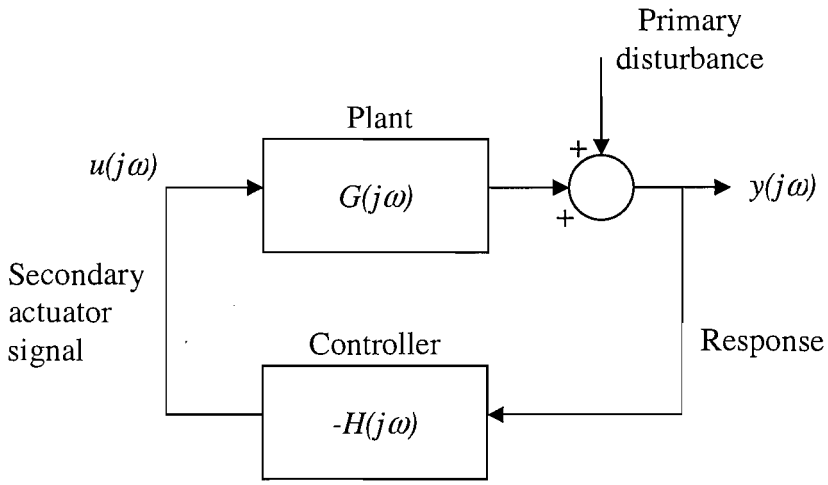

Figure 1.7 *Block diagram of a negative feedback control system including the plant and the controller.*

A very large number of papers have been concerned with vibration isolation problems and feedback active vibration control methods have been discussed. Karnopp (1995) proposed a velocity feedback control method for obtaining a non-resonant response, which has been applied to various vibration isolation systems.

Position feedback has been investigated by Friswell and Inman (1999a). This strategy makes the rigidity increase and the transmissibility decrease, as shown by Bhat (1991a,b,c). However, to have zero transmissibility, the rigidity must be infinite, so the feedback coefficient must be infinite. Hence it is impossible to have zero transmissibility with the usual feedback control methods. An interesting discussion of the theory of velocity or position feedback control of large space structures is presented by Goh and Caughey (1985). In their work, the problem of instability caused by the interaction of the actuator dynamics is analysed and it is shown that velocity feedback can be unstable, while position feedback was a valid alternative. However, in their study an inertial actuator, whose resonance frequency is very close to the resonance frequency of the controlled structure, was used. As will be discussed later in this thesis, for these applications, the actuator resonance must have a lower natural frequency than that of the controlled structure.

The trade-off between damping low-frequency resonances and achieving good high-frequency isolation may be overcome by skyhook damping. This was investigated by Beard, von Flotow and Schubert (1994). In their study, skyhook damping implementation was possible using reactive actuators since no base dynamics were taken into account in the control frequency range, so that an inertial ground was available. The effect of skyhook damping has also been investigated for an infinite impedance base (Kim, Elliott and Brennan, 1999 and 2001), or for a base without significant mobility. Also, a passive implementation of a virtual skyhook vibration isolation system is investigated by Griffin *et al.* (2002). The design and realization of the virtual skyhook damper involves the design of both the primary and secondary suspension systems. The primary suspension system is designed to meet the static deflection criteria and uses low damping to provide low transmissibility at high frequencies. The secondary mass-spring-damper is tuned close in frequency to the primary system's resonance, and has high damping. This yields a lightly damped primary system whose motion is limited at resonance by the virtual skyhook damper without increasing the transmissibility at higher frequencies.

The stability of the feedback controller can be established from the frequency responses of the plant and controller, which are assumed to be individually stable. This is determined by whether the polar plot of the open loop frequency response, $G(j\omega)H(j\omega)$, encloses the Nyquist point (-1,0) (Skogestad and Postlethwaite, 1996). For example, if reactive actuators are used, the system can be described as a rigid piece of equipment, which is supported on top of a base by a set of mounts (springs and dashpots in general) and a reactive actuator. In this case a direct velocity feedback control proves to be unconditionally stable. This is shown by Serrand *et al.* (2000) and Benassi *et al.* (2002a). The real part of the plant's frequency response is always positive and the control loop has infinite gain margin and a phase margin of 90°, since its Nyquist plot is entirely on the right hand side of the imaginary axis.

In the study by Serrand *et al.* (1998 and 2000), the effect of the base structure dynamics on the formulation of direct velocity feedback control was investigated. In the case of a reactive implementation of the control actuators, the secondary forces were generated by reacting off the flexible base structure. Therefore the classical model of perfect skyhook damping was not valid and the stability of direct velocity feedback control had to be reconsidered (Balas, 1978). It was found that no instability

or vibration amplification was encountered from potential re-excitation of the flexible base by the secondary actuators in the frequency range of analysis. Moreover, changes in the dynamics of the base plate did not destabilize the control system, illustrating its robustness.

On the other hand, considering the effects of the equipment and the mounts on the stability of the overall system, there are severe limitations. In theory, direct velocity feedback is unconditionally stable, provided the equipment can be modelled as a rigid body and the mounts as a lumped parameter spring and dampers. In practice, instability occurs at very low frequencies due to phase shifts of the electrical equipment used, the flexibility in the equipment structure, and the effect of resonances in the mount. It is found that although an ideal system might be unconditionally stable, real systems are often conditionally stable. Causes of instability at low and high frequencies in real systems are investigated by Miller *et al.* (1992a,b), Li and Gibson (1992), Ahmadian *et al.* (1993), and Ananthaganeshan *et al.* (2001).

The practical implementation of feedback control can be either analogue (Swanson and Miller, 1993, Franklin, 1994, and Howard and Hansen, 1997) or digital (Gerhold and Rocha, 1987, Hodgson, 1991, and Melcher, 1992). The essential components in an active control system are the sensor (to detect the vibration), an electronic controller and actuators. They all play an important role in active vibration control and often place limits on the system performance (Gardonio *et al.*, 1996, Elliott *et al.*, 1998 and 2001a). Accelerometers often need signal conditioning devices, which consist of filters to reject unwanted signals. These filters introduce extra phase shift at low frequencies, which is sometimes critical to the stability of the feedback vibration control system (Ananthaganeshan *et al.*, 2001 and Benassi *et al.*, 2002a). Actuators are used in active vibration control to generate a secondary vibrational response, and in practice they can be configured either to react off the base structure or function as an inertial actuator. This was investigated by Elliott *et al.*, (2001b). This choice also influences the stability margin. In general, the design of a feedback controller involves a trade-off between performance (the attenuation of the disturbance) and robust stability (the ability to remain stable under changing conditions).

An important question in active vibration control relates to actuator and sensor placement (Hiramoto *et al.*, 2000). The use of co-located sensor-actuator pairs is attractive, because control loops for co-located sensor-actuator pairs can easily be guaranteed to be robustly stable (Sun, 1996 and Preumont, 1997 and 2001).

Furthermore, because of the relative ease of implementation, active structural elements for vibration control with co-located sensing and actuation have gained much interest.

In conclusion, applications with actuators, controllers and passive mounts in an active isolator package provide many benefits including simplicity, effective vibration isolation, noise attenuation, higher static stiffness, dynamic adaptability, and safety. This suggests that there is ample motivation for the use of active mounting systems.

1.1.11 Modelling

Many studies of isolators involve systems having only a single mount vibrating in one direction (Gardonio and Elliott, 1996), and analytical methods can be used effectively. A more detailed study is needed for a system with many mounts (Sutton *et al.*, 1997, Brennan, 1997, and Brennan *et al.*, 2000), each of which is a distributed flexible component. The finite element method (FEM) could be employed for this type of study, although it generates large matrix models that require long simulations on a relatively small frequency range of analysis (Petyt, 1998). On the other hand, finite element models are very appropriate for describing complex structures, compared to analytical methods, and can be corrected using test results (Mottershead and Friswell, 1993). Two alternative approaches are also suitable. The first one is the statistical energy analysis (SEA) approach studied in great detail by Lyon and Dejong (1995) and Ohayon and Soize (1998). This approach is based on power transmission concepts using coupling factors between source and receiver structures, assuming the two structures to be of either infinite or semi-infinite extent. Unfortunately, this simplification could lead to some problems in the so-called low-mid-frequency range. The second approach is based on impedance and mobility matrices (IMM). Recent studies on active isolation by Gardonio *et al.* (1997a,b, 1998, 1999, 2000) have suggested the need for mathematical models which give a detailed analysis of the coupled vibration transmission mechanism and, at the same time, provide a summary of the overall phenomenon and allow a global interpretation of the dynamics of the active isolator system. Good results have been obtained by using the IMM approach, where the system is divided into individual components and each component is studied in terms of input and transfer mobilities or impedances (Liang *et al.*, 1992). The form of a point mobility of a typical structure depends upon the frequency range. At low frequencies, a freely suspended structure moves as a rigid body in a possible

six-degree-of-freedom system. Alternatively, a structure that is connected to ground behaves as a spring and dashpot combination. These are the simplest mobility elements, which may be added in various arrangements to model more complicated structures in what is called a lumped element formulation. In the second zone, at higher frequencies than the rigid body motion, the structure is free to move in its modes of natural vibration. The mobility of each mode is that of a single degree of freedom system. The point mobility of a structure therefore looks like the summation of all the modal responses. At high frequencies, or with heavy damping, the modes overlap in such a way that the mobility tends to resemble that of an equivalent infinite structure (Meirovitch, 1967 and 1990, and Crandall *et al.* 1978).

Formulae for point and transfer mobilities of various homogeneous structures such as beams, plates, and shells are given by Bishop and Johnson (1960) and Leissa (1969).

In this thesis, a matrix model has been used which assumes that the system is divided into elements, the dynamics of each of which, modelled either as lumped or distributed systems, is evaluated using point or transfer mobility terms.

1.1.12 Applications

Isolating a piece of delicate equipment from the vibration of a base structure is of practical importance in various engineering fields. Examples are the vibration isolation of the instrument boxes in an aircraft and the isolation of telescopes on satellites. An active isolation system can be implemented over a broad frequency band using different feedback control strategies (Gennesseaux, 1997).

There are many possible applications for damping systems (Ivers and Miller, 1991), including space structures (Kaplow and Velman, 1980), aircraft, automobiles, electronic components (Scheuren *et al.*, 1995), satellites, marine structures, consumer products, disk drives, and defence systems. One industry that is particularly interested in active damping systems is the semiconductor industry. Many machines used by the semiconductor industry are sensitive to disturbances from floor vibration from sound pressure deviations, and from their own internal moving parts (Alvarez-Salazar, 2002). Examples include laser-based systems and photolithography systems.

The Navy is also interested in active vibration damping to create an undetectable submarine (Senior, 2002). Currently, the five main sources of submarine noise and vibration are: machinery vibration, propeller/propulsion noise and vibration, global hull resonances, flow noise, and cavitations. The first three of these sources are tonal

noises that have frequencies in the range of 10 to 100 Hz. The last two are broadband noises, which means they have frequencies exceeding 10 kHz. Due to the limited recoverable strains of current materials and the constant need for novel active damping system, new active damping materials are to be explored. A very interesting and promising active vibration control solution is the "Smart Spring" mounting system, developed by BAE Systems and ALSTOM for the US Office of Naval Research (Daley *et al.*, 2002). The main application of this technology is the machinery isolation from the hull in marine vessels. The "Smart Spring" mounting system is a hybrid active/passive system, based on a force feedback, which aims to zero the mounting stiffness.

1.2 Contributions of the thesis

The contributions of this thesis can be summarized as:

- The theoretical analysis and experimental study of the stability and performance of an inertial actuator with inner force feedback control.
- The theoretical design and experimental construction of a novel device, based on an inertial actuator with inner displacement feedback, for active vibration control.
- The theoretical and experimental development of an active vibration isolation system using an inertial actuator with either inner force or inner displacement feedback control.
- The theoretical and experimental analysis of the equivalent impedance and its approximations for active vibration control of panels.

1.3 Overview of the thesis

The first necessary step for developing and understanding how inertial actuators can be used to either isolate sensitive pieces of equipment or suppress the vibrations of a plate is to analyse their dynamic behaviour and their topologies of construction. In Chapter 2 the mechanical model of a typical inertial actuator is investigated, followed by the analysis of the electro-magnetic components that are actually needed to supply the required force. Before entering the main part of the thesis, Chapter 2 reviews the main properties of the inertial actuators that have been used in the experimental phases of this research.

Chapter 3 presents the theory behind the use of an inertial actuator with inner feedback control. In particular, when the total transmitted force by the inertial actuator is measured and fed back to the actuator, the actuator resonance frequency is lowered as if mass was added to the actuator moving mass. On the other hand, if the measured total transmitted force is integrated before being fed back, the overall effect on the actuator is to add damping to it, implementing, in essence, a skyhook damper. The first strategy turns out to be very sensitive to stability issues, even though it performs very well. The second strategy, however, is more robust, but it does not perform as well as the first. The idea of implementing a phase-lag compensator as a trade-off between the two previous strategies is then discussed.

Alternatively, we would like to be able to access the internal structure of the inertial actuator, modify its resonance frequency if it happens to be too high for the application and apply suitable control strategies in order to minimize the equipment velocity in a vibration isolation system, or minimize the total power in a vibrating panel. In Chapter 4 a new inertial actuator is presented, which suggests a very interesting way to design an inertial actuator using inner displacement feedback control, which turns out to be more robust, simpler and therefore cheaper than the strategies described in Chapter 3.

In Chapter 5 the active vibration isolation problem will be discussed using an inertial actuator and equipment velocity feedback. A review of different single loop and

optimal control strategies for active vibration isolation using an inertial actuator will be presented. For all of them, a matrix model has been used which assumes that the system is divided into four elements: base structure, passive mounts, equipment, and inertial actuator. Feedback stability margins and performance are considered for each case. In particular, once the theoretical analysis is completed, a realistic case using real commercial components is analysed. The aims of the chapter are to introduce one of the practical applications of an inertial actuator and to discuss two of the main constraints that a designer must take into account when working on vibration control with inertial actuators. These constraints are the fact that the inertial actuator resonance frequency has to be lower than the first resonance frequency of the controlled structure, and the fact that the resonance must be well damped in order to guarantee good stability margins.

Chapter 6 analyses the active vibration isolation problem when the piece of equipment is installed (through passive mounts) on a flexible base and controlled with an inertial actuator having inner actuator force feedback. The specific problem considered in Chapter 6 is what can be done to minimize the equipment velocity using the devices described in Chapter 3, when the inertial actuator resonance frequency is lower than the first equipment resonance frequency. In Chapter 7, experiments are described to compare with the theoretical findings.

In Chapter 8, the same piece of equipment is controlled using an inertial actuator with inner actuator displacement feedback. Chapter 8 suggests that using the device described in Chapter 4 for vibration isolation guarantees good stability margins and performance. The critical importance of the proof-mass of the inertial actuator will also be discussed. The experiments in Chapter 9 serve to verify and validate the theory. They also demonstrate the ability to build such a device for active isolation purposes.

Active suppression of panel vibration is an important issue in many engineering applications and meeting stringent constraints such as maximum strength and minimum weight is a difficult task to accomplish.
Chapter 10 addresses these issues and analyses optimal solutions in order to minimise the total power of a vibrating plate. A vibrating flexible finite plate is considered and

its equivalent impedance for global control is obtained. The study is performed at a theoretical level, and aims to determine approximations to the equivalent impedance in order to reduce the total power of the vibrating plate. These results are then compared to the performance of passive treatments based on springs and dampers.
In Chapter 11, approximations to the equivalent impedance are proposed, obtained by a passive device as well as an active device, based on a modified inertial actuator with inner displacement feedback control. The vibration suppression of a flexible plate is then investigated experimentally, using the modified inertial actuator.

The overall results of this research are then discussed in the conclusions in Chapter 12, along with suggestions for further future work.

Chapter 2

Inertial actuator review

2.1 Introduction

An inertial actuator is a mass supported on a spring and driven by an external force. The force in small actuators is normally generated by an electromagnetic circuit. The suspended mass can either be the magnets with supporting structure or in some cases the coil itself. Unlike reactive actuators, inertial actuators do not need to react off the base structure, so they can be used as modules that can be directly installed on a vibrating structure. This feature makes them very useful.

Inertial actuators are mainly used for active control purposes (Holloway, 1993), including active vibration control of space structures (Garcia *et al.*, 1995), active isolation systems on satellites (Flint *et al.*, 2000) and active noise and vibration control on turbo-prop aircraft (Hinchliffe *et al.*, 2002). On a larger scale, applications of inertial actuators can be found in civil structures. In actively controlled civil structures, inertial actuators are common because the can generate the large forces required. On a smaller scale, inertial actuation can be used to suppress vibration and structure-borne noise using MEMS-based active tuned mass dampers (Dosch *et al.*, 1995).

2.2 Dynamic model

A simple mechanical model of an inertial actuator is shown in Figure 2.1. A proof-mass, m_a, is suspended on a spring, k_a, and a damper, c_a, and in parallel with them, an actuator force f_a drives the proof-mass. The presence of an inertial force f_i acting on the inertial actuator mass must also be considered. v_a and v_e are, respectively, the moving mass velocity and the base velocity.

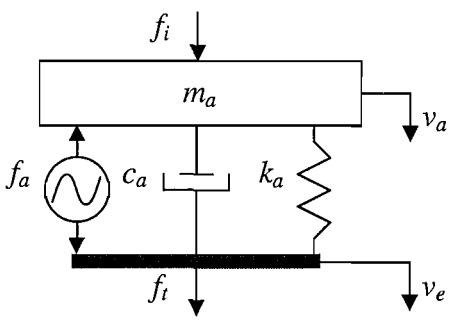

Figure 2.1 *Mechanical model and sign convention of an inertial actuator.*

The equation describing the dynamics of the system in Figure 2.1 is given by

$$j\omega m_a v_a + c_a(v_a - v_e) + k_a(v_a - v_e)/j\omega = f_i - f_a, \tag{2.1}$$

where v_a and v_e are complex velocities and an $e^{j\omega t}$ time dependence is assumed. Important parameters in characterising the behaviour of an inertial actuator are its resonance frequency, which is given by

$$\omega_a = \sqrt{\frac{k_a}{m_a}} \tag{2.2}$$

and the actuator damping ratio, defined as

$$\zeta_a = \frac{1}{2}\frac{c_a}{\sqrt{k_a m_a}}. \tag{2.3}$$

The transmitted force f_t is a linear function of the actuator force f_a and the equipment velocity v_e, and may be written as

$$f_t = T_a f_a - Z_a v_e, \tag{2.4}$$

where

$$T_a = \frac{-\omega^2 m_a}{k_a - \omega^2 m_a + j\omega c_a} \tag{2.5}$$

is the blocked response of the actuator and

$$Z_a = \frac{j\omega m_a k_a - \omega^2 m_a c_a}{k_a - \omega^2 m_a + j\omega c_a} \tag{2.6}$$

is its mechanical impedance. The blocked response of a typical actuator with ζ_a = 4.7% is illustrated in Figure 2.2, showing the resonance at its natural frequency. At high frequency this response tends to unity, with no phase shift, indicating that the transmitted force f_t follows the actuator force f_a since the mass provides a stable inertial platform off which to react the force. The mechanical impedance of the actuator, as plotted in Figure 2.3, is mass-controlled at low frequency, stiffness-controlled at higher frequency and at the resonance frequency is dominated by the actuator's damping. It is given by the parallel of the stiffness term k_a and damping term c_a, with the series of the mass term m_a.

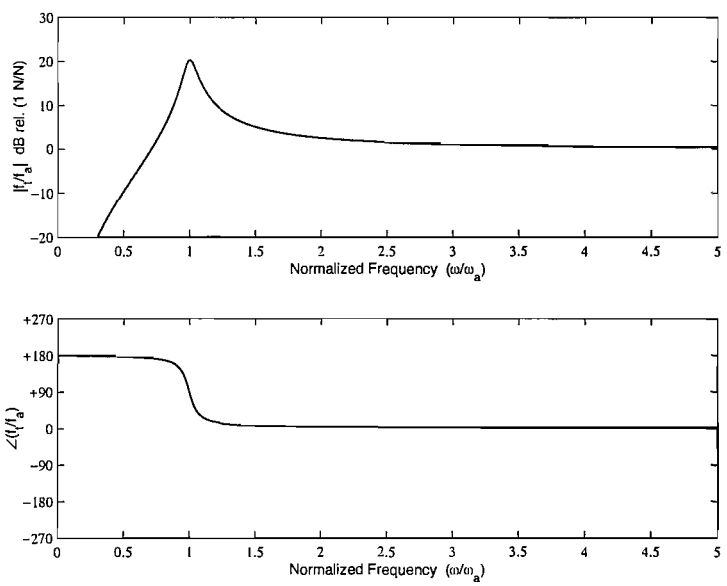

Figure 2.2 *Blocked response, transmitted force per unit actuator force, of the inertial actuator as a function of normalized frequency.*

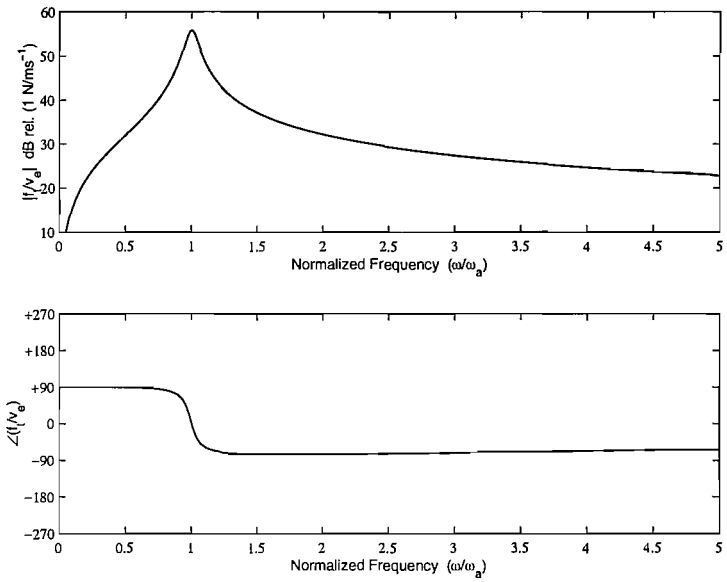

Figure 2.3 *Mechanical impedance, reaction force per unit imposed velocity, of the inertial actuator as a function of normalized frequency.*

The inertial response of the system is computed by setting the control force to zero in equation (2.1). The relative displacement x (between the actuator's proof-mass and the actuator's reference base) per unit inertial force f_i is therefore given by

$$\frac{x}{f_i} = \frac{1}{-\omega^2 m_a + j\omega c_a + k_a} \tag{2.7}$$

and is illustrated in Figure 2.4. In the low frequency regime (below the mechanical resonance) the actuator's inertial response is dominated by the mechanical stiffness. In fact, the response of the system to a static force is equal to $1/k_a$. The height of the resonance is dependent on any internal mechanical damping ($1/\omega_a c_a$) and in some cases eddy current damping. At this resonance, a phase shift occurs. Beyond the mechanical resonance, the inertial response is dominated by the actuator's mass. In this region, the phase of the transfer function is flat.

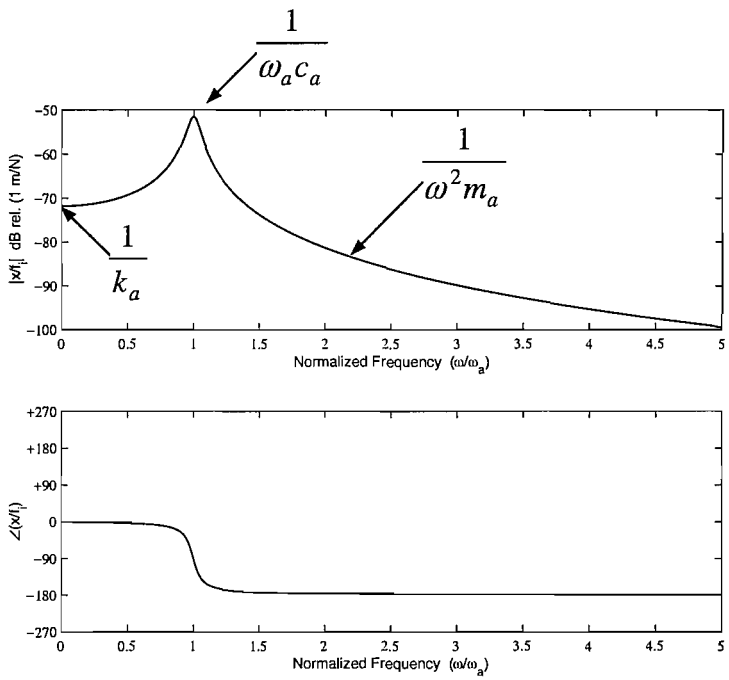

Figure 2.4 *Inertial response, relative displacement per unit inertial force, of the inertial actuator.*

2.3 Electro-magnetic model

In the previous section, in presenting and applying the dynamic model of the inertial actuator, the machine which would supply the force $f_a(t)$ to the system was not modelled, because the internal dynamics of such a machine are well beyond the bandwidth of the structural response. Consequently, they do not contribute significantly to the dynamics of the structure. However, knowing the model of the driving mechanism is essential in order to size and apply the right actuator for a given problem.

Inertial actuators are direct drive, limited motion devices that utilize a permanent magnet field and a coil winding to produce a force proportional to the current applied to the coil. These non-commutated electromagnetic devices are used in linear applications requiring linear force output, and high acceleration, or high frequency actuation. There is extensive literature concerning the modelling of these devices, and

it will be here only reviewed. For a more extensive description of their modelling and operation, see Basak (1996), Boldea *et al.* (1997), and CSA Engineering (2002).

The electromechanical conversion mechanism of an inertial actuator is governed by the Lorentz Force Principle. This law of physics states that if a current-carrying conductor is placed in a magnetic field, a force will act upon it. The magnitude of this force is determined by the magnetic flux density B, the current i, and the orientation of the field and the current vectors. Furthermore, if a total of N conductors (in series) of a length l are placed in the magnetic field, the force acting upon the conductors is given by

$$f = k_b BliN\,, \tag{2.8}$$

where k_b equals a constant. The ratio of the force to current $f/i = K_f$ in equation (2.8) is called the magnetic force constant. Figure 2.5 is a simplified illustration of this law of physics.

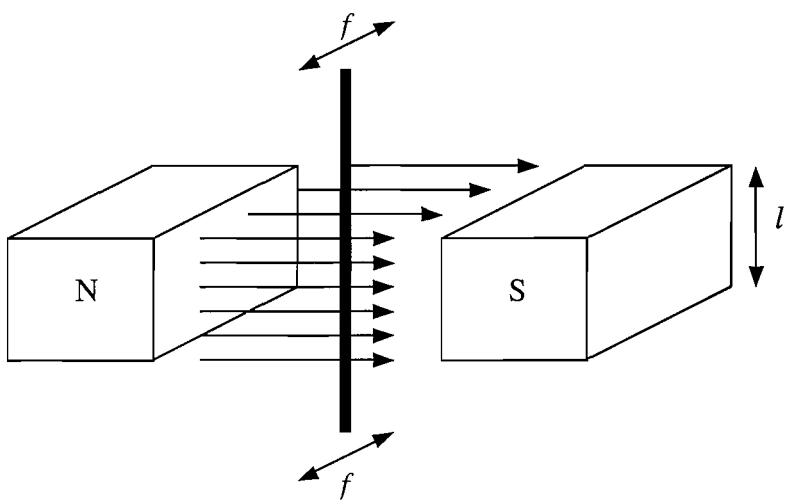

Figure 2.5 *Illustration of the Lorentz Force Principle*.

In Figure 2.5, the direction of the force generated is a function of the direction of current and magnetic field vectors. Specifically, it is the cross product of the two vectors. If current flow is reversed, the direction of the force on the conductor will also reverse. If the magnetic field and the conductor length are constant, as they are in an inertial actuator, then the generated force is directly proportional to the input

current. Figure 2.5 also illustrates that a conductor moving though a magnetic field will have a voltage induced across the conductor. The magnitude of the voltage, V_b, is dependent on the magnetic flux density, B, the length of the conductor, l, and the speed of the proof-mass, v_a, as the moving mass traverses the field. The voltage potential induced in the conductor (i.e. the back EMF) is given by

$$V_b = k_E \, l \, v_a \, N \ , \tag{2.9}$$

where k_E equals a constant and N equals the total number of the conductors of length l. Equations (2.8) and (2.9) can be restated as follows: a device that contains a permanent magnet field and a coil winding moving in the field will produce a force proportional to the current carried in the coil and a voltage proportional to the velocity of the proof-mass.

In its simplest form, an inertial actuator is a tubular coil of wire situated within a radially oriented magnetic field as shown in Figure 2.6.

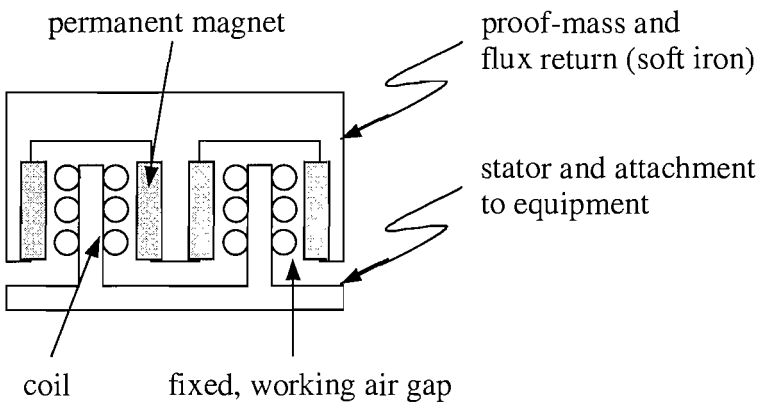

Figure 2.6 *Schematic of an inertial actuator.*

The field is produced by permanent magnets embedded on the inside diameter of a ferromagnetic cylinder, arranged so that the magnets facing the coil are all of the same polarity. An inner core of ferromagnetic material set along the axial centreline of the coil, joined at one end to the permanent magnet assembly, is used to complete the magnetic circuit. The force generated axially upon the coil when current flows though the coil will produce relative motion between the field assembly and the coil,

provided the force is large enough to overcome friction, inertia, and any other forces from loads attached to the coil.

An inertial actuator is a single-phase device. Application of a voltage across the two coil leads will generate a current in the coil, causing the coil to move axially along the air gap. The direction of the movement is determined by the direction of current flow in the wire. Within certain limits defined by the magnetic circuit geometry, the force produced by an inertial actuator is linearly proportional to the current through its coil, as shown in equation (2.8).

Figure 2.7 depicts the equivalent electrical circuit of an inertial actuator. When a voltage V is applied across the terminals, a current i circulates through windings of resistance R. At the same time, the actuator generates a back electromotive force (EMF), given by equation (2.9). This back EMF V_b is proportional to the proof-mass velocity, v_a , by a constant K_b and can be rewritten as

$$V_b = K_b\, v_a. \tag{2.10}$$

It must be said that it directly opposes the applied voltage and the ratio between K_f and K_b is constant. In addition, the actuator coil has an inductive voltage drop (this value is usually small, often negligible)

$$V_l = L(di/dt). \tag{2.11}$$

Letting V_c represent the iR drop across the coil, application of Kirchhoff's Voltage Law thus gives the equation that describes the inertial actuator

$$V = V_c + V_b + V_l. \tag{2.12}$$

It is now possible to derive all of the parameters needed in sizing and applying inertial actuators.

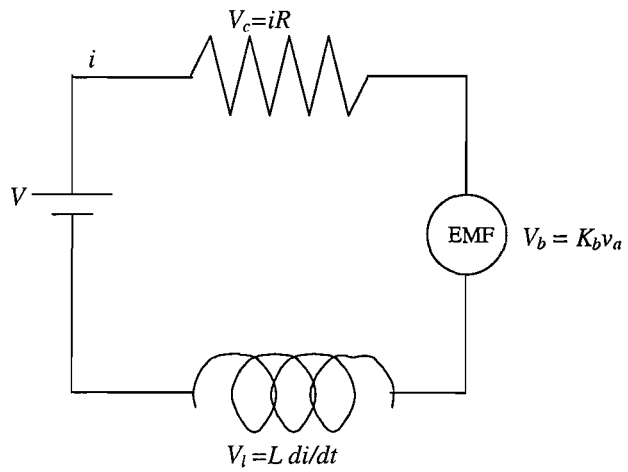

Figure 2.7 *Equivalent electrical circuit of an inertial actuator.*

2.4 Practical issues concerned with inertial actuator design

The performance of an inertial actuator is constrained by several factors, but in general the system will follow the equations described above. The first constraint is the possibility of fatigue of the mechanical spring elements that support the moving mass. Fatigue issues can generally be avoided through careful design of the flexures to ensure that the flexure material never experiences displacements that would push the stresses above allowable fatigue limits (Anderson *et al.*, 2001).

Depending on the actuation orientation with respect to gravity or other static accelerations, the effective end-stop limit can be reduced as the suspended mass is brought closer to one end stop. The worst case is when the actuator output axis is aligned with the local static acceleration field, which is the case in the problem analysed in this thesis. The severity of the gravity induced sag can be related directly to the inverse of the square of the internal resonance frequency (the relative displacement x of the proof-mass is given by $x = \frac{m_a g}{k_a} = \frac{g}{\omega_a^2}$, where $g \approx 9.8$ ms^{-2}).

Consequently the lower the frequency, the greater the sag. Unfortunately, low resonance frequencies are required by design in order to provide good performance, for example, in vibration isolation systems (Elliott *et al.*, 2001a).

The sag can be offset with a constant DC field (CSA Engineering, 2002) in the coil, but this creates a constant power consumption that might be undesirable in some applications. Another solution is to design the flexures to tolerate a large range of motion (Minus K Technology, 2002, and Motran Inc., 2002) such that any induced sag is a minor portion of the total stroke. This however introduces the possibility of cubic stiffening of the flexures in some designs which lead to distortions in the force output at large strokes. Finally, another interesting solution is proposed by Chase *et al.* (1999), where a controller, based on the measurement of the relative displacement of the proof-mass and its velocity with respect to the actuator's base, centres the moving mass at mid-stroke.

The performance of an inertial actuator is also limited by the resistive nature of the actuator coil. Due to this resistance, power is internally dissipated inside of the coil. Higher drive levels cause more dissipation and excessive levels could damage the coils. Finally, in the high frequency range there are generally limitations introduced by the power amplifiers used to drive the actuator. As a general rule, actuator force output scales with the available magnet volume and hence overall actuator weight (Flint *et al.*, 2000). Performance can be enhanced by using higher grade magnets but this can result in a serious cost penalty.

Stroke may be specified as the total displacement from one end of travel to the other end, or as a ± displacement from a mid-stroke reference. The mass or volume of an inertial actuator increases as its stroke and blocked force increase. This condition results from the added magnet materials needed in long stroke applications, as well as the additional back-iron needed to carry the flux of the added magnet. The trade off between maximum allowable stroke and maximum driving force must be considered (Lindner *et al.*, 1991, 1994, and 1997). In fact, $f_{a(\max)} = \omega^2 m_a x_{\max}$, which indicates that at low frequency larger strokes are allowed for a given maximum driving force. At higher frequencies, a given maximum driving force poses severe limitations on the stroke.

A second design constraint is given by the force constant expressed by equation (2.6), which can also be expressed in relation to the maximum allowable driving force through the equation $f_{a(\max)} = K_f i_{\max}$, where i_{max} is the maximum current that can be provided to the actuator.

2.5 Examples of inertial actuators

For the experiments, three kinds of inertial actuators were considered. The actuator used in Chapter 7 was a modified commercial shaker LDS Ling Dynamic Systems V101, while the actuator used in Chapter 9 was a modified ULTRA Electronics Active Tuned Vibration Attenuator (ATVA). The Aura AST-2B-04 inertial actuators were also tested, but the specs vary from one to another because precision manufacturing is not guaranteed. For this reason, they were not used in the active control experiments.

A simplified schematic of the LDS inertial actuator is assumed to be that one shown in Figure 2.6, in which the proof-mass is a moving permanent magnet and the stator holds the coil. In this configuration only one current is present and the movement of the proof-mass is in the vertical direction. It must be said that the LDS actuator was not taken apart in order to determine its exact construction, even if most of it can be found in the manuals. The product is sealed, and opening it would cause damage. A picture of an LDS V101 is shown in Figure 2.8. In reality, the LDS V101 is mostly used as a shaker which reacts off a base structure. Figure 2.9 shows how a simple modification allowed us to use this type of actuator as an inertial actuator. Four soft steel springs were used to sustain the weight of the case, which acted as the moving mass of the inertial actuator. Previously, four elastic bands were used, but they showed a very limited linear range.

Table 2.1 reports some of the main properties of the actuator. Apart from the dynamic mass, which was gathered from the manual, the other electro-mechanical properties were measured experimentally. The actuator was mounted on a rigid steel block, whose mass is 6 kg. At the base of the steel block, soft foam was placed in order to have the base dynamics at very low frequency. A force gauge was installed between the inertial actuator and the base. The measured dynamic response (output force per unit input voltage) is shown in Figure 2.10. After the resonance at about 11 Hz, the response is flat up to approximately 500 Hz.

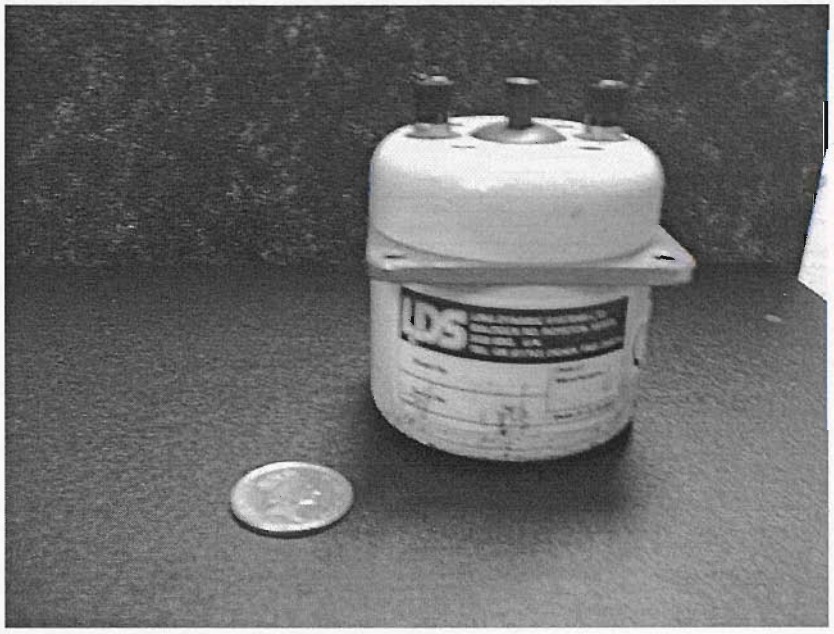

Figure 2.8 *LDS Ling Dynamic Systems V101 used in the experiments in Chapter 7.*

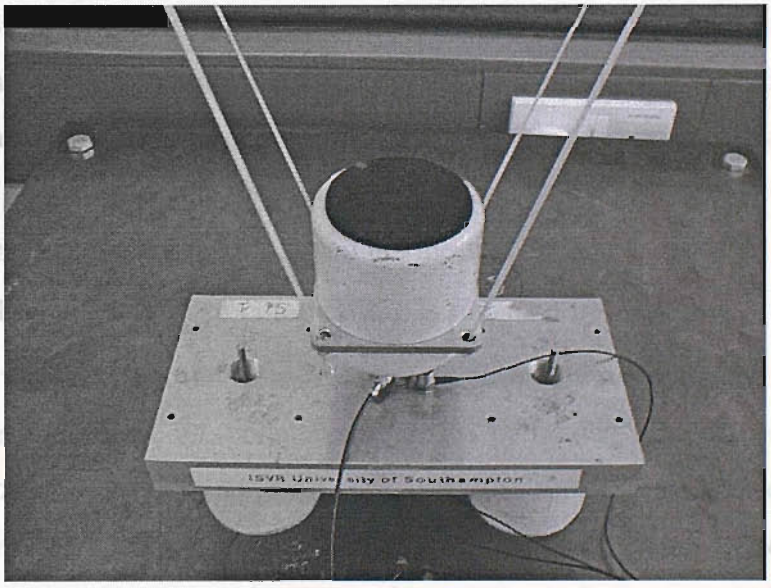

Figure 2.9 *Modification of the LDS Ling Dynamic Systems V101 in order to make it operate as an inertial actuator.*

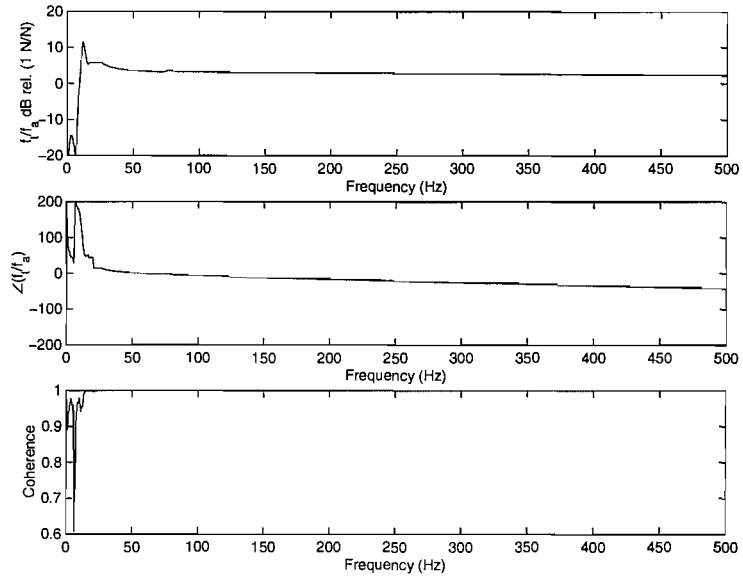

Figure 2.10 *Measured dynamic response of the LDS Ling Dynamic Systems V101 inertial actuator. The input is white noise, connected to the actuator's leads, and the output is the force gauge measurement.*

The phase plot in Figure 2.10 shows that an extra phase shift is present in the system, beside the 180° phase shift due to the actuator (Figure 2.2). This is mainly due to the inductance in the coil. In fact, the measurement of the electrical impedance (output voltage per unit input current) of the LDS V101 (Figure 2.11) reveals that the phase is not constantly zero over the frequency range. At 500 Hz, the magnitude of the electrical impedance is about 4.17 Ω and the mechanical resonance at 11 Hz is hardly noticeable. The magnetic force constant K_f is obtained by multiplying the values in Figure 2.10, which shows the measured force/voltage, by the values in Figure 2.11, which shows the measured voltage/current. In particular, the magnitude of the magnetic force constant ends up being reasonably flat above the resonance frequency, since the measured dynamic response slightly descends and the electrical impedance increases over frequency. Also, the phase of the magnetic force constant looks like the theoretical curve in Figure 2.2, where a 180° phase shift occurs. By summing the experimental phases in Figure 2.10 and Figure 2.11, it can be noted that the extra phase shift in Figure 2.10 is mostly compensated for by the electrical impedance.

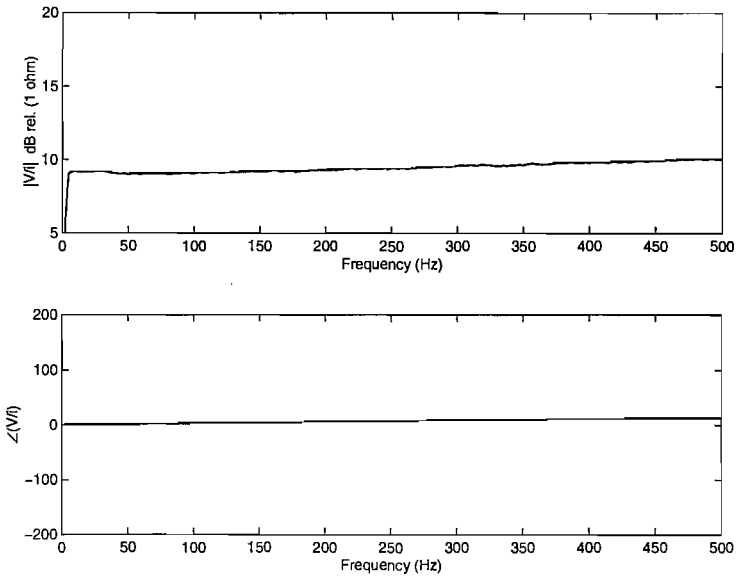

Figure 2.11 *Measured electrical impedance of the LDS Ling Dynamic Systems V101 inertial actuator.*

An unsealed ULTRA ATVA (with no manual) was available for the experiments described in Chapter 9, so that the internal components could be accessed. Figure 2.12 shows a picture of the ULTRA actuator as it can be purchased from ULTRA Electronics Ltd. and Figure 2.13 shows a schematic cross-section of some of its internal components (Hinchliffe *et al.*, 2002). The ULTRA ATVA consists of a magnetised mass mounted between two springs with an electrical coil driven by an input signal.

The dynamic response of the ULTRA actuator was tested. The actuator was mounted in the same manner as it was described previously for the LDS actuator. Figure 2.14 shows the measured dynamic response of the system and the coherence obtained during the measurement. The presence of several resonances in the frequency response can be noted. In particular, the actuator's main resonance frequency is at 73.8 Hz, while the internal resonance at 150 Hz is due to a rocking mode of the internal dynamic mass. The presence of other resonances in the frequency response at 400 Hz and 1550 Hz due to internal dynamics can also be noted. Also, at higher frequencies, the magnitude is not flat. Table 2.1 reports other features of this actuator.

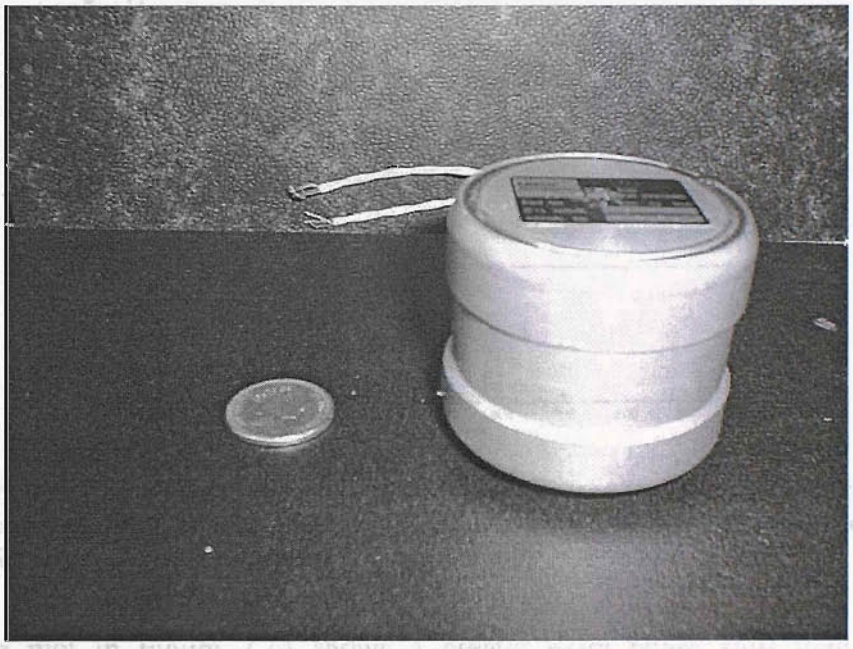

Figure 2.12 *ULTRA Active Tuned Vibration Attenuator used in the experiments in Chapter 9.*

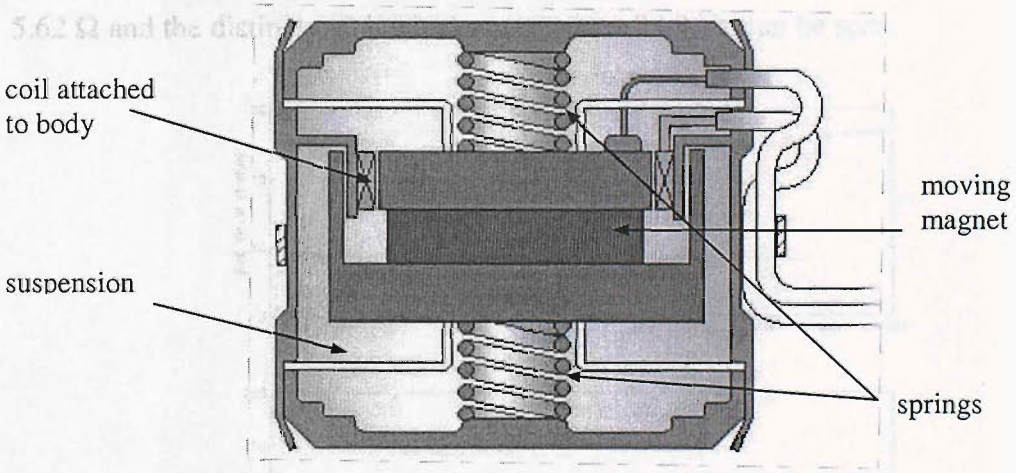

Figure 2.13 *Schematic of the cross-section of an ULTRA Active Tuned Vibration Attenuator used in the experiments in Chapter 9.*

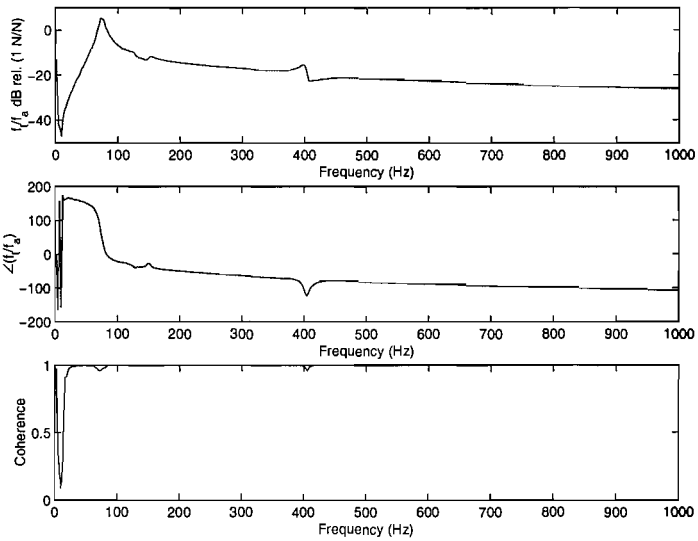

Figure 2.14 *Dynamic response of the ULTRA inertial actuator. The input is white noise, connected to the actuator's leads, and the output is the force gauge measurement.*

The phase plot in Figure 2.14 shows a greater extra phase shift than expected theoretically, which is in part due to the electrical impedance. The measurement of the electrical impedance of the ULTRA actuator (Figure 2.15) shows this phase shift, as well as the ascending magnitude. This behaviour is mainly described by an impedance, dominated by a resistor at low frequency, and an inductance at high frequency ($R + j\omega L$). At 500 Hz, the magnitude of the electrical impedance is about 5.62 Ω and the distinct mechanical resonance at 73.8 Hz can be seen.

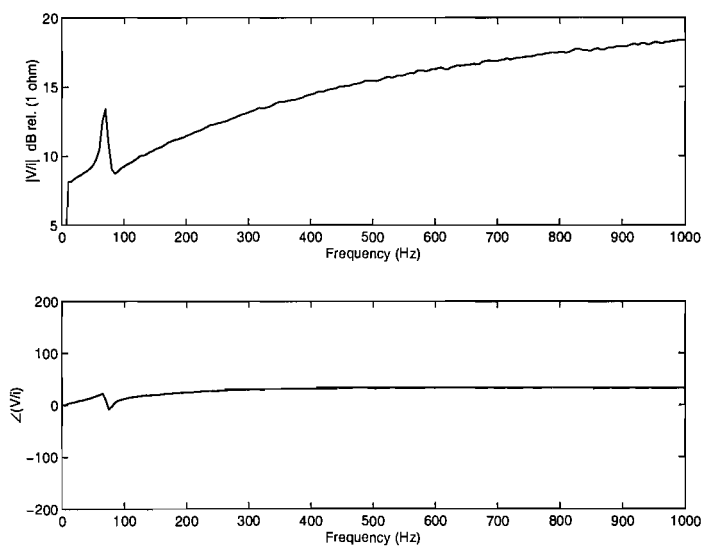

Figure 2.15 *Measured electrical impedance of the ULTRA inertial actuator.*

The Aura AST-2B-04 is designed to be used as a body shaker in videogames. Despite its low cost, it showed a very interesting behaviour. Unfortunately, these actuators are assembled by hand, and therefore show slightly different properties depending on the unit. However, they can be used effectively in active control applications (Li *et al.*, 1999). Table 2.1 shows the properties of one of our units. Apart from the dynamic mass, which was gathered from (Cazzolato, 2002), the properties of the Aura actuator were measured experimentally. Figure 2.16 shows a picture of that unit and Figure 2.17 shows its schematic. Since no casing is present, the schematic was obtained by direct inspection. It is composed of a housing, a moveable mass (which consists of a permanent magnet and a core), flexible diaphragms as springs, and a coil. The mass is supported on two diaphragms which are fixed to the housing. One diaphragm is bolted to each side of the mass. Unlike the ULTRA actuator, which is provided with two flying leads, the Aura actuator and the LDS V101 are provided with two terminal posts.

Figure 2.18 shows the measured dynamic response of the Aura actuator between input force and output moving mass acceleration, which is proportional to the transmitted force f_t , as it will be explained in Chapter 3. After the resonance frequency, the response gradually descends.

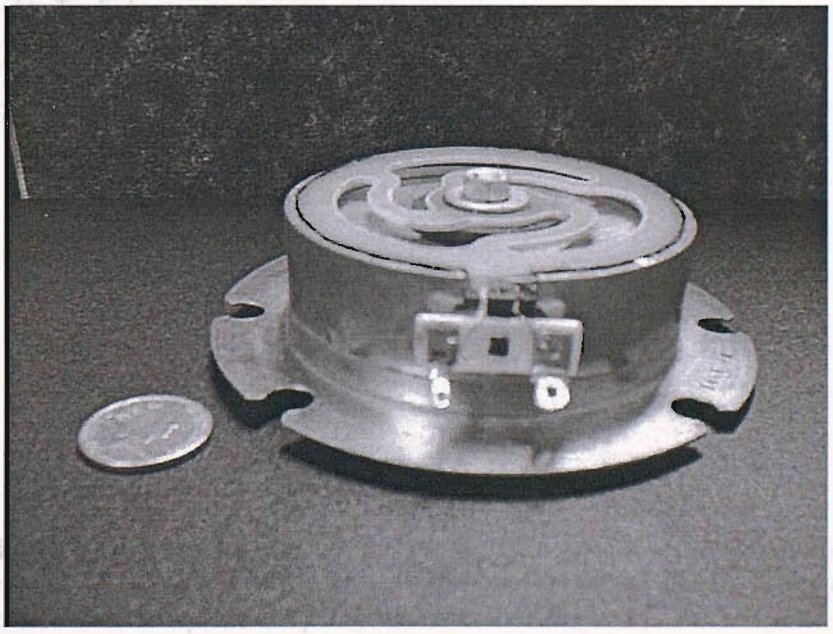

Figure 2.16 *Aura AST-2B-04 inertial actuator.*

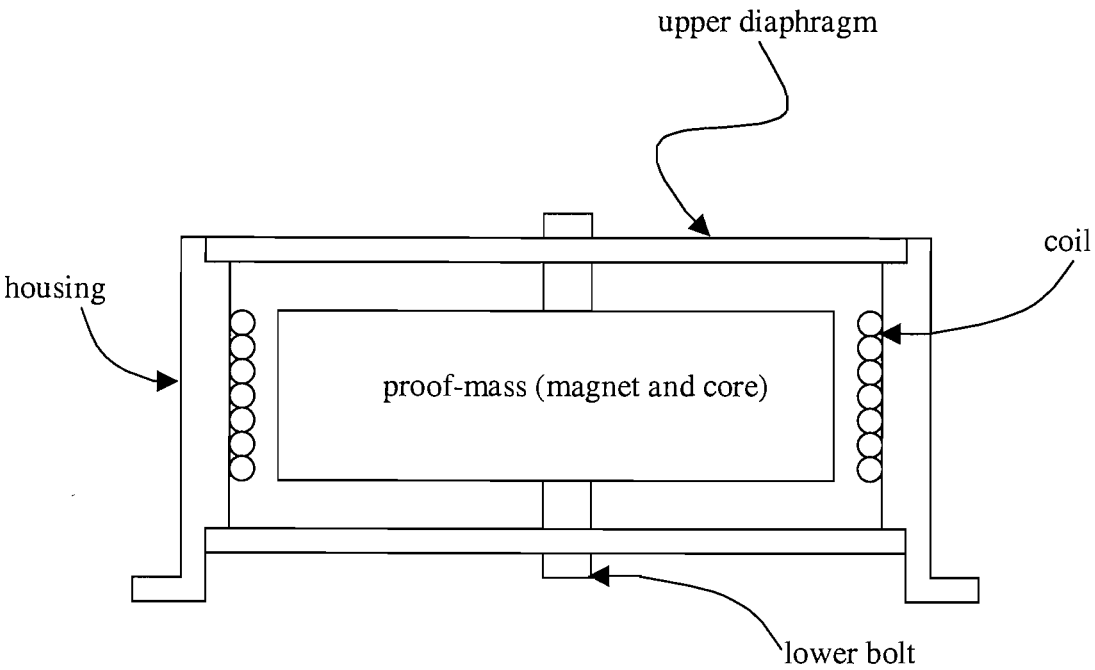

Figure 2.17 *Schematic of the cross-section of an Aura AST-2B-04.*

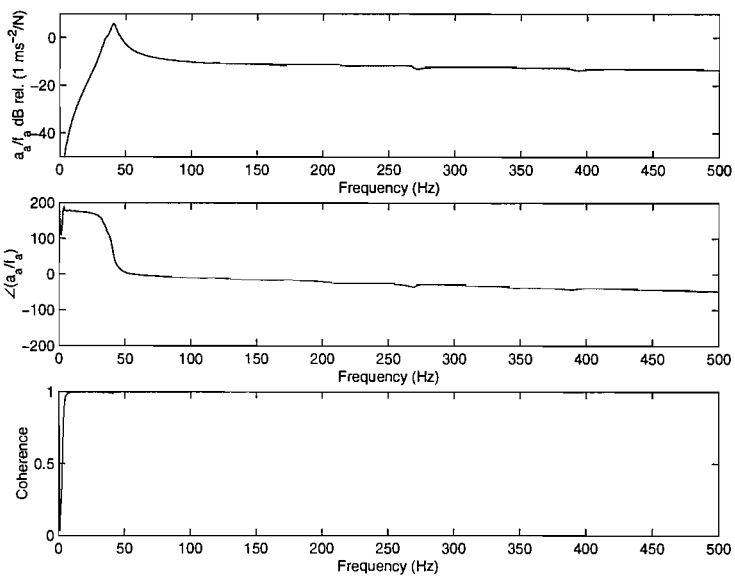

Figure 2.18 *Measured dynamic response of the Aura AST-2B-04 inertial actuator. The input is white noise, connected to the actuator's terminal posts, and the output is the proof-mass acceleration.*

The phase plot in Figure 2.18 shows an extra phase shift, which is present in the system mainly due to the inductance in the coil. This is confirmed by the measurement of the electrical impedance in Figure 2.19. At 500 Hz, the magnitude of the electrical impedance is about 4.37 Ω and the mechanical resonance is at 44.5 Hz.

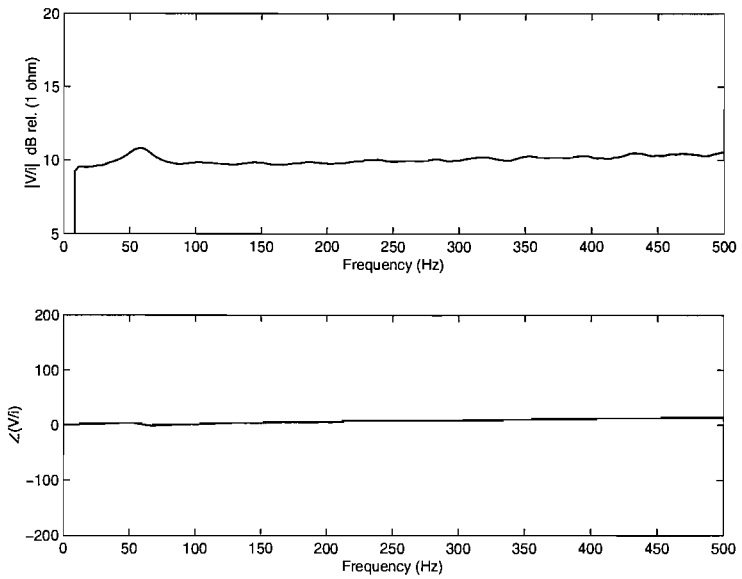

Figure 2.19 *Measured electrical impedance of the Aura AST-2B-04 inertial actuator.*

Some of the properties of the three actuators were measured directly and some estimated by inspection, without damaging them. Table 2.1 shows the comparative results. In particular, the magnetic force constant K_f was gathered from the high frequency behaviour of the ratio between transmitted force and actuator input voltage, and the electrical impedance. This latter physical quantity was computed by subtracting 1 Ω from the ratio between the measured voltage across a system composed by the actuator and a 1 Ω resistor placed in series, and the voltage across that 1 Ω resistor.

	Modified LDS V101	ULTRA ATVA	Aura AST-2B-04
resonance frequency	11 Hz	73.8 Hz	44.5 Hz
damping ratio ζ	4.8 %	4 %	4 %
total mass	1.01 kg	0.42 kg	0.64 kg
dynamic mass m_a	0.91 kg	0.24 kg	0.4 kg
magnetic force constant K_f	13.5 N/A	30 N/A	7 N/A
electrical impedance	4.17 Ω	5.62 Ω	4.37 Ω
stiffness k_a	3900 N/m	51000 N/m	31000 N/m
stroke	±1.25 mm	±3 mm	±2 mm
max input voltage	±10 V	±4 V	±8.3 V
max input current	1.5 A	1.5 A	1.3 A
max bandwidth tested	2000 Hz	2000 Hz	2000 Hz
overall diameter	65 mm	60 mm	120 mm
height	65 mm	50 mm	30 mm
cost	$450	?	$12
remarks	usually used as a reactive actuator	presence of resonances in the frequency response due to internal dynamics	flat response after the resonance and up to 1 kHz, but magnitude depends on unit

Table 2.1 *Comparative results obtained experimentally of the inertial actuators used in the active control experiments.*

Chapter 3

Inertial actuator with inner force feedback

3.1 Introduction

In this chapter, the behaviour of an inertial actuator (Figure 3.1) with inner feedback control strategies, based on the measurement of the total transmitted force f_t, is analysed. m_a is the inertial actuator dynamic mass (= 0.91 Kg), c_a is the inertial actuator damping factor (= 5.8 N/ms^{-1}), k_a is the inertial actuator spring stiffness (= 3900 N/m), f_a is the control force, v_a is the velocity of the moving mass, and v_e is the inertial actuator base velocity. These specific values of the parameters were used to match the behaviour of the commercial shaker LDS Ling Dynamic Systems V101.

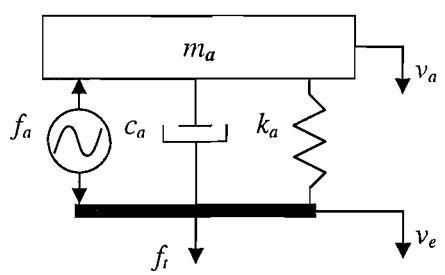

Figure 3.1 *Mechanical model and sign convention of an inertial actuator.*

The transmitted force, f_t, can be expressed as a function of the control force and the equipment velocity as in equation (2.4). In this specific case, the magnitude and phase of the blocked actuator response, T_a, is plotted in Figure 3.2(a) from which it can be seen that T_a is negative at low frequency. In fact, when f_a is positive, the spring and damper components within the actuator are expanded and therefore they generate a force which tends to restore the system to its natural condition. Given the sign convention in Figure 3.1, this force is equal to $-f_t$. Also, it can be seen that f_t tends to f_a above the inertial actuator's natural frequency.

The magnitude and phase of the frequency response of the mechanical impedance of the passive components of the inertial actuator, Z_a, is shown in Figure 3.2(b), in which it can be seen that the real part is always greater than zero (passive behaviour). Also, at high frequency, the impedance tends to the damping term, as shown in Figure 2.3 as well.

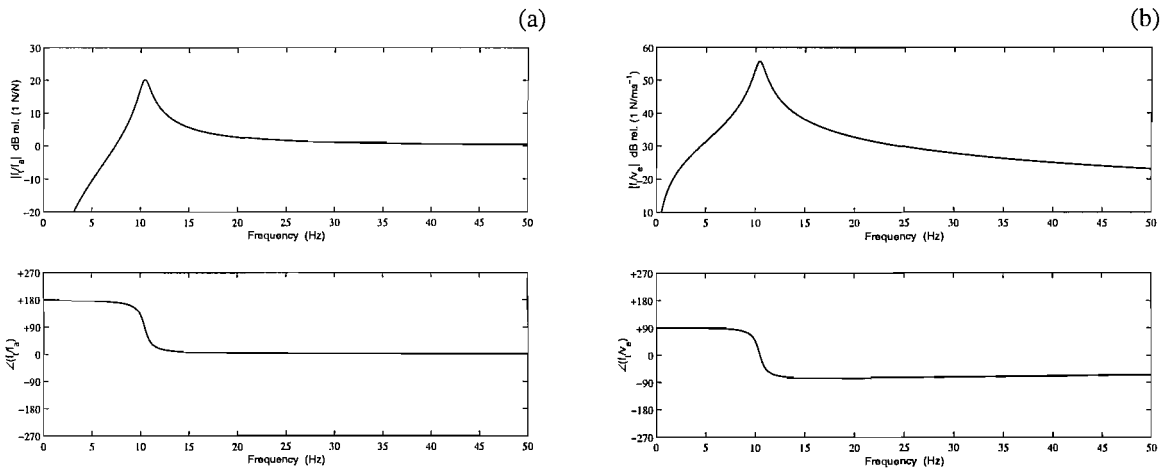

Figure 3.2 *(a): Magnitude and phase of the blocked response of the inertial actuator. (b): Magnitude and phase of the frequency response of the mechanical impedance of the passive components of the inertial actuator.*

3.2 Direct force feedback control

The inertial actuator with inner actuator force feedback control is shown schematically in Figure 3.3. The transmitted force f_t is measured and fed back to the inertial actuator through a feedback controller with frequency response $H(j\omega)$. The command signal f_c can be considered, in control terms, as the reference point (Franklin *et al.*, 1994). In this section the stability and performance of the actuator with various types of inner actuator force feedback will be discussed.

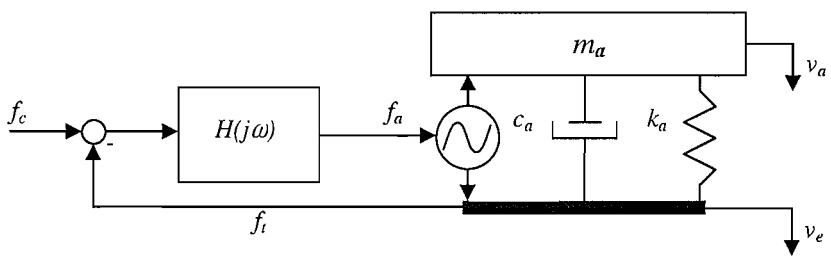

Figure 3.3 *Schematic of an inertial actuator and implementation of the inner force feedback control loop.*

If $H(j\omega) = h_f$, where h_f is a positive constant, direct force feedback is implemented. The Nyquist plot of the open loop response of the blocked actuator response is shown in Figure 3.4, which allows the relative stability of the system to be assessed (Franklin *et al.*, 1994). Direct force feedback control is seen to be unconditionally stable in this ideal case since for no feedback gain would the Nyquist plot enclose the (–1,0) point. At low frequency, the Nyquist plot does lie very close to the real axis, however, and therefore instability is likely to occur at high gains in real systems where an additional low frequency phase shift may be present due to the electronic components (Brennan *et al.*, 2002, and Benassi *et al.*, 2002b).

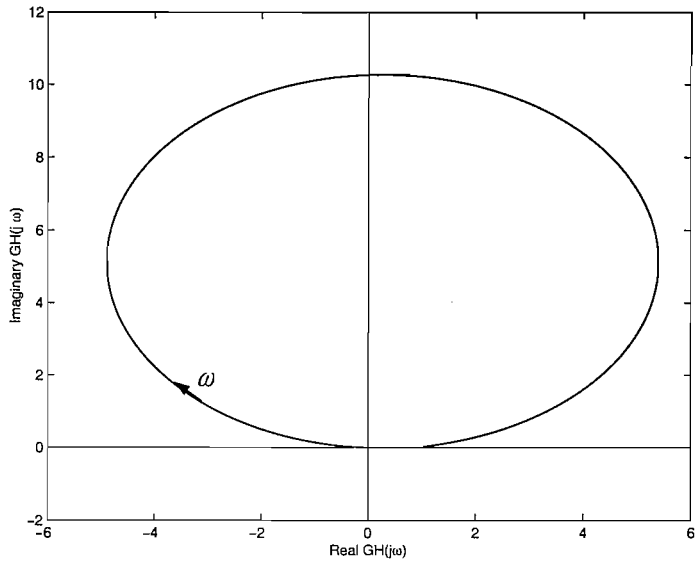

Figure 3.4 *Nyquist plot of the open loop response for the inertial actuator with direct force feedback (h_f = 1) attached to a rigid structure.*

It can also be noted that at high frequency the Nyquist plot does not go to the origin and this is due to the fact that the magnitude in the corresponding Bode plot (Figure 3.2(a)) tends to a constant.

An important assumption that underlies the result shown in Figure 3.4 is that the supporting structure which the inertial actuator is attached to is assumed to be perfectly rigid. For a more general analysis equation (2.4) can be expanded with the base velocity v_e written in terms of the input mobility of the structure Y_e as

$$v_e = Y_e f_t . \tag{3.1}$$

Substituting equation (3.1) into equation (2.4) the plant transfer function in this case, between actuator force f_a and transmitted force f_t, is given by

$$G_f = \frac{f_t}{f_a} = \frac{T_a}{1 + Z_a Y_e} . \tag{3.2}$$

The difference between the blocked plant response, T_a, and that when it is loaded by the structure, is the factor $(1+Z_aY_e)^{-1}$. If the structure is vibrating with velocity v_{ep} before the actuator is attached, its velocity after the actuator has been attached is given by

$$v_e = v_{ep} + Y_e f_t . \tag{3.3}$$

Assuming that the actuator is undriven, $f_a = 0$, then f_t from equation (2.4) will be equal to $-Z_a v_e$. Substituting this into equation (3.3), the fractional change in the structure's velocity due to the attachment of the undriven actuator (i.e. its passive effect on the structure's vibration) is given by

$$\frac{v_e}{v_{ep}} = \frac{1}{1-Y_eZ_a}, \tag{3.4}$$

which provides some physical interpretation of the effect of the mobility of the structure on the inertial actuator's plant response with inner force feedback. The reciprocal frequency response of the plant in the case of direct force feedback control, from equation (3.2), can be written as

$$G_f^{-1} = T_a^{-1}[1+Z_aY_e]. \tag{3.5}$$

The reciprocal of the blocked actuator response T_a (Figure 3.2(a)) has a phase shift between 0° and +180°. Both Z_a and Y_e are passive terms and thus their individual phase shift is between ±90°. Consequently Z_aY_e and thus $[1+Z_aY_e]$ could vary between ±180°. The overall phase shift of equation (3.2) can therefore, in general, range between -180° and +360° ; and so in most general case a constant gain feedback loop is only conditionally stable. In the case of the ideal inertial actuator, however, the phase of Z_a is

restricted to being between 0° and +90° below its natural frequency and between -90° and 0° above its natural frequency.

One of the applications of the device described in this section, as will be discussed in Chapter 6, is the vibration isolation of a sensitive piece of equipment using an outer equipment velocity feedback loop to provide skyhook damping. In order to implement a stable outer closed-loop system with an inertial actuator, the actuator resonance must be below the first resonance frequency of the structure under control (Elliott *et al.*, 2001a, and Benassi *et al.*, 2002a). The modification of the plant response due to loading by the structure is not as severe in this case as in the most general case described above. For example the Nyquist plot of a system composed of an inertial actuator with inner force feedback control mounted on a rigid piece of equipment, which is connected to a vibrating base through a resilient mount, is shown in Figure 3.5, in which the natural frequency of the equipment on its resilient mount is about twice the actuator's natural frequency. The phase shift of the plant is again restricted to between 0° and +180°, with the first loop, at low frequency, determined by the behaviour of the inertial actuator, while the smaller loop, at higher frequency, describes the dynamic loading effect of the equipment on its resilient mount on the actuator.

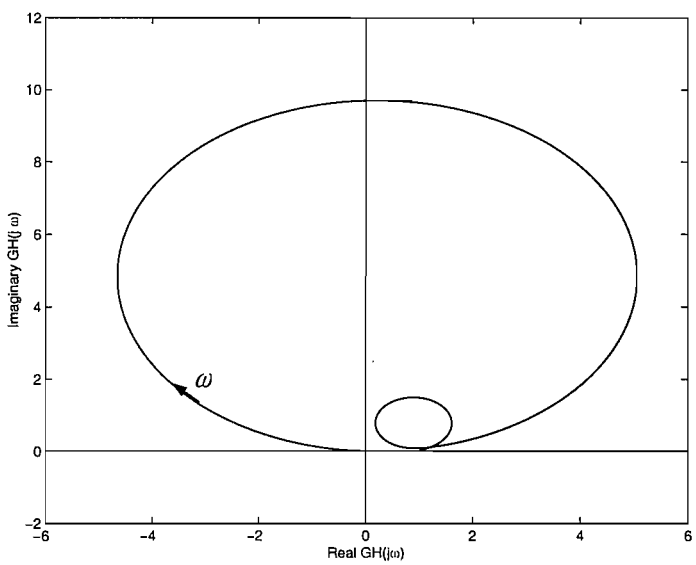

Figure 3.5 *Nyquist plot of the open loop response for the inertial actuator with direct force feedback ($h_f = 1$) attached to a flexible structure.*

The secondary force f_a for the inner force feedback system shown in Figure 3.3 is given by

$$f_a = h_f (f_c - f_t) \tag{3.6}$$

which, when substituted into equation (2.4) and expanded, provides the closed loop transmitted force as a function of the command signal and the equipment velocity. This is given by

$$f_t = \frac{-\omega^2 m_a h_f}{k_a + j\omega c_a - \omega^2 m_a (1+h_f)} f_c - \frac{j\omega m_a k_a - \omega^2 m_a c_a}{k_a + j\omega c_a - \omega^2 m_a (1+h_f)} v_e . \tag{3.7}$$

which can be grouped as

$$f_t = T'_{a1} f_c - Z'_{a1} v_e . \tag{3.8}$$

where T'_{a1} and Z'_{a1} are the blocked response and mechanical impedance of the actuator, as modified by the inner feedback. The closed-loop response of the actuator with inner force feedback is given by the transmitted force f_t per unit control command f_c , as plotted in Figure 3.6(a). When the inner feedback gain h_f increases, the transmitted force tends to the control command f_c. This means that the transmitted force can be regulated using the command signal f_c. A second important aspect is that when the feedback gain h_f increases, the actuator resonance is shifted to lower frequencies, while its magnitude increases. The transmitted force f_t is proportional to the acceleration of the moving mass m_a and consequently inner force feedback is equivalent to feeding back the acceleration of the moving mass. Inner force feedback control can thus be physically interpreted as adding an "apparent" mass to the inertial actuator moving mass (Benassi *et al.*, 2002c). Although this lowering of the actuator's natural frequency is desirable when used for active isolation, it makes the stability of the inner feedback loop even more sensitive to low frequency phase shifts.

Figure 3.6(b) shows the transmitted force f_t per unit equipment velocity, v_e, which is equal to the impedance of the actuator with inner force feedback. The lowering of the resonance frequency can again be observed. It can also be seen that as the feedback gain h_f is increased, the actuator's impedance becomes smaller, particularly at high frequencies, as predicted by equation (3.7).

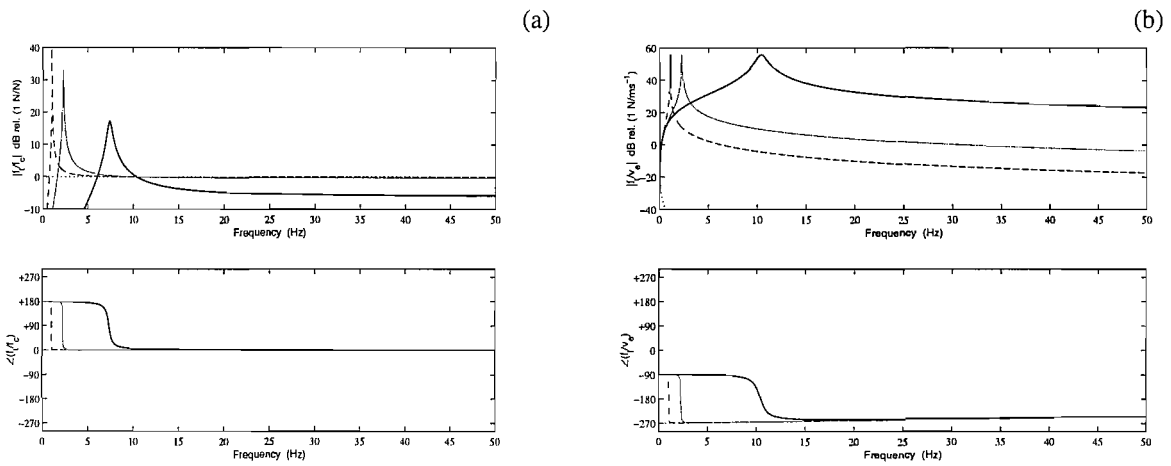

Figure 3.6 *(a): Transmitted force per unit control command for the inertial actuator with inner force feedback when different feedback gains h_f are used: h_f =1 (solid), h_f =20 (faint), h_f =100 (dashed), and h_f =100,000 (dotted). (b): Frequency response of the actuator's mechanical impedance when h_f =0 (solid), h_f =20 (faint), h_f =100 (dashed), and h_f =100,000 (dotted).*

3.3 Integrated force feedback control

If the inner feedback controller in Figure 3.3 is given by $H(j\omega) = \frac{h_{if}}{j\omega}$, then integrated force feedback control is implemented. The effect of an integrator in the feedback loop is to rotate the Nyquist plot of the plant response by 90° clockwise. The Nyquist plot of the open loop response for the actuator with integral force feedback on a rigid base, for example, is shown in Figure 3.7, which is a rotated version of Figure 3.4. The Nyquist plot now lies entirely on the right hand side of the complex plane, so that this control system is

inherently more robust than direct force feedback. In particular low frequency phase shifts, due to conditioning electronics, of up to +90° will not destabilize the system. Also, high frequency perturbations of the plant response due to the finite mobility of the structure under control, as discussed above, will not destabilize the system since for the isolation example, whose effect on force feedback was shown in Figure 3.5, the Nyquist plot will still be on the right hand side of the complex plane with integral force feedback.

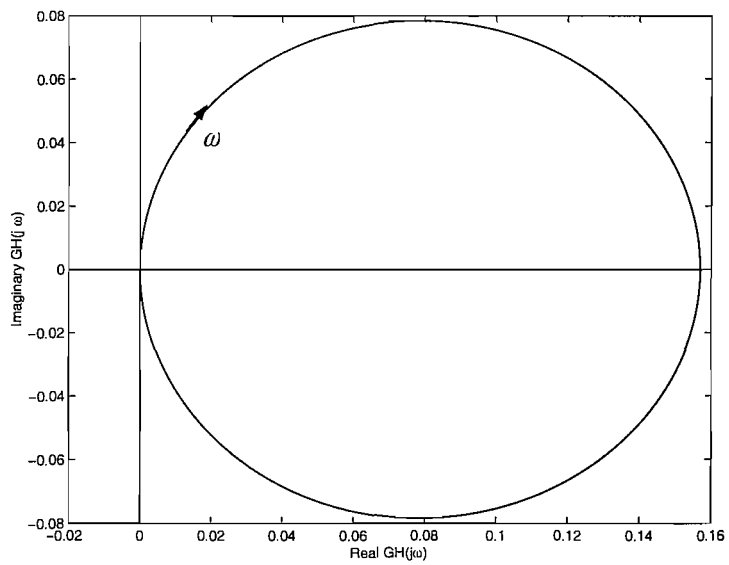

Figure 3.7 *Nyquist plot of the open loop response of the inertial actuator with integrated inner force feedback* $H(j\omega)=h_{if}/j\omega$*., with* $h_{if} = 1$.

The actuator force in this case is given by

$$f_a = \frac{h_{if}}{j\omega}\omega_1(f_c - f_t) \tag{3.9}$$

where ω_1 is introduced to ensure that h_{if} is dimensionless, and is assumed to have the value 138.2 rad/s for reasons that will be evident later. When equation (3.9) is substituted into equation (2.4), the transmitted force becomes

$$f_t = \frac{j\omega m_a h_{if} \omega_1}{k_a + j\omega c_a - \omega^2 m_a + j\omega m_a h_{if} \omega_1} f_c - \frac{j\omega m_a k_a - \omega^2 m_a c_a}{k_a + j\omega c_a - \omega^2 m_a + j\omega m_a h_{if} \omega_1} v_e \qquad (3.10)$$

which can be written in the compact form

$$f_t = T'_{a2} f_c - Z'_{a2} v_e . \qquad (3.11)$$

where T'_{a2} and Z'_{a2} are the blocked response and mechanical impedance of the actuator, as modified by the inner feedback. The blocked response of the actuator, the transmitted force f_t per unit control command f_c, with integral force feedback, is plotted in Figure 3.8(a). Unlike the previous case, the resonance frequency does not change significantly when the feedback gain increases, although f_t does tend to f_c when very high gains are implemented. For relatively low values of the feedback gain, however, the magnitude falls off above the resonance frequency and a phase shift occurs. Compared to the force feedback control, as shown in Figure 3.5(a), in which the closed loop response tends to unity with no phase shift at higher frequencies even for moderate feedback gains, higher integral feedback gains are needed with this control strategy in order to obtain the same levels of transmitted force.

Figure 3.8(b) shows the frequency response of the actuator's mechanical impedance, f_t / v_e, for different feedback gains h_{if}. When the feedback gain h_{if} is increased, the impedance is reduced at the resonance frequency and for very high values of feedback gain the magnitude is reduced over the whole frequency range shown in Figure 3.8(b). The physical interpretation of this behaviour is that the integral of the transmitted force is proportional to the velocity of the actuator's proof-mass, and integral force feedback thus adds damping to the system.

An intermediate scheme based on the measurement of the integrated transmitted force f_t was also analysed. The inner feedback gain $H(j\omega)$ was chosen to be a positive real constant h_{if}. The Nyquist plot is shown in Figure 3.6 and the transmitted force per unit equipment velocity is shown in Figure 3.8(b). Unlike the other schemes, the transmitted force per unit control command f_c shows the weakness of this strategy. In fact, for very

high values of the gain h_{if}, f_t / f_c tends to h_{if}, but when h_{if} assumes reasonable values, f_t / f_c tends to $j\omega$, which means that it is frequency dependent. For this reason, the implementation of this feedback control scheme is not recommended.

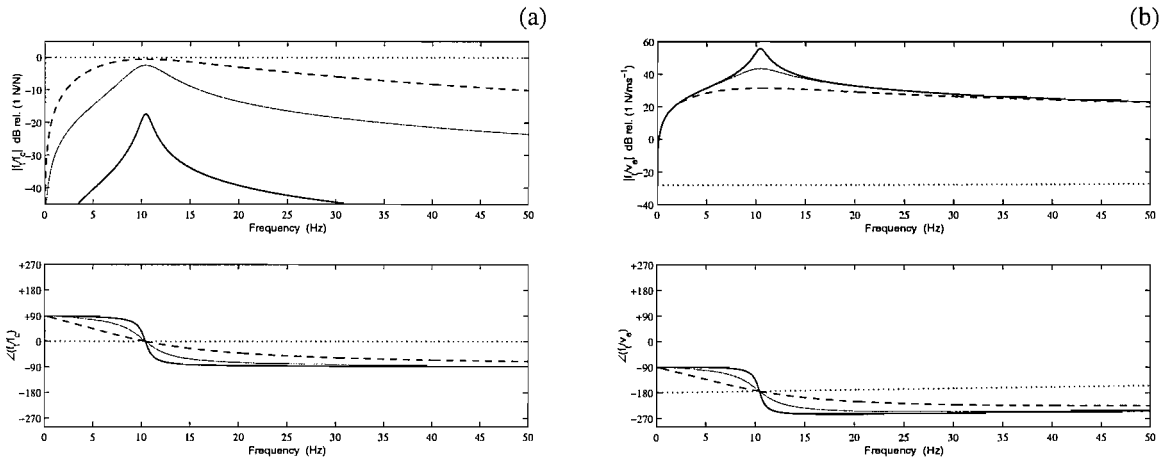

Figure 3.8 *(a): Transmitted force per unit control command for the inertial actuator with inner integral force feedback when different feedback gains h_{if} in $H(j\omega)= h_{if}/j\omega$ are used: $h_{if}=1$ (solid), $h_{if}=20$ (faint), $h_{if}=100$ (dashed), and $h_{if}=100,000$ (dotted). (b): Frequency response of the actuator's mechanical impedance when $h_{if}=0$ (solid), $h_{if}=20$ (faint), $h_{if}=100$ (dashed), and $h_{if}=100,000$ (dotted).*

The force feedback control scheme does not guarantee a good stability margin at low frequency. This is especially true when the feedback gain is increased. In addition, when real electronic components are added to the ideal system, the stability margin rapidly decreases and the overall system falls very close to the unstable region. On the other hand, from a performance point of view, this scheme offers very good results using lower feedback gains than the other schemes, as it will be discussed in Chapter 6. When an integrator is added to the system, the overall system significantly improves its stability margin. This can be noted in the Nyquist plot, which is rotated by 90° clockwise. On the other hand, if high performance is needed, very high gains are necessary. It would therefore be a good idea to alter the inner feedback loop in such a way that it behaves like a force feedback controller at frequencies higher than a certain appropriate value and it

behaves like an integrated force feedback controller at low frequencies. By doing so, the system will preserve a high stability margin at low frequency and will also preserve good performance at high frequency. All these aspects will be discussed in the next sections.

3.4 Phase-lag compensator

The frequency response of a phase lag compensator, $H(j\omega) = h_{pl}\dfrac{j\omega + \omega_1}{j\omega}$, is plotted in Figure 3.9 for the case where $\omega_1 = 138.2$ rad/s. If this is used as the inner controller in Figure 3.3, the Nyquist plot of the open loop system is shown in Figure 3.10. The stability of the closed loop system is between the behaviour of the previous two cases. In particular, at low frequency the stability margin of the closed loop system is almost as good as the integrated force feedback case and this is due to the -90° phase shift that the phase-lag controller adds to the plant response at low frequency. At higher frequencies the controller does not add any additional phase shifts and the behaviour of the plant is preserved. The stability of the controller is also robust to the effect of a finite mobility in the attached structure, since it will affect the Nyquist plot in a similar way to that shown in Figure 3.5.

The value of ω_1 is chosen in order to provide a reasonable trade-off between stability of the overall system (especially at low frequency) and its performance. Since the inertial actuator resonance frequency is responsible for the conditional stability of the system, by adding an integrator to the feedback loop, the corresponding portion in the Nyquist plot is rotated by 90° clockwise, leading the closed-loop system away from a potential instability. In order to guarantee this feature, ω_1 must be greater than the inertial actuator resonance frequency. On the other hand, in order to guarantee good performance, ω_1 should be small, such that the closed loop system can benefit from the inner force feedback controller. In this study, ω_1 was chosen to be $2\pi \cdot 22 = 138.16$ rad/s, where 22 Hz corresponds to the equipment-dominated resonance frequency of the vibration isolation problem discussed in Chapter 6. A detailed discussion on the appropriate choice of ω_1 is given in Benassi *et al.* (2002c).

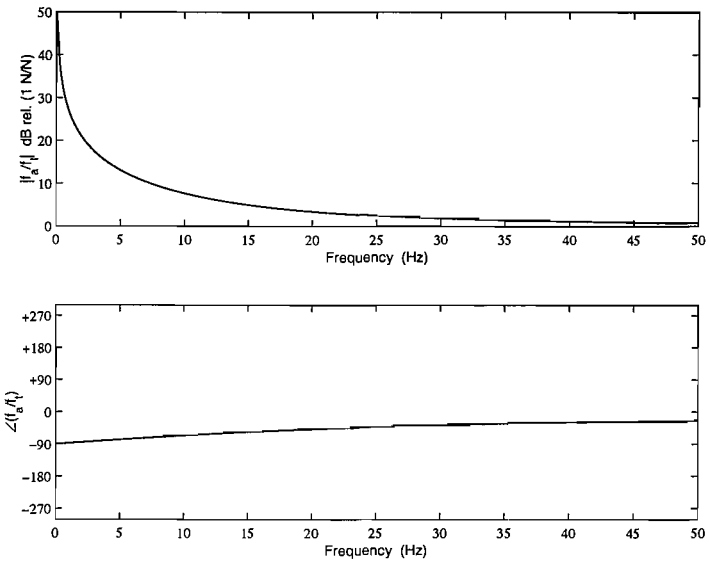

Figure 3.9 *Frequency response of the phase lag compensator* $H(j\omega)=h_{pl}(j\omega + \omega_l)/j\omega$, *with* $h_{pl} = 1$ *and* $\omega_l = 138.2$ *rad/s.*

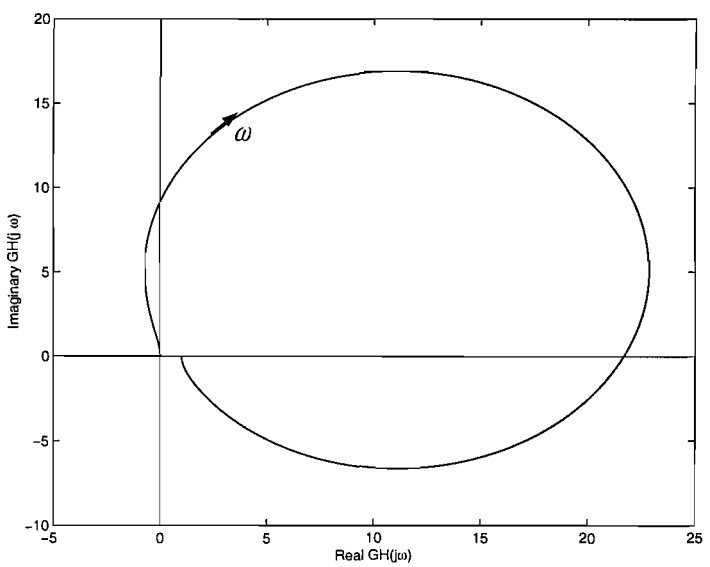

Figure 3.10 *Nyquist plot of the blocked actuator response when the phase-lag compensator* $H(j\omega)=h_{pl}(j\omega + \omega_l)/j\omega$ *is implemented, with* $h_{pl} = 1$ *and* $\omega_1 = 2\pi \cdot 22 Hz$.

The actuator force in this case is given by

$$f_a = h_{pl}\frac{j\omega+\omega_1}{j\omega}(f_c - f_t). \tag{3.12}$$

Substituting this into equation (2.4), the transmitted force becomes

$$\begin{aligned} f_t = & \frac{-\omega^2 m_a h_{pl} + j\omega m_a h_{pl}\omega_1}{k_a + j\omega c_a - \omega^2 m_a(1+h_{pl}) + j\omega m_a h_{pl}\omega_1} f_c \\ & - \frac{j\omega m_a k_a - \omega^2 m_a c_a}{k_a + j\omega c_a - \omega^2 m_a(1+h_{pl}) + j\omega m_a h_{pl}\omega_1} v_e \end{aligned} \tag{3.13}$$

which can be written in the compact form

$$f_t = T'_{a3} f_c - Z'_{a3} v_e \tag{3.14}$$

where T'_{a3} and Z'_{a3} are the blocked response and mechanical impedance of the actuator, as modified by the inner feedback. Figure 3.11(a) shows the transmitted force per unit control force. As the feedback gain h_{pl} increases, f_t tends to f_c at all frequencies. Compared to the previous control scheme (Figure 3.8(a)), at frequencies higher than the resonance frequency, the magnitude is more level, indicating a better performance at high frequency since f_t is closer to f_c than in the previous case. Also, unlike the previous case, there is a smaller phase-lag at frequencies higher than the resonance frequency.

Figure 3.11(b) shows the frequency response of the actuator's mechanical impedance for different feedback control gains h_{pl}. When the feedback gain h_{pl} increases, the impedance f_t / v_e tends to zero, but this is only achieved for large values of the gain. Otherwise, the behaviour is similar to the previous case. Compared to the uncontrolled case (solid line), when the controller is activated the first resonance is no longer present in the impedance equation. This can be physically explained considering the fact that when the feedback gain h_{pl} in the phase-lag compensator increases, the closed loop system tends to an equivalent system in which the inertial activator has been removed.

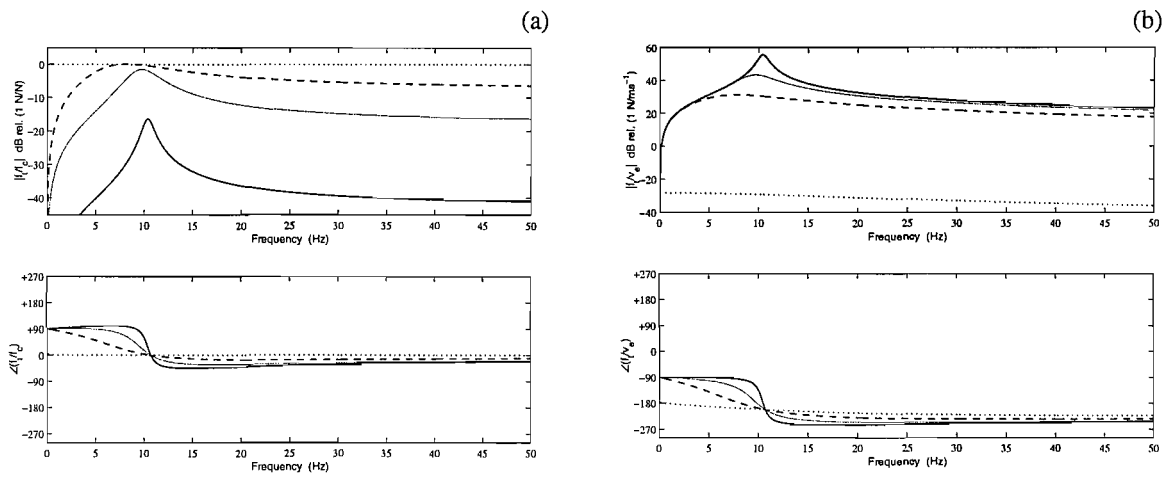

Figure 3.11 *(a): Transmitted force per unit control command when different feedback gains h_{pl} in the phase-lag compensator are used: h_{pl} =1 (solid), h_{pl} =20 (faint), h_{pl} =100 (dashed), and h_{pl} =100,000 (dotted). (b): Frequency response of the impedance when h_{pl} =0 (solid), h_{pl} =20 (faint), h_{pl} =100 (dashed), and h_{pl} =100,000 (dotted).*

3.5 Conclusions

An analysis of different inner feedback control strategies using an inertial actuator, based on the measurement of the transmitted force, has been presented. Physical interpretation, feedback stability margins and performance were considered for each case.

The main finding is that using a phase-lag compensator, the most important advantage is the fact that it enhances the stability margin of the system at low frequency and, thanks to its phase recovery, restores the original behaviour of the force feedback control strategy at higher frequencies.

Chapter 4

Inertial actuator with inner displacement feedback

4.1 Introduction

In this chapter we consider the effect of having an inner displacement feedback loop operating between the proof-mass and the inertial actuator reference plane, instead of the inner force feedback loop considered in the previous chapter. It is found that damping of the actuator can be achieved by feeding back the derivative of the relative displacement of the proof-mass. In addition, the inertial actuator's natural frequency can be lowered or increased by feeding back either negative or positive inner proportional displacement feedback. Self-levelling can also be implemented by feeding back the integral of the relative displacement, which overcomes the problem of excess actuator displacement due to gravitational forces on the moving mass (i.e. static sag due to low resonance frequency).

A mechanical model of an inertial actuator was derived in Chapter 2, and is shown again in Figure 4.1 for convenience, where the effect of $H(j\omega)$ should be neglected at this stage. A proof-mass, m_a, is suspended on a spring, k_a, and a damper, c_a, and in parallel with them, the actuator force f_a drives the mass, which is also affected by the inertial force f_i (due to gravity for example). v_a and v_e are, respectively, the moving mass velocity and the base velocity.

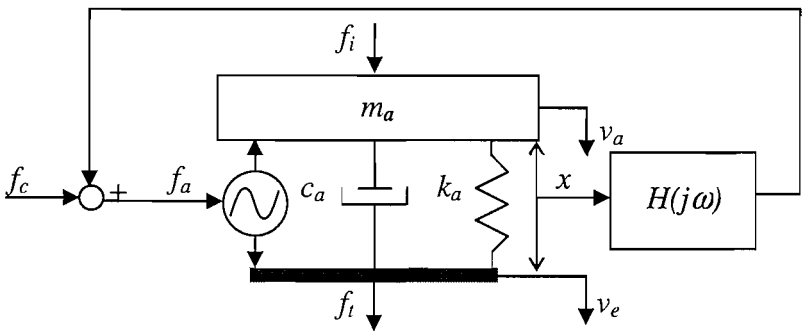

Figure 4.1 *Schematic of an inertial actuator and implementation of the inner displacement feedback control.*

The equation describing the dynamics of the system in Figure 4.1 is given by equation (2.1), where v_a and v_e are complex velocities. In Figure 4.1, x is the relative displacement between the inertial actuator's proof-mass and the inertial actuator's reference base so that $j\omega x = v_a - v_e$.

The inertial actuator used for the experiments described below was a mechanically modified version of an active tuned vibration absorber (ATVA) manufactured by ULTRA Electronics, described by Hinchliffe *et al.* (2002) and analysed in detail in Chapter 2, from which the internal springs were removed, leaving the proof-mass (m_a = 0.24 Kg) attached to the case by eight thin flexible supports. This modification in the stiffness (so that k_a = 2000 N/m) changed the actuator resonance frequency from 73.8 Hz to 14.5 Hz. The measured damping ratio was used to estimate the damping factor as c_a = 18 N/ms^{-1}. Figure 4.2 shows the dynamic response of the relative displacement of the proof-mass, x, per unit actuator force, f_a, of this modified ULTRA inertial actuator. Both measured data and theoretical prediction, calculated from equation (2.1), are plotted, where the measured data was divided by Bl/R, where Bl is the magnetic force constant of the inertial actuator and R is the inertial actuator electrical impedance, which was found to be resistive within this frequency range. This scaling was necessary in order to ensure the same units of displacement per unit force for both curves. In an electro-mechanical actuator the damping is given by the sum of the mechanical and electromagnetic damping and the latter is increased by the fact that a voltage amplifier was used to drive the actuator, which had a very low internal impedance.

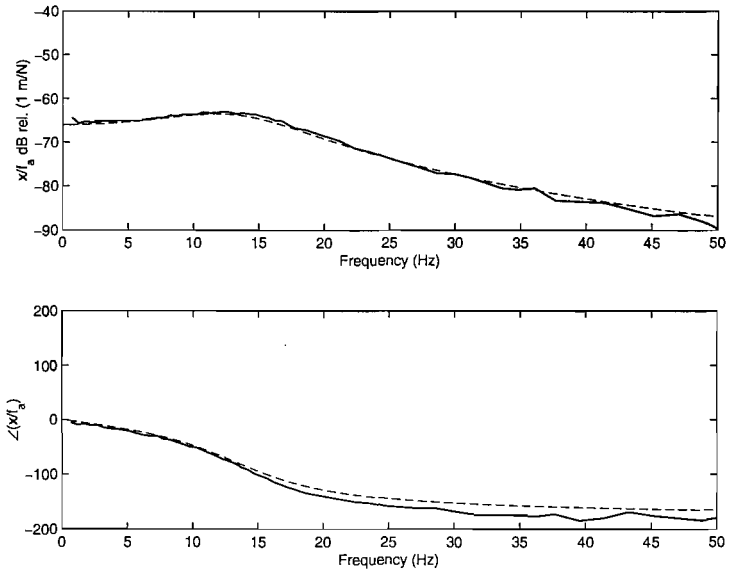

Figure 4.2 *Frequency response of the relative displacement of the proof-mass per unit actuator force of the ULTRA inertial actuator. The solid line shows the measured data, while the dashed line shows the theoretical prediction.*

The displacement of the proof-mass was measured using strain gauges on the suspensions. A pair of strain gauges (RS 632-180-N11-MA5-120-23), connected to self-compensate for temperature changes, was installed on opposite sides of one of the internal thin flexible supports which hold the proof-mass inside the actuator. Each strain gauge is a 5mm rectangular foil type, and consists of a pattern of resistive foil which is mounted on a backing material. The strain gauges used in the actuator are connected to a Wheatstone Bridge circuit with a combination of four active gauges (full bridge). The complete Wheatstone Bridge, which was installed inside the inertial actuator, is excited with a stabilised DC supply and with additional conditioning electronics can be zeroed at the null point of measurement. As stress is applied to the bonded strain gauge, a change of resistance takes place and unbalances the Wheatstone Bridge. This results in a signal output related to the stress value, which is proportional to the proof-mass relative displacement. As the signal value is small (a few millivolts) the signal conditioning electronics provides amplification to increase the signal level to ±1 V, a suitable level for the active vibration isolation application.

In the following sections we will discuss how self-levelling can be implemented by feeding back the integrated displacement, which overcomes the problem of excess

actuator displacement due to gravitational forces on the moving mass (i.e. static sag due to low resonance frequency). The damping of the actuator can also be modified by feeding back the derivative of the relative displacement of the inertial actuator. In addition, the inertial actuator's natural frequency can be lowered or increased by feeding back inner proportional displacement feedback with either a positive or negative gain.

4.2 An inertial actuator with self-levelling capabilities

Self-levelling systems can be used to reduce static deflections, and systems based on integrated displacement feedback control have been described in the literature. For example, Horning and Schubert (1988) discuss the need for self-levelling in automotive applications and in "rocket-propelled missiles where a substantially constant acceleration is sustained for an appreciably long time". The most practical method of generating the forces required to counteract the manoeuvring loads is probably the use of air mounts (Elliott, 2000), but the pressure control mechanism must be fast enough to follow the changes in load.

The self-levelling system described here uses the inherent actuator force $f_a(t)$ to level its proof-mass. The sensing element which measures the position of the actuator proof-mass relative to the inertial actuator reference plane was a strain gauge, although an optical sensor was also investigated for this purpose. The strain gauge was attached in such a way that the sensor is in its neutral position when the moving mass is at its desired operating height. The electrical signal is integrated and amplified by the controller, providing electric power to operate the actuation device within the inertial actuator. The system produces a force that is proportional to the integral of the signal from the sensor.

When a force of constant magnitude is applied to the moving mass, causing a relative deflection of the mass on its spring element, the sensor applies an electrical signal proportional to the mass relative displacement to the integral controller. In response, the controller generates an electrical signal that continues to increase in magnitude as long as the relative displacement is not zero. The signal from the controller is applied to the inertial actuator, which generates a force in a direction that decreases the mass deflection. The force follows the controller signal and continues to increase in

magnitude as long as the relative deflection is not zero. At some point in time the force will exactly equal the constant force applied on the moving mass, requiring a relative displacement of zero. The output from the sensor is zero, therefore the output from the controller no longer increases but is maintained at a constant magnitude required for the actuator to generate a force exactly equal to the constant force applied to the moving mass.

The isolation system remains in this equilibrium condition until the force applied to the moving mass changes and causes a nonzero signal to be generated by the sensing element, and the process starts all over again. When air mounts are used (Horning and Schubert, 1988), a proportional scaled signal from the sensor may be used to operate an electromechanical servo valve, the flow response of the servo valve being proportional to its excitation signal. The servo valve fluid flow output is directed into the chamber of an air spring to produce the desired force applied to the supported body. The control function remains integral in nature since the internal pressure of the actuator responds to the volume output from the servo valve, which is the integral of its flow output. Hence, in this case, no electrical integration of the sensor signal is needed.

The inertial actuator with inner displacement feedback control is shown schematically in Figure 4.1. The relative displacement x is measured and fed back to the inertial actuator through a feedback controller with frequency response $H(j\omega)$, which in the first instance is equal to $g_I / j\omega$. The control command f_c can be considered, in control terms, as the reference point (Franklin *et al.*, 1994). If we assume that the control force is given by the sum of a control command f_c and the time integral of the measured relative displacement between the inertial actuator proof-mass and its reference base, multiplied by a gain g_I

$$f_a = f_c + g_I \int x(t)dt \tag{4.1}$$

then a self-levelling device is implemented.

In order to examine the stability of the closed-loop system, composed of the inertial actuator and the self-levelling controller, the open loop gain was computed. It is given by the product of the plant response, $G(j\omega)$ (measured relative displacement per unit control force, x/f_a, obtained from equation (2.1) by imposing $f_i = 0$ and $v_e = 0$, since

it is assumed to be mounted on a rigid base), multiplied by the control law $H(j\omega) = \frac{g_I}{j\omega}$

$$G(j\omega)H(j\omega) = \frac{1}{\left(-\omega^2 m_a + j\omega c_a + k_a\right)}\left(\frac{g_I}{j\omega}\right). \tag{4.2}$$

The faint line in Figure 4.3(a) shows the calculated Nyquist plot from equation (4.2), when g_I is equal to 60,000 in equation (4.1). It can be noted that the system is conditionally stable and the Routh-Hurwitz criterion can be used to show that the system is only stable if $\lambda<1$ (Elliott, 2000), where

$$\lambda = \frac{g_I}{2\zeta_a \omega_a k_a} . \tag{4.3}$$

When g_I is equal to 60,000, the corresponding λ is equal to 0.4, which also coincides with the negative real part of $G(j\omega)H(j\omega)$ when the imaginary part is zero in Figure 4.3. The low frequency measurements in Figure 4(b) cannot be considered very reliable because of noise limitations, even though the general behaviour of the open loop system is clear, including the behaviour due to the real integrator.

In a real system, the integrator's control law is not described by equation (4.2), but more realistically by an equation that includes a cut off frequency (at 1.5 Hz in this case), a finite DC magnitude, and a phase shift at DC of 0°, rather than 90°, as in the ideal case described by equation (4.2). A realistic expression for such control law is given by

$$H_1(j\omega) = \frac{g_I}{1 + j\omega 0.106} . \tag{4.4}$$

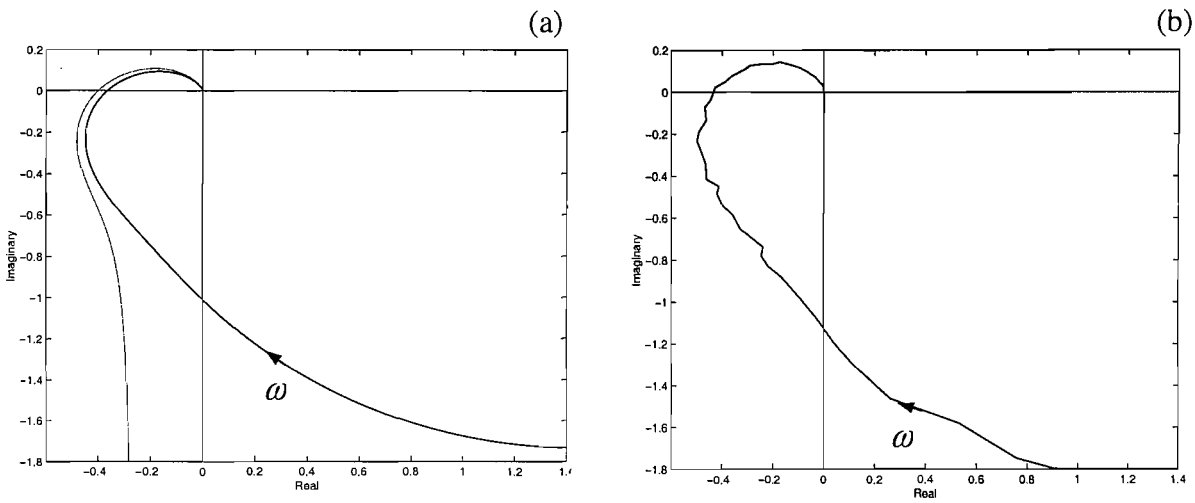

Figure 4.3 *(a): Predicted Nyquist plot of the open loop transfer function, inertial actuator displacement per unit secondary force, when the controller includes a realistic (solid) or ideal (faint) model of the integrator in the controller. λ was set to 0.4. (b): Corresponding measured data.*

Consequently, the ideal open-loop system response described by equation (4.2) is then replaced by a more realistic equation given by

$$G(j\omega)H_1(j\omega) = \frac{1}{\left(-\omega^2 m_a + j\omega c_a + k_a\right)} \frac{g_I}{\left(1 + j\omega 0.106\right)}, \tag{4.5}$$

which shows that at DC the Nyquist plot starts at $\frac{g_I}{k_a}$ on the positive real axis, and then behaves as shown by the solid line in Figure 4.3(a). The experimental result shown in Figure 4.3(b) is very close to this.

The response of the actuator to an inertial force, f_i, can be computed by setting the control command to zero. The relative displacement x per unit inertial force f_i, when an ideal self-levelling device is implemented, is then given by

$$\frac{x}{f_i} = \frac{1}{-\omega^2 m_a + j\omega c_a + k_a + H_1(j\omega)}, \tag{4.6}$$

whose behaviour is plotted in Figure 4.4 for different values of the inner displacement feedback gain g_I. Without integral displacement feedback (solid line), the response of the system to a static force is equal to $1/k_a$, while with ideal integral displacement feedback it tends to zero, which shows that the servo action of the feedback controller will compensate for any static load. In realistic implementations, as described by equation (4.6), the static deflection is equal to $1/(k_a + g_I)$. The low frequency behaviour is important because it determines how well the system performs in cases like an aircraft manoeuvre or a vehicle turn. In other words, besides counter-balancing the sagging effect due to gravity, the system must be able to centre the proof-mass and prevent it from banging against the stop-ends during manoeuvres. For example, without control the relative displacement of the proof-mass, due to the gravitational force $f_i = m_a g$, where $g = 9.8$ ms^{-2} is the gravitational acceleration, on the spring k_a is given by $x = \frac{f_i}{k_a} = 1.2$ mm, while with the self-levelling control the relative displacement is equal to $x = \frac{f_i}{k_a + g_I} = 38$ μm. In case of a $10g$ manoeuvre the relative displacement without control would be an unsatisfactory 11.8 mm, while with control this distance would be reduced to 0.38 mm. However, at the inertial actuator resonance frequency, enhancement of the response is experienced and this enhancement increases with the gain g_I, until the system becomes unstable. When the actuator stiffness, k_a, decreases, the critical value of the gain g_I decreases as well and therefore in order to have the same stability margin, lower gains are needed.

Figure 4.5 shows the experimental proof-mass relative displacement x per unit control command f_c, which is given by

$$\frac{x}{f_c} = \frac{1}{-\omega^2 m_a + j\omega c_a + k_a + H_1(j\omega)}, \tag{4.7}$$

which has the same form as equation (4.6) whose theoretical relative displacement per unit force is shown in Figure 4.5. In both theory and experiment the increase in

magnitude at the resonance can be noted, which is a sign that the system is getting closer to instability, along with an additional phase shift at low frequency.

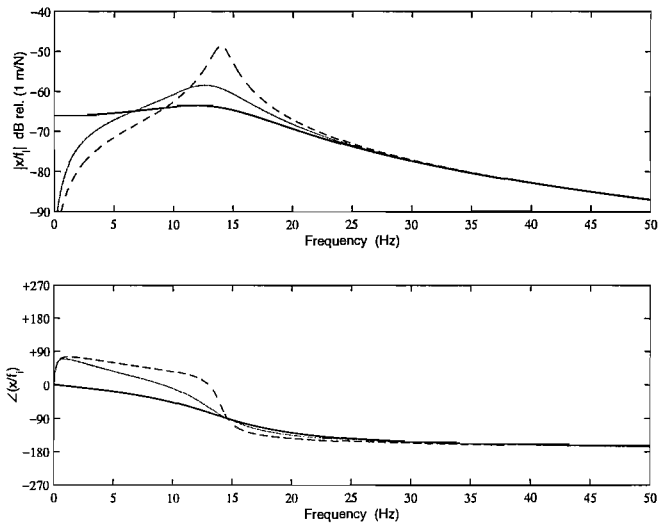

Figure 4.4 *Predicted inertial response of the system when different ideal inner self-levelling feedback loop gains g_I are used: g_I = 0 (solid, corresponding to λ = 0, i.e. no control), g_I = 60,000 (faint, λ = 0.4), and g_I = 105,000 (dashed, λ = 0.7).*

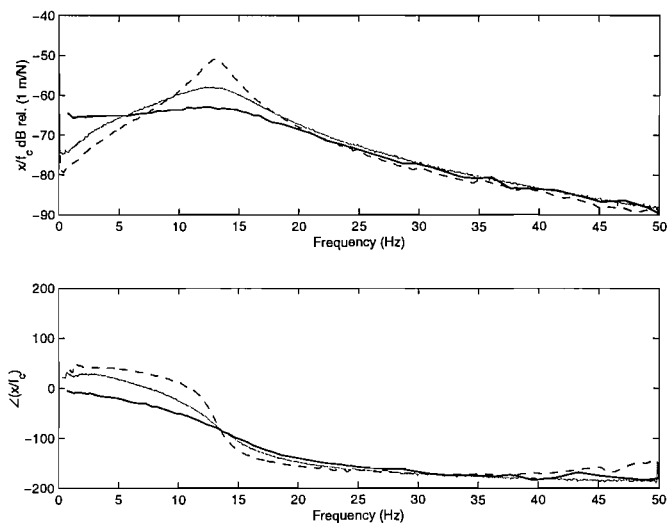

Figure 4.5 *Measured relative displacement of the proof-mass per unit command force for the passive system (control off, solid) and for two values of the integral feedback gain: λ = 0.4 (faint), and λ = 0.7 (dashed). The theoretical prediction for this response is the same as that shown in Figure 4.4.*

4.3 Inertial actuator with PID control

4.3.1 Proportional feedback

In the previous section we saw that with a displacement sensor integral control gave a self-levelling action. In this section we discuss the physical effect of proportional and derivative control in a general PID controller.

If the inertial actuator resonance frequency is too high for the specific application, it can be lowered using a negative direct position feedback control loop, $H_2(j\omega) = g_P$, where g_P is negative. In order to determine whether the closed-loop system in Figure 4.1 is stable with such a controller, the open loop gain was computed. It is given by the product of the plant response, $G(j\omega)$, defined before, multiplied by $H_2(j\omega)$

$$G(j\omega)H_2(j\omega) = \frac{1}{-\omega^2 m_a + j\omega c_a + k_a}(g_P) \ . \tag{4.8}$$

The maximum feedback gain g_P before instability is equal to the value of the stiffness term k_a. Figure 4.6 shows the corresponding theoretical and experimental Nyquist plot for a value of the gain g_P that is equal to $-k_a/2$, which guarantees a 6 dB stability margin. Lowering the resonance frequency also implies that smaller values of the gain g_I are needed for self-levelling purposes.

Figure 4.7 shows the theoretical and measured proof-mass displacement x per unit control command f_c described in equation (4.7) when the inner feedback controller, $H_2(j\omega)$, comprises the proportional term, g_P, only and this is either positive or negative. If the position feedback gain was positive, the natural frequency is increased, with no danger of instability. When negative position feedback gains are implemented, the actuator resonance frequency can be lowered, but stability issues emerge if the total system stiffness tends to zero.

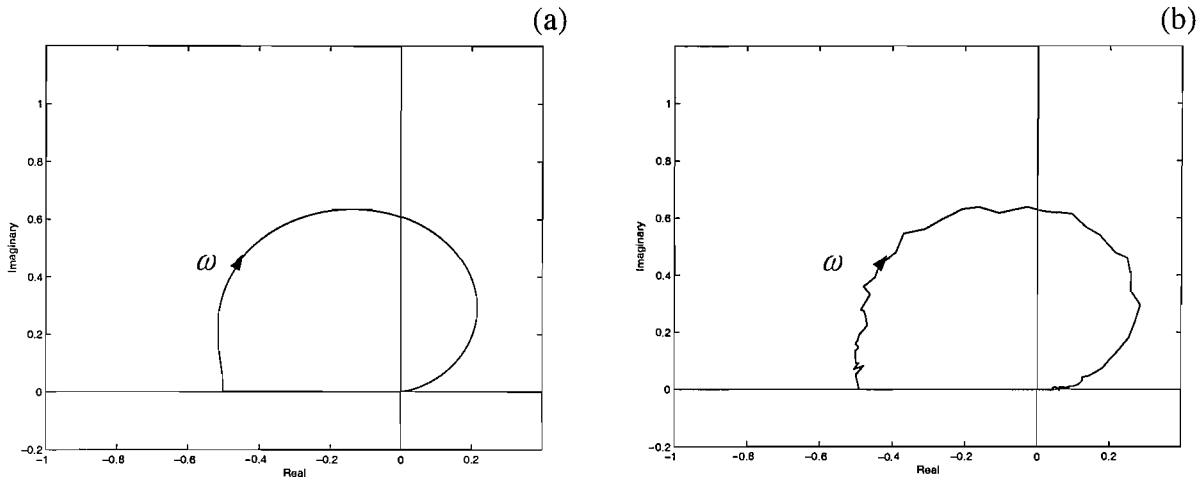

Figure 4.6 *(a): Predicted Nyquist plot of the open loop transfer function, inertial actuator relative displacement per unit secondary force, when the controller is a proportional device based on a negative position feedback gain. For ω = 0 the system guarantees a 6 dB stability margin when g_P = -1000. (b): Corresponding measured data.*

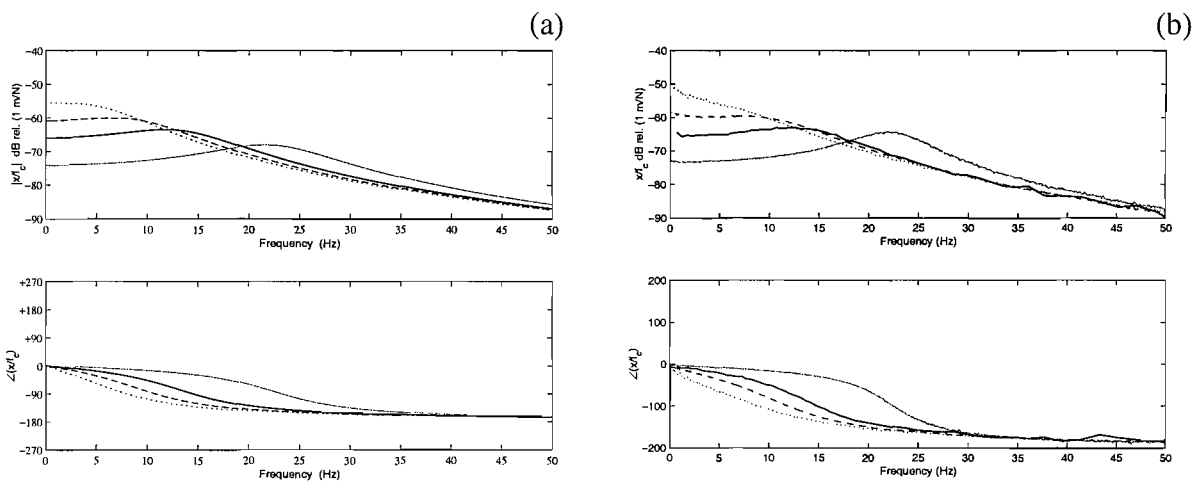

Figure 4.7 *(a): Predicted relative displacement of the inertial actuator's proof-mass per unit command force for the passive system (control off, solid) and for three values of the proportional feedback gain: g_P = +3100 (faint), g_P = -900 (dashed), and g_P = -1400 (dotted). (b): Corresponding measured data.*

4.3.2 Derivative feedback

The stability analysis of the closed-loop system when an ideal derivative controller, $H_3(j\omega) = j\omega g_V$, is used within the inner loop, is obtained by studying the open loop transfer function

$$G(j\omega)H_3(j\omega) = \frac{1}{-\omega^2 m_a + j\omega c_a + k_a}(j\omega g_V) \tag{4.9}$$

which is composed of the product of the plant response, $G(j\omega)$, times the controller's response. In a real implementation, the frequency response of the circuit used to generate the derivative term has a cut-off frequency, after which the input signal is just multiplied by a constant gain (Ananthaganeshan *et al.*, 2001). As long as this cut-off frequency lies above the maximum frequency of interest, then $H_3(j\omega)$ can be considered as a good approximation to this part of the feedback controller when modelling realistic systems. Figure 4.8 shows the predicted Nyquist plot of the open loop system, described by equation (4.9), and the corresponding measured data. Theory and experiment agree well, and they both lie in the positive real half plane, indicating that by increasing the controller gain g_V, damping is added to the dynamics of the inertial actuator. At frequencies higher than the plotted range of interest, the experimental curve enters the third quadrant. This mainly happens because the circuit used to generate the derivative term is, in reality, a high pass filter (Ananthaganeshan *et al.*, 2001), so that its magnitude becomes constant after a certain frequency and its phase tend to zero. This indicates that in a real implementation the stability margin of the closed-loop system is reduced and the amount of damping that can be added to the system is large, but finite. An additional limitation is that the noise that is present in the measured signal is amplified by the derivative controller. Figure 4.9 shows the frequency response of the uncontrolled inertial actuator and the controlled system when an inner derivative feedback loop is implemented. A value of the feedback gain g_V was chosen so that is equal to the uncontrolled c_a so that the overall value of the damping constant is doubled. The uncontrolled case is already damped appropriately, but since the self-levelling integral feedback loop tends to increase the magnitude of the resonance, an additional damping term will be required when the whole PID controller is implemented, as discussed below. The experimental measurements and

theoretical predictions again agree well, indicating that using an inner derivative feedback controller it is possible to add damping and therefore change the dynamic behaviour of an inertial actuator.

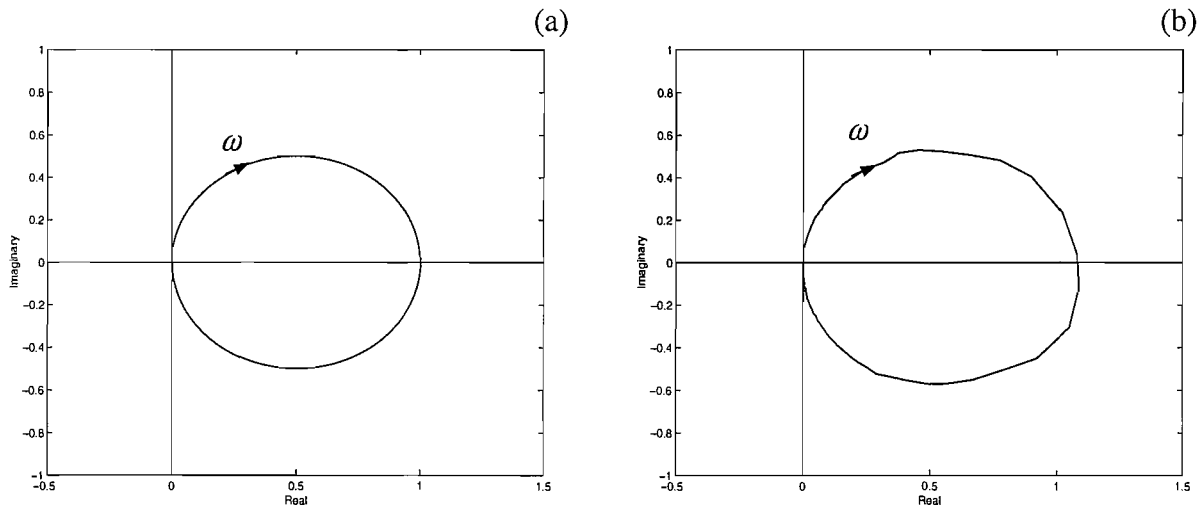

Figure 4.8 *(a): Predicted Nyquist plot of the open loop transfer function, inertial actuator displacement per unit secondary force, when the controller is the derivative of the relative displacement (g_V = 18). (b): Corresponding measured data.*

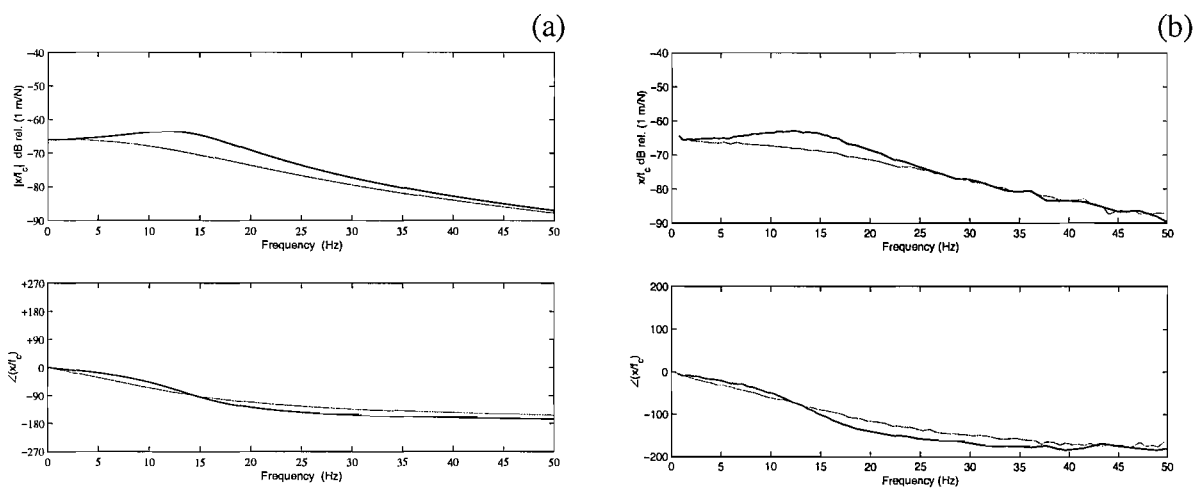

Figure 4.9 *(a): Predicted relative displacement of the proof-mass per unit command force for the passive system (control off, solid) and for one values of the derivative feedback gain: g_V = 18 (faint). (b): Corresponding measured data.*

4.3.3 Combined PID feedback

If the integral displacement term, the proportional term and the derivative of the displacement are added in parallel within the inner feedback controller, the control law in Figure 4.1 becomes of the form

$$H(j\omega) = H_1(j\omega) + H_2(j\omega) + H_3(j\omega) \tag{4.10}$$

which describes a typical ideal PID controller. An image of the real PID controller which was used during the experiments is shown in Figure 4.10 and its schematic is given in Appendix B.

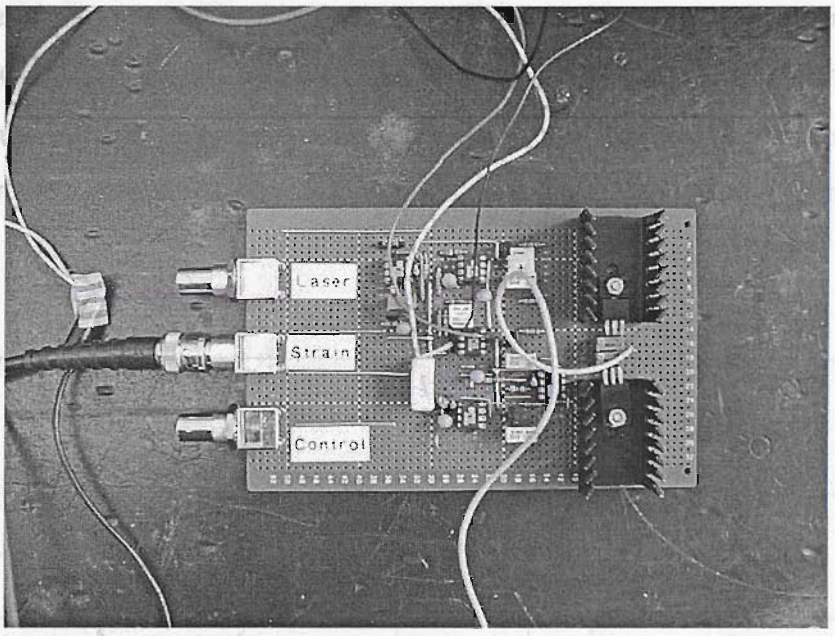

Figure 4.10 *Image of the PID controller and summing box used within the inner feedback loop. "Control" indicates the control signal input, "Strain" indicates the strain gauge signal input and "Laser" indicates the displacement laser sensor input, which was used to validate the strain gauge measurements.*

In order to determine whether the closed-loop system in Figure 4.1 is stable with such a controller, the open loop gain was computed. It is given by the product of the plant response, $G(j\omega)$, multiplied by $H(j\omega)$

$$G(j\omega)H(j\omega) = \frac{1}{-\omega^2 m_a + j\omega c_a + k_a}\left(g_P + \frac{g_I}{1 + j\omega 0.106} + j\omega g_V\right) \qquad (4.11)$$

Figure 4.11 shows the corresponding theoretical and experimental Nyquist plot for a value of the gain g_P that is equal to $-k_a/2$, a value of g_I which guarantees $\lambda = 0.4$, and a value of g_V = 18. The closed loop system is conditionally stable, and the stability depends on the combined choice of the proportional gain and the self-levelling gain. The curve starts off at $\frac{g_P + g_I}{k_a}$ and then intersects the real axis in its negative portion before reaching the origin. Figure 4.12 shows the theoretical and measured proof-mass relative displacement x per unit control command f_c for the uncontrolled inertial actuator and for the modified inertial actuator, when the inner feedback controller, $H(j\omega)$, has the same value of the gains as above. In this case the inertial actuator natural frequency was lowered to about 10 Hz and this configuration was used in the active vibration isolation problem discussed in the next section.

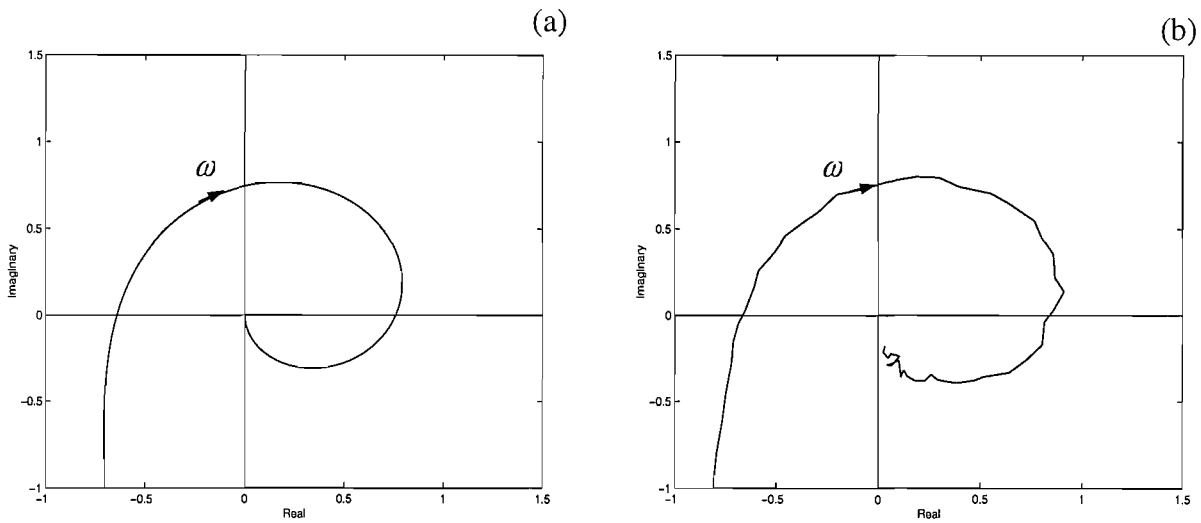

Figure 4.11 *(a): Predicted Nyquist plot of the open loop transfer function, inertial actuator relative displacement per unit secondary force, when the controller is a PID with proportionality gain g_P = -1000, self-levelling coefficient λ = 0.4, and derivative gain g_V = 18. (b): Corresponding measured data.*

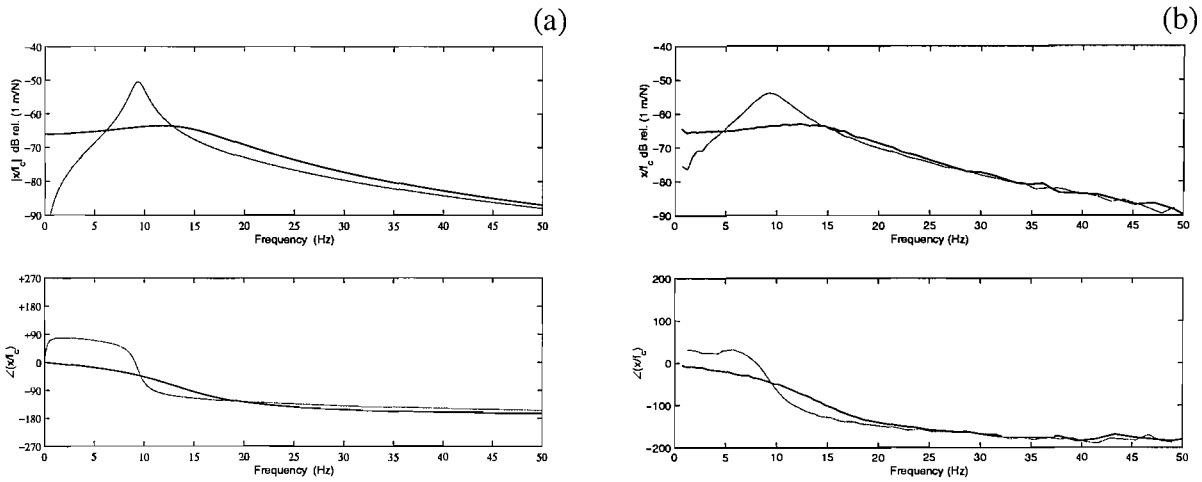

Figure 4.12 *(a): Predicted relative displacement of the proof-mass per unit command force for the passive system (control off, solid) and with the inner PID feedback controller on (faint), with g_P = -1000, λ = 0.4, and g_V = 18. (b): Corresponding measured data.*

In summary, if it is necessary to reduce the resonance frequency of the actuator, because it is greater or equal to the first structural mode of the system that needs to be isolated, this can be done with a negative position feedback gain. If this action induces unwanted deflections because of the low stiffness of the closed-loop system, then a self-levelling mechanism can be employed, which is based on a integral displacement feedback. By doing so, however, the overall system gets closer to instability and additional damping is needed. Another reason why damping may be necessary is if an outer velocity feedback is to be implemented. It was shown by Elliott *et al.* (2001a) that this kind of system is conditionally stable and the vicinity to the Nyquist point depends on how well damped the inertial actuator is. For these reasons the implementation of an inner rate feedback control turns out to be very effective in increasing the damping of the actuator.

From Figure 4.1, the equation that describes the complete modified inertial actuator once the inner PID feedback control, described by equation (4.10), is implemented, can be calculated. It is given by

$$f_t = \frac{-\omega^2 m_a}{-\omega^2 m_a + j\omega c_a + k_a + H(j\omega)} f_c - \frac{\left(j\omega m_a k_a - \omega^2 m_a c_a\right)\cdot\left(H(j\omega) + j\omega Z_a\right)}{\left(-\omega^2 m_a + j\omega c_a + k_a + H(j\omega)\right) j\omega Z_a} v_e \quad (4.12)$$

where $Z_a = c_a + \frac{k_a}{j\omega}$ is the mechanical impedance of the actuator suspension. Equation (4.12) can be grouped as

$$f_t = T_a' f_c - Z_a' v_e \ , \tag{4.13}$$

where T_a' and Z_a' are the blocked response and mechanical impedance of the actuator, as modified by the inner displacement feedback. Figure 4.13 shows the predicted and measured blocked response of the uncontrolled inertial actuator and the modified inertial actuator. At frequencies higher than the actuator resonance, the transmitted force f_t tends to the control command f_c. This means that the blocked response shows that the transmitted force f_t can be regulated using the control command f_c. Figure 4.14 shows the calculated and measured mechanical impedance of the actuator before and after control. When g_V increases, the mechanical impedance increases at high frequencies. The magnitude plot in Figure 4.14 shows that, starting from the solid line which tends, at high frequency, to c_a = 18 N/ms^{-1}, the damping of the device increases to $c_a + g_V$ = 36 N/ms^{-1}. The phase plot in Figure 4.14 shows that above resonance, the mechanical impedance is damping dominated and the system shows a skyhook damping behaviour.

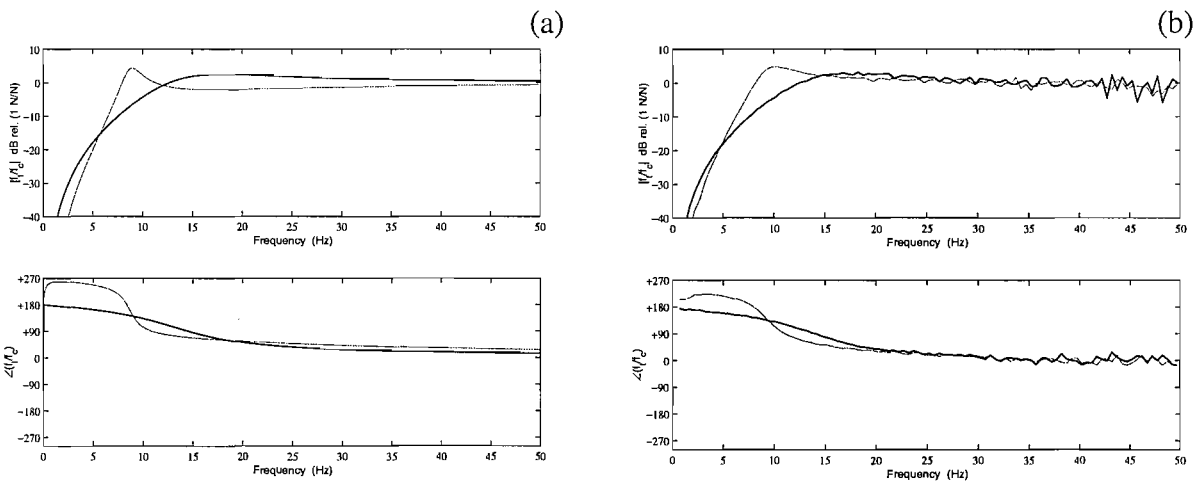

Figure 4.13 *(a): Predicted blocked response of the inertial actuator (solid) and the modified inertial actuator when g_P = -1000, λ = 0.4 and g_V = 18 (faint). (b): Corresponding measured data.*

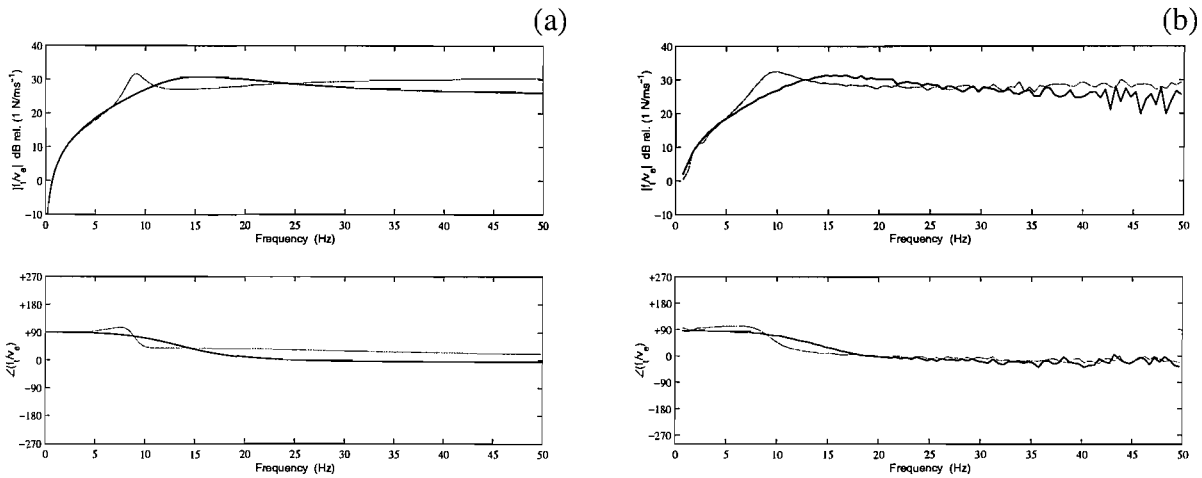

Figure 4.14 *(a): Predicted mechanical impedance of the inertial actuator (solid) and the modified inertial actuator when* g_P *= -1000,* λ *= 0.4 and* g_V *= 18 (faint). (b): Corresponding measured data.*

4.5 Conclusions

Actuators with very low resonance frequencies have large displacements due to gravity. To solve this problem, a new device has been proposed. It is based on an inertial actuator with very low stiffness and an inner PID feedback loop which uses the measurement of the relative displacement between the actuator base and the actuator moving mass. The control law is the sum of an integral term, which provides self-levelling and solves the sagging problem, a derivative term, which provides the device with sufficient initial damping to guarantee a very good stability margin, and a positive or negative proportional term, which determines the actuator resonance frequency.

Chapter 5

Active isolation theory with equipment velocity feedback

5.1 Introduction

Isolators are generally required to protect a piece of delicate equipment in a severe vibration environment. Often, very little can be done to reduce the base vibration since it is either of high impedance or characterized by complex dynamics. The isolation of any vibration-sensitive equipment from base vibration is therefore usually performed on the transmission paths (mounts). The fundamental benefit provided by any mount is reduced structural vibration. However, with such passive mounts there is a trade-off between low and high frequency isolation performances depending on the damping of the mount. In fact, a major challenge is to make the mount as stiff as possible, statically, to better support the equipment, and dynamically as soft as possible, to better isolate it. This is difficult to accomplish with passive elastometric mounts, as described by Crede and Ruzicka (1996) and Ungar (1992).

To provide a more favourable static and dynamic stiffness compromise, active isolation solutions must be used, which are usually based on mounts and actuators.

Applications with actuators and passive mounts in an active isolator package provide many benefits including simplicity, effective vibration isolation, noise attenuation, higher static stiffness, dynamic adaptability, and safety. This suggests that there is ample motivation for the use of active mounting systems.

This chapter deals with the stability analysis of a single degree of freedom system, composed of a piece of equipment, which is mounted on a base through a mount. Active control is performed through an inertial actuator. The aim of this chapter is to introduce the vibration isolation problem, provide its general model formulation and describe a popular control strategy based on the measurement of the equipment velocity. This simple control strategy is compared with an optimal LQG approach in Appendix A. Some practical issues that the designer has to cope with to build a real system are also discussed.

5.2 Complete model formulation

We assume the system to be composed of a vibrating base at the bottom, a piece of equipment mounted on top of the vibrating base through a passive mount, and an inertial actuator installed on the equipment. Figure 5.1 shows the mechanical model and the sign convention. Each velocity or force is assumed to be positive in the direction indicated by the corresponding vector. The equations that describe the system in Figure 5.1 can be written as

$$v_1 = Y_{11} f_1 \tag{5.1}$$

$$v_1 = v_2 \tag{5.2}$$

$$f_1 + f_2 = 0 \tag{5.3}$$

$$\begin{Bmatrix} f_2 \\ f_3 \end{Bmatrix} = \begin{bmatrix} Z_{11}^a & Z_{12}^a \\ Z_{21}^a & Z_{22}^a \end{bmatrix} \begin{Bmatrix} v_2 \\ v_3 \end{Bmatrix} + \begin{bmatrix} -1 \\ 1 \end{bmatrix} f_a \tag{5.4}$$

$$v_3 = v_4 = v_5 \tag{5.5}$$

$$f_3 + f_4 + f_5 = 0 \tag{5.6}$$

$$v_4 = Y_{44} f_4 \tag{5.7}$$

$$\begin{Bmatrix} f_5 \\ f_6 \end{Bmatrix} = \begin{bmatrix} Z_{11}^m & Z_{12}^m \\ Z_{21}^m & Z_{22}^m \end{bmatrix} \begin{Bmatrix} v_5 \\ v_6 \end{Bmatrix} \tag{5.8}$$

$$v_6 = v_7 \tag{5.9}$$

$$f_6 + f_7 = 0 \tag{5.10}$$

$$v_7 = Y_{77}(f_7 + f_p), \tag{5.11}$$

where the mobilities and impedances are defined as

$$Y_{11} = \frac{1}{j\omega m_a}$$

$$Y_{44} = \frac{1}{j\omega m_e}$$

$Y_{77} = plate - mobility$ (Gardonio and Elliott, 1998)

$$Z_{11}^a = Z_{22}^a = -Z_{12}^a = -Z_{21}^a = c_a + \frac{k_a}{j\omega}$$

$$Z_{11}^m = Z_{22}^m = -Z_{12}^m = -Z_{21}^m = c_m + \frac{k_m}{j\omega}.$$

Equations (5.1), (5.7) and (5.11) can be grouped as

$$\begin{Bmatrix} v_1 \\ v_4 \\ v_7 \end{Bmatrix} = \begin{bmatrix} Y_{11} & 0 & 0 \\ 0 & Y_{44} & 0 \\ 0 & 0 & Y_{77} \end{bmatrix} \begin{Bmatrix} f_1 \\ f_4 \\ f_7 \end{Bmatrix} + \begin{bmatrix} 0 \\ 0 \\ Y_{77} \end{bmatrix} f_p \tag{5.12}$$

and rewritten as

$$\mathbf{v} = \mathbf{Y}\mathbf{f} + \mathbf{Y}_\mathbf{p} f_p \,. \tag{5.13}$$

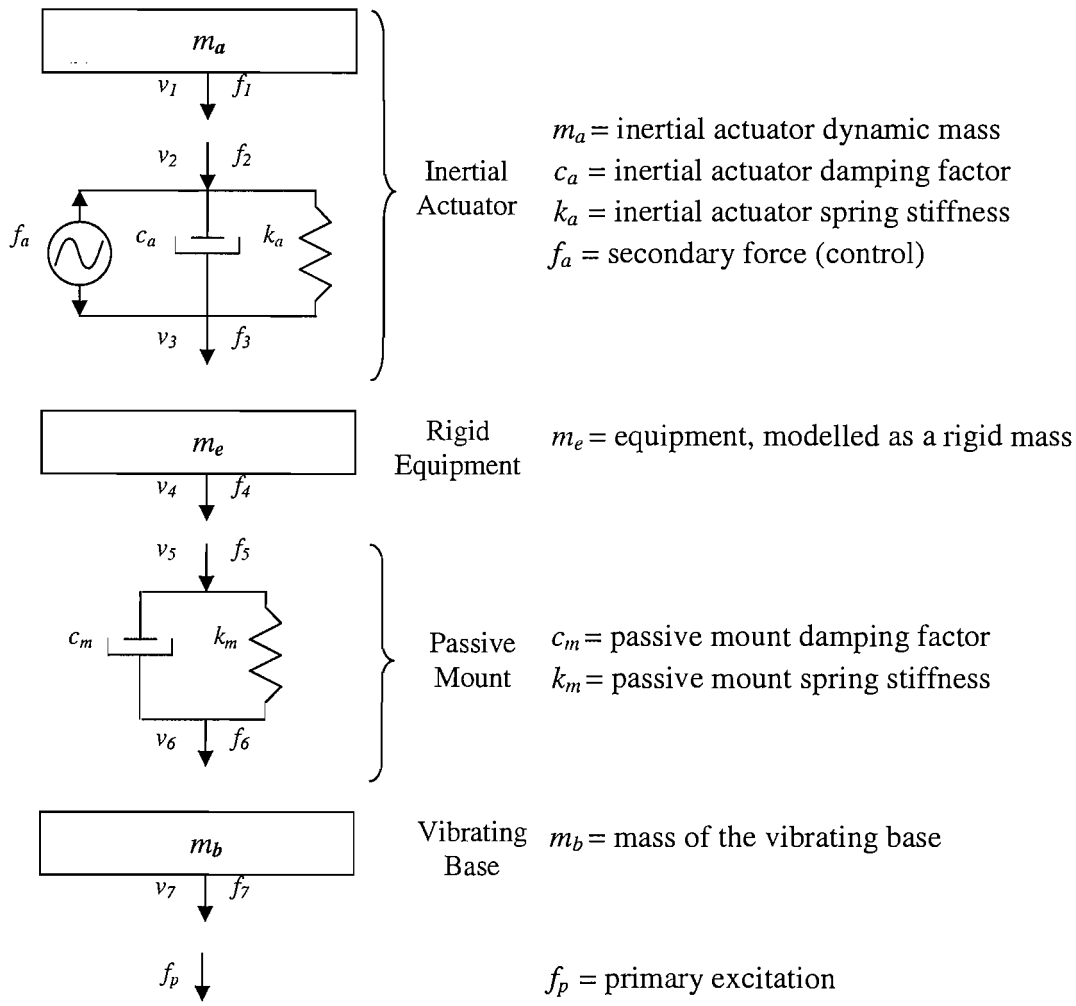

Figure 5.1 *Mechanical model of the vibration isolation system and sign convention.*

Considering equations (5.3), (5.6), (5.10), and (5.2), (5.5), (5.9), then equations (5.3), (5.4), (5.6), (5.8) and (5.10) can be grouped as

$$\begin{Bmatrix} f_1 \\ f_4 \\ f_7 \end{Bmatrix} = -\begin{bmatrix} Z_{11}^a & Z_{12}^a & 0 \\ Z_{21}^a & Z_{22}^a + Z_{11}^m & Z_{12}^m \\ 0 & Z_{21}^m & Z_{22}^m \end{bmatrix} \begin{Bmatrix} v_1 \\ v_4 \\ v_7 \end{Bmatrix} + \begin{bmatrix} 1 \\ -1 \\ 0 \end{bmatrix} f_a \tag{5.14}$$

and rewritten as

$$\mathbf{f} = -\mathbf{Z}\mathbf{v} + \mathbf{Z}_\mathbf{a} f_a . \tag{5.15}$$

In summary, equations (5.13) and (5.15) represent a condensed form of the model of the system. Substituting equation (5.15) into (5.13)

$$\mathbf{v} = [I + \mathbf{YZ}]^{-1}\mathbf{YZ}_\mathbf{a} f_a + [I + \mathbf{YZ}]^{-1}\mathbf{Y}_\mathbf{p} f_p \tag{5.16}$$

and substituting equation (5.13) into (5.15)

$$\mathbf{f} = [I + \mathbf{ZY}]^{-1}\mathbf{Z}_\mathbf{a} f_a - [I + \mathbf{ZY}]^{-1}\mathbf{ZY}_\mathbf{p} f_p . \tag{5.17}$$

From equations (5.16) and (5.17) it is possible to compute all the velocities and forces of interest within the system. Expanding equation (5.16), the analytical expressions for v_1, v_4 and v_7 can be obtained:

$$\begin{Bmatrix} v_1 \\ v_4 \\ v_7 \end{Bmatrix} = \frac{1}{\tilde{D}} \begin{bmatrix} (1 + Y_{44}Z_{11}^m + Y_{77}Z_{22}^m)Y_{11} \\ -(1 + Y_{77}Z_{22}^m)Y_{44} \\ Y_{77}Z_{21}^m Y_{44} \end{bmatrix} f_a + \frac{1}{\tilde{D}} \begin{bmatrix} Y_{11}Z_{12}^a Y_{44}Z_{12}^m Y_{77} \\ -(1 + Y_{11}Z_{11}^a)Y_{44}Z_{12}^m Y_{77} \\ (1 + Y_{11}Z_{11}^a + Y_{11}Z_{11}^a Y_{44}Z_{11}^m + Y_{44}Z_{11}^m + Y_{44}Z_{22}^a)Y_{77} \end{bmatrix} f_p \tag{5.18}$$

where

$$\tilde{D} = 1 + Y_{11}Z_{11}^a + Y_{11}Z_{11}^a Y_{44}Z_{11}^m + Y_{11}Z_{11}^a Y_{77}Z_{22}^m + Y_{44}(Z_{11}^m + Z_{22}^a) + Y_{44}Z_{22}^a Y_{77}Z_{22}^m + Y_{77}Z_{22}^m \tag{5.19}$$

Similarly, expanding equation (5.17), the analytical expressions for f_1, f_4 and f_7 can be obtained. It is given by

$$\begin{Bmatrix} f_1 \\ f_4 \\ f_7 \end{Bmatrix} = \frac{1}{\tilde{D}} \begin{bmatrix} 1+Y_{77}Z_{22}^{m} \\ -(1+Y_{77}Z_{22}^{m}) \\ Y_{44}Z_{12}^{m} \end{bmatrix} f_a + \frac{1}{\tilde{D}} \begin{bmatrix} Y_{11}Z_{12}^{a}Y_{44}Z_{12}^{m}Y_{77} \\ -(1+Y_{11}Z_{11}^{a})Y_{44}Z_{12}^{m}Y_{77} \\ Y_{77}Z_{22}^{m}(1+Y_{11}Z_{11}^{a}+Y_{44}Z_{22}^{a}) \end{bmatrix} f_p . \tag{5.20}$$

Equations (5.18) and (5.20) lead to identical expressions as those that will be used in this thesis.

5.3 Equipment velocity feedback control

In this section, a simplified system is considered and a matrix model has been used which assumes that the system is divided into four elements: rigid base, passive mount, equipment, and inertial actuator. The dynamics of each of these elements modelled as lumped systems is evaluated using point mobility terms. Figure 5.2 shows the system and the numerical values assumed for the simulations. With these values the actuator has a natural frequency of about $\frac{1}{2\pi}\sqrt{\frac{k_a}{m_a}}$ = 10.4 Hz and a damping ratio of about ζ=4.5%, and the equipment mount has a natural frequency of about $\frac{1}{2\pi}\sqrt{\frac{k_m}{m_e}}$ = 21.5 Hz (but the presence of the vibration neutraliser pushes that frequency to higher values) and a damping ratio of about ζ=5.2%.

The equation that describes the influence of the primary excitation, f_a, and the base velocity, v_b, on the equipment velocity, v_e, can be shown to be

$$v_e = \frac{Y_e T_a}{1+Z_m Y_e + Y_e Z_a} f_a + \frac{Y_e Z_m}{1+Z_m Y_e + Y_e Z_a} v_b \ , \tag{5.21}$$

where

$$Y_e = \frac{1}{j\omega m_e} = \text{Mobility of the rigid equipment} \tag{5.22}$$

$$Z_m = c_m + \frac{k_m}{j\omega} = \text{Impedance of the passive mount.} \tag{5.23}$$

T_a is the blocked response of the actuator described by equation (2.5) and Z_a is its mechanical impedance (equation (2.6)).

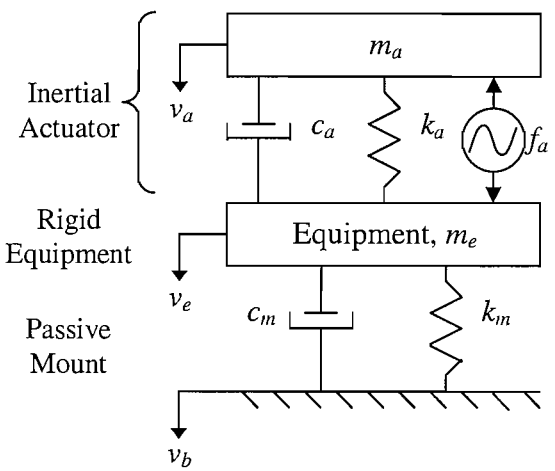

m_a = Inertial actuator dynamic mass = 0.91 Kg
c_a = Inertial actuator damping factor = 5.8 Ns/m
k_a = Inertial actuator spring stiffness = 3900 N/m
m_e = Equipment mass = 1.08 Kg
c_m = Passive mount damping factor = 18 Ns/m
k_m = Passive mount spring stiffness = 20000 N/m

f_a = Control force (secondary force)
v_a = Inertial actuator velocity
v_e = Equipment velocity
v_b = Base velocity

Figure 5.2 *Schematic of a vibration isolation system with an inertial actuator.*

Equation (5.21) can be rewritten as

$$v_e = G(j\omega) f_a + G_d(j\omega) v_b \tag{5.24}$$

The first term, $G(j\omega)$, can be regarded as the system plant, while the second term, $G_d(j\omega)$, is the disturbance transfer function. Figure 5.3 shows a schematic of the

vibration isolation system with an inertial actuator with velocity feedback control, where the feedback path is described by

$$f_a = -H(j\omega)v_e. \tag{5.25}$$

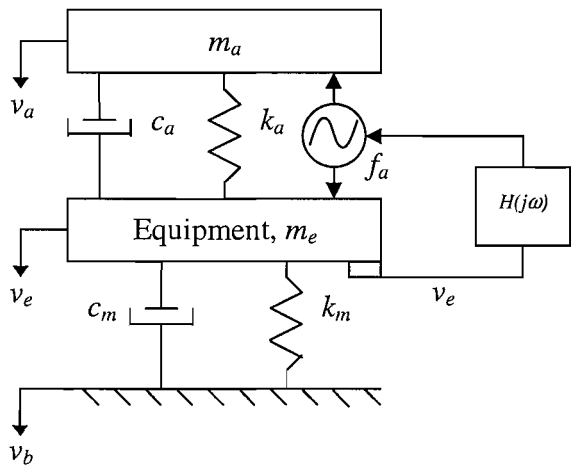

Figure 5.3 *Schematic of an active vibration isolation system with an inertial actuator and feedback control.*

Considering the feedback controller to be a real positive constant, $H(j\omega) = h_v$, then direct equipment velocity feedback is implemented and the corresponding Bode plot of the open loop system, $G(j\omega)H(j\omega)$, is shown in Figure 5.4(a). The first peak, at about 9 Hz, is an actuator-dominated resonance in which m_a and m_e are moving almost out of phase and the second peak at about 24 Hz is an equipment-dominated resonance in which m_a hardly moves at all. The additional phase shift at low frequency due to the actuator resonance can destabilize the feedback system (Preumont *et al.*, 1993). This is better shown in the Nyquist plot in Figure 5.4(b), where a portion of the curve at low frequency lies on the negative side of the x-axis. In particular, the real part of the actuator complex conjugate poles become positive when $h_v = \dfrac{c_a k_m}{k_a} = 29$ leading the system to the unstable region

(Elliott *et al.*, 2001). The transmissibility of the system, defined as the ratio between equipment velocity and base velocity, is given by

$$\frac{v_e}{v_b} = \frac{Y_e Z_m}{1 + Z_m Y_e + Y_e Z_a + Y_e T_a H(j\omega)}. \tag{5.26}$$

When $H(j\omega) = h_v$ is set to zero, equation (5.26) provides the transmissibility of the system without control (passive system). In Figure 5.5, when the gain is set to 29, the maximum attenuation at the equipment resonance is about 8 dB, while the average attenuation within the 15-30 Hz frequency range, is about 3 dB. On the other hand, the effect of velocity feedback on the inertial actuator leads the system to a potential instability, therefore the implementation of direct velocity feedback control represents a trade-off between performance and stability. Strictly speaking, the implementation of direct velocity feedback described in this section is not a skyhook damping implementation, but above the actuator resonance, it can be considered so.

Velocity feedback control and skyhook damping implementations have been extensively analysed in the literature (Miu, 1991 and 1993, Howard and Hansen, 1997 and 2000, and Clark *et al.*, 1998), even using inertial actuators (Serrand *et al.*, 2000). The purpose of the following sections and the next chapters is to investigate the limitations of direct velocity feedback control and overcome them using the devices described in Chapter 3 and Chapter 4.

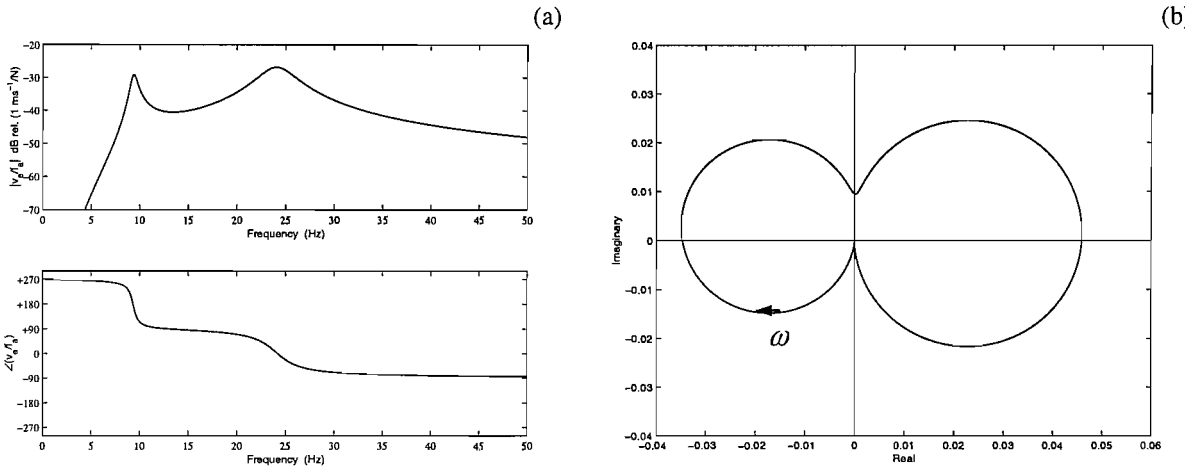

Figure 5.4 *(a): Bode plot of the open loop response for the vibration isolation system with direct velocity feedback (h_v = 1) attached to a rigid base, and (b) corresponding Nyquist plot.*

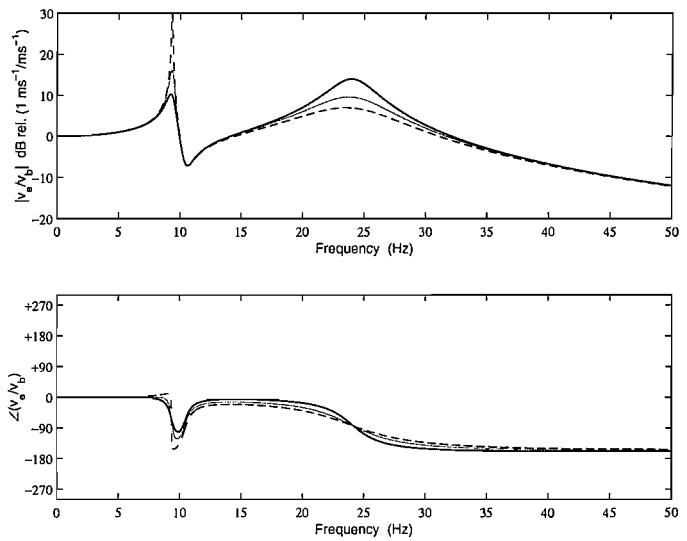

Figure 5.5 *Transmissibility of a vibration isolation system with an inertial actuator and velocity feedback control. Different velocity feedback gains are used: h_v = 0 (solid, no control), h_v = 15 (faint), h_v = 29 (dashed).*

5.4 Integrated equipment velocity feedback contol

In Figure (5.3), if the controller is given by an integrator of the form $H(j\omega) = \frac{h_{iv}}{j\omega}$, where h_{iv} is a real positive constant, the feedback stability of the closed loop system is then dramatically improved (Figure 5.6), and in particular this is illustrated by the Nyquist plot in Figure 5.6(b). Since part of the Nyquist curve lies within the unit circle centred at (-1, 0), then enhancement is expected at low and high frequency. The transmissibility is illustrated in Figure 5.7. Although high gains might be required, the integrated velocity feedback control provides a very good attenuation within a considerable frequency range, which also includes the equipment-dominated resonance. In particular, for h_{iv}=10,000, the average attenuation within the frequency range 8 Hz to 28 Hz is over 5 dB.

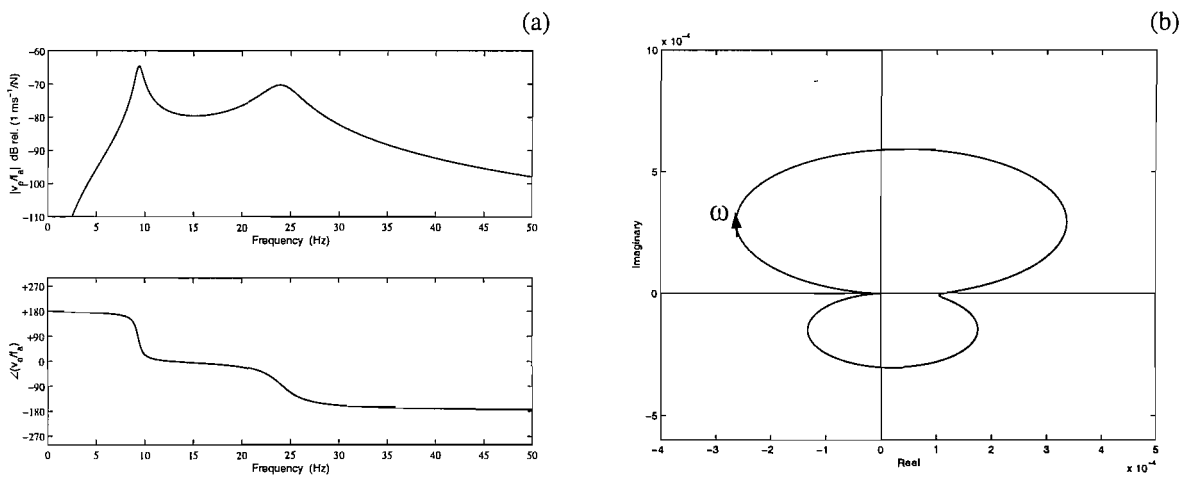

Figure 5.6 *(a): Bode plot of the open loop response for the vibration isolation system with integrated velocity feedback (h_{iv} = 1) attached to a rigid base, and (b) corresponding Nyquist plot.*

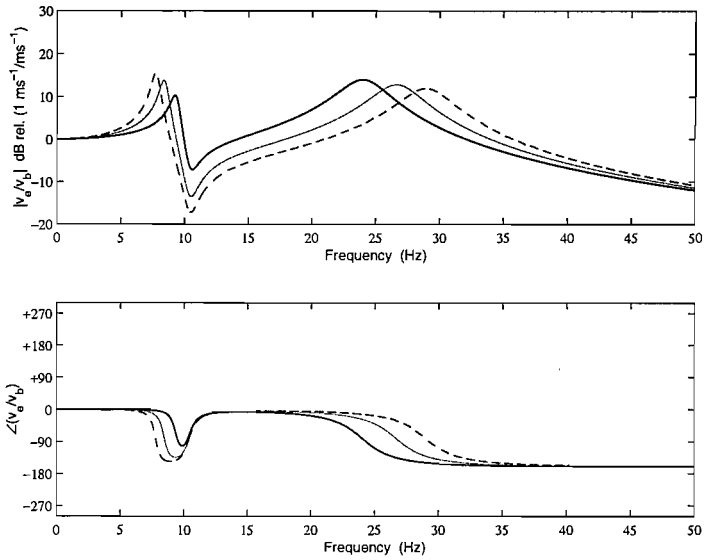

Figure 5.7 *Transmissibility of a vibration isolation system with an inertial actuator and integrated velocity feedback control. Different integrator gains are used:* $h_{iv} = 0$ *(solid, no control),* $h_{iv} = 5{,}000$ *(faint), and* $h_{iv} = 10{,}000$ *(dashed).*

Expanding the transmissibility equation for this kind of controller, it can be noted that the effect of h_{iv} on the actuator resonance is to influence k_a , leading the overall system to a lower first resonance frequency. Past the actuator resonance frequency, h_{iv} acts on k_m, indicating that absolute equipment position feedback is implemented, and this is why the equipment dominated resonance increases. When h_{iv} tends to infinity, no effect of the actuator is experienced and perfect isolation is expected, since the transmissibility goes to zero. This indicates that, past the first resonance, skyhook stiffness is implemented and when the gain tends to infinity, the equipment tends to a pinned system.

5.5 The use of other feedback controllers

When a low pass filter, given by

$$H(j\omega) = \frac{h_{lp}}{1 + j\omega\tau} \tag{5.27}$$

is used as a controller in equation (5.25), the stability and performance of the closed loop system depend on the choice of the cut-off frequency $\frac{1}{\tau}$. When the chosen cut-off frequency is greater than the equipment-dominated resonance frequency, then the closed loop system behaves in a similar way to the direct velocity feedback case, where the feedback gain $h_v = h_{lp}$. When the cut-off frequency lies before the actuator's natural frequency, then the closed loop system behaves like in the integrated velocity control case. For intermediate values of the cut-off frequency, the system turns out to be conditionally stable and shows an intermediate behaviour between the previous two cases, but is no better than either.

When a high pass filter is used in equation (5.23), described by

$$H(j\omega) = h_{hp} \frac{j\omega\tau}{1 + j\omega\tau}\ , \tag{5.28}$$

the stability and performance of the closed loop system again depend on the choice of the cut-off frequency $\frac{1}{\tau}$. By studying the stability behaviour and performance of the closed loop system when varying the cut-off frequency, a good compromise was found when the cut-off frequency was chosen to lie between the actuator's natural frequency and the equipment dominated resonance frequency. Figure 5.8(a) shows the Bode plot of the open loop system when $\tau = \frac{1}{2\pi 20}$, and Figure 5.8(b) shows the corresponding Nyquist plot when a 6 dB stability margin is guaranteed by applying a gain of $h_{hp} = 50$. The closed

loop system is conditionally stable, although the stability was improved, compared to the direct velocity feedback control case, by means of a derivative element which acts at frequencies below the actuator's natural frequency. Figure 5.9 shows the transmissibility of the system for the same value of feedback gain. Above about 22 Hz, the vibration is attenuated and the maximum attenuation is about 8 dB, while at frequencies between 10 Hz and 22 Hz, a slight enhancement, of about 2 dB, in the response is shown. When the cut-off frequency is chosen to be smaller than 20 Hz, the stability of the closed loop system is more critical, and lower gains must be used. Consequently, smaller attenuations are observed above a certain frequency, and smaller enhancement is predicted between the actuator's natural frequency and the equipment frequency. When the cut-off frequency is greater than the equipment dominated resonance frequency, greater gains can be used and greater attenuations can be obtained at higher frequencies. However, greater enhancements, of the order of 8 dB, are predicted between the first two frequencies. For this reason a cut-off frequency of 20 Hz was considered to be a good trade-off and this achieves a performance that is significantly better than velocity feedback alone, as shown in Figure 5.5.

Finally, when a notch filter, given by

$$H(j\omega) = h_n \frac{1-\omega^2\tau^2}{1+j\omega 4\tau-\omega^2\tau^2} \tag{5.29}$$

is used as a controller in equation (5.25), the stability and performance of the closed loop system will depend on the choice of the notch frequency $\frac{1}{\tau}$.

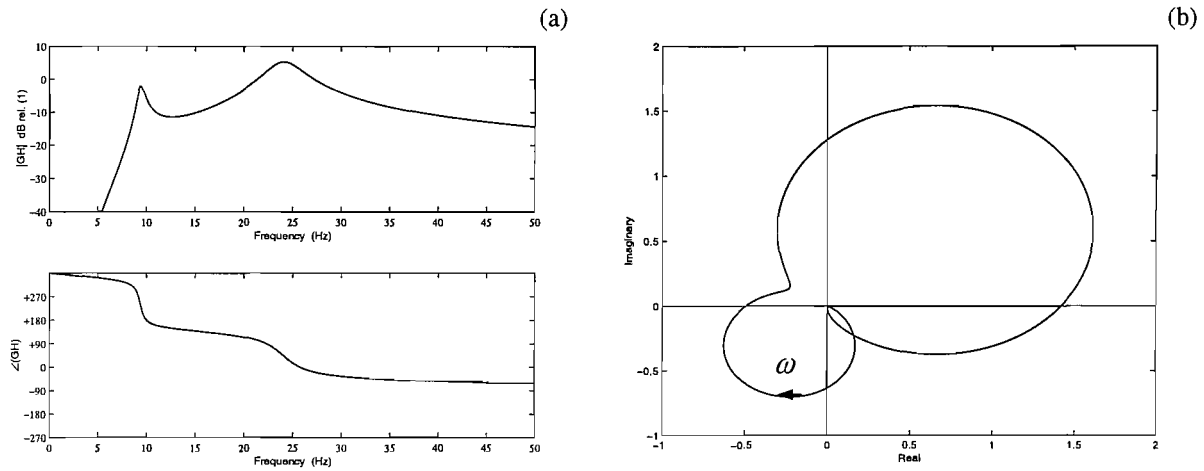

Figure 5.8 *(a): Bode plot of the open loop response for the vibration isolation system with a high pass filter (h_{hp} = 50) attached to a rigid base, and (b) corresponding Nyquist plot.*

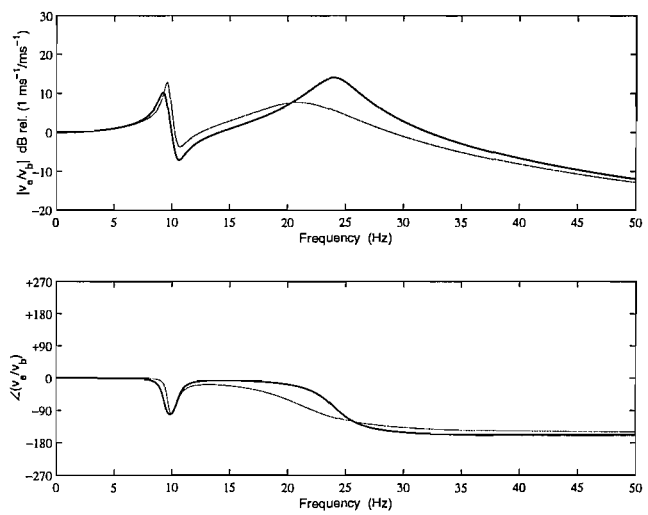

Figure 5.9 *Transmissibility of a vibration isolation system with an inertial actuator and a high pass filter. Different feedback gains are used: h_{hp} = 0 (solid, no control) and h_{hp} = 50 (faint).*

When the notch frequency is equal to the actuator's natural frequency at 10.4 Hz, good performance is obtained. Figure 5.10(a) shows the Bode plot of the open loop system when $\tau = \frac{1}{2\pi 10.4}$, and Figure 5.10(b) shows the corresponding Nyquist plot when a 6 dB stability margin is guaranteed by applying a gain of $h_n = 700$. The Nyquist plot shows that at low frequency the curve is quite close to the critical point (-1,0), therefore any phase lags at low frequency may reduce the stability margin quite substantially, as will be explained in the next section. Figure 5.11 shows the transmissibility of the system before and after control, given the above values of notch frequency and feedback gain. Although some enhancement is predicted at low frequency, the attenuation at higher frequencies is quite remarkable, showing that notching out the actuator's natural frequency is in principle a good control strategy for vibration isolation.

Unfortunately, if the notch frequency is set to be close, but different from the actuator's natural frequency, then the gain h_n must be reduced considerably in order to guarantee a 6 dB stability margin. Consequently, the attenuation of the equipment-dominated resonance is reduced as well. This is a clear limitation of this strategy and the design of the notch filter would require detailed knowledge of the response of the mounted actuator.

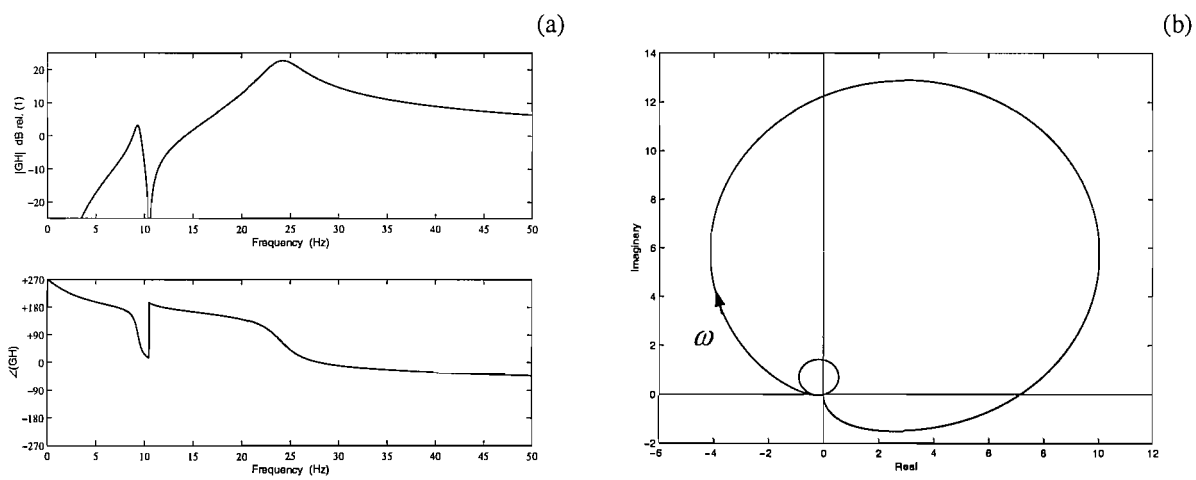

Figure 5.10 *(a): Bode plot of the open loop response for the vibration isolation system with a notch filter (h_n = 700) attached to a rigid base, and (b) corresponding Nyquist plot.*

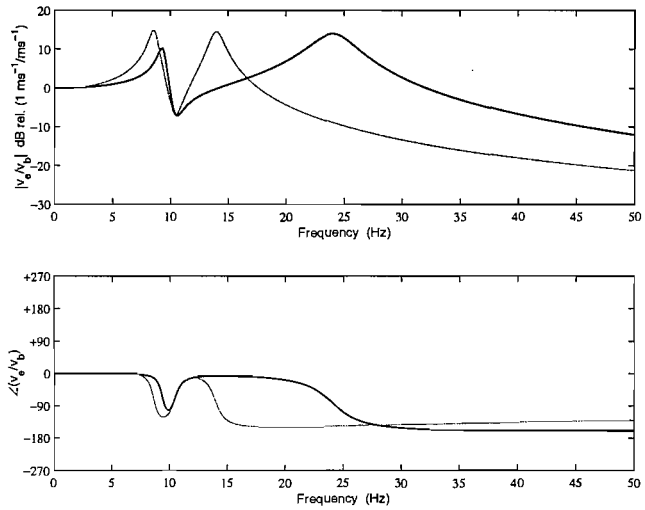

Figure 5.11 *Transmissibility of a vibration isolation system with an inertial actuator and a notch filter. Different feedback gains are used:* $h_n = 0$ *(solid, no control) and* $h_n = 700$ *(faint).*

5.6 Realistic closed-loop model formulation

5.6.1 Effect on integrated equipment velocity feedback

The closed loop system, when integrated velocity feedback control is implemented, is unconditionally stable for any feedback gain h_{iv}. This is true only for ideal integrators. In fact, when the pole of the integrator is not exactly zero, the derivative of the Nyquist plot about $\omega = 0$ is not zero, but it is positive. Therefore, from $\omega = 0$, the Nyquist plot initially starts in the third quadrant. This means that the curve encircles the point (-1,0) for h_{iv} greater than a certain critical value (Figure 5.14). In other words, using real integrators, the system becomes conditionally stable. Also, high frequency causes of instability may affect the overall system. An analysis of the complete system with integrated velocity feedback shows how sensitive the closed loop system is with respect to some of the most common causes of high and low frequency instability.

In real systems many other components are present in the control loop (Ren, *et al.*, 1997 and Ananthaganeshan *et al.*, 2001). Figure 5.12 illustrates a more realistic block diagram for a practical active isolation system based on integrated equipment velocity control. Accelerometers are very common vibration transducers, and their output is often amplified by a charge amplifier, which behaves like a high-pass filter. If velocity is needed, the measured signal must be integrated. Ideal integrators do not exist, therefore their dynamics must be taken into account in the overall stability analysis. In the control segment of the loop, after the controller, a power amplifier is usually employed to amplify the signal and make it appropriate for the actuator. Also, a delay is usually present, mostly due to transmission lags of the electric signal.

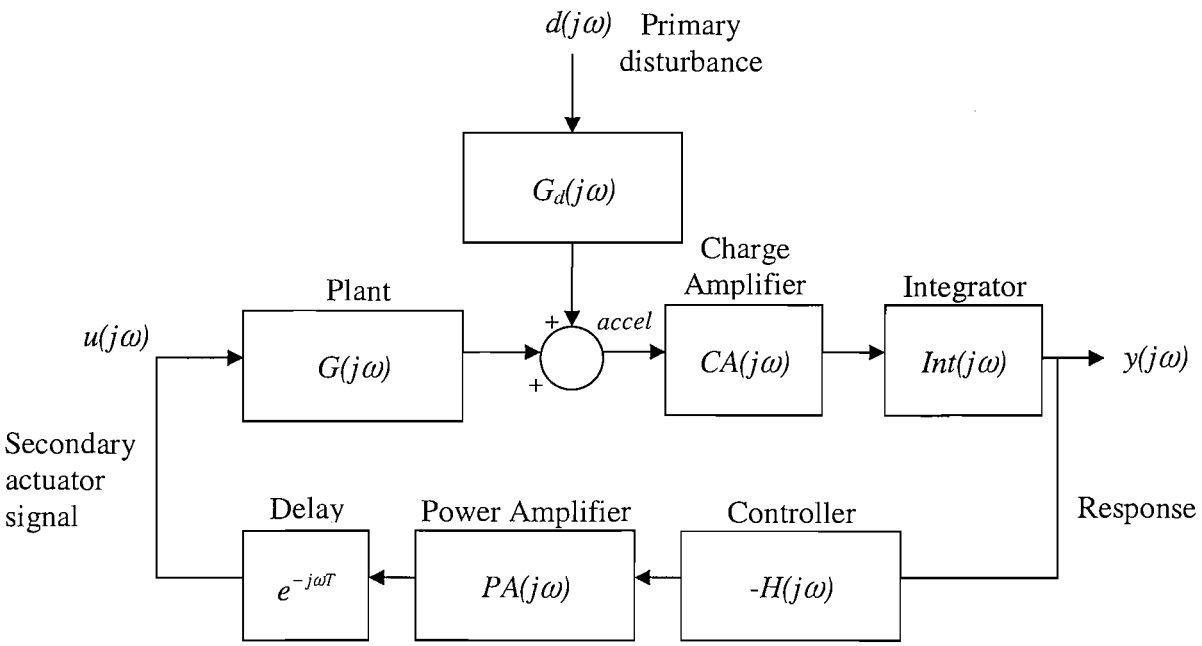

Figure 5.12 *Block diagram of a realistic feedback control system including the plant, the controller, and the electronic components.*

The following equations illustrate the dynamics of the components in Figure 5.12. The numerical values have been chosen according to off-the-shelf commercial components currently used in the laboratory. In particular, the charge amplifier cut-off frequency is 1 Hz. In this case, the plant is different from equation (5.24) because in this case its output is

acceleration, not velocity. The controller is composed of a second order high-pass filter and an integrator.

$$G(j\omega) = \frac{j\omega Y_e T_a}{1 + Z_m Y_e + Y_e Z_a} \tag{5.30}$$

$$H(j\omega) = \frac{-\omega^2 0.1326}{(1 + j\omega 0.1326)^2} \cdot \frac{h_{iv}}{1 + j\omega 0.0909} \tag{5.31}$$

$$CA(j\omega) = \frac{j\omega 0.159}{1 + j\omega 0.159} \tag{5.32}$$

$$Int(j\omega) = \frac{1}{1 + j\omega 0.251} \tag{5.33}$$

$$PA(j\omega) = \frac{j\omega 0.1326}{1 + j\omega 0.1326} \tag{5.34}$$

A description of the effects of the main causes of instability in the vibration isolation problem using inertial actuators with inner and outer feedback control loops is given in Benassi *et al.* (2002a). The open loop frequency response function of the system shown in Figure 5.12 can be written as

$$G\ (j\omega)H_t(j\omega) = G(j\omega)CA(j\omega)Int(j\omega)H(j\omega)PA(j\omega)e^{-j\omega T} \tag{5.35}$$

where the $e^{-j\omega T}$ term represents a delay, as show in Figure 5.12, while the closed loop frequency response function is given by

$$v_e = \frac{G_d(j\omega)}{1 + G(j\omega)H_t(j\omega)} v_b \tag{5.36}$$

where

$$G_d = \frac{j\omega Y_e Z_m}{1 + Z_m Y_e + Y_e Z_a} \tag{5.37}$$

In particular, the overall frequency response of all the electronic components, given by

$$H_t(j\omega) = CA(j\omega)Int(j\omega)H(j\omega)PA(j\omega)e^{-j\omega T}, \qquad (5.38)$$

is plotted in Figure 5.13. Given the realistic system in Figure 5.12 and also assuming a time delay T=0.001 seconds, the maximum gain h_{iv} that guarantees the system to be stable is about 6500 (it would be about 6000 if the base were flexible). This is illustrated in Figure 5.14. For this value of the feedback gain, the maximum attenuation in the closed loop response (Figure 5.15) is computed to be 6 dB, while the average attenuation between the two main resonance frequencies is 3 dB. At the critical point (-1,0), the frequency value that the Nyquist plot assumes is 9.4 Hz.

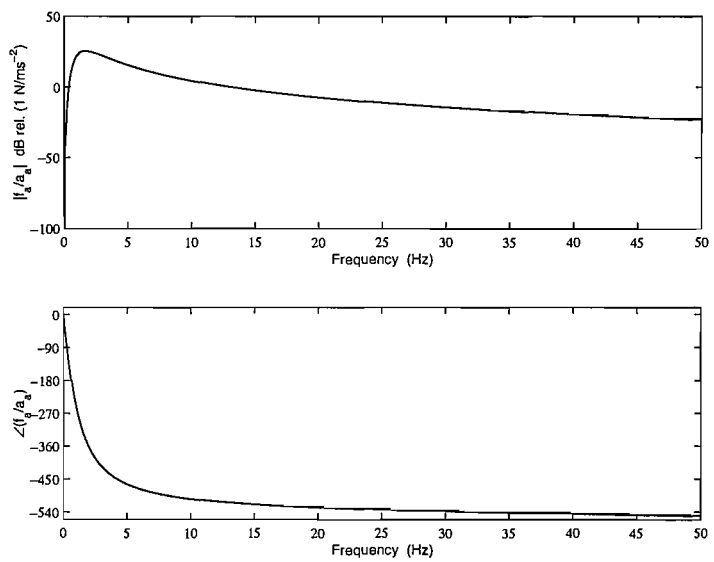

Figure 5.13 *Bode plot of the overall frequency response of all the electronic components.*

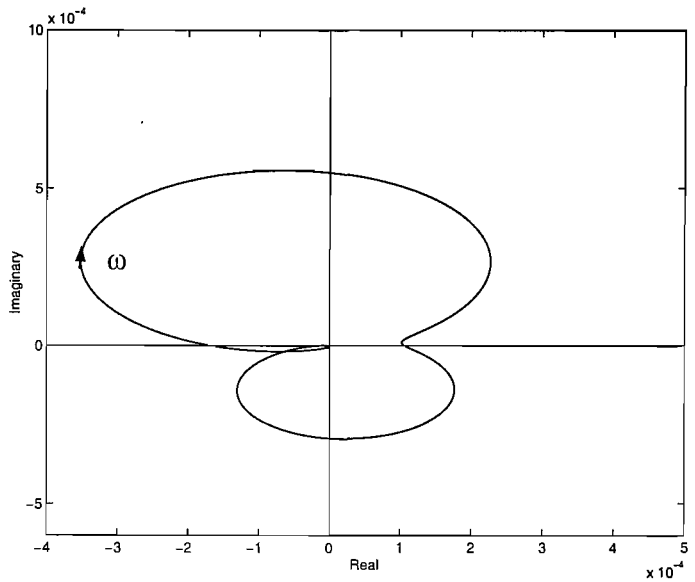

Figure 5.14 *Nyquist plot of the open loop response for a realistic vibration isolation system with integrated velocity feedback (h_{iv} = 1) attached to a rigid base. The delay is assumed to be 0.001 seconds.*

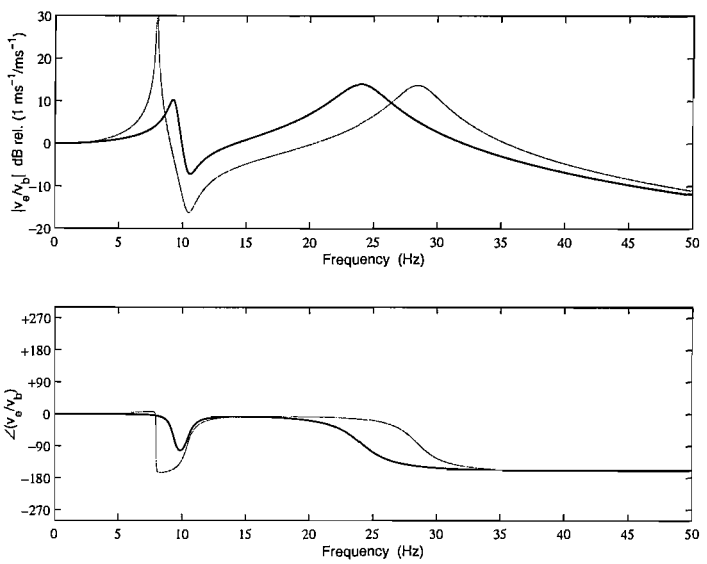

Figure 5.15 *Transmissibility of the ideal system without control (solid) and the realistic (faint) vibration isolation system with an inertial actuator and integrated velocity feedback control. Realistic electronic components are simulated, the delay is assumed to be 0.001 seconds, and the feedback gain is set to 6500.*

5.6.2 Effect on inner force feedback

In real systems based on inner force feedback control, unlike the integrated control solution, the force gauge measurement does not need to be integrated, but it still needs a charge amplifier. A typical Nyquist plot for such a system is shown in Figure 5.16, where, unlike the theoretical model in Figure 3.5, the closed-loop system turns out to be conditionally stable. The first loop describes the inertial actuator resonance, the second is associated to the equipment dynamics and the loop about the origin is due to the time delay present in the system, which affects its behaviour especially at high frequency by adding a term to the phase which is dependent on frequency (ωT).

In summary, although inner force feedback control is, in principle, a very effective control strategy, in real systems it raises robustness issues, which greatly limit its performance.

An analysis of the system with inner integrated force feedback shows that in this case the phase margin is big enough to still allow large gains before instability in spite of the additional phase shifts due to instrumentation.

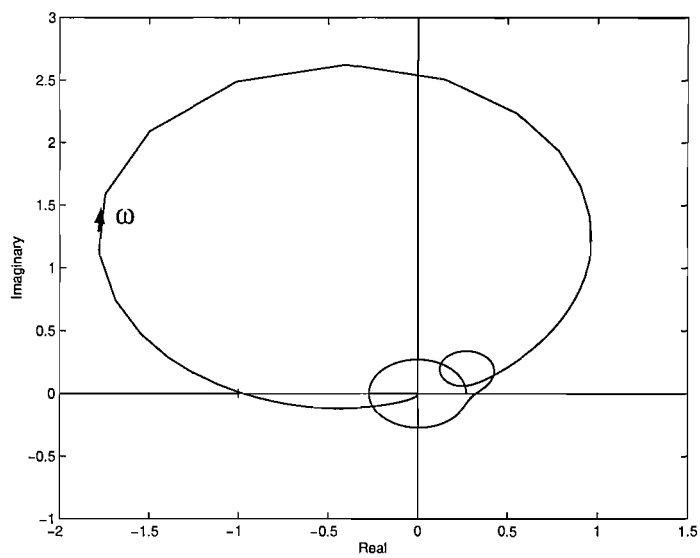

Figure 5.16 *Nyquist plot of the open loop response for a realistic vibration isolation system with direct force feedback ($h_f = 1$) attached to a rigid base.*

5.7 Equipment isolation when the inertial actuator resonance frequency is greater than the structural frequency of interest

When the inertial actuator resonance frequency is greater than the equipment resonance frequency of interest, the overall system turns out to be more difficult to control, therefore, when possible, an actuator resonance frequency below the structural frequency is recommended (Zimmerman *et al.*, 1990, Preumont *et al.*, 1993, Elliott *et al.*, 2001a, Benassi *et al.*, 2002a).

Placing the cut-off frequency of the inertial actuator above the highest frequency of interest is not a feasible method of reducing the effects of the actuator dynamics on control design. In fact, the magnitude of the actuator force output rises at 40 dB/decade below the resonance frequency and the output force level would be severely limited at low frequencies, typically where the highest level of control force are required. Also, if the structure is very flexible, the model approaches a partial differential equation model with an infinite number of frequencies. Hence, by placing the cut-off frequency of the inertial actuator between two structural frequencies, potential unstable closed loops can be created due to the effect of the residual uncontrolled modes (Balas, 1978, and Goh and Caughey, 1985).

In this section the actuator mass was changed to 0.5 kg, its stiffness was changed to 60,000 N/m, and its damping to 10 N/ms^{-1}. This choice leads to an equipment resonance frequency of about 21 Hz and an inertial actuator resonance frequency of about 55 Hz.

When direct equipment velocity feedback is used to control the equipment velocity, an additional phase shift due to the structure compromises the feedback stability. The Nyquist plot (Figure 5.17) shows a portion of the curve at low frequency that lies in the negative real plane. In contrast to the corresponding case described in Section 5.2, this loop is the equipment-dominated resonance.

When the feedback gain is set to 240, the stability limit is reached. In this configuration the closed loop behaviour shows good attenuation (15 dB maximum, 7 dB average) within 45 and 65 Hz, but also amplification between 19 and 23 Hz. This phenomenon, which can be up to 20 dB, is exactly the opposite of what we aimed. In other words, the inertial

actuator is not able to be effective at frequencies below its own resonance frequency, where it turns out to be counterproductive.

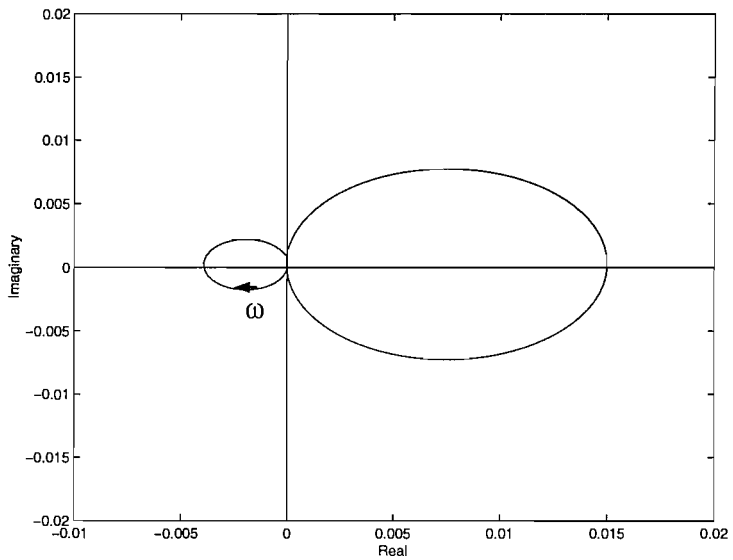

Figure 5.17 *Nyquist plot of the open loop response for the vibration isolation system with direct velocity feedback (h_v = 1) attached to a rigid base. In this case, the actuator's natural frequency is greater than the equipment-dominated resonance frequency.*

When integrated velocity feedback is applied, the Nyquist plot is rotated by 90°, as described in Section 5.3. Poor performance and poor robustness are also seen for real systems with this strategy.

5.8 Conclusions

A review of strategies for active vibration isolation using an inertial actuator with outer velocity feedback control was presented. A matrix model has been used which assumes that the system is divided into four elements: base, passive mounts, equipment, and inertial actuator. Feedback stability limits and performance were considered. In particular,

once the theoretical analysis was completed, a realistic case using real commercial components was analysed.

The performance of active isolation systems with inertial actuators and direct equipment velocity feedback is known to be limited by the actuator resonance. The effect of various simple compensator circuits in the feedback loop were investigated, and it was found that a simple high-pass filter significantly improved the trade-off between high frequency attenuation and low frequency enhancement.

Integrated equipment velocity feedback control is unconditionally stable for an ideal system, while it is only conditionally stable for real systems.

Throughout this study it has been assumed that the actuator resonance frequency was below the equipment natural frequency. If the inertial actuator resonance frequency is greater than the equipment natural frequency, it is shown that the overall system is more difficult to control and the control strategies here presented do not show good results.

Another way of overcoming the performance problems associated with the actuator resonance would be to lower it by means of an inner force feedback control loop or implementing an inner displacement feedback. In the first case, an apparent mass is added to the inertial actuator moving mass, while in the second case stiffness is removed from the inertial actuator, as discussed in the following chapters.

Chapter 6

Active vibration isolation theory with an inertial actuator controlled with inner force feedback

6.1 Introduction

This chapter deals with the stability and performance analysis of a single degree of freedom system for active vibration isolation using the control strategies described in Chapter 3. This is based on inner actuator force feedback to improve the response of the actuator and outer equipment velocity feedback to minimize the equipment vibration.

A matrix model has been used which assumes that the system is divided into four elements: the vibrating plate, a passive mount, the equipment, and the inertial actuator. In contrast to the analysis in Chapter 5, the base structure is not assumed to be perfectly rigid. The dynamics of each of these elements are evaluated using mobility or impedance functions. Figure 6.1 shows the typical system that has been used in this study and the numerical values assumed for the simulations. With these values the actuator has a resonance frequency at 11 Hz and a damping ratio of about ζ=4.5%, the equipment mounting system has a resonance frequency at 24 Hz and a damping ratio of about ζ=5.2%, and the vibrating base has a first resonance frequency of about 46 Hz and a damping ratio of about ζ=4.8%.

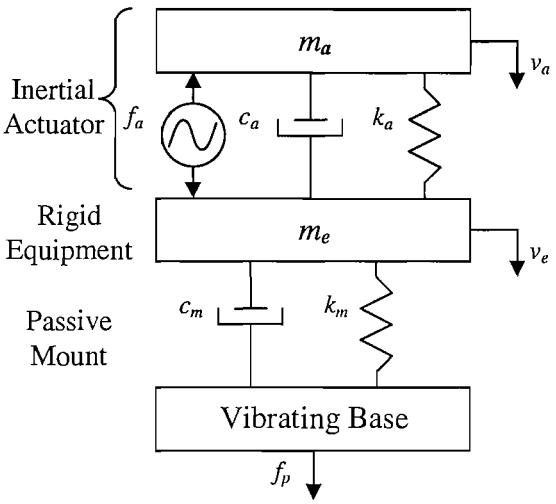

m_a = Inertial actuator dynamic mass = 0.91 Kg
c_a = Inertial actuator damping factor = 5.8 N/ms^{-1}
k_a = Inertial actuator stiffness = 3900 N/m
m_e = Equipment mass = 1.08 Kg
c_m = Passive mount damping factor = 18 N/ms^{-1}
k_m = Passive mount stiffness = 20000 N/m

The mechanical properties of the vibrating plate, which is a steel plate with two clamped edges and two free edges, are fully described by Gardonio *et al.* (1997a)

f_p = Primary force (disturbance)
f_a = Secondary force (control)
v_a = Inertial actuator dynamic mass velocity
v_e = Equipment velocity

Figure 6.1 *Mechanical model of an active vibration isolation system with an inertial actuator.*

Details of the mobilities and impedances used to describe the system can be found in Chapter 5, along with the sign conventions and the complete model equations.

6.2 Inner actuator force feedback and outer equipment velocity feedback control

Figure 6.2 shows the schematic of the entire system when the inner force feedback loop is implemented. The expression for the equipment velocity as a function of the primary force, f_p, and the transmitted force, f_t, is given by

$$v_e = \frac{Y_e Z_m Y_b}{1 + Z_m (Y_e + Y_b)} f_p + \frac{Y_e (1 + Y_b Z_m)}{1 + Z_m (Y_e + Y_b)} f_t \,. \qquad (6.1)$$

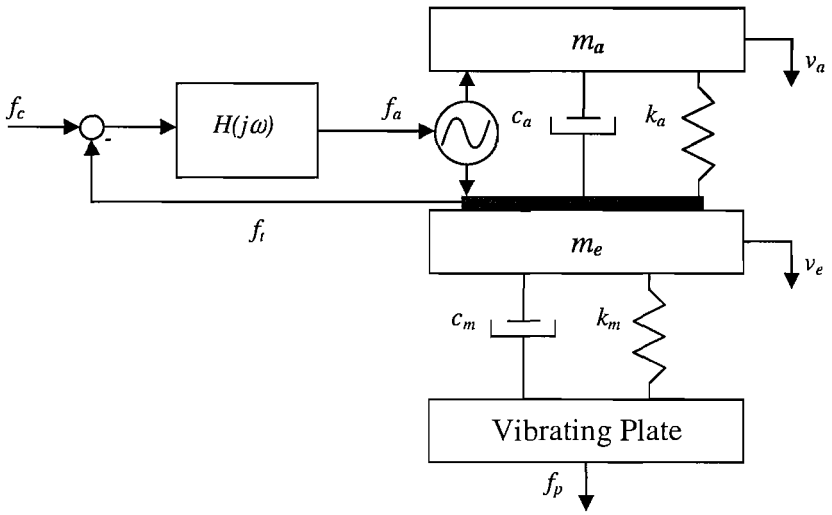

Figure 6.2 *Schematic of an active vibration isolation system with an inertial actuator and implementation of the inner feedback control.*

Substituting equation (3.6) into equation (6.1), the expression of the equipment velocity, when the inner force feedback loop is implemented, is given by

$$v_e = \frac{Y_e Z_m Y_b}{1 + Z_m(Y_e + Y_b + Y_e Z_{a1}^{'} Y_b) + Y_e Z_{a1}^{'}} f_p + \frac{Y_e T_{a1}^{'}(1 + Y_b Z_m)}{1 + Z_m(Y_e + Y_b + Y_e Z_{a1}^{'} Y_b) + Y_e Z_{a1}^{'}} f_c . \quad (6.2)$$

When the control force, f_c , is set to zero and the direct force feedback gain h_f tends to infinity, $Z_{a1}^{'}$ tends to zero and the equipment velocity per unit primary excitation, v_e / f_p , describes a system as if the actuator is no longer present.

Figure 6.3 shows a schematic of the system when both inner and outer loops are implemented. The outer loop is a velocity feedback loop, which aims to take energy away from the system, through a controller which has the dimensions of an impedance Z_D, which in the first instance will be taken as a constant real positive gain. In fact,

$$f_c = -Z_D v_e . \quad (6.3)$$

Substituting equation (6.3) into equation (6.2) the equipment velocity per primary force, when the dual-loop is implemented, is given by

$$v_e = \frac{Y_e Z_m Y_b}{1 + Z_m(Y_e + Y_b + Y_e Z_{a1}^{'} Y_b) + Y_e Z_{a1}^{'} + Y_e T_{a1}^{'}(1 + Y_b Z_m) Z_D} f_p . \qquad (6.4)$$

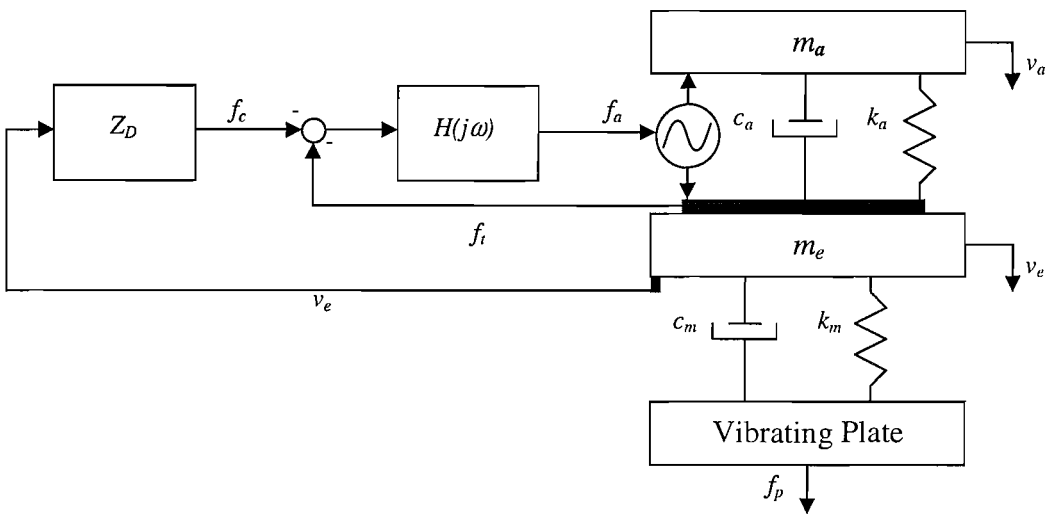

Figure 6.3 *Schematic of an active vibration isolation system with an inertial actuator and implementation of the inner force feedback control loop and the outer equipment velocity feedback control.*

Figure 6.4(a) shows the equipment velocity per unit control command, v_e / f_c, for different values of the inner force feedback gain h_f. The effect of increasing the equipment velocity and the lowering of the first resonance can be noted. Figure 6.4(b) shows the corresponding Nyquist plot, which determines the stability of the closed loop system once the outer velocity feedback control is implemented. The ideal closed-loop system is conditionally stable and a portion of the Nyquist plot relative to the first resonance lies within the unit circle centred at (-1,0), which indicates an enhancement of the closed-loop response. When the inner force feedback gain h_f is increased, considering that the system with inner force feedback control is unconditionally stable (Figure 3.4), the effect of

increasing the outer velocity feedback gain Z_D is good attenuation and unconditional stability for all frequencies greater than the first resonance, which happens to be at very low frequency. Unfortunately, as shown in Section 3.1, at low frequencies the Nyquist plot lies very close to the critical point and therefore instability is likely to happen especially to real systems where an additional phase shift is present due to the electronic components. In summary, from a stability point of view, the force and velocity controller raises some concerns and special attention must be paid when real systems are implemented.

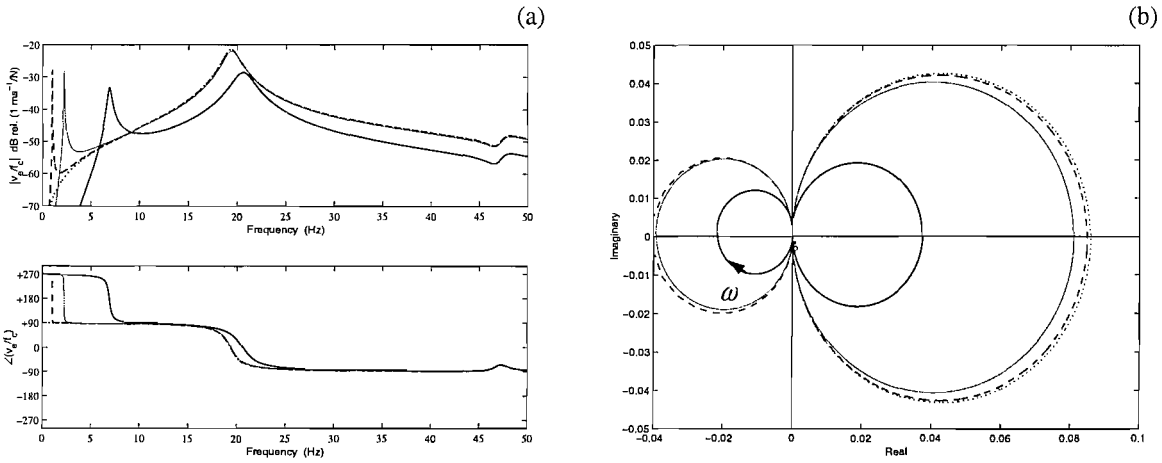

Figure 6.4 *(a): Equipment velocity per unit control command when different inner force feedback loop gains h_f are used: h_f = 1 (solid), h_f = 20 (faint), h_f = 100 (dashed), and h_f = 100,000 (dotted). (b): Nyquist plot of the equipment velocity per unit control command when h_f = 20 (faint), h_f = 100 (dashed), and h_f = 100,000 (dotted). The solid line shows the case when no control is implemented.*

Figure 6.5 shows the equipment velocity per unit primary excitation, v_e / f_p , for different values of the gain h_f when no outer loop is implemented. Although the direct inner force feedback loop causes the equipment velocity v_e to increase, it has the beneficial effect of bringing the first resonance to lower frequencies (in particular, see the faint line). Figure 6.6 shows the equipment velocity per unit primary excitation when the inner force feedback control and the outer velocity feedback control are implemented. Performance-wise, attenuation can be achieved with relatively low gains. In conclusion, there is a trade-off between performance and stability margin, which makes the inner force feedback and

outer equipment velocity feedback control scheme very interesting on one hand, but on the other hand it makes it impractical because of the stability issues discussed above.

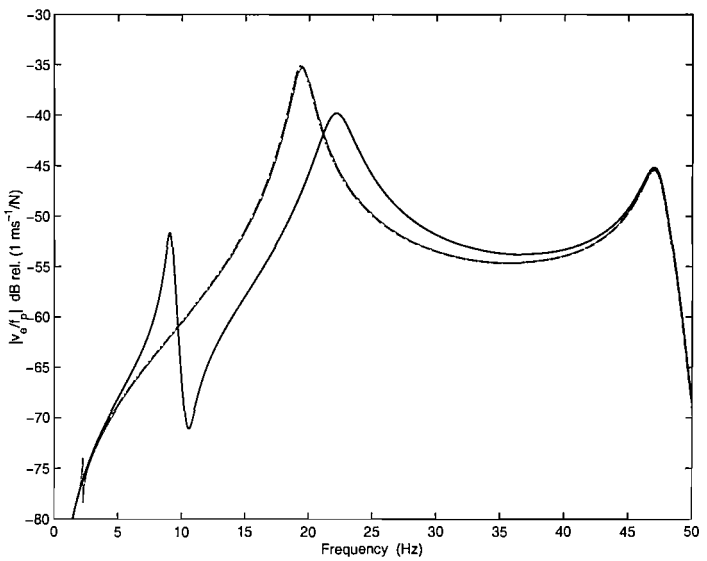

Figure 6.5 *Equipment velocity per unit primary force when h_f = 0 (solid), h_f = 20 (faint), h_f = 100 (dashed), and h_f = 100,000 (dotted). In this case, no outer loop is implemented.*

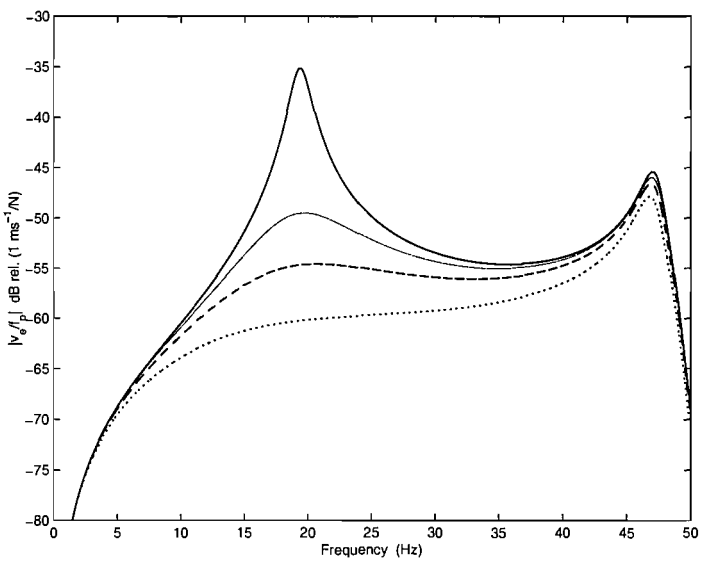

Figure 6.6 *Equipment velocity per primary excitation when the inner force feedback gain h_f = 100 and different outer velocity feedback control gains are used: Z_D=0 (solid), Z_D=50 (faint), Z_D=100 (dashed), and Z_D=200 (dotted).*

The mechanical impedance of the equipment when the inner force feedback control and the outer equipment velocity feedback control are implemented is given by

$$Z = \frac{j\omega m_a k_a - \omega^2 m_a (c_a + h_f Z_D)}{k_a + j\omega c_a - \omega^2 m_a (1 + h_f)} \tag{6.5}$$

which is plotted in Figure 6.7. Even for low values of the inner force gain h_f, the equipment mechanical impedance tends to Z_D past the first resonance frequency, which indicates that the overall system tends to a skyhook damper. When $h_f = 0$, the mechanical impedance tends to c_a above the resonance frequency. In conclusion, damping is added to the system in the form of the desired impedance Z_D, which is a positive real constant value that can be imposed by the designer.

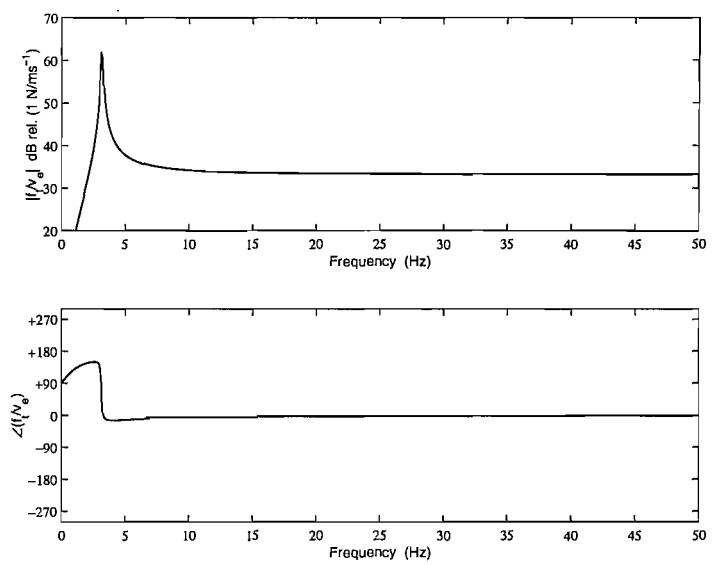

Figure 6.7 *Mechanical impedance of the equipment when the inner force feedback control and the outer velocity feedback control are implemented.* h_f = *10 and* Z_D = *50.*

6.3 Integrated inner actuator force feedback and outer equipment velocity feedback control

Substituting equation (3.10) into equation (6.1), when the inner feedback loop is based on integrated force feedback control, the expression for the equipment velocity, v_e, as a function of the primary excitation, f_p, and the control command, f_c, is given by

$$v_e = \frac{Y_e Z_m Y_b}{1 + Z_m(Y_e + Y_b + Y_e Z_{a2}^{'} Y_b) + Y_e Z_{a2}^{'}} f_p + \frac{Y_e T_{a2}^{'}(1 + Y_b Z_m)}{1 + Z_m(Y_e + Y_b + Y_e Z_{a2}^{'} Y_b) + Y_e Z_{a2}^{'}} f_c . \quad (6.6)$$

Even in this case, when the control force, f_c , is set to zero and the integrated inner force feedback gain h_{if} tends to infinity, $Z_{a2}^{'}$ tends to zero and the equipment velocity per unit primary excitation, v_e / f_p , describes a system as if the actuator is no longer present. It can be noted that for $f_c = 0$, when h_{if} tends to infinity, $Z_{a2}^{'}$ tends to zero, and v_e / f_p describes a system as if the actuator is no longer present. Substituting equation (6.3) into equation (6.6) the equipment velocity per primary force is given by

$$v_e = \frac{Y_e Z_m Y_b}{1 + Z_m(Y_e + Y_b + Y_e Z_{a2}^{'} Y_b) + Y_e Z_{a2}^{'} + Y_e T_{a2}^{'}(1 + Y_b Z_m) Z_D} f_p \quad (6.7)$$

and represents the effect of the integrated inner force feedback control and the outer velocity feedback control. Figure 6.8(a) shows the equipment velocity per unit command signal for different values of the inner feedback gain h_{if}. For high values of the inner feedback gain h_{if} the first resonance is very damped, following the behaviour described in Chapter 3. Figure 6.8(b) shows the corresponding Nyquist plot of v_e / f_c for different inner feedback gains, which determines the stability of the closed-loop system once the outer velocity feedback control is implemented. When the inner feedback gain h_{if} is increased, since the system with the inner control loop is unconditionally stable and very robust, the effect of increasing Z_D is good attenuation and unconditional stability. Figure 6.9 shows the equipment velocity per unit primary excitation for different values of the inner

feedback gain h_{if} when no outer control is present. It is clear that the outer velocity feedback loop is needed, since the effectiveness of the sole inner feedback loop is not outstanding.

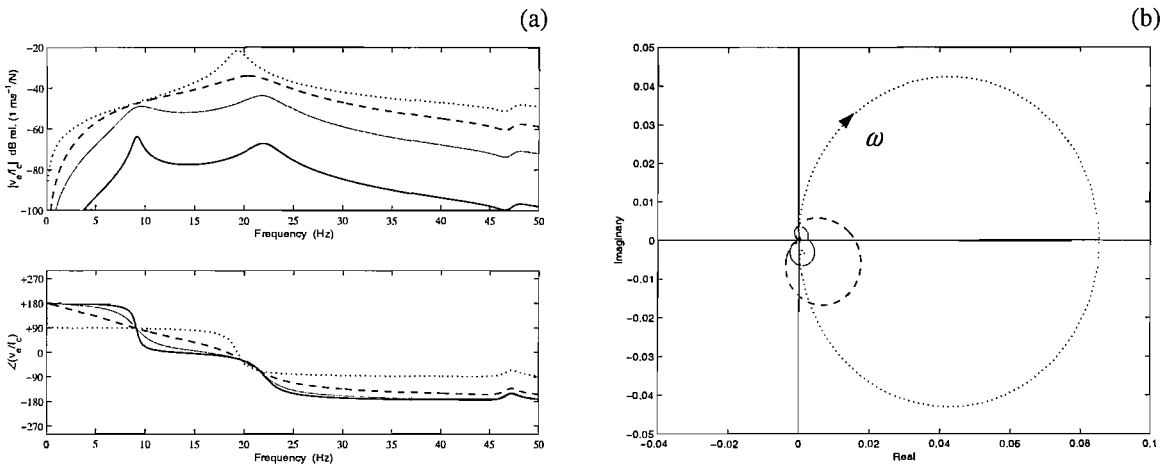

Figure 6.8 *(a): Equipment velocity per unit control command when different inner feedback loop gains h_{if} in $H(j\omega)= h_{if}/j\omega$ are used: h_{if} = 1 (solid), h_{if} = 20 (faint), h_{if} = 100 (dashed), and h_{if} = 100,000 (dotted). (b): Nyquist plot of the equipment velocity per unit control command when h_{if} = 20 (faint), h_{if} = 100 (dashed), and h_{if} = 100,000 (dotted). The solid line shows the case when no control is implemented.*

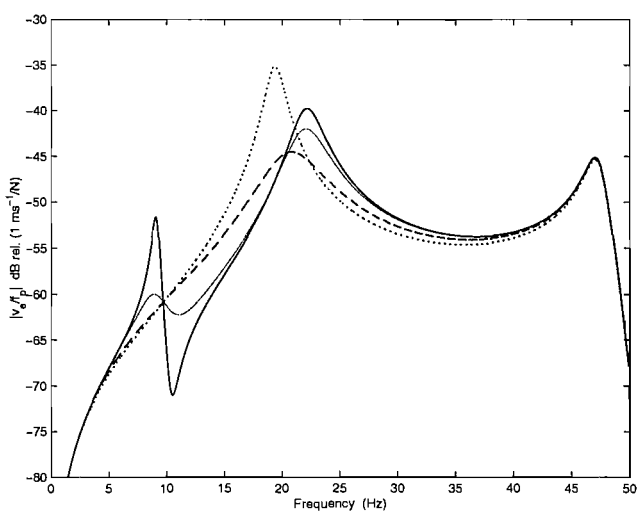

Figure 6.9 *Equipment velocity per unit primary force when h_{if} = 0 (solid), h_{if} = 20 (faint), h_{if} = 100 (dashed), and h_{if} = 100,000 (dotted).In this case, no outer loop is present.*

Figure 6.10 shows the equipment velocity per unit primary excitation when the integrated inner force feedback and the outer equipment velocity feedback control are implemented. The effect of the inner feedback gain h_{if} can be seen from the damped first resonance frequency. It is also shown that good vibration isolation performance can be achieved, but high gains are needed. Also, at frequencies slightly higher than the equipment resonance frequency, enhancement (rather than attenuation) is experienced due to the velocity feedback, as explained in Section 5.4. This does not indicate good performance. In summary, the integrated inner force feedback control and outer velocity control posses a high stability margin. This is mainly due to the fact that even under ideal conditions, the stability plot entirely lies on the positive x-axis semi-plane. On the other hand, good performance can be achieved, but high outer loop gains are needed.

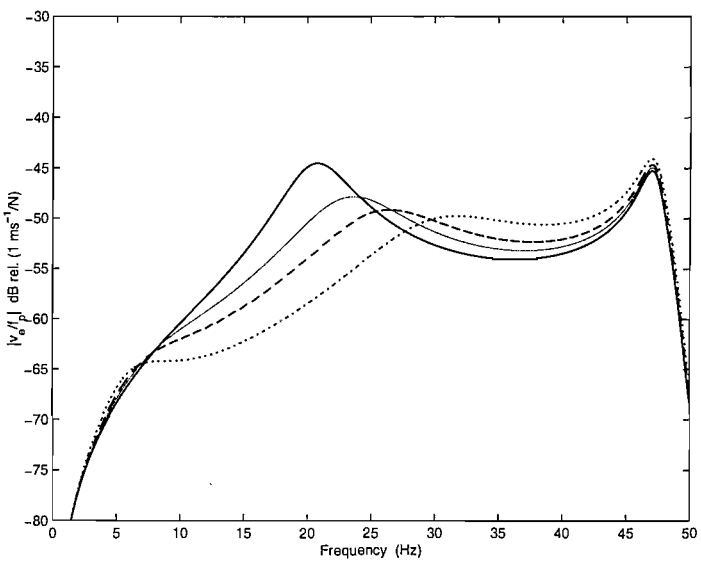

Figure 6.10 *Equipment velocity per primary excitation when the inner loop gain h_{if} = 100 and different outer velocity feedback control gains are used: Z_D=0 (solid), Z_D=50 (faint), Z_D=100 (dashed), and Z_D=200 (dotted).*

The mechanical impedance of the equipment when the dual-loop control is implemented is given by

$$Z = \frac{j\omega m_a (k_a + h_{if} Z_D) - \omega^2 m_a c_a}{k_a + j\omega c_a - \omega^2 m_a + j\omega m_a h_{if}} \tag{6.8}$$

and is illustrated in Figure 6.11. Like in the previous case, the mechanical impedance tends to Z_D past the first resonance frequency, which indicates that the overall system tends to a skyhook damper. However, higher gains are needed to achieve this behaviour.

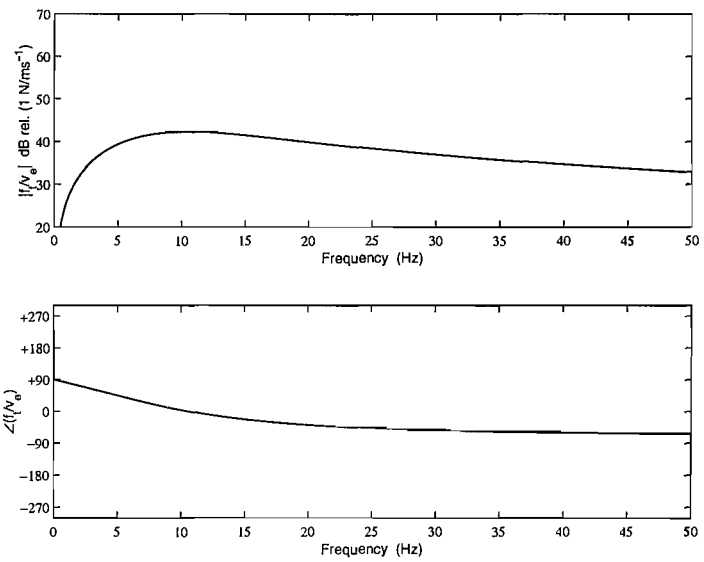

Figure 6.11 *Mechanical impedance of the equipment when the inner integrated force feedback control and the outer velocity feedback control are implemented. In particular, $h_{if} = 100$ and $Z_D = 100$.*

So far, it has been shown that the inner force and outer equipment velocity feedback control strategy does not have an acceptable stability margin, but it performs very well. On the contrary, the integrated inner force and outer equipment velocity control strategy is more stable, but it requires higher gains in order to achieve comparable performance. In the next section a solution is presented which offers both a good stability margin and good performance.

6.4 Inner actuator phase-lag feedback and outer equipment velocity feedback control

Substituting equation (3.13) into equation (6.1), when the inner feedback loop is based on a phase-lag compensator and the outer loop is a velocity feedback, the expression for the equipment velocity is given by

$$v_e = \frac{Y_e Z_m Y_b}{1 + Z_m (Y_e + Y_b + Y_e Z_{a3}^{'} Y_b) + Y_e Z_{a3}^{'}} f_p + \frac{Y_e T_{a3}^{'} (1 + Y_b Z_m)}{1 + Z_m (Y_e + Y_b + Y_e Z_{a3}^{'} Y_b) + Y_e Z_{a3}^{'}} f_c \quad (6.9)$$

Substituting equation (6.3) into equation (6.9) the equipment velocity per primary force is given by

$$v_e = \frac{Y_e Z_m Y_b}{1 + Z_m (Y_e + Y_b + Y_e Z_{a3}^{'} Y_b) + Y_e Z_{a3}^{'} + Y_e T_{a3}^{'} (1 + Y_b Z_m) Z_D} f_p \quad (6.10)$$

Figure 6.12(a) shows the equipment velocity per unit control command for different values of the inner gain h_{pl}. It can be noted that for high gains the first resonance is very damped. This is due to the fact that at low frequency the overall system behaves as if the integrated inner force controller is implemented. Figure 6.12(b) shows the corresponding Nyquist plot of v_e / f_c for different inner feedback gains. When the gain h_{pl} is increased, since the system with the inner control loop is unconditionally stable and very robust, the effect of increasing Z_D is good attenuation and unconditional stability. Figure 6.13 shows the equipment velocity per unit primary force for different values of the gain h_{pl} when no outer lop is implemented. Even in this case, the outer equipment velocity feedback loop is needed in order to achieve some effective attenuation on the equipment resonance.

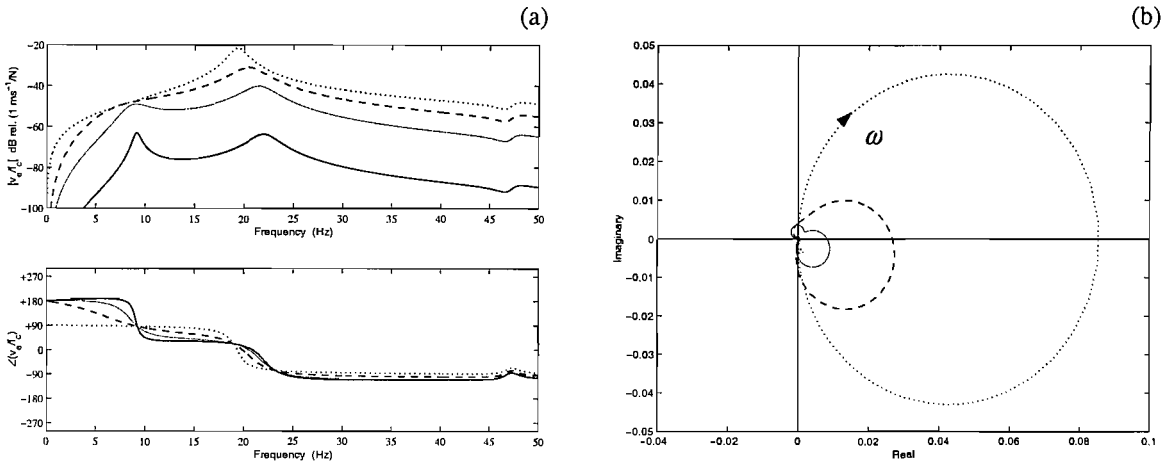

Figure 6.12 *(a): Equipment velocity per unit control command when different inner feedback gains h_{pl} in the phase-lag compensator are used: h_{pl} = 1 (solid), h_{pl} = 20 (faint), h_{pl} = 100 (dashed), and h_{pl} = 100,000 (dotted). (b): Nyquist plot of the equipment velocity per unit control command when h_{pl} = 20 (faint), h_{pl} = 100 (dashed), and h_{pl} = 100,000 (dotted). The solid line shows the case when no control is implemented.*

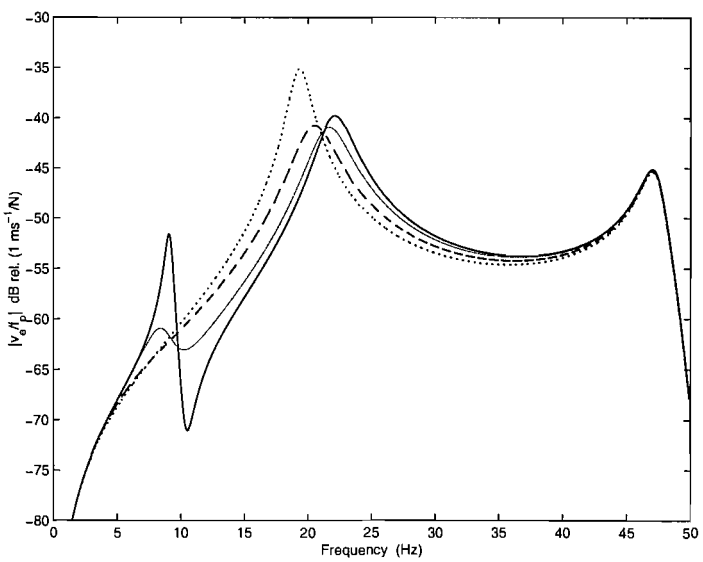

Figure 6.13 *Equipment velocity per unit primary excitation when h_{pl} = 0 (solid), h_{pl} = 20 (faint), h_{pl} = 100 (dashed), and h_{pl} = 100,000 (dotted). No outer loop is present.*

Figure 6.14 shows the equipment velocity per unit primary excitation when both the inner phase-lag feedback loop and the outer equipment velocity feedback loop are implemented. Good vibration isolation conditions can be achieved at the mounted natural frequency of the equipment. This is due to the fact that at higher frequencies the inertial actuator behaves as an almost perfect force source. The system with both inner and outer feedback loops thus has a good stability margin and it performs well. Unlike the previous case, at frequencies slightly higher than the equipment resonance frequency attenuation is experienced. In conclusion, from a stability point of view, the system has a very good margin and it performs very well.

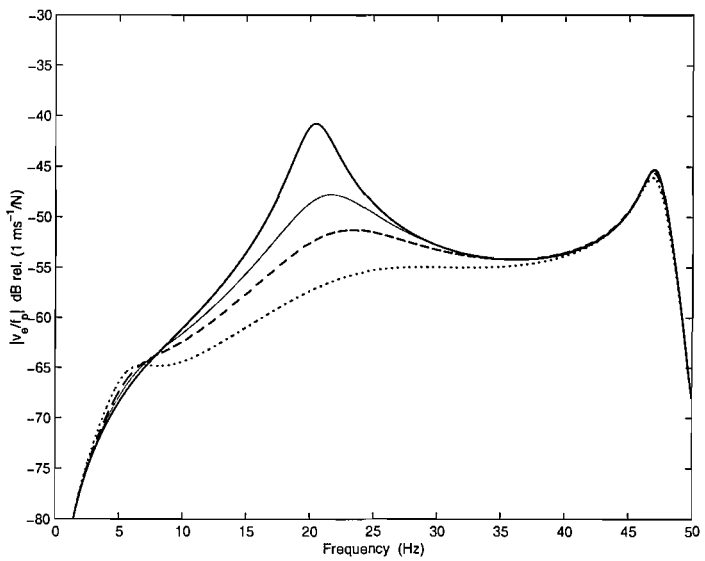

Figure 6.14 *Equipment velocity per primary excitation when the inner feedback loop gains h_{pl} = 100 and different outer velocity feedback control gains are used: Z_D=0 (solid), Z_D=50 (faint), Z_D=100 (dashed), and Z_D=200 (dotted).*

The mechanical impedance of the equipment when both inner force feedback control and outer velocity feedback control are implemented is given by

$$Z = \frac{j\omega m_a(k_a + h_{pl}\omega_1 Z_D) - \omega^2 m_a(c_a + h_{pl} Z_D)}{k_a + j\omega c_a - \omega^2 m_a(1 + h_{pl}) + j\omega m_a h_{pl}\omega_1} \tag{6.11}$$

which is plotted in Figure 6.15 for an inner phase-lag controller gain of $h_{pl} = 100$ and an outer velocity gain of $Z_D = 100$. It can be noted that the actuator impedance $Z = f_t / v_e$ tends to the desired impedance, Z_D, past the first resonance frequency, which indicates that the overall system of the inertial actuator with both feedback loops tends to a skyhook damper, as required. However, unlike the previous case (Figure 6.11), the tendency to a skyhook damper is a bit more pronounced in this case (it can be seen from the phase recovery at higher frequencies) and this is due to the force-feedback-like behaviour of the system at higher frequencies.

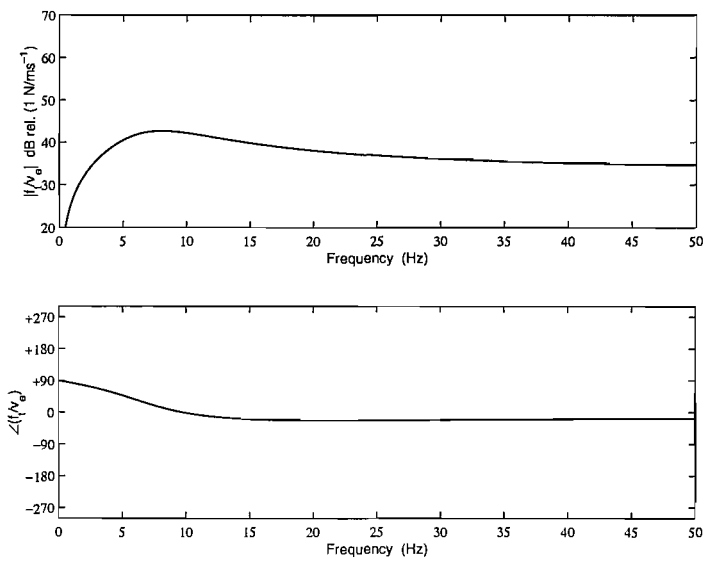

Figure 6.15 *Mechanical impedance of the equipment when the inner phase-lag control and the outer velocity feedback control are implemented.* h_{pl} *= 100 and* Z_D *= 100.*

The force requirement f_a for the three feedback control schemes presented in this chapter has been investigated (Benassi *et al.*, 2002b). The aim was to determine if reasonable force quantities can be provided by the inertial actuator, given the computed gains which provide the desired performance of the closed loop system. The actuator requirement f_a per unit primary force f_p was found to be

$$f_a = \frac{H(j\omega)(Z_a - Z_D)Y_e Z_m Y_b}{1 + Z_m(Y_e + Y_b) + Y_e Z_a(1 + Y_b Z_m) + H(j\omega)T_a + H(j\omega)T_a Z_m(Y_e + Y_b) + H(j\omega)T_a Y_e Z_D(1 + Y_b Z_m)} f_p \tag{6.12}$$

where T_a is the blocked response and Z_a is the mechanical impedance described in equation (2.4) and $H(j\omega)$ is the inner controller in Figure 6.3. When the inner force and outer equipment velocity feedback control scheme is implemented, for high gains the closed loop system gets closer to instability, therefore higher forces f_a are required to control its behaviour. When the integrated inner force and outer equipment velocity or inner phase-lag and outer velocity control schemes are implemented, lower values of the force f_a are needed compared to the previous case, but it must be taken into account the fact that the performance of the closed loop system is worse than the performance of the first case.

6.5 Conclusions

An analysis of different feedback control strategies for active isolation using an inertial actuator, based on a inner actuator force feedback loop and an outer equipment velocity feedback loop, was presented. Physical interpretation, feedback stability margins and performance were considered for each case. It was found that an inner feedback loop based on a phase-lag compensator and an outer equipment velocity feedback loop provide a very good compromise between stability and performance of the system.

In order to establish how well this dual-loop control strategy performs compared with an optimal feedback control strategy, some simulations of full state feedback, optimised using LQG control theory, are presented in Appendix A. If the control effort in these simulations is adjusted to be similar to those used by the dual-loop controller, very similar overall attenuations in the equipment velocity are obtained.

Chapter 7

Experiments with inner actuator force feedback

7.1 Introduction

Isolating a piece of delicate equipment from the vibration of a base structure is of practical importance in various engineering fields. Examples are the vibration isolation of the instrument boxes in an aircraft and the isolation of telescopes on satellites. An active isolation system can be implemented over a broad frequency band using different feedback control strategies.

This chapter describes the experimental work on the active isolation of a rigid piece of equipment structure from the vibration of a flexible base structure. The objective is to study the performance and control stability issues associated with the active vibration isolation system. Particular emphasis is placed on the isolation of low frequency vibration (0~50Hz), in which the equipment resonance lies and for which the mounts can be assumed to behave as lumped springs and dampers. The theoretical work is described in Chapter 6. Another objective of this work is then to compare those theoretical findings with the experiments.

7.2 Description of the experimental set-up

In this section the equipment and set-up used to perform the experiments are described. Figure 7.1 shows the active mount system used in the experimental work. It consists of an aluminium rigid mass, two mounts placed symmetrically underneath the aluminium mass and one electromagnetic shaker to produce the control force. The aluminium plate had been previously shown (Serrand, 1998) to behave as a rigid mass up to 1000 Hz, which is well above the maximum frequency of interest in this experimental study. The shaker is placed on top of the mass and its weight is held by a suspension system. This arrangement is necessary in order for the shaker to behave as an inertial actuator. This system is attached to a flexible plate made of steel. Accelerometers and force gauges are used as sensors.

7.2.1 The equipment

The receiving body (simulating a delicate piece of equipment) is composed of a thick aluminium plate. The receiver behaves as a rigid mass in the frequency range 0~1000 Hz. At 1000 Hz, the passive isolation provides such good performances and the axial plate motion is so small that any little errors in the equipment rigidity assumption would bring no change to the assessment of the controller performances. The receiver is thus considered fully rigid in the frequency range of analysis. Further details are given in Table C1 in Appendix C and Gardonio *et al.* (1996).

7.2.2 The passive mounts

The passive isolation consists of a pair of rings of rubber each of which is mounted between two aluminium discs. The top disc is rigidly connected to the piece of equipment while the bottom disc can be bolted to the vibrating base structure. The passive parts of both mounts were assumed to have the same mechanical properties. Figure 7.2 shows a schematic diagram of the system and further details are given in Table C2 and Table C3 in Appendix C.

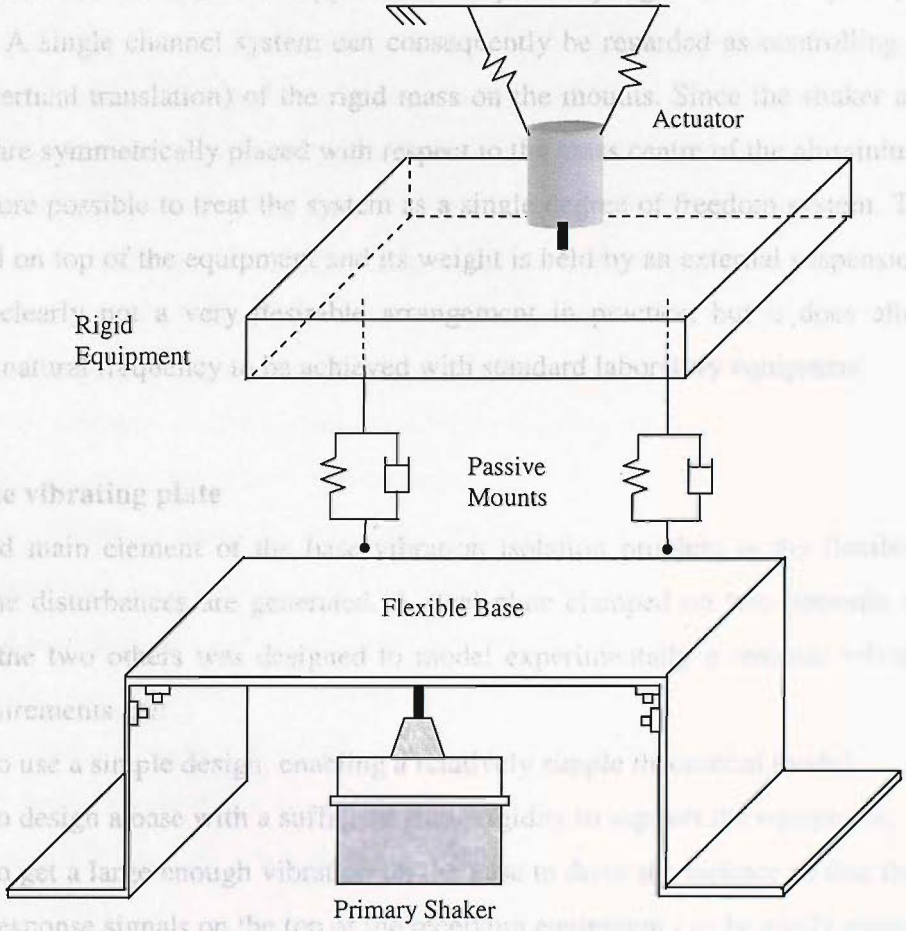

Figure 7.1 *Schematic of a two mount active isolation system with a rigid equipment structure on a flexible base.*

7.2.3 The inertial actuator

The active force is provided by an electromechanic shaker fixed on top of the piece of equipment. A single shaker is placed in the middle of the equipment structure so that the shaker itself acts as the inertial mass, as illustrated in Figure 7.1. The mechanical properties of the actuator are given in Table C4 in Appendix C.

Its main components comprise a coil moving in the steady magnetic field of a permanent magnet. The force generated and transmitted to the piece of equipment is proportional to the product of the instantaneous current in the coil and the magnetic flux density. The

shaker can only generate axial forces and therefore only the axial motion can be entirely controlled, since the mass is supposed to be perfectly rigid in the frequency range of interest. A single channel system can consequently be regarded as controlling the heave mode (vertical translation) of the rigid mass on the mounts. Since the shaker and rubber mounts are symmetrically placed with respect to the mass centre of the aluminium plate, it is therefore possible to treat the system as a single degree of freedom system. The shaker is placed on top of the equipment and its weight is held by an external suspension system. This is clearly not a very desirable arrangement in practice, but it does allow a low actuator natural frequency to be achieved with standard laboratory equipment.

7.2.4 The vibrating plate

The third main element of the base vibration isolation problem is the flexible base on which the disturbances are generated. A steel plate clamped on two opposite edges and free on the two others was designed to model experimentally a realistic vibrating base. The requirements are:

1. to use a simple design, enabling a relatively simple theoretical model;
2. to design a base with a sufficient static rigidity to support the equipment;
3. to get a large enough vibration on the base to drive the isolator so that the velocity response signals on the top of the receiving equipment can be easily measured.

The requirement of a good dynamic range of plate vibration was motivated by the high expected efficiency of the passive isolation of the mounts. A low axial stiffness of the passive mounts provides an efficient attenuation of the axial vibration at high frequency. To be able to assess the effectiveness of an active isolation in a wider frequency range than in the vicinity of the axial equipment rigid body modes, a strong plate motion is necessary in order to recover a measurable vibration signal on the top of the equipment that is not too corrupted by measurement noise.

The choice of a clamped-free-clamped-free plate was made in the attempt to fulfil all these requirements (Leissa, 1969). A complete analysis of the design and construction of the vibrating plate can be found in Gardonio's work (1996, 1997a,b,c) and its main physical and geometrical properties are listed in Table C5. A Matlab program of the coupled dynamics was written as the basis for all the theoretical simulations.

The first plate resonance lies around 33 Hz and the modal damping was assumed to be 1% to better fit the experimental results.

Appendix C lists the first nine modes of the base supporting plate. The experimental modal frequencies listed in Table C6 are lower than those predicted by the theoretical model. This can be explained by the imperfections of the clamping conditions. The strengthening pieces connecting the plate to the ticker vertical supports prevent almost any bending of the plate at the clamped edges at low frequencies in one sense of rotation (downwards) but not in the other (upwards). The second imperfection lies in the fact that the vertical supports are not absolutely rigid especially at low frequency. This acts to reduce the stiffness of the system, therefore shifting down the natural frequencies, particularly those for the lower order modes.

The main differences between model and experiments at higher frequencies arise as the spacing between two consecutive bolts connecting the plate to the strengthening pieces is no longer negligible compared to the wavelength of the propagating wave. The junction between the strengthening pieces and the plate itself can thus not be regarded as a perfectly clamped junction. Secondly, the system dynamics will become affected by small structural details as the frequency increases, since the wavelength will get shorter. Further details about this topic are given in Serrand (1998).

7.2.5 The primary shaker

As shown in Figure 7.1, one shaker was used as primary force to drive the system. It was placed in the centre of the flexible base and it was driven by the output of the signal generator within the FFT analyser. Its main properties are described in Table C7.

The foundation is not only moved by the shaker but also by the two cylindrical mounts as they are stretched and compressed. These two forces couple the dynamics of the plate and the isolator.

7.2.6 Sensors

Before any control technique is applied, identification of the experimental system and the characteristics of each instrument used are important.

The force generated by the primary shaker is monitored using a piezoelectric force gauge (B&K type 8200) whose bottom side is bolted to the shaker and the top side is stuck to the

plate (Figure 7.2). The acceleration of the centre of the piece of equipment is measured at one point on the equipment using a piezoelectric accelerometer (B&K type 4375) monitoring the vertical motion. The total transmitted force to the equipment is measured by a second piezoelectric force gauge (B&K type 8200) whose top side is bolted to the secondary shaker (the inertial actuator) and bottom side is bolted to the centre of the aluminium mass. A complete list of the equipment used is given in Appendix C, Table C8. After having analysed the different elements constituting the parts of the isolation problem, it is now possible to investigate the dynamics of the complete system when different control strategies are applied to the laboratory set-up shown in Figure 7.3 and Figure 7.4. This will be achieved by measuring the rigid mass response to the shaker excitation moving the flexible plate underneath.

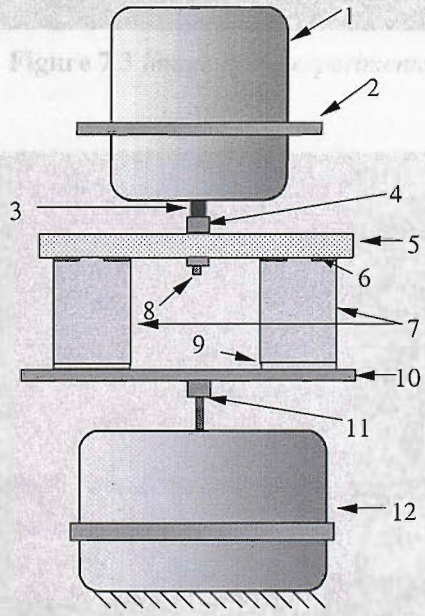

1 Electromagnetic Actuator
2 Suspension System
3 Support
4 Force Gauge
5 Rigid Equipment
6 Adapter
7 Rubber Mounts
8 Accelerometer
9 Steel Washer
10 Flexible Base
11 Force Gauge
12 Primary Shaker

Figure 7.2 *Schematic of the location of sensors and actuator within the experimental set-up.*

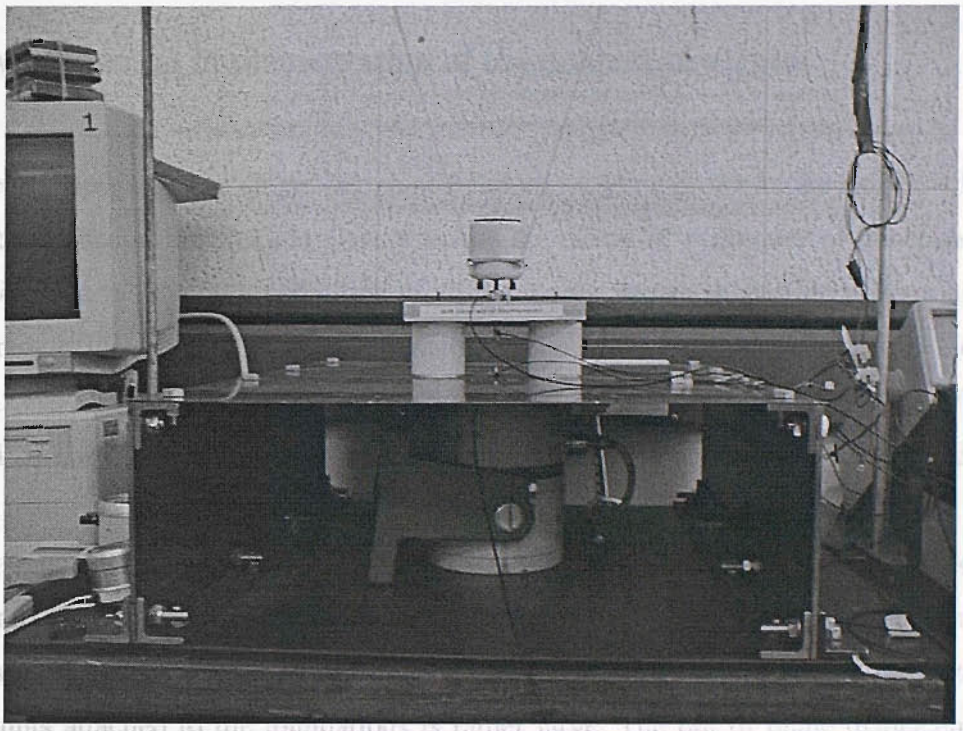

Figure 7.3 *Image of the experimental set-up.*

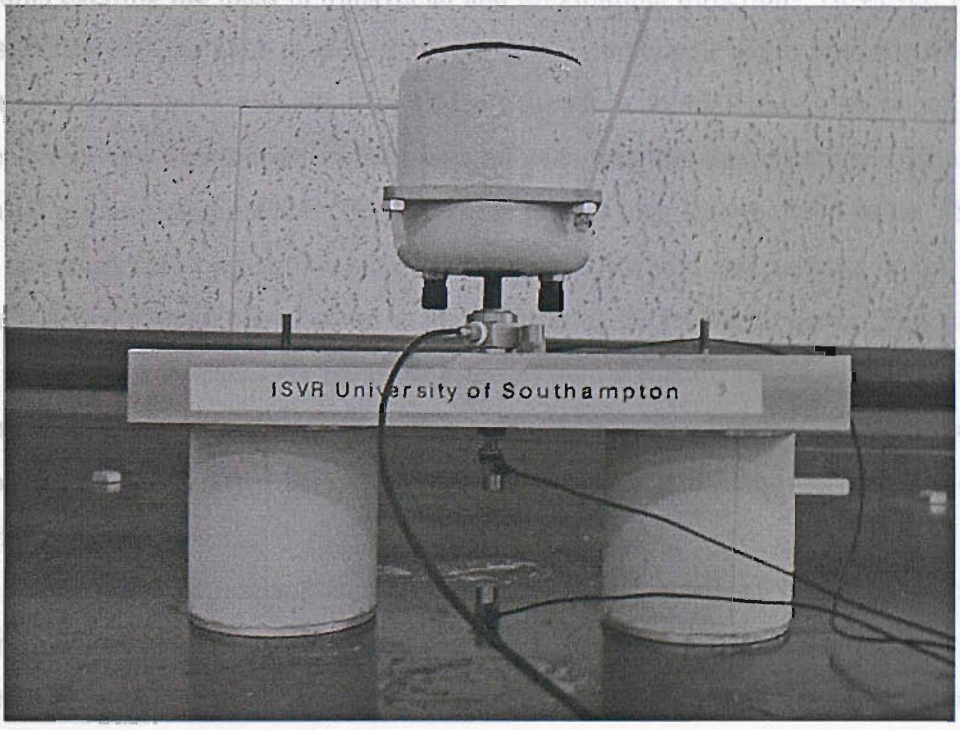

Figure 7.4 *Image of the core of the experimental set-up, which consists of the piece of equipment, which is mounted on top of passive rubber rings. The suspended inertial actuator is connected to the receiver and a force gauge in between measures the total transmitted force to the equipment.*

7.3 Experimental implementation of the control strategies

In order to approximate a single degree of freedom isolation problem, the shaker is located under the centre of the flexible plate which is the centre of symmetry of the foundation. The excitation is then on a nodal line of all the modes whose shapes are not symmetrical compared to this centre. They are then not excited and do not contribute to the plate motion. Provided the centre of the rigid mass of the isolation system is exactly at the vertical of the plate centre, both rubber mounts undergo the same displacement and the system tends to a single degree of freedom isolation problem.

Setting apart the issue of how to position the primary and secondary shakers at the exact locations, such an idealization is obviously not perfect. Neither the rubber rings nor the shakers have a point connection with the plate. For instance, the surface at the bottom of the mounts attached to the foundations is rather large. The out of plane displacement of the support may therefore generate moments and displacements in torsion at the bottom of the mounts exciting the mass in transversal and longitudinal directions. However, because of the symmetry of the plate modes involved, these components act in opposite directions on the two mounts and cancel out. This effect is therefore unlikely to be significant.

Another effect that was present in the measurements was that the resonance frequency of the inertial actuator dominated mode was a little greater than the predicted value. This was due to the suspension system, which in theory had to hold the actuator mass, but in practice it added a small contribution to the stiffness of the inertial actuator. This property of the system was detected by measuring the system dynamic response using different suspension systems. In order to reduce this effect, both rubber bands and steel wires with very soft springs were tested. It was decided to use the latter solution because it showed a better linear behaviour.

Before conducting the experiments, the transfer functions of all the mechanical and electronic components were measured and their phase characteristics were accurately analysed for a better interpretation of the experimental measurements. The smallest frequency increment possible was chosen and the gathered data was not treated in the first place. Then some minor post-processing was performed on the data, as it will be presented in the next section.

Figure 7.5 shows a comparison between the measured plant response from primary force to equipment velocity and the simulation. The inertial actuator dominated resonance is at about 11 Hz. It can be noted that the real system appears more damped. At about 22 Hz the simulated equipment resonance shows a very good agreement with the experimental data, both in terms of magnitude and phase. The first flexible plate modal frequency which is visible from the accelerometer placed at the centre of the set-up is at about 40 Hz and its discrepancy with the simulation was explained in the previous section. Very good coherence was obtained during all the experimental measurements, and Figure 7.6 shows one example of it, taken from a force and velocity feedback scheme. At frequencies higher than 5 Hz the coherence is almost always unity, and at frequencies lower than 5 Hz the really poor coherence indicates that the experimental measurements have no physical meaning at such low frequencies.

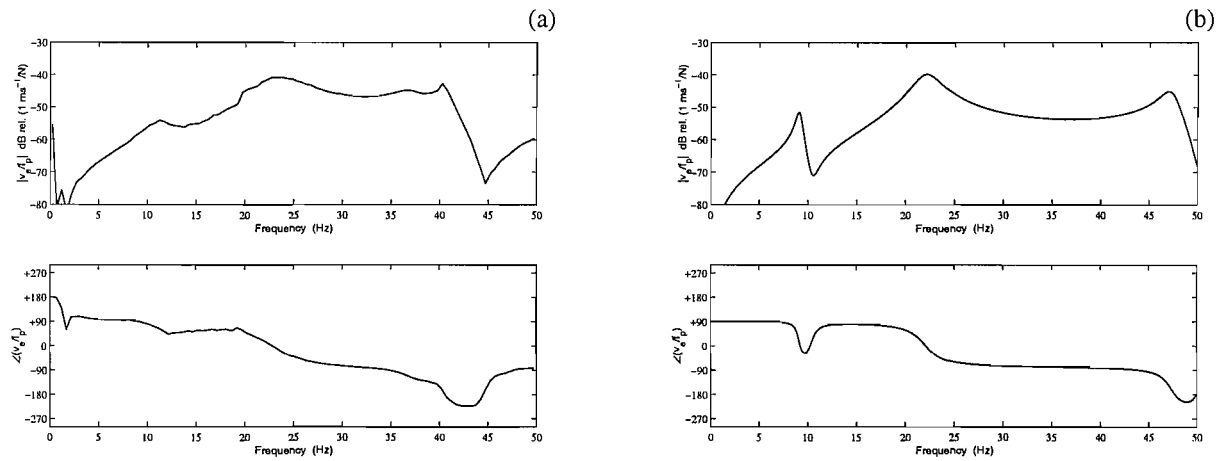

Figure 7.5 *(a): Measured and (b) simulated equipment velocity per primary excitation.*

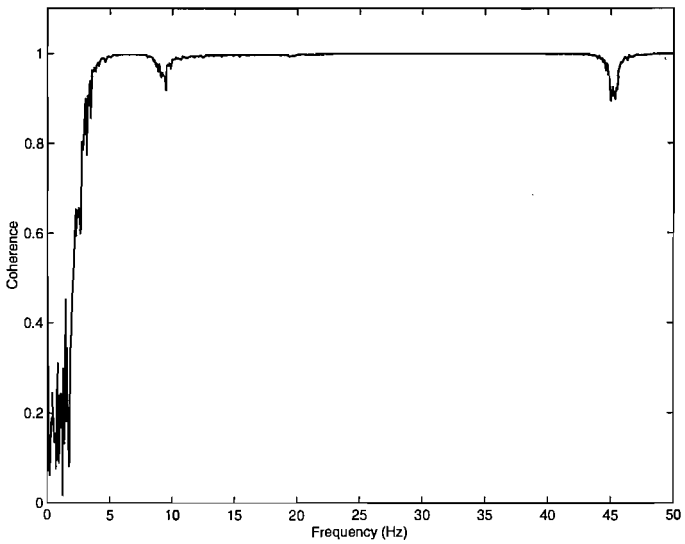

Figure 7.6 *Example of measured coherence of the system.*

7.3.1 Velocity feedback control

In order to evaluate the stability properties of the closed loop system by analysing the behaviour of the open loop system, white noise from the FFT analyser was used to drive the inertial actuator. This signal was also connected to channel A of the analyser. When the equipment structure was excited, the acceleration signal at centre of the piece of equipment was measured using an accelerometer. The acceleration signal was then passed to a charge amplifier and integrated to a velocity signal by a module inside the charge amplifier. The integrator was operated in conjunction with a high-pass filter, whose cut-off frequency was preset to be 1 Hz. Finally the velocity signal was connected to channel B of the analyser to measure the frequency response function of the equipment velocity per unit secondary force. Figure 7.7 shows the experimental set-up, and Figure 7.9(a) shows the Nyquist plot obtained from this measurement. The vectors of the measured signals contain 801 values each, and they cover the frequency range 0~50 Hz.

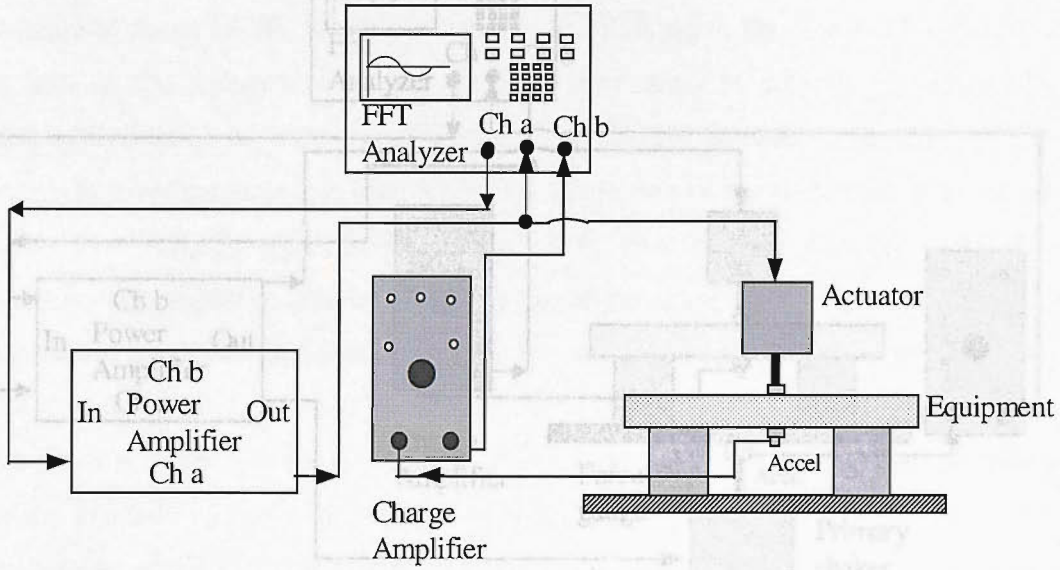

Figure 7.7 *Experimental set-up in order to measure the equipment velocity per unit secondary excitation.*

In order to evaluate the performance of direct velocity feedback control described in Chapter 5, the FFT analyser was used to measure the frequency response of the equipment velocity per primary excitation as well as generate the white noise signal. The white noise signal drove the primary shaker to excite the flexible base, and the excitation force signal was measured by a force transducer connected to channel A of the analyser. When the equipment structure was excited, the acceleration signal measured as close as possible to the centre of the equipment was gathered via an accelerometer. The acceleration signal was then passed to a charge amplifier and integrated to a velocity signal. The integrator was operated in conjunction with a high-pass filter, whose cut-off frequency was preset to be 1 Hz. Finally, the velocity signal was connected to channel B of the analyser to measure the frequency response function of the absolute equipment velocity per unit excitation force. A built-in filter in the analyser was employed to reduce aliasing. Figure 7.8 shows the experimental set-up, and Figure 7.9(b) shows the experimental results.

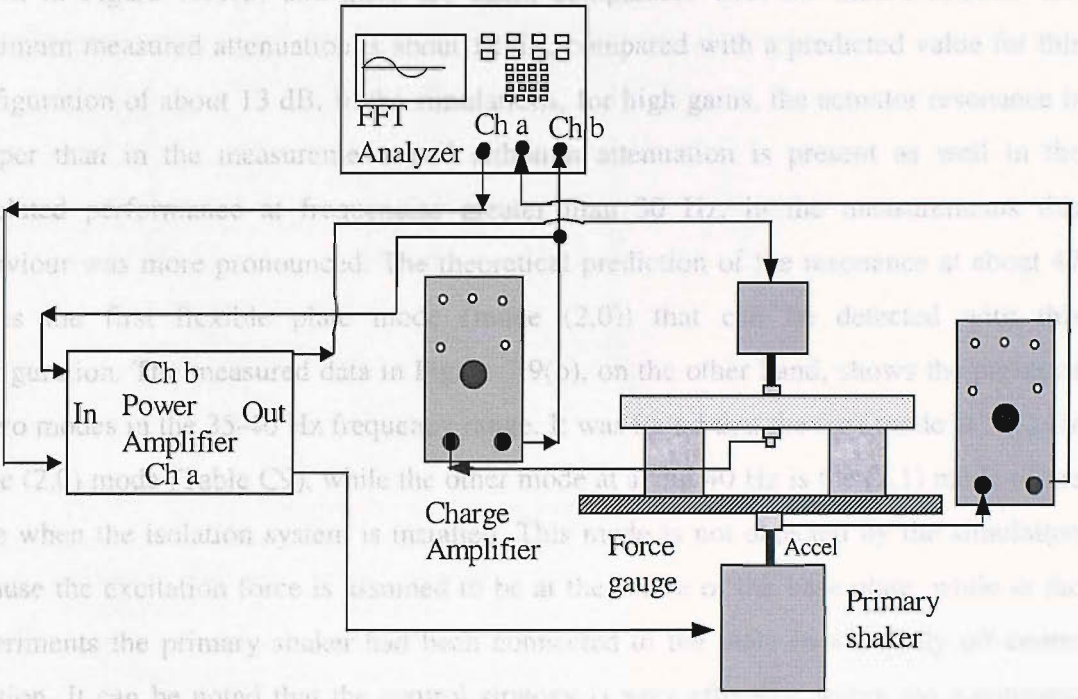

Figure 7.8 *Experimental set-up in order to measure the equipment velocity per unit primary excitation.*

The measured plant response from secondary shaker input to integrated accelerometer output for the active isolation system with the inertial actuator is shown in Figure 7.9(a), which is similar to the simulated response shown in Figure 7.11(a), except for a more pronounced behaviour of the flexible base in the measured data. There is no primary disturbance arising from the base support and the loop on the left hand side of the Nyquist plot, which is due to the actuator resonance, indicates enhancement of the system response for gains within the stability region. The spectrum of the measured equipment velocity, normalized by the primary force, is shown in Figure 7.9(b) with no control and with three values of feedback gain. Attenuation of the vibration at the mounted equipment resonance at about 23 Hz can be achieved using this arrangement, but some enhancement of the disturbance at the actuator resonance frequency (11 Hz) then occurs, as predicted. This enhancement increases rapidly if the feedback gain is further increased until the system becomes unstable. Almost no attenuation was observed in the base resonances with this control scheme. The results of the computer simulations of the inertial control system are

shown in Figure 7.11(b) and these are again comparable with the measurements. The maximum measured attenuation is about 12 dB, compared with a predicted value for this configuration of about 13 dB. In the simulations, for high gains, the actuator resonance is sharper than in the measurements and although attenuation is present as well in the simulated performance at frequencies greater than 30 Hz, in the measurements this behaviour was more pronounced. The theoretical prediction of the resonance at about 47 Hz is the first flexible plate mode (mode (2,0)) that can be detected with this configuration. The measured data in Figure 7.9(b), on the other hand, shows the presence of two modes in the 35-40 Hz frequency range. It was found that the first mode at 37.2 Hz is the (2,0) mode (Table C9), while the other mode at about 40 Hz is the (2,1) mode of the plate when the isolation system is installed. This mode is not detected by the simulation because the excitation force is assumed to be at the centre of the base plate, while in the experiments the primary shaker had been connected to the plate in a slightly off-centre location. It can be noted that the control strategy is very effective within the equipment frequency range and effective in a minor way at higher frequencies. In any case, active vibration isolation is achieved since "the frequency response plot of the transfer function shows that damping values sufficient to control the resonance have no adverse effect on high frequency isolation" (Karnopp, 1995).

Figure 7.9 shows the untreated data as it was gathered, comprising 801 points in the range 0~50 Hz. 25 averages were taken in the frequency domain by the analyser. For a clearer presentation of the experimental results, the collected data was averaged every 8 data points and the results are shown in Figure 7.10. It was decided to apply this simple treatment to all the data collected and present the experimental results in this form.

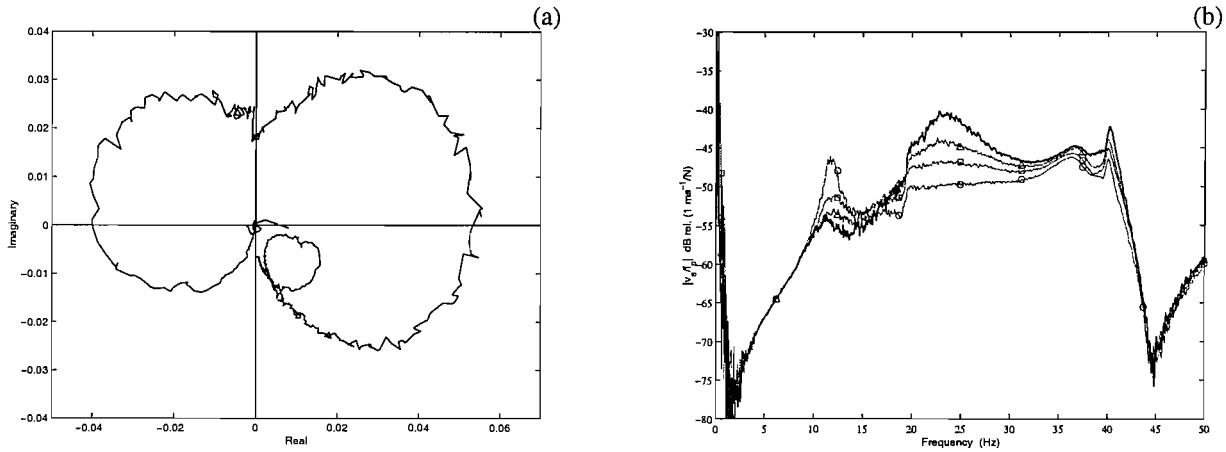

Figure 7.9 *(a): Nyquist plot of the untreated measured open loop response from secondary shaker input to integrated accelerometer output. (b): untreated measured velocity of the equipment per unit primary excitation. Results are shown for the passive system (control off, solid line) and for three values of feedback gain (faint lines): h_v =8 (triangle), h_v = 15 (square), and h_v = 22 (circle). For gains greater than 22 the system was unstable.*

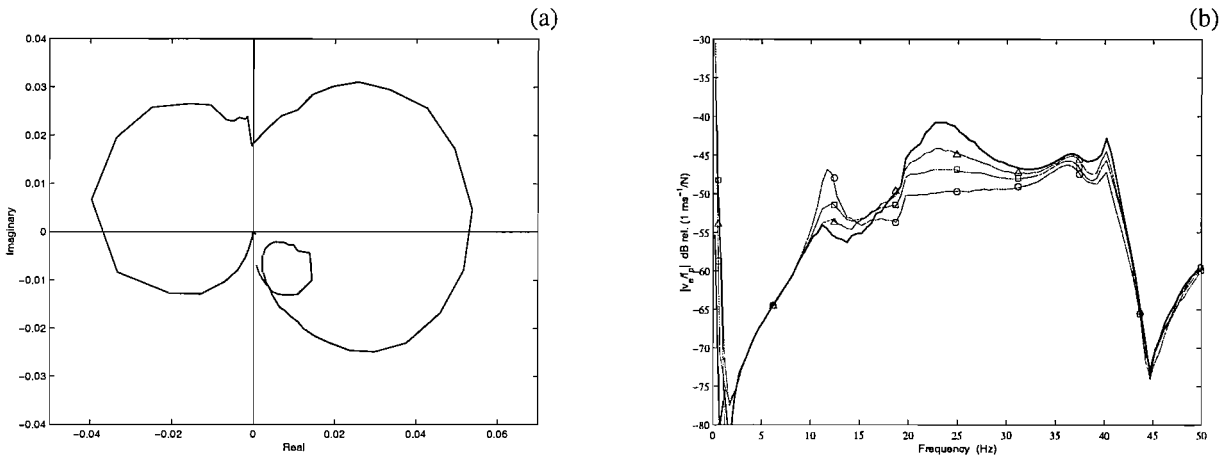

Figure 7.10 *(a): Nyquist plot of the treated measured open loop response from secondary shaker input to integrated accelerometer output. (b): treated measured velocity of the equipment per unit primary excitation. Results are shown for the passive system (control off, solid line) and for three values of feedback gain (faint lines): h_v =8 (triangle), h_v = 15 (square), and h_v = 22 (circle). For gains greater than 22 the system was unstable.*

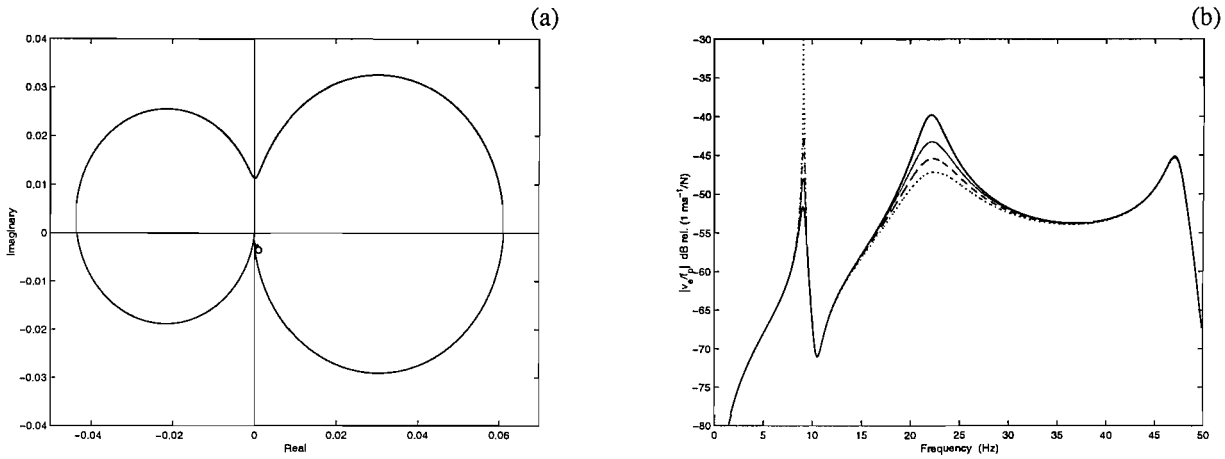

Figure 7.11 *(a): Nyquist plot of the simulated open loop response from secondary shaker input to integrated accelerometer output. (b): simulated velocity of the equipment per unit primary excitation. Results are shown for the passive system (control off, solid line) and for three values of feedback gain: h_v =8 (faint line), h_v = 15 (dashed line), and h_v = 22 (dotted line). For gains greater than 22.5 the simulated system was unstable.*

The following considerations were drawn while working on this first control strategy, but they were then applied to all the other experiments.

Due to the imperfect operation of the electrical equipment and low coherence suffered at low frequencies, the corresponding plots from the experiment show very high values at very low frequencies. Smooth curves at low frequencies are observed in the simulation since perfect operation of the electrical equipment is assumed. Also, in the simulations the feedback control gain relating the secondary force to the control velocity in unit of N/ms^{-1} must account for the different gains used in the experimental feedback loop, which comprises the charge amplifier gain, the power amplifier gain and the sensitivity of the actuator. The sensitivity of the accelerometer is directly taken into account by the charge amplifier. The feedback control gain values were therefore measured from the different components of the experimental set-up and modelled in the simulation for comparison purposes. The open and closed loop frequency response functions for velocity feedback control with 1 Hz and 10 Hz charge amplifier cut-off frequency were obtained keeping all the other conditions unchanged. It was experienced that when the amplifier cut-off

frequency within the charge amplifier is increased from 1 Hz to 10 Hz the maximum attainable gain reduces considerably.

7.3.2 Integrated velocity feedback control

In this experiment the same configurations as before were used in order to evaluate the stability properties and the performance of the closed loop system. The only difference was an ISVR-built passive integrator (R = 470 KΩ, C = 2.2 μF), which was used as a controller in the feedback loop before the power amplifier. This allowed the equipment velocity signal to be connected to the FFT analyser for measurement purposes, and also to be integrated within the feedback leg of the experimental set-up.

The measured plant response, from secondary shaker input to integrated velocity output, for the active isolation system with the inertial actuator is shown in Figure 7.12(a), which reasonably matches with the simulated response shown in Figure 7.13(a), except for a more pronounced behaviour of the flexible base. Even in this case there is no primary disturbance arising from the base support. Compared to the previous case, the Nyquist plot appears rotated by 90° clockwise. This is due to the effect of the integrator in the controller. Also, the presence of low frequency phase shifts can be seen. The spectrum of the measured equipment velocity, normalized by the primary force, is shown in Figure 7.12(b) with no control and with three values of feedback gain. It can be seen that attenuation of the vibration at the mounted equipment resonance can be achieved using this arrangement, but that some enhancement of the disturbance at the actuator resonance frequency then occurs. This is due to the non-perfect characteristics of the electronic components that were used during the experiments. This enhancement increases rapidly if the feedback gain is further increased until the system becomes unstable. The results of the computer simulations of the inertial control system with an ideal integrator show good agreement with the measurements (Figure 7.13b)). The maximum measured attenuation is about 8 dB and the tendency of separating the first two resonances apart when the gain is increased is clearly observed and predicted by the simulations. In summary, integrated velocity feedback control is unconditionally stable for an ideal system, while it is conditionally stable for real systems. The performance of an ideal integrated velocity feedback controller is good within a considerable frequency range, but unfortunately high

gains may be needed to obtain substantial attenuation and this is clearly a limit because in real systems high gains do not guarantee stability.

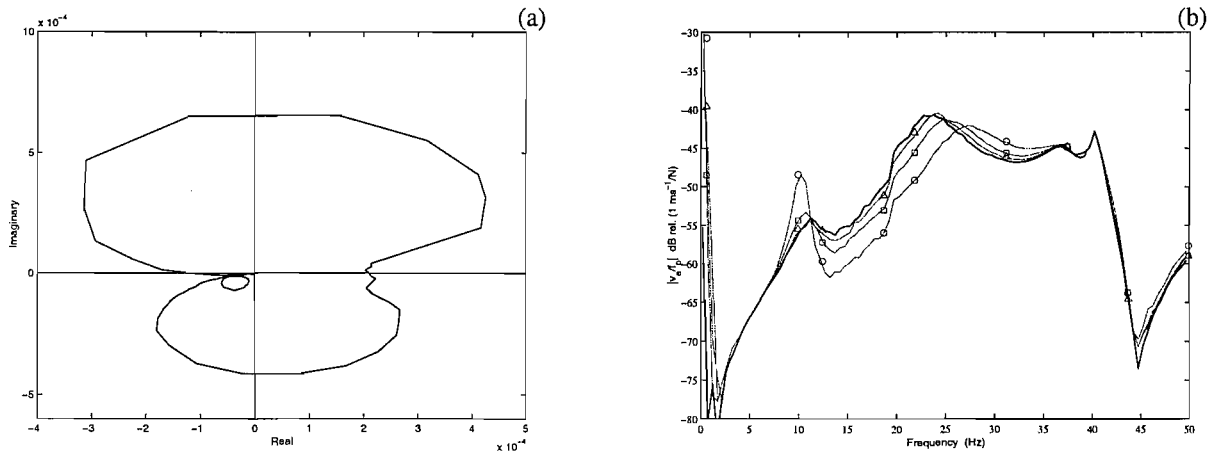

Figure 7.12 *(a): Nyquist plot of the treated measured open loop response from secondary shaker input to integrated accelerometer output when the controller is an integrator. (b): treated measured velocity of the equipment per unit primary excitation. Results are shown for the passive system (control off, solid line) and for three values of feedback gain (faint lines): h_{iv} =1000 (triangle), h_{iv} = 3000 (square), and h_{iv} = 6000 (circle). For gains greater than 6000 the system was unstable.*

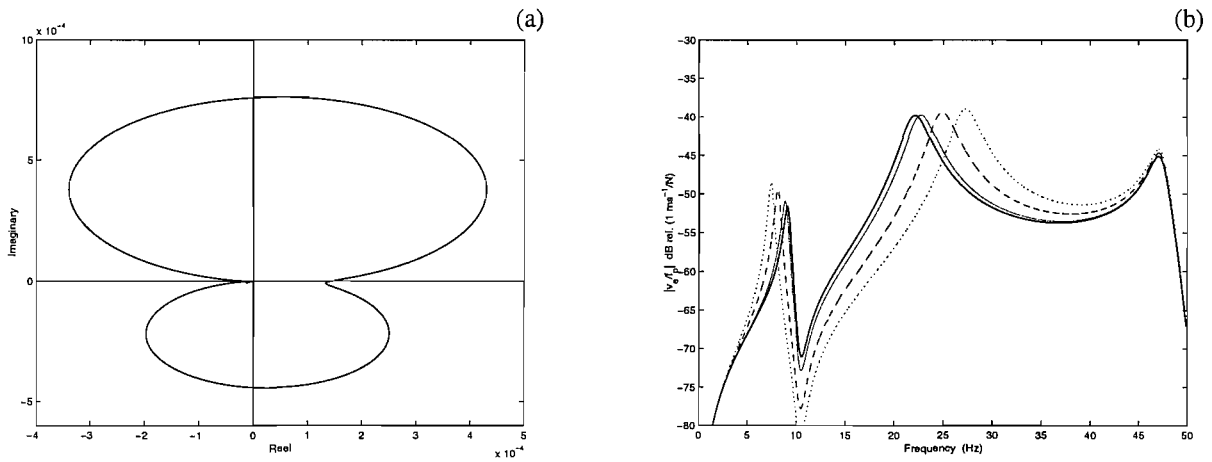

Figure 7.13 *(a): Nyquist plot of the simulated open loop response from secondary shaker input to integrated accelerometer output when the controller is an integrator. (b): simulated velocity of the equipment per unit primary excitation. Results are shown for the passive system (control off, solid line) and for three values of feedback gain: h_{iv} =1000 (faint line), h_{iv} = 5000 (dashed line), and h_{iv} = 10000 (dotted line). The ideal system is unconditionally stable.*

7.3.3 Inner force feedback control

In order to evaluate the stability properties of the closed loop system by analysing the behaviour of the open loop system, white noise form the FFT analyser was used to drive the inertial actuator. This signal was also connected to channel A of the analyser. When the equipment structure was excited, the force signal between the inertial actuator and the piece of equipment was measured using a B&K 8200 force gauge. The force signal was then passed to a charge amplifier. Finally the force signal, which is in fact the transmitted force to the equipment, was connected to channel B of the analyser to measure the frequency response function of the transmitted force per unit secondary force. Figure 7.14 shows the experimental set-up, and Figure 7.17(a) shows the Nyquist plot obtained from this measurement.

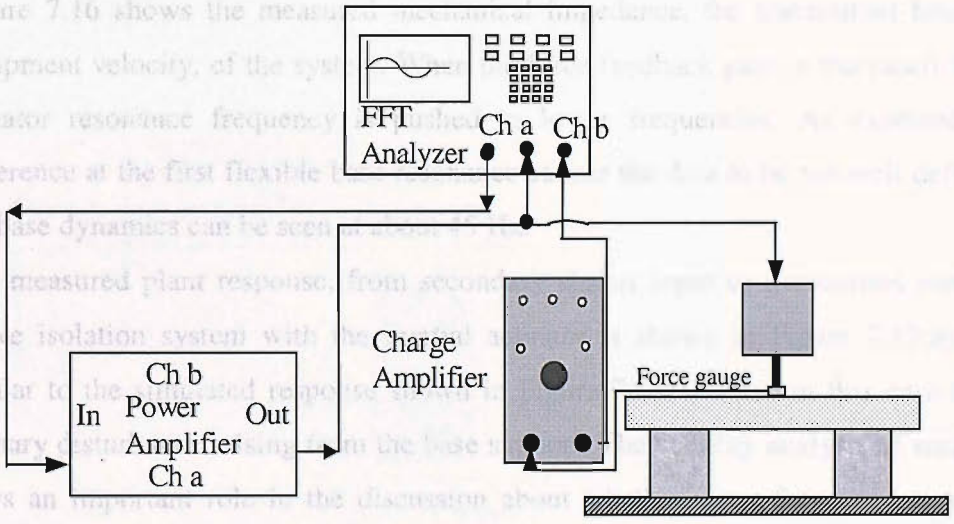

Figure 7.14 *Experimental set-up in order to measure the total transmitted force per unit secondary excitation.*

In order to evaluate the performance of this strategy, the FFT analyser was used to measure the frequency response of the equipment velocity as well as generate the white noise signal. The white noise signal drove the primary shaker to excite the flexible base, and the excitation force signal was measured by a force transducer which was also connected to channel A of the analyser. When the equipment structure was excited, the

acceleration signal at the centre of the equipment was measured using an accelerometer. The acceleration signal was then connected to a charge amplifier and converted to a velocity signal similarly to the previous cases. Finally, the velocity signal was connected to channel B of the analyser to measure the frequency response function of the equipment velocity per unit excitation force. A built-in filter in the analyser was employed to reduce aliasing. Unlike the previous cases however, this feedback control strategy is based on the measurement of the transmitted force to the equipment. To implement this feature the force gauge between the inertial actuator and the equipment measures the transmitted force, whose signal is then fed to a charge amplifier. The output of the amplifier becomes the input to the power amplifier, which in fact acts as the gain module within the feedback leg. The amplified signal is then connected to the inertial actuator. Figure 7.15 shows a practical implementation of the experimental set-up, and Figure 7.17(b) shows the experimental results.

Figure 7.16 shows the measured mechanical impedance, the transmitted force per unit equipment velocity, of the system. When the force feedback gain in increased, the inertial actuator resonance frequency is pushed to lower frequencies. As expected, the low coherence at the first flexible base resonance causes the data to be not well defined. Also, the base dynamics can be seen at about 45 Hz.

The measured plant response, from secondary shaker input to transmitted force, for the active isolation system with the inertial actuator is shown in Figure 7.17(a), which is similar to the simulated response shown in Figure 7.18(a). Also in this case there is no primary disturbance arising from the base support. The stability analysis of such a system plays an important role in the discussion about whether inner force and outer velocity feedback control is a good solution to the equipment isolation problem. At low frequency, as predicted by the simulations, the Nyquist plot lies very close to the critical point and therefore instability is likely to happen when the gain is increased because of the electronic components.

The spectrum of the measured equipment velocity, normalized by the primary force, is shown in Figure 7.17(b) with no control and with three values of feedback gain. It can be seen that enhancement of the vibration at the mounted equipment resonance is experienced using this arrangement, as predicted by theory.

An important aspect is that, when the gain h_f increases, the actuator resonance frequency is shifted to lower frequencies, while its magnitude increases, getting closer to the unstable region (Chapter 3). In the experiments, the first resonance frequency was lowered to 8.75 Hz. The corresponding simulation is plotted in Figure 7.18(b). Although an ideal system is unconditionally stable, and therefore the inertial actuator's resonance frequency can be lowered considerably, in a real system the inertial actuator's resonance frequency can be lowered only to a certain value, determined by the stability condition. Also, since the ideal Nyquist plot does not lie in the unit circle centred at (-1,0) as much as the measured one, smaller enhancement is predicted by the simulation at the equipment resonance.

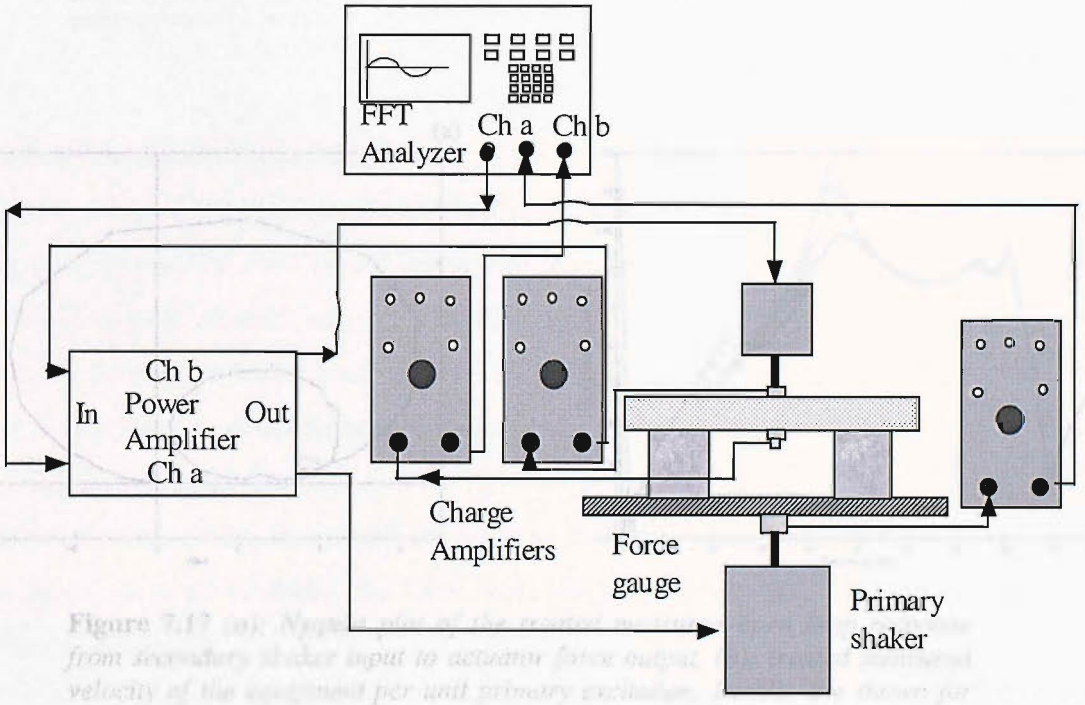

Figure 7.15 *Experimental set-up in order to measure the equipment velocity per unit primary excitation when force feedback control is implemented.*

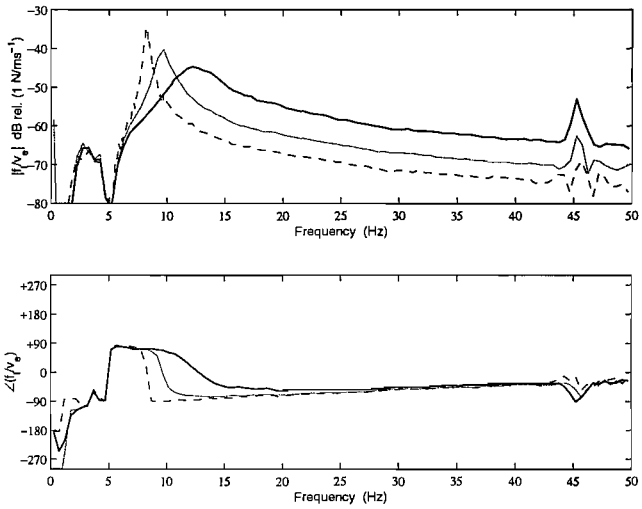

Figure 7.16 *Bode plot of the measured mechanical impedance, transmitted force per unit equipment velocity, of the active system. Three force feedback gains h_f have been analysed: h_f = 0 (bold line), h_f = 3 (faint line), and h_f = 10 (dashed line).*

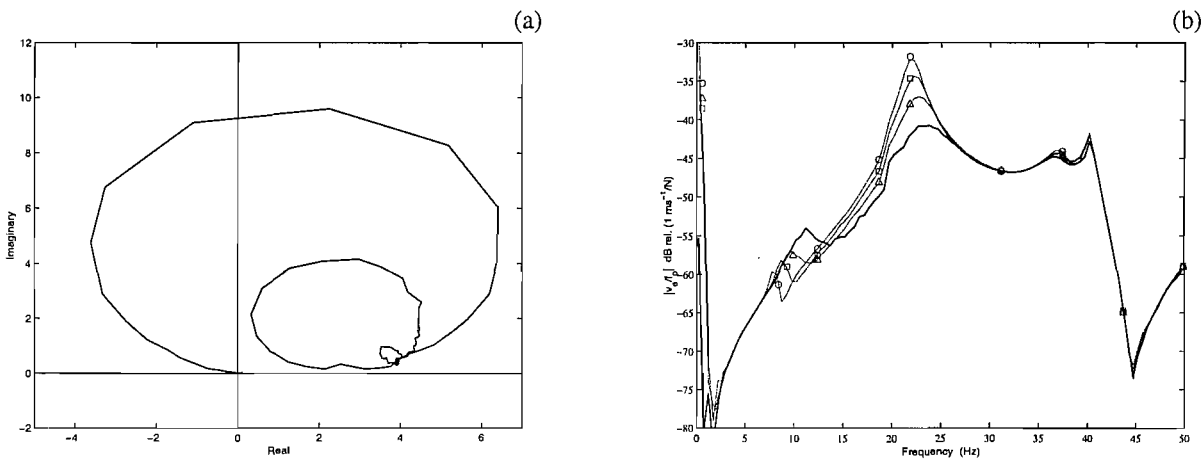

Figure 7.17 *(a): Nyquist plot of the treated measured open loop response from secondary shaker input to actuator force output. (b): treated measured velocity of the equipment per unit primary excitation. Results are shown for the passive system (control off, solid line) and for three values of feedback gain (faint lines): h_f =3 (triangle), h_f = 6 (square), and h_f = 10 (circle). For gains greater than 10 the system was unstable.*

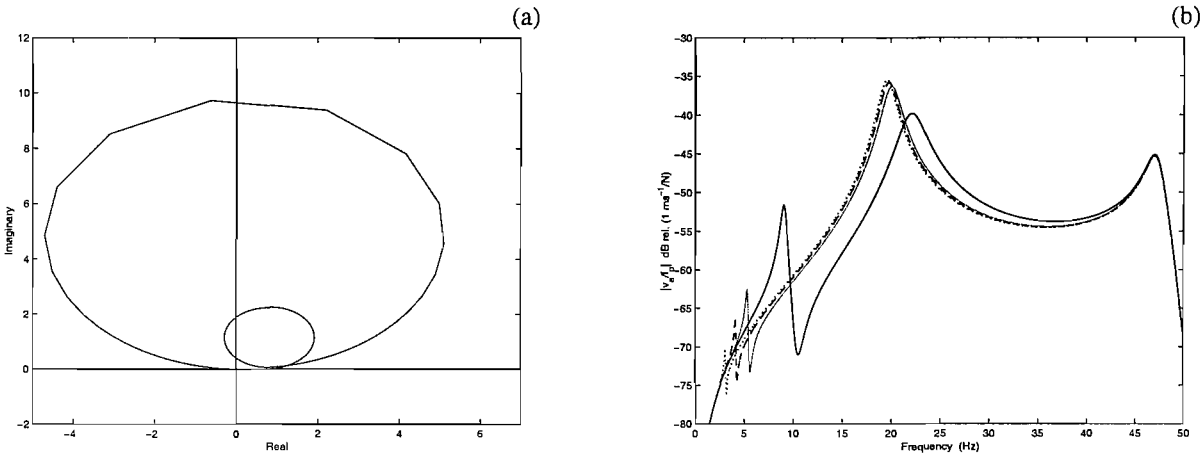

Figure 7.18 *(a): Nyquist plot of the simulated open loop response from secondary shaker input to actuator force output. (b): simulated velocity of the equipment per unit primary excitation. Results are shown for the passive system (control off, solid line) and for three values of feedback gain:* $h_f = 3$ *(faint line),* $h_f = 6$ *(dashed line), and* $h_f = 10$ *(dotted line). The ideal system is unconditionally stable.*

7.3.4 Integrated inner force feedback control

In this experiment, the same configurations described above were used in order to evaluate the stability properties and the performance of the closed loop system. The only difference was an ISVR-built passive integrator, which was used as a controller in the feedback loop before the power amplifier. This allowed the transmitted force signal to be connected to the FFT analyser for measurement purposes, and also to be integrated within the feedback leg of the experimental set-up.

Figure 7.19 shows the mechanical impedance, the transmitted force per unit equipment velocity, of the system. When the force feedback gain in increased, the inertial actuator resonance is damped.

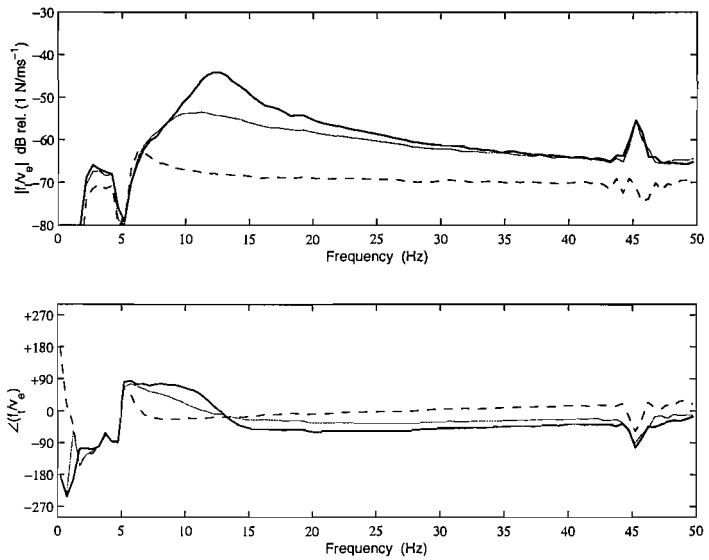

Figure 7.19 *Bode plot of the measured mechanical impedance, transmitted force per unit equipment velocity, of the active system, when the integrated force feedback scheme is implemented. Three force feedback gains h_{if} have been analysed: $h_{if} = 0$ (bold line), $h_{if} = 500$ (faint line), and $h_{if} = 2500$ (dashed line).*

The measured plant response, from secondary shaker input to integrated force output, for the active isolation system with the inertial actuator is shown in Figure 7.20(a), which matches very closely the simulated response shown in Figure 7.21(a). The Nyquist plot is rotated by 90° clockwise compared to the previous case and this is due to the effect of the integrator in the controller.

In addition, the closed loop system is now significantly more stable than in the previous case despite the presence of low frequency causes of instability. The spectrum of the measured equipment velocity, normalized by the primary force, is shown in Figure 7.20(b) with no control and with three values of feedback gain. The corresponding simulations are shown in Figure 7.21(b). Also in this case the theoretical findings match quite well with the experimental measurements and in particular both effects on the first two resonances were experienced. Firstly, the magnitude of the inertial actuator resonance is attenuated. This damping effect was predicted and theoretically explained. Secondly, at the equipment resonance, the magnitude of the transfer function is greater then when no control is implemented (from this follows that an outer equipment velocity feedback loop is needed) and its frequency lowered. It was very difficult to increase the gain in such a way that it

would set the closed loop system unstable. Such high gains were difficult to obtain with the power amplifiers in use. Most of the time, the power limit was reached before reaching the stability limit. This definitely showed how robust this solution is.

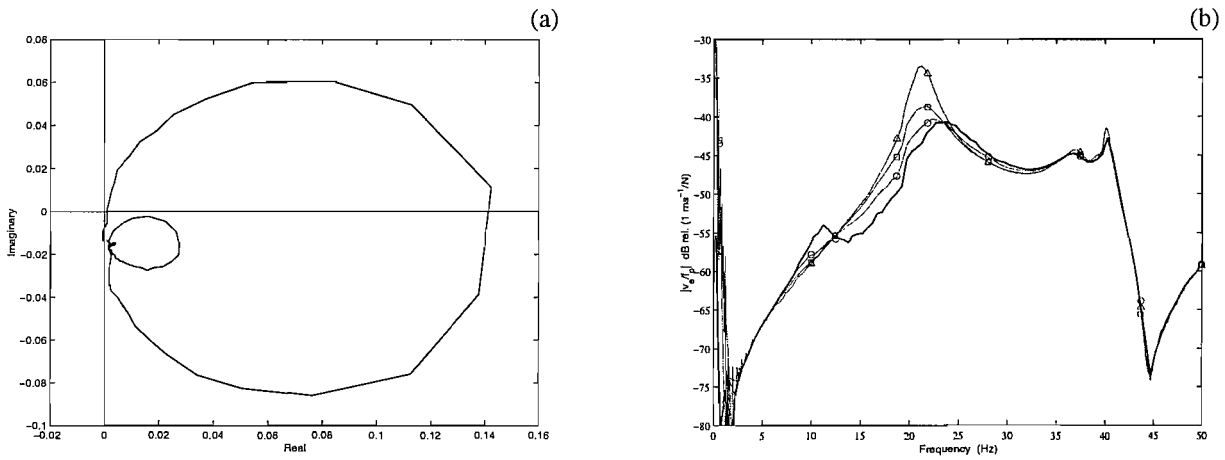

Figure 7.20 *(a): Nyquist plot of the treated measured open loop response from secondary shaker input to integrated force output. (b): treated measured velocity of the equipment per unit primary excitation. Results are shown for the passive system (control off, solid line) and for three values of feedback gain (faint lines): h_{if} =500 (triangle), h_{if} = 1000 (square), and h_{if} = 2500 (circle). For gains greater than 2500 the system was still stable, but limitations due to the electronics occurred.*

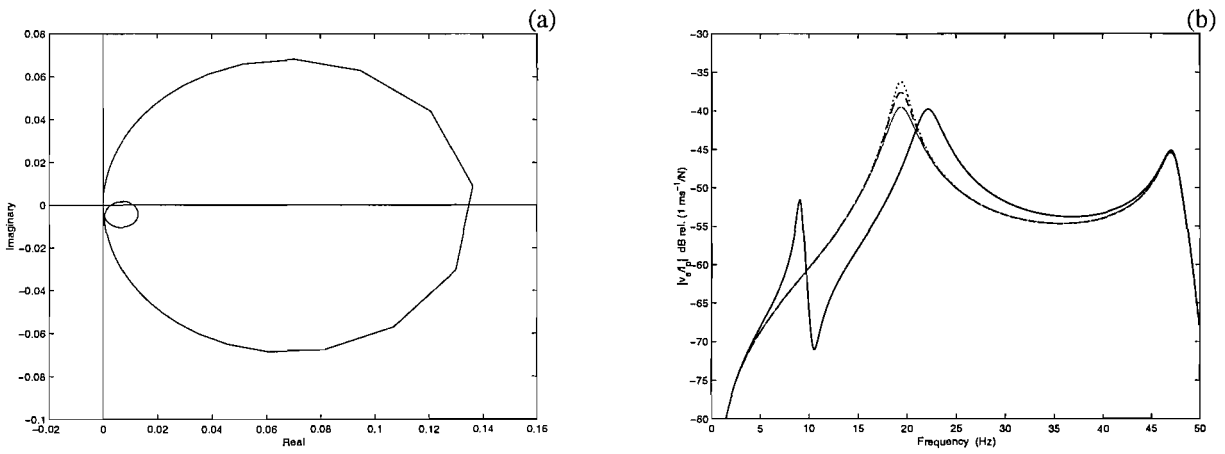

Figure 7.21 *(a): Nyquist plot of the simulated open loop response from secondary shaker input to integrated force output. (b): simulated velocity of the equipment per unit primary excitation. Results are shown for the passive system (control off, solid line) and for three values of feedback gain: h_{if} =500 (faint line), h_{if} = 1000 (dashed line), and h_{if} = 2500 (dotted line).*

7.3.5 Inner actuator force feedback and outer equipment velocity feedback control

In this case the plant is considered to be the original plant with in addition the inner force feedback loop. In order to evaluate the stability properties of the closed loop system, white noise from the FFT analyser was used to drive the command signal. This signal was also connected to channel A of the analyser. When the equipment structure was excited, the acceleration signal at centre of the equipment was measured using an accelerometer and then integrated. The integrator was operated in conjunction with a high-pass filter, whose cut-off frequency was preset to be 1 Hz. Finally, the velocity signal was connected into channel B of the analyser to measure the frequency response function of the absolute equipment velocity per unit command signal. The inner feedback loop was implemented using the signal from the force gauge underneath the inertial actuator. This signal was then connected to a charge amplifier, amplified and then connected to the secondary shaker. An ISVR-built passive summing box was used to add the command signal (white noise in this case, while it was the amplified equipment velocity in the performance measurement) to the output of the signal conditioner which carried the total transmitted force information. Figure 7.22 shows a practical implementation of the experimental set-up, and Figure 7.24(a) shows the Nyquist plot obtained from this measurement for different values of the inner feedback gain.

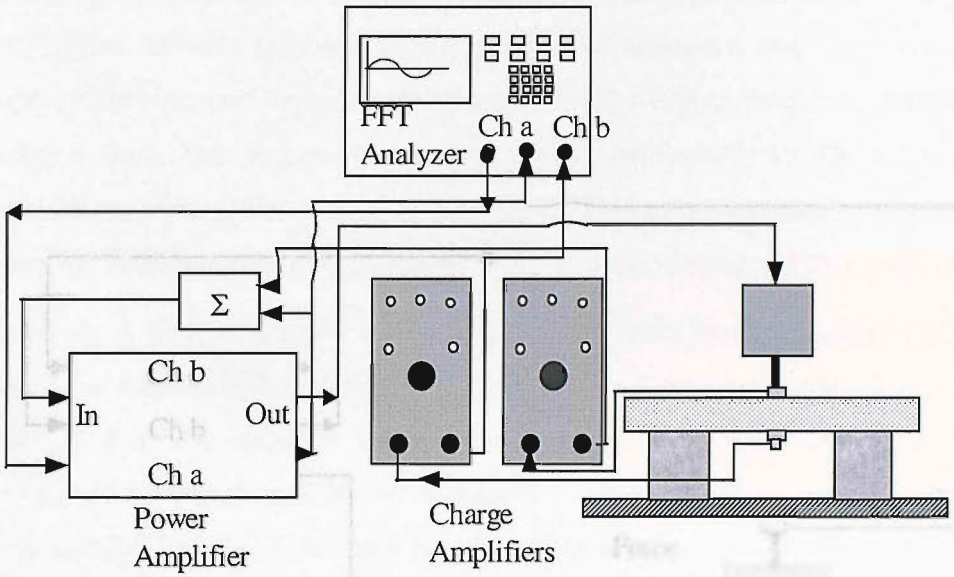

Figure 7.22 *Experimental set-up in order to measure the equipment velocity per control command.*

The set-up in Figure 7.22 was modified in order to evaluate the performance of this strategy. The FFT analyser was used to measure the frequency response of the equipment velocity per primary excitation as well as generate the white noise signal. The white noise signal drove the primary shaker to excite the flexible base, and the excitation force signal was measured by a force transducer connected to channel A of the analyser. When the equipment structure was excited, the equipment acceleration was measured and integrated. The velocity signal was then connected to channel B of the analyser to measure the frequency response function of the absolute equipment velocity per unit excitation force. A built-in filter in the analyser was employed to reduce aliasing. Figure 7.23 shows the experimental set-up, and Figure 7.24(b) shows the experimental results.

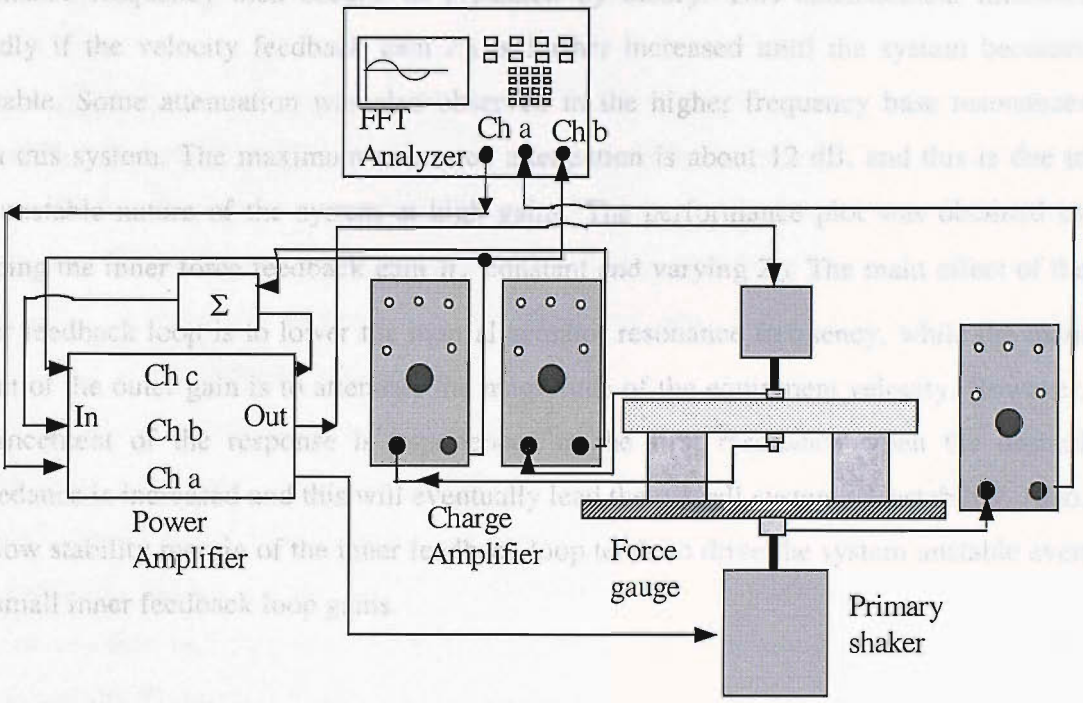

Figure 7.23 *Experimental set-up in order to measure the equipment velocity per unit primary excitation when the inner force feedback control and the outer direct velocity feedback control are implemented.*

The measured plant response, from control command to integrated accelerometer output, for the active isolation system with the inertial actuator is shown in Figure 7.24(a), which is similar to the simulated response shown in Figure 6.4(b). In this case there is no primary disturbance arising from the base support and three Nyquist plots are shown for different inner force feedback loop gains. The conclusion that can be drawn is that by increasing the inner feedback loop gain, the closed loop system (when the outer loop is also implemented) gets closer to instability.

The spectrum of the measured equipment velocity, normalized by the primary force, is shown in Figure 7.24(b) with no control and with three values of feedback gain. This can be compared to the theoretical simulations of Figure 6.6. There is good agreement between simulations and theory, even if it must be taken into account the fact that in the simulation higher gains were used to show the potentials of this scheme. Experimentally, an attenuation of the vibration at the mounted equipment resonance can be achieved using this arrangement, but some enhancement of the disturbance at the inertial actuator

resonance frequency then occurs, as predicted by theory. This enhancement increases rapidly if the velocity feedback gain Z_D is further increased until the system becomes unstable. Some attenuation was also observed in the higher frequency base resonances with this system. The maximum measured attenuation is about 12 dB, and this is due to the unstable nature of the system at high gains. The performance plot was obtained by keeping the inner force feedback gain h_f constant and varying Z_D. The main effect of the inner feedback loop is to lower the inertial actuator resonance frequency, while the main effect of the outer gain is to attenuate the magnitude of the equipment velocity. However, enhancement of the response is experienced at the first resonance when the desired impedance is increased and this will eventually lead the overall system to instability. Also, the low stability margin of the inner feedback loop tends to drive the system unstable even for small inner feedback loop gains.

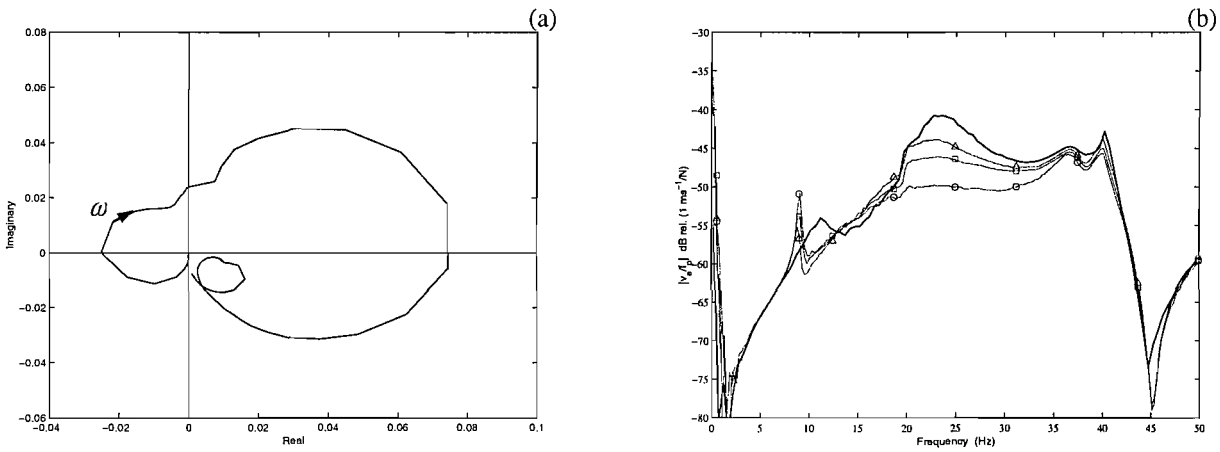

Figure 7.24 *(a): Nyquist plot of the treated measured open loop response from command signal to integrated accelerometer output when h_f = 6. (b): Treated measured velocity of the equipment per unit primary excitation. Results are shown for the passive system (control off, solid line) and for three values of the velocity feedback gain (faint lines) when the force feedback gain was set to h_f = 6: Z_D =20 (triangle), Z_D = 30 (square), and Z_D = 50 (circle). For gains greater than 50 the system was unstable.*

7.3.6 Integrated inner actuator force feedback and outer equipment velocity feedback control

The same experimental set-up described above was used in this case in order to evaluate the stability properties and the performance of the closed loop system. The only difference was an ISVR-built passive integrator, which was used as a controller in the inner feedback loop before the power amplifier. This allowed the transmitted force signal to be connected to the FFT analyser for measurement purposes, and also to be integrated within the feedback leg of the experimental set-up.

The measured plant response, from control command to integrated force output, for the active isolation system with the inertial actuator is shown in Figure 7.25(a), which matches closely the simulated response shown in Figure 6.8(b). Despite the presence of low frequency causes of instability due to the electronics, the closed loop system is now more stable than in the previous case. The spectrum of the measured equipment velocity, normalized by the primary force, is shown in Figure 7.25(b) with no control and with three values of feedback gain. The corresponding simulations are shown in Figure 6.10. Also in this case the theoretical findings match with the experimental measurements and in particular both effects on the first two resonances were experienced. Firstly, the magnitude of the inertial actuator resonance is attenuated and slightly shifted to lower frequencies. Secondly, at the equipment resonance, the magnitude of the transfer function is well attenuated, while at frequencies slightly greater than the second resonance a little enhancement is experienced, as predicted in Figure 6.10.

Even in this case, it was very difficult to increase the outer loop gain in such a way that it would set the closed loop system unstable. Such high gains were difficult to obtain with the power amplifiers in use. The maximum attenuation that was obtained was about 13 dB, but it must be noted that this does not represent a limit due to stability issues. This limit was reached because of the power limit of the audio amplifiers that were used during the experiments.

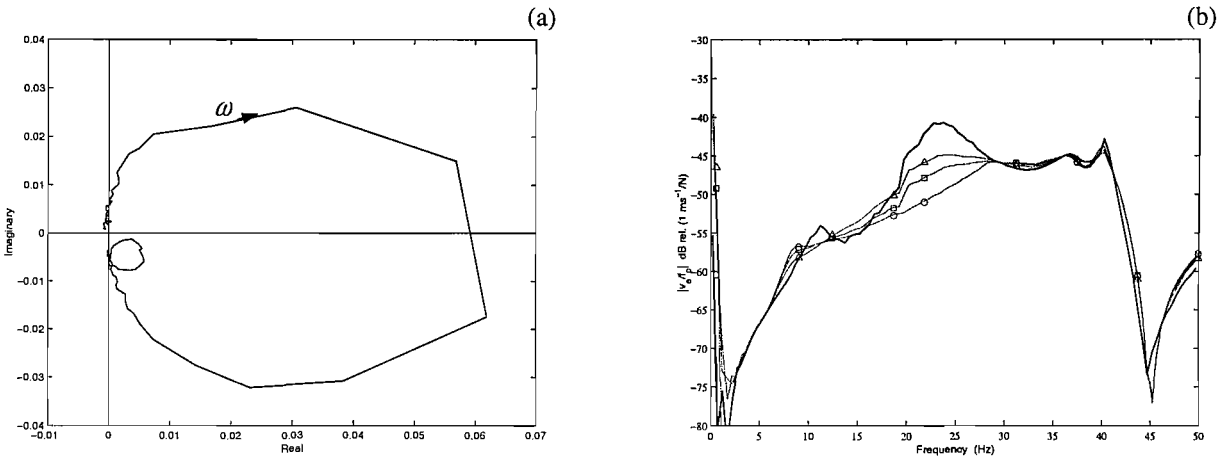

Figure 7.25 *(a): Nyquist plot of the treated measured open loop response from command signal to integrated accelerometer output when an integrator is added within the inner feedback loop. Results are shown for h_{if} = 2500. (b): Treated measured velocity of the equipment per unit primary excitation. Results are shown for the passive system (control off, solid line) and for three values of the velocity feedback gain (faint lines) when the force feedback gain was set to h_{if} = 2500: Z_D =60 (triangle), Z_D = 80 (square), and Z_D = 100 (circle). For gains greater than 100 the system was still stable, but limitations due to the electronics occurred.*

7.3.7 Inner phase-lag compensator and outer equipment velocity feedback control

The same configurations as above were used in this experiment. The only difference was a passive phase-lag compensator (R_1 = 720 KΩ, R_2 = 72 KΩ, C = 0.1 μF), which was employed as a controller in the inner feedback loop before the power amplifier. This allowed the transmitted force signal to be connected to the FFT analyser for measurement purposes, and also to be integrated within the feedback leg of the experimental set-up. The measured plant response, from control command to integrated force output, for the active isolation system with the inertial actuator is shown in Figure 7.26(a), which matches the simulated response shown in Figure 6.12(b). Despite the presence of low frequency causes of instability due to the electronics, the closed loop system is now more stable than in the inner force and outer velocity feedback control scheme. However, since the Nyquist plot is not entirely on the right hand side of the imaginary axis and portions of it intersect the negative part of the x-axis, instabilities may happen at very high outer velocity feedback gains Z_D. As predicted by the simulations, by increasing the inner feedback loop gain h_{pl}, the stability properties of the overall feedback system improve. The spectrum of the

measured equipment velocity, normalized by the primary force, is shown in Figure 7.26(b) with no control and with three values of feedback gain. The corresponding simulations are shown in Figure 6.14. Also in this case the theoretical findings match with the experimental measurements and in particular both effects on the first two resonances were experienced. In fact, below the second cut-off frequency of the phase-lag compensator (22 Hz), the systems behaves as if integrated inner force and outer equipment velocity feedback control was implemented, whereas at frequencies higher than 22 Hz, the system behaves as if inner force and outer velocity feedback control was implemented. As a result, the magnitude of the inertial actuator resonance is attenuated and slightly shifted to lower frequencies and at the equipment resonance, the magnitude of the transfer function is well attenuated, while at frequencies slightly greater than the second resonance no enhancement is experienced, unlike the previous case. Even in this case it was very difficult to increase the outer loop gain Z_D in such a way that it would set the closed loop system unstable. Such high gains were difficult to obtain with the power amplifiers in use. The maximum attenuation that was obtained was about 13 dB, but it must be noted that this does not represent a limit due to stability issues.

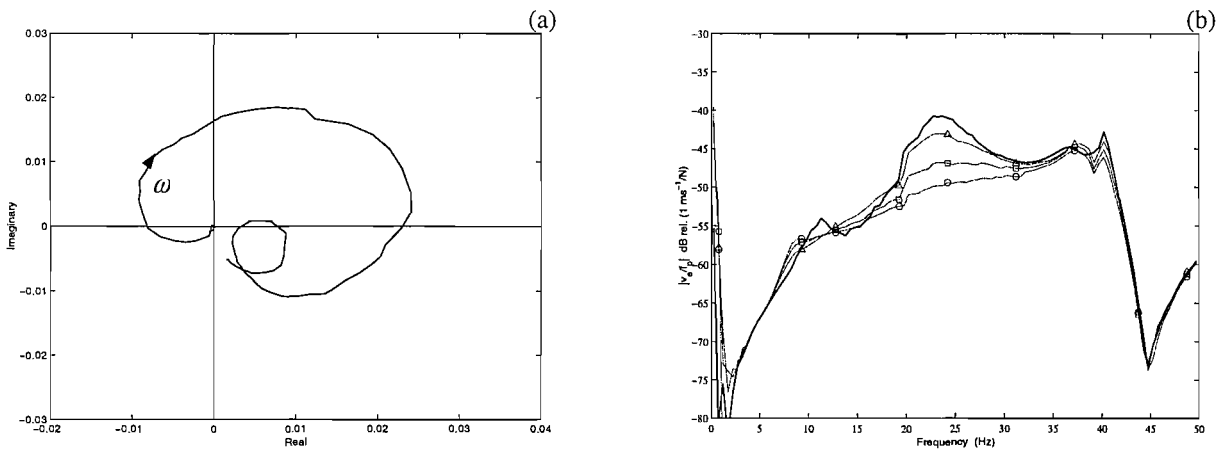

Figure 7.26 *(a): Nyquist plot of the treated measured open loop response from command signal to integrated accelerometer output when a phase-lag compensator is added within the inner feedback loop. Results are shown for* h_{pl} *= 100. (b): Treated measured velocity of the equipment per unit primary excitation. Results are shown for the passive system (control off, solid line) and for three values of the velocity feedback gain (faint lines) when the force feedback gain was set to* h_{pl} *= 100:* Z_D *=20 (triangle),* Z_D *= 50 (square), and* Z_D *= 100 (circle).*

7.4 Conclusions

The objective of this experimental work was to investigate the active isolation of an equipment structure from a vibrating base structure using an inertial actuator with inner force feedback. The dynamics and control mechanisms of the mounted rigid equipment structure on a flexible base plate have been studied experimentally and the results have been compared to the theoretical findings previously obtained. The equipment velocity responses measured from the experiments agree reasonably well with the predicted results, which demonstrates that the theoretical model can be used to help to understand the dynamics of the overall system. Good stability margins of several feedback control strategies are verified in the experimental implementations.

It was found from the simulations and the experiments that from a stability point of view, the inner actuator force feedback and outer equipment velocity feedback control scheme does not guarantee a good stability margin at low frequency. This is especially true when the outer velocity gain is increased. On the other hand, from a performance point of view, this scheme offers very good results using lower power than the other schemes. When an integrator is added to the inner loop, the overall system significantly improves its stability characteristics. On the other hand, if high performance is needed, very high gains are necessary.

The use a phase-lag compensator within the inner feedback loop and an outer velocity feedback loop then appears to be very effective. In fact, simulations and experiments show that a strong reduction of the equipment resonance can be achieved, together with very good stability margins.

Chapter 8

Active isolation theory with an inertial actuator having inner actuator displacement feedback

8.1 Introduction

In this chapter the active vibration isolation problem using an inertial actuator with inner actuator displacement feedback control is investigated. The same equipment structure used in the previous chapter and the same modified inertial actuator used in Chapter 2 will be considered in a simulation study, which will be followed, in the next chapter, by the experimental results. It will be seen that the ratio of actuator to equipment mass $\mu = m_a/m_e$ is an important parameter. In the first part of the study, μ will be about 0.2, while in the second part of the chapter, it has been changed so that the ratio $\mu = m_a/m_e = 1$ in order to describe the importance of the mass ratio in the performance.

8.2 Simulations with a flexible base

In this section we consider the use of an inertial actuator with inner feedback for the active isolation of a rigid equipment structure supported on a flexible base by a resilient mount. The arrangement, very similar to the arrangement described in

Chapter 6, is illustrated schematically in Figure 8.1 and is described fully by Benassi *et al.* (2002d, 2003b). It consists of a flexible steel base plate 700mm × 500mm × 1.85mm thick, clamped on the two longer sides, which supports a rigid equipment structure modelled as a point mass (m_e = 1.08 Kg) on which is mounted an ULTRA inertial actuator. The equipment structure is supported by a mount, which has stiffness, k_m = 20000 N/m, and damping, c_m = 18 N/ms^{-1}. The model assumes that the system is divided into four elements: a vibrating plate acting as the base structure, a passive mount, the equipment, and the inertial actuator.

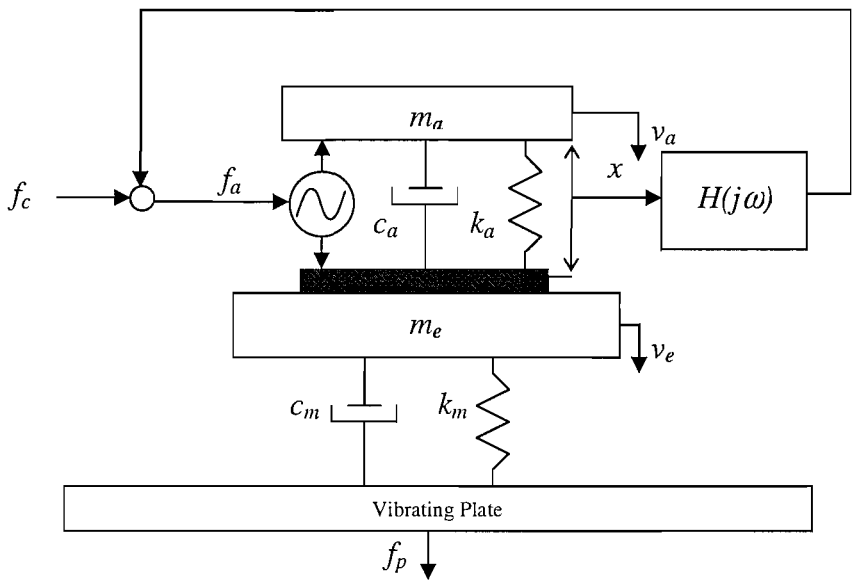

Figure 8.1 *Schematic of a vibration isolation system with an inertial actuator and implementation of the inner control based on inertial actuator displacement feedback.*

The uncontrolled actuator has a resonance frequency of 14.5 Hz and has a damping ratio of about ζ_a = 0.4, the mounted equipment has a resonance frequency of about 21.5 Hz and a damping ratio of about ζ = 5.2%, and the vibrating base has a first resonance frequency of about 44.8 Hz and a damping ratio of about ζ = 4.8%. An inner displacement feedback loop is used to modify the response of the inertial actuator, as discussed in Chapter 4, and an outer velocity feedback system, illustrated in Figure 8.2, is used to provide active skyhook damping for the equipment.

The expression for the equipment velocity as a function of the primary force f_p and the transmitted force f_t, is given by equation (6.1)

$$v_e = \frac{Y_e Z_m Y_b}{1 + Z_m (Y_e + Y_b)} f_p + \frac{Y_e (1 + Y_b Z_m)}{1 + Z_m (Y_e + Y_b)} f_t , \tag{8.1}$$

where, using the usual notation, Y_e is the mobility of the equipment structure, Y_b is the mobility of the base structure and Z_m is the mechanical impedance of the mount. Since the equipment structure is assumed to behave entirely like a rigid body of mass m_e, its input mobility is equal to $Y_e = 1/(j\omega m_e)$. The mount is assumed to have a negligible mass, and so without loss of generality its impedance can be written as

$$Z_m = \frac{k_m}{j\omega} + c_m , \tag{8.2}$$

where k_m is the mount's stiffness and c_m its damping factor, both of which may be frequency dependent. Substituting equation (4.13) into equation (8.1), the expression for the equipment velocity, when the modified inertial actuator is attached on the equipment, is given by

$$v_e = \frac{Y_e Z_m Y_b}{1 + Z_m (Y_e + Y_b + Y_e Z_a^{'} Y_b) + Y_e Z_a^{'}} f_p + \frac{Y_e T_a^{'} (1 + Y_b Z_m)}{1 + Z_m (Y_e + Y_b + Y_e Z_a^{'} Y_b) + Y_e Z_a^{'}} f_c . \tag{8.3}$$

If the control law of the outer feedback loop is assumed to take the form $f_c = -Z_D v_e$, as shown in Figure 8.4, where Z_D can be interpreted as the desired impedance of the outer feedback system, then equation (8.3) can be used to derive the equipment velocity per primary force with both feedback loops as given by

$$v_e = \frac{Y_e Z_m Y_b}{1 + Z_m (Y_e + Y_b + Y_e Z_a^{'} Y_b) + Y_e Z_a^{'} + Y_e T_a^{'} (1 + Y_b Z_m) Z_D} f_p . \tag{8.4}$$

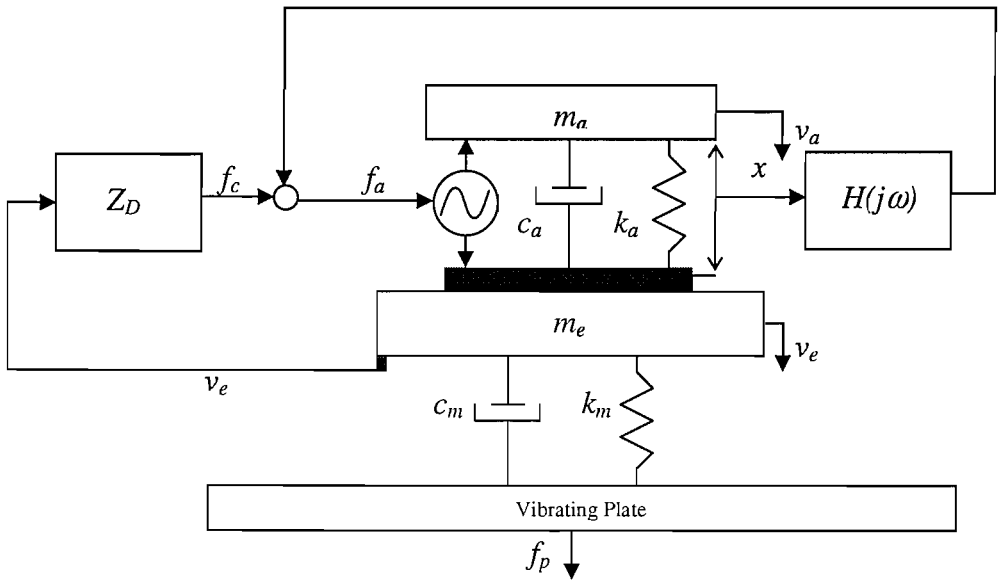

Figure 8.2 *Schematic of a vibration isolation system with an inertial actuator and implementation of the inner control based on displacement feedback and the outer velocity feedback control.*

The stability of the closed loop system can be assessed from Figure 8.3, which shows the predicted Nyquist plot of the open loop response of the plant, based on the modified inertial actuator on the passive isolation system and described by the second term of equation (8.3), and the outer equipment velocity feedback control gain Z_D. In this configuration, a gain of $Z_D = 60$ guarantees a 6 dB stability margin. Figure 8.4 shows the equipment velocity per unit primary excitation for the uncontrolled case and for different gains in the outer feedback loop. There is a difference between the equipment-dominated resonance frequency when no device is installed (solid line), and the new resonance frequency of the system when the modified inertial actuator is applied on top of the piece of equipment (faint line). This is due to the actuator acting as a tuned vibration neutraliser, as explained by den Hartog (1985). This "passive" effect of the modified inertial actuator with inner feedback on the equipment dynamics can be seen from the response when the outer loop is not implemented ($Z_D = 0$), which shows a lowered and well damped first resonance frequency, dominated by the actuator's response, as well as a damped equipment resonance frequency. In this case, the damping effect seems to be more evident than the mass-loading effect. When the inner feedback gain g_V is increased, substantial damping is

added to the system and both the first and second resonances are well attenuated, while attenuation at higher frequencies is experienced for high values of the gain g_V. Good vibration isolation conditions can be achieved at the mounted natural frequency of the equipment by the modified inertial actuator and the outer velocity feedback loop. The outer loop, with response Z_D, improves the behaviour of the equipment-dominated resonance, but it also enhances the magnitude of the inertial actuator resonance, as expected, by up to 10 dB at 10 Hz in Figure 8.4. When $Z_D = 60$ (dashed line in Figure 8.4), an impressive 24 dB attenuation is present at the equipment resonance frequency compared to the case where no device is installed.

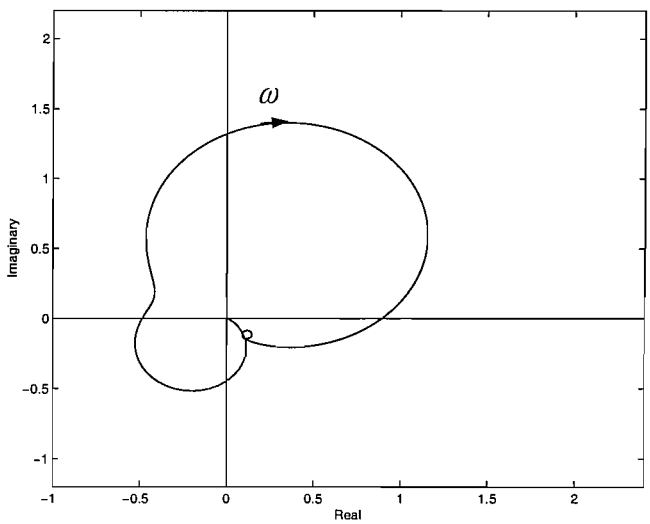

Figure 8.3 *Predicted Nyquist plot of the open loop transfer function of the complete system in Figure 8.2, equipment velocity per unit command signal, when g_P = -1000, the self-levelling coefficient λ = 0.4, the derivative gain g_V = 18, and the outer velocity control feedback gain Z_D = 60. The modified inertial actuator is directly installed on the equipment.*

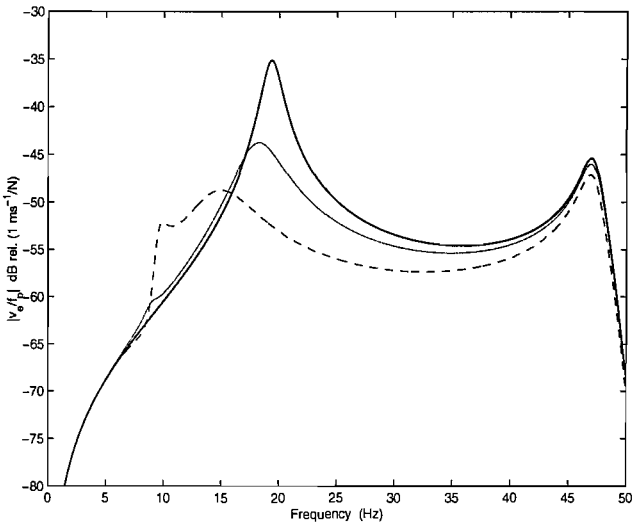

Figure 8.4 *Predicted frequency response of the equipment velocity per primary excitation when no modified inertial actuator is installed (solid), when the modified inertial actuator is installed but no outer velocity feedback loop is implemented (faint), and when both the modified inertial actuator and the outer velocity feedback loop are implemented with* Z_D = *60 (dashed). Under ideal conditions stability is guaranteed when* $Z_D < 120$.

The mechanical impedance of the modified actuator with outer velocity feedback loop is given from equation (4.10) and equation (4.12) by substituting $f_c = -Z_D v_e$

$$Z = \frac{\left(j\omega m_a k_a - \omega^2 m_a c_a\right)\cdot\left[H(j\omega) + j\omega Z_a\right] - j\omega^3 m_a Z_a Z_D}{\left(k_a + j\omega c_a - \omega^2 m_a + H(j\omega)\right) j\omega Z_a}, \qquad (8.3)$$

which is plotted in Figure 8.5 for the same values of the PID gains used in Chapter 4 and an outer velocity gain of $Z_D = 60$. It can be noted that the actuator impedance $Z = f_t / v_e$, past the first resonance frequency, tends to the desired impedance plus the derivative gain and the mechanical damping factor, $Z_D + g_V + c_a = 96$ N/ms^{-1}, which indicates that the overall system, composed of the modified inertial actuator with outer feedback loop, is similar to a skyhook damper.

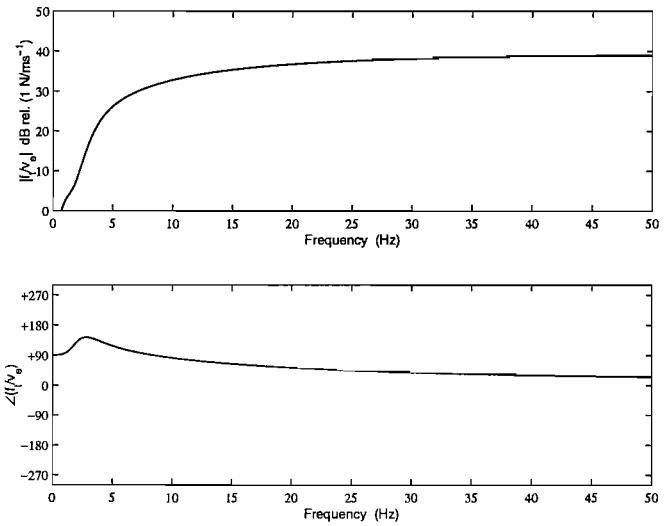

Figure 8.5 *Mechanical Impedance of the inertial actuator with inner and outer feedback loops when the inner displacement feedback control and the outer velocity feedback control are implemented. In particular,* $g_P = -1000$, $\lambda = 0.4$, $g_V = 18$ *and* $Z_D = 60$.

8.3 Importance of the mass ratio between equipment mass and inertial actuator proof-mass

In this section, the importance of the mass ratio between equipment mass and inertial actuator moving mass, $\mu = m_a/m_e$, will be discussed. In a realistic application, this ratio is likely to be less than 1, and in the specific simulated and experimental case described in this chapter and in Chapter 9 using the ULTRA actuator the ratio $\mu = m_a/m_e$ is equal to 0.2. The equations derived in the last section still hold when the ratio in increased to about 1, which applies to the case where an LDS Ling V101 shaker is used, whose internal mass is m_a = 0.91 Kg. For values of the mass ratio close to unity, the mechanical impedance shows that very good damping can be achieved by the inertial actuator with inner feedback, but without outer velocity feedback and this implies that the same values of the outer gain Z_D can be used to achieve a better performance than the case described in the previous section.

Figure 8.6 shows the Nyquist plot of the equipment velocity per unit command signal for different values of the inner velocity loop gain g_V when the mass ratio is about 1. The effect of the inner velocity feedback gain of increasing the damping at the

equipment-dominated resonance frequency and the inertial actuator resonance frequency can be noted. When the inner velocity feedback gain g_V is increased, the portion of the curve on the left-hand side of the imaginary axis decreases, adding damping to the actuator resonance. This is highly beneficial to the overall system because it is more stable to begin with. The Nyquist plot also suggests that the effect of increasing Z_D is good attenuation of the equipment-dominated resonance, and enhancement of the actuator resonance. It can be noted from the dashed line that the maximum gain Z_D that is allowed before instability is 220.

Figure 8.7 shows the equipment velocity per unit primary force for different values of the gain g_V. There is a difference between the equipment-dominated resonance frequency when no device is installed (solid line), and the new resonance frequencies of the system when the modified inertial actuator is applied on top of the piece of equipment. In terms of performance, Figure 8.7 also shows the behaviour of the complete system when the device is installed and no outer loop is implemented. It is the situation depicted in Figure 8.1, where no command f_c is present. The faint line shows the effect of the self-levelling controller, which is an enhancement of the magnitude of the first resonance frequency. When the gain g_V is increased, substantial damping is added to the system and both the first and second resonances are well attenuated, while attenuation at higher frequencies is experienced for high values of the gain g_V. From a performance point of view, both g_P and g_I must be considered as set values. g_P determines the position in frequency of the actuator resonance, and g_I determines the response of the actuator. However, if g_I is increased, the device moves closer to instability and therefore only g_V can be considered as significant in improving the performance of the device. Also, between g_V = 20 (dotted line) and g_V = 100 (dashed-dotted line) the shape of the curve in Figure 8.7 changes considerably. In fact, when g_V is increased, the device starts behaving as an overdamped system. As a result, high attenuation of the equipment resonance can be achieved, but at the same time the device is mass-dominated. This leads to a lower resonance at about 15 Hz, which increases in magnitude when g_V increases within the overdamped region.

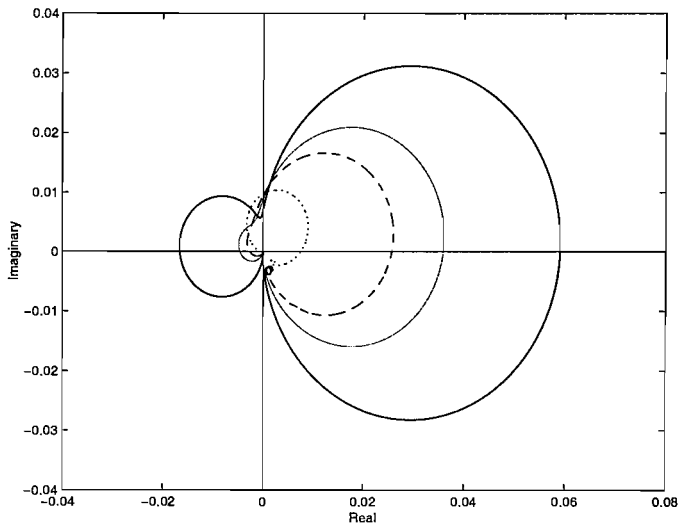

Figure 8.6 *Nyquist plot of the equipment velocity per unit command signal when λ=0.4 and different inner feedback loop gains g_V are used: g_V =0 (solid), g_V =10 (faint), g_V =20 (dashed), and g_V =100 (dotted). Mass ratio* $\mu \cong 1$.

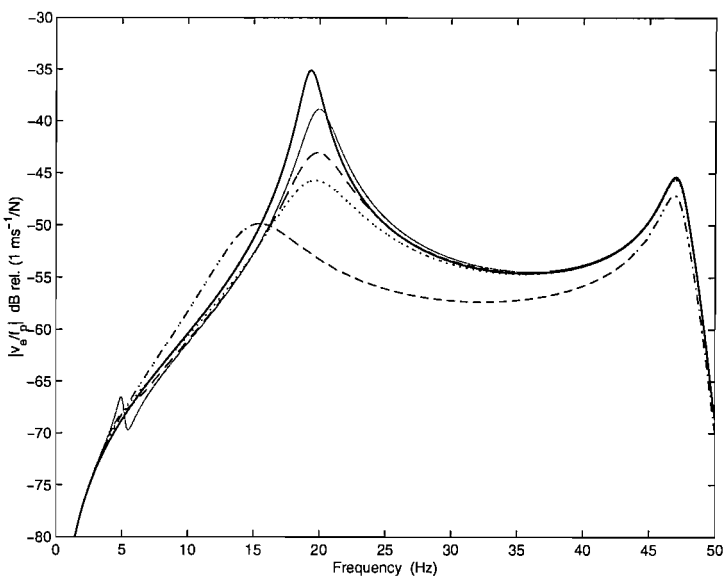

Figure 8.7 *Equipment velocity per unit primary force when no device is installed on the equipment (solid) and with an inertial actuator attached with inner feedback, where λ=0.4, g_P = 200, and different inner feedback loop gains g_V are used: g_V =0 (faint), g_V =10 (dashed), g_V =20 (dotted), and g_V =100 (dashed-dotted). Mass ratio* $\mu \cong 1$.

Figure 8.8 shows the equipment velocity per unit primary excitation when both inner and outer feedback loops are implemented so that the outer controller is added to the "passive" effect provided by the device and its inner controller. The outer loop, based on Z_D, improves the behaviour of the equipment-dominated resonance, but it also enhances the magnitude of the inertial actuator resonance, as expected. For example, when Z_D = 200 (dotted line), an additional 18 dB attenuation is present at the equipment resonance frequency compared to the "passive" case, which leads to an overall 30 dB attenuation compared to the uncontrolled case in Figure 8.7. The comparison between the case where no device is installed on the equipment (solid line in Figure 8.7) and the performance plot in Figure 8.8 suggests that care must be taken to avoid possible instabilities due to the actuator resonance, but this feature can be achieved and, more importantly, a considerable attenuation in the equipment velocity can be obtained.

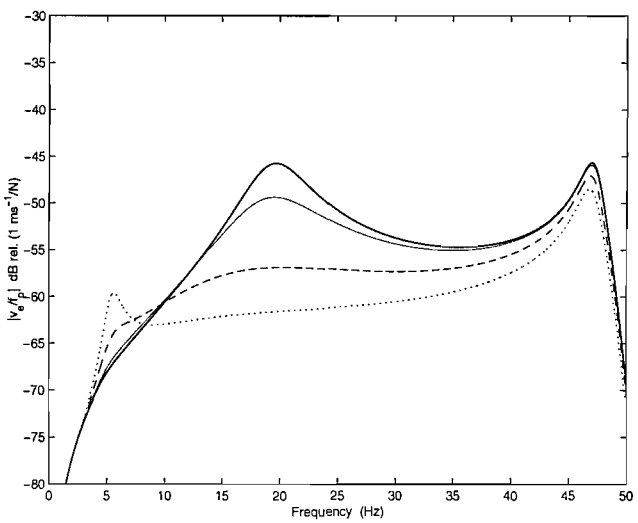

Figure 8.8 *Equipment velocity per primary excitation when the inner feedback loop gains λ=0.4, g_P = 200, and g_V =20 are used, and different outer velocity feedback control gains are implemented: Z_D=0 (solid), Z_D=20 (faint), Z_D=100 (dashed), and Z_D=200 (dotted). Under ideal conditions, stability is guaranteed when Z_D < 220.*

In conclusion, even if a modified inertial actuator with low mass ratio $\mu = m_a/m_e$ does not seem to provide the closed loop system with the same vibration attenuation as the above case, it becomes very helpful both in terms of stability and performance when the outer equipment velocity feedback loop is implemented. In fact, implementing the outer velocity feedback loop, good attenuation can be achieved.

As described in Chapter 2, the actuation force is proportional to $m_a\ddot{x}$, x being the relative displacement of the proof-mass. But $m_a\ddot{x} = -\omega^2 m_a x$, which indicates that at low frequency, in order to obtain considerable force, long strokes are needed. This puts a limit in the size of the actuator and its performance. Also, since m_a is involved in these considerations, this implies that μ also limits the size of the actuator, because for smaller μ, longer strokes are necessary.

8.4 Conclusions

It was found that the new device is effective in actively isolating a piece of equipment from the vibrations of a base structure. Although the overall system is conditionally stable, very good performance can be achieved.

When the device is installed on top of the equipment and no outer loop is implemented, the overall system can achieve good performance if the ratio μ between the moving mass of the actuator and the equipment mass is large. When μ is small, the passive effect is consequently small, but encouraging performance can still be obtained with the outer feedback loop. Another important effect of the choice of μ is the limitation imposed on the stroke of the inertial actuator.

Chapter 9

Experiments on active isolation with an inertial actuator having inner actuator displacement feedback

9.1 Introduction

This chapter describes the experimental work on the active isolation of a rigid piece of equipment structure from the vibration of a flexible base structure using a modified inertial actuator and an outer velocity feedback control. The objective is to validate the theoretical findings described in Chapter 8 and to study the performance and control stability issues associated with the active vibration isolation system. Particular emphasis is placed on the isolation of low frequency vibration (0~50Hz), in which the equipment resonance lies and for which the mounts can be assumed to behave as lumped springs and dampers. The inertial actuator that was used for the experiments was the modified ULTRA ATVA described in Chapter 4, while the equipment and set-up used to perform the active vibration isolation experiments are very similar to what was used in Chapter 7.

9.2 Description of the experimental set-up

Figure 9.1 shows the active mount system used in the experimental work. It consists of an aluminium rigid mass, two mounts placed symmetrically underneath the aluminium mass

and one electromagnetic shaker to produce the control force. The inertial actuator is placed on top of the mass and no suspension system is required. Finally, an accelerometer is used to measure the equipment velocity and unlike the experiments described in Chapter 7 no force gauges are used, making the system easier to assemble and more structurally robust. Figure 9.16 shows a closer image of the apparatus and it can be noted that also in this case the shaker can only generate axial forces and therefore only the axial motion can be entirely controlled, since the mass is supposed to be perfectly rigid in the frequency range of interest.

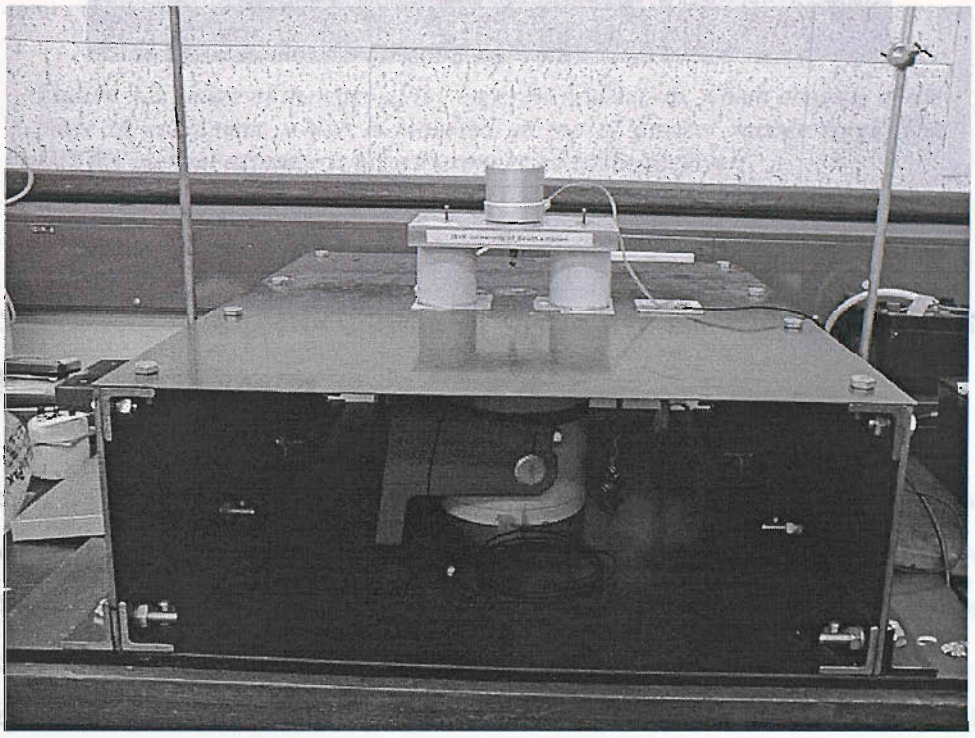

Figure 9.1 *Image of the experimental set-up, which consists of the piece of equipment, which is mounted on top of passive rubber rings, which is attached to a plate. Underneath the plate, a shaker supplies the primary force. The ULTRA inertial actuator is directly connected to the equipment.*

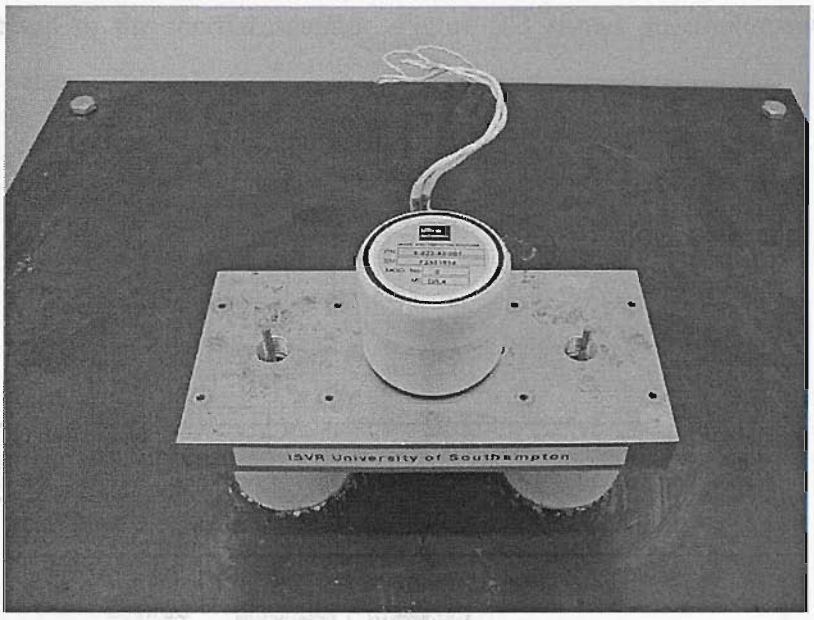

Figure 9.2 *Image of the core of the experimental set-up, which consists of the piece of equipment, which is mounted on top of passive rubber rings. The ULTRA inertial actuator is directly connected to the receiver.*

9.3 Experimental implementation of the active isolation system with the modified inertial actuator

The new experimental set-up was considered to be that described in Chapter 7 with in addition the inner displacement feedback loop described in Chapter 4. In order to evaluate the stability properties of the closed loop system, white noise from the FFT analyser was used to drive the command signal. This signal was also connected to channel A of the analyser. The acceleration signal at centre of the equipment was measured using an accelerometer and then integrated. The integrator was operated in conjunction with a high-pass filter, whose cut-off frequency was preset to be 1 Hz. Finally, the velocity signal was connected into channel B of the analyser to measure the frequency response function of the equipment velocity per unit command signal. The inner feedback loop was implemented using the signal from the strain gauge internal to the inertial actuator. This signal was then connected to a signal amplifier and fed to the PID controller, the output of which was then connected to the summing box. The output of the summing box was

finally connected to the inertial actuator. Figure 9.3 shows an implementation of the experimental set-up.

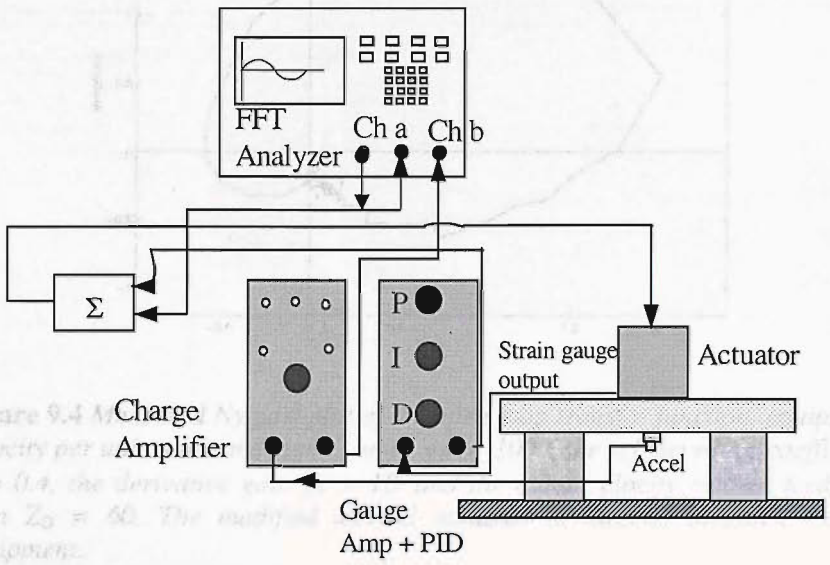

Figure 9.3 *Experimental set-up in order to measure the equipment velocity per unit command signal when the inner PID feedback control scheme is implemented.*

The stability of the closed loop system can be assessed from Figure 9.4, which shows the measured Nyquist plot of the open loop response of the plant, based on the modified inertial actuator on the passive isolation system and the outer velocity feedback control gain Z_D. In this experimental configuration, a gain of $Z_D = 45$ guarantees a 6 dB stability margin. The corresponding theoretical prediction is shown in Figure 8.3, which shows that the same stability margin is guaranteed when $Z_D = 60$.

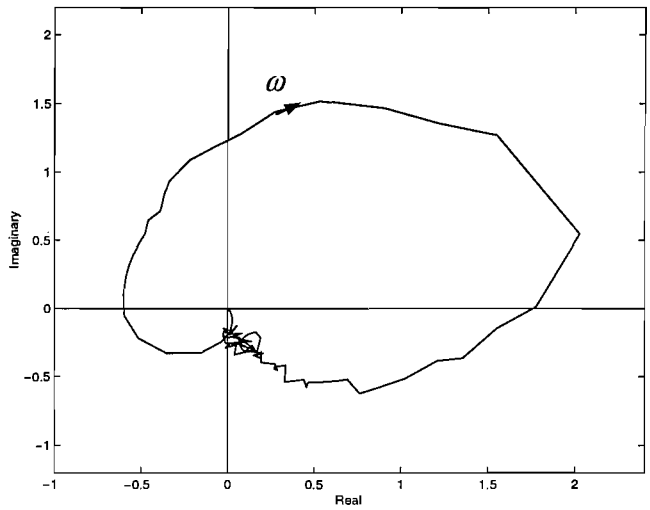

Figure 9.4 *Measured Nyquist plot of the open loop transfer function, equipment velocity per unit command signal, when g_P = -1000, the self-levelling coefficient λ = 0.4, the derivative gain g_V = 18, and the outer velocity control feedback gain Z_D = 60. The modified inertial actuator is directly installed on the equipment.*

The set-up in Figure 9.3 was then modified in order to evaluate the performance of the active isolation system with both an inner actuator displacement feedback loop and an outer equipment velocity feedback loop, as shown in Figure 9.5. The FFT analyser was used to measure the frequency response of the equipment velocity per primary excitation as well as generate the white noise signal. The white noise signal drove the primary shaker to excite the flexible base, and the excitation force signal was measured by a force transducer connected to channel A of the analyser. When the equipment structure was excited, the equipment acceleration was measured and integrated. The velocity signal was then connected to channel B of the analyser to measure the frequency response function of the equipment velocity per unit excitation force. A built-in filter in the analyser was employed to reduce aliasing. As explained above, both inner and outer feedback loops were implemented.

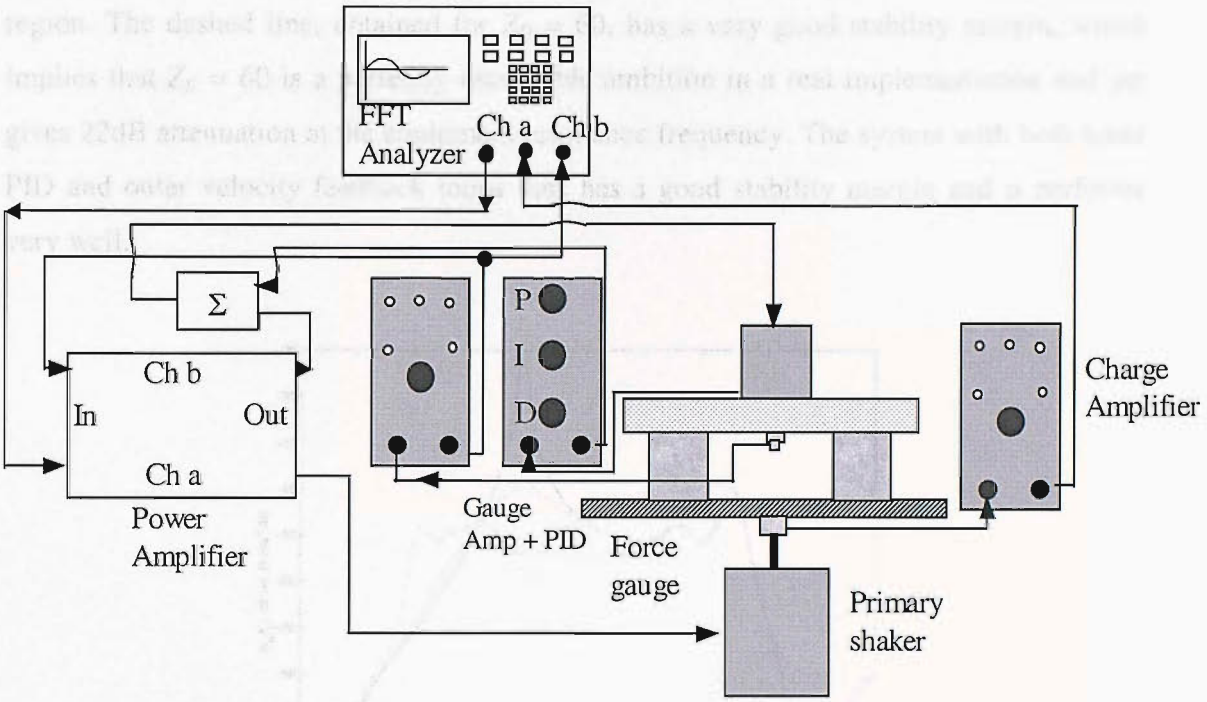

Figure 9.5 *Experimental set-up in order to measure the equipment velocity per unit primary excitation when the inner PID feedback control and the outer velocity feedback control schemes are implemented.*

Figure 9.6 shows the equipment velocity per unit primary excitation for the uncontrolled case, with the inertial actuator attached having only the inner feedback loop connected, and for different gains in the outer feedback loop. As explained in the previous chapter, there is a difference between the equipment-dominated resonance frequency when no device is installed (solid line), and the new resonance frequency of the system when the modified inertial actuator is applied on top of the piece of equipment (faint line). This "passive" effect of the modified inertial actuator with inner feedback on the equipment dynamics can be seen from the response when the outer loop is not implemented ($Z_D = 0$), which shows a lowered and well damped equipment resonance frequency. Even better vibration isolation conditions can be achieved at the mounted natural frequency of the equipment by the modified inertial actuator and the outer velocity feedback loop. The outer loop, with response Z_D, improves the behaviour of the equipment-dominated resonance, but it also enhances the magnitude of the inertial actuator resonance more than in the theoretical predictions in Figure 8.4, which is a sign of being closer to the unstable

region. The dashed line, obtained for Z_D = 60, has a very good stability margin, which implies that Z_D = 60 is a perfectly reasonable ambition in a real implementation and yet gives 22dB attenuation at the equipment resonance frequency. The system with both inner PID and outer velocity feedback loops thus has a good stability margin and it performs very well.

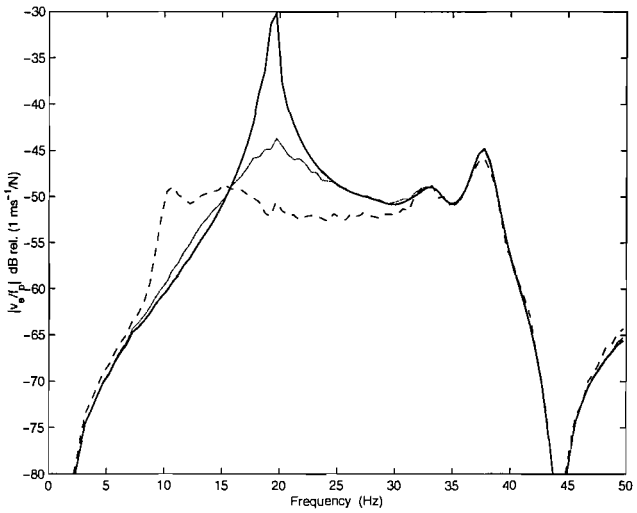

Figure 9.6 *Measued frequency response of the equipment velocity per primary excitation when no modified inertial actuator is installed (solid), when the modified inertial actuator is installed but no outer velocity feedback loop is implemented (faint), and when both the modified inertial actuator and the outer velocity feedback loop are implemented with Z_D = 60 (dashed). Under experimental conditions stability is guaranteed when Z_D < 90.*

9.4 Conclusions

The objective of this experimental work was to investigate the active isolation of a two-mount flexible equipment structure from a vibrating base structure using a new device, based on an inertial actuator with inner displacement feedback control. The equipment velocity responses measured from the experiments agree reasonably well with the predicted results. Good stability margins of the multi-channel feedback control system are verified in the experimental implementations.

It was found from the simulations and the experiments that the new device is effective in actively isolate a piece of equipment from the vibrations caused by an underneath base structure.

Chapter 10

The equivalent impedance of power-minimising vibration controllers on plates

10.1 Introduction

Inertial actuators could be used for the control of vibration on flexible structures as well as for active isolation. Whereas for active isolation it is clear that the target impedance of the actuator, Z_D in the loops previously described, should just be very large, it is not clear what this target impedance should be in the more general active vibration control case. In this chapter feedforward control of vibration on infinite and finite plates is considered in an attempt to understand what the target impedance should be in this case.

A description has been given in Bardou *et al.* (1997) and Brennan *et al.* (1995, 1998) of the performance of two possible strategies that can be used to design an active vibration controller: total power minimization and maximization of the power absorption of the secondary source (Sharp *et al.*, 2002).

In this chapter, the total power generated by all the forces acting on the structure is used as a function to be minimised, as described by Howard *et al.* (2000). This approach has also been used as a noise control technique by Elliott *et al.* (1991) and Tanaka *et al.* (1988). If we assume the system to be linear such that the velocity fields produced by the forces can be superimposed, then the total power has a known minimum value that is associated with an optimal solution, as shown by Elliott *et al.*

(1991, 1997) and Nelson and Elliott (1992). This solution can be compared to what the passive treatments manage to accomplish. Since this solution is optimal, no other strategy can perform better. The question is then how well a certain passive control scheme performs with respect to the optimal solution when the optimal impedance is replaced with its equivalent passive approximation, as shown in Figure 10.1. This is one of the main issues discussed here.

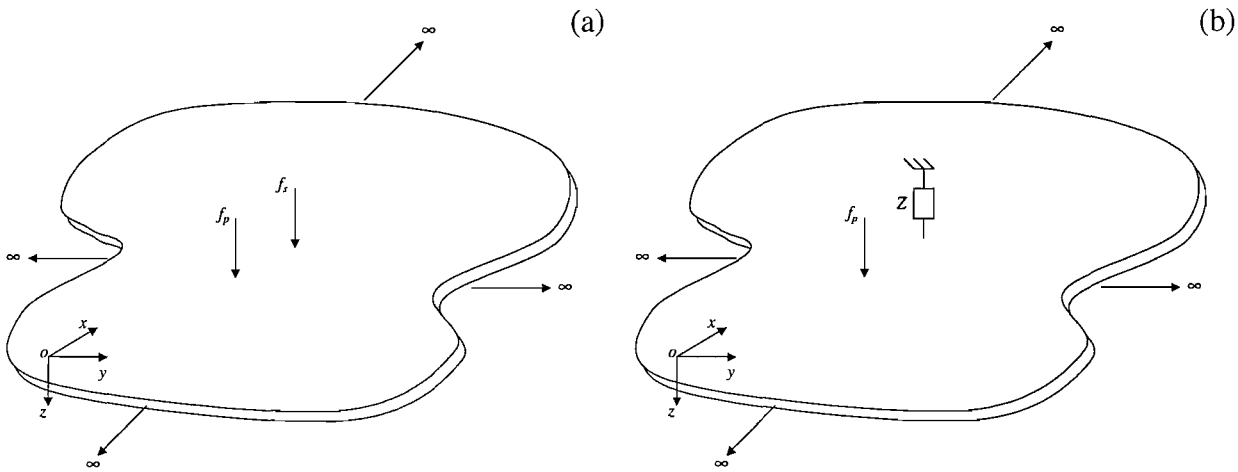

Figure 10.1 *(a): A point primary force and a point secondary force applied to an infinite thin plate. (b): A point primary force and an equivalent impedance applied to an infinite thin plate.*

A lot of work has been carried out in order to synthesize load impedances which achieve desired performances (using semi-definite programming, for example, by Titterton, 1999), and in this study optimal impedances and impedances generated by passive devices (also studied by Guicking *et al.*, 1989) will be compared. The goal is to use these devices in order to reduce the total power, acting on a local basis, as also illustrated by Yuan (2002). Also, unlike most of the literature on this subject, the primary disturbance will be considered to be broadband rather than single frequency (Titterton, 1999 and Fuller *et al.*, 1997), and so the realisability of the equivalent impedance must be addressed.

One of the limitations of some of the models presented in the literature is that the primary force and the secondary control force are acting along the same axis. In real systems, there will inevitably be some mismatch between the point of application of the primary force and the point of application of the secondary force. This issue has

been addressed by Jenkins *et al.* (1993), and their results show that appreciable reductions in total power can only be achieved if the secondary force is applied at a distance within $3\lambda_f / 8$ from the primary force, where λ_f is the flexural wavelength in the receiving structure at the frequency of interest.

Infinite plates will be considered first and finite plates will then be analysed. In particular a flexible plate, clamped on two edges and free on the other two, will be considered. Then, the optimisation of the spring/damper approximation to the equivalent impedance is discussed, followed by the conclusions.

10.2 Equivalent impedance for global control of vibrating infinite plates

In order to analyse the problems described in the introduction, we now examine a single point secondary force f_s separated by a distance r from a point primary force, f_p, both forces being applied along the z-axis on an infinite plate. This configuration is depicted in Figure 10.1(a). The expression for the driving point mobility $Y_{00} = \dfrac{\dot{z}_0(\omega)}{f_0(\omega)}$ for an infinite plate, where $\dot{z}_0(\omega)$ is the velocity in the z direction, evaluated at a point $P_0 = (x_0, y_0)$, and $f_0(\omega)$ is the excitation force at P_0, is given by

$$Y_{00} = \frac{\omega}{8Dk^2} = \frac{1}{8\sqrt{Dm}}, \tag{10.1}$$

where $D = \dfrac{EI}{1-\upsilon^2}$ is the plate's bending stiffness, E is its Young's modulus, $I = \dfrac{h^3}{12}$, where h is the plate thickness, υ is the Poisson's ratio, $m = \rho h$ is the mass per unit area, and ρ is the density of the plate material. It is important to note that Y_{00} is independent of frequency and it is real. The transfer mobility, between two points $P_1 = (x_1, y_1)$ and $P_0 = (x_0, y_0)$, $Y_{10} = \dfrac{\dot{z}_1(\omega)}{f_0(\omega)}$ is given by (Cremer *et al.*, 1988)

$$Y_{10} = \frac{\omega}{8Dk^2}\left[H_0^{(2)}(kr) - H_0^{(2)}(-jkr)\right], \tag{10.2}$$

where $r = \sqrt{(x_1 - x_0)^2 + (y_1 - y_0)^2}$ is the distance between the points, $k = \frac{\omega}{c_D}$, $c_D = \sqrt[4]{\frac{D}{m}}\sqrt{\omega}$ is the phase velocity, and $H_0^{(2)}(\cdot)$ is the second kind of Hankel function of 0^{th} order. This function can be written as

$$H_0^{(2)}(kr) = J_0(kr) - jY_0(kr), \tag{10.3}$$

where $J_0(kr)$ is the 0^{th} order Bessel function of the first kind and $Y_0(\cdot)$ is the 0^{th} order Bessel function of the second kind. While $H_0^{(2)}(kr)$ has real and imaginary parts, $H_0^{(2)}(-jkr)$ is entirely imaginary.

It is now possible to define a cost function that will be used as the reference for all the remaining computations. The chosen cost function is the total power supplied to the plate, which is given by the sum of the power Π_p due to the primary force acting in P_0 and the power Π_s due to the secondary force acting in P_1. It can be expressed as

$$\Pi = \Pi_p + \Pi_s \tag{10.4}$$

and rewritten considering that the total power is also one half of the real part of the forces times the complex transverse velocity of the plate at the position of the application of the forces. This total power can also be written as (Jenkins *et al.* 1993)

$$\Pi = \frac{1}{2}\mathrm{Re}\left\{f_p^* v_p + f_s^* v_s\right\} = A\left|f_s\right|^2 + f_s^* b + b^* f_s + c, \tag{10.5}$$

which is a quadratic form where the parameters of the last term of equation (10.5) are

$$A = \frac{1}{2}\mathrm{Re}(Y_{11}) \;,\; b = \frac{1}{2}\mathrm{Re}(Y_{10}) f_p \,,\; c = \frac{1}{2}\left|f_p\right|^2 \mathrm{Re}(Y_{00}), \tag{10.6,7,8}$$

where Y_{11} is the driving point mobility at location $P_1 = (x_1, y_1)$. In particular, the power of the primary force only, which provides the power of the system without any sort of treatment, is given by setting the secondary force in equation (10.5) to zero. This leads to

$$\Pi_p = c \ . \tag{10.9}$$

Equation (10.5) has a well-defined minimum value

$$\Pi_{opt} = c - \frac{|b|^2}{A}, \tag{10.10}$$

which is associated with an optimal secondary force f_{so} given by (Nelson *et al.*, 1992)

$$f_{so} = -\frac{b}{A} = -\frac{\mathrm{Re}(Y_{10})}{\mathrm{Re}(Y_{11})} f_p . \tag{10.11}$$

In the particular case of an infinite plate, from equation (10.1) follows that

$$\mathrm{Re}(Y_{00}) = Y_{00}, \tag{10.12}$$

and from equation (10.2) and equation (10.3) the real part of the transfer mobility for an infinite plate is given by

$$\mathrm{Re}(Y_{10}) = Y_{00} J_0(kr). \tag{10.13}$$

Thus the optimal solution in equation (10.11) can be rewritten as (Jenkins *et al.* 1993)

$$f_{so} = -J_0(kr) f_p \tag{10.14}$$

and its corresponding power is given by

$$\Pi_{opt} = [1 - J_0^2(kr)]\Pi_p . \tag{10.15}$$

The effectiveness of the optimal solution can be established by comparing equation (10.15) with the power input due to the primary disturbance f_p, given by equation (10.9). Equation (10.15) is plotted in Figure 10.2 as a function of *kr*. The optimal secondary force significantly reduces the total power supplied to the plate for values of *kr* below about 1. However, this attenuation tends to zero for larger values of *kr*. Thus placing the secondary force close to the primary force allows the system to perform well over a broad range of frequencies. If the location of the secondary force were to coincide with the location of the primary force, then the total power would be zero at all frequencies, which indicates a total cancellation of the disturbance.

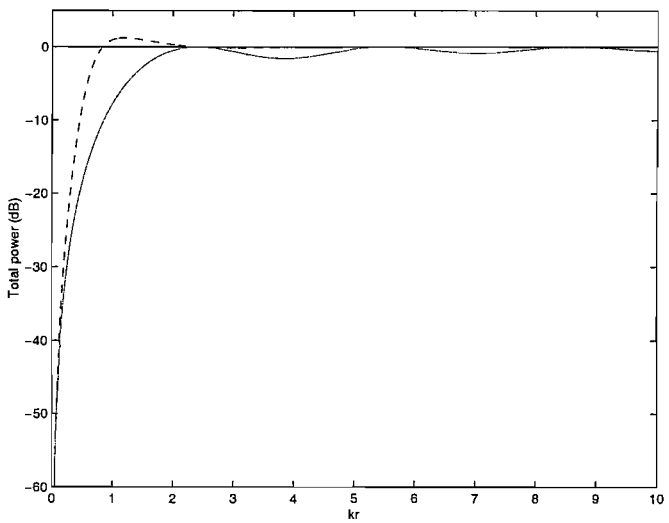

Figure 10.2 *Total power transmitted to an infinite plate, normalized to that due to the primary force only, when the primary and optimal secondary forces are applied (faint), and when the secondary force is replaced by a spring, whose stiffness is given by equation (10.23) (dashed).*

The optimal "equivalent" impedance that is presented to the system in order to obtain such attenuation in the total power is now computed. The velocity v_s of the base at

P_1, where the secondary force is acting, is given by a combination of the effects of the primary force, f_p, and the secondary force, f_s, at P_1

$$v_s = Y_{10} f_p + Y_{11} f_s , \tag{10.16}$$

where $Y_{00} = Y_{11}$ in this case. If the secondary force f_s is chosen to be the optimal solution, f_{so}, described in equation (10.14) and substituting equation (10.14) into equation (10.16), the velocity of the base at P_1 as a function of the primary force, when the optimal solution is implemented, is found to be

$$v_{so} = [Y_{10} - Y_{11} J_0(kr)] f_p . \tag{10.17}$$

From equation (10.14) it follows that

$$f_p = -\frac{1}{J_0(kr)} f_{so} , \tag{10.18}$$

which substituted into equation (10.17) provides a way of calculating the equivalent impedance presented by te secondary actuator to the plate. This is given by

$$Z_{opt} = \frac{f_{so}}{v_{so}} = -\frac{J_0(kr)}{Y_{10} - Y_{11} J_0(kr)} = -\frac{J_0(kr)}{Y_{11}[H_0^{(2)}(kr) - H_0^{(2)}(-jkr) - J_0(kr)]} , \tag{10.19}$$

and it expresses the impedance that the secondary optimal force is presenting to the system in order to minimise the cost function given by the total power. The numerator of equation (10.19) is real, and its denominator is purely imaginary, thus Z_{opt} is entirely reactive (Elliott *et al.*, 1991). Considering only the first terms of the series expansion (Abramowitz *et al.*, 1972) of equation (10.19) in terms of *kr*, an approximated expression can be obtained

$$\frac{f_{so}}{v_{so}} \cong \frac{\frac{(kr)^2}{4} - 1}{jY_{11}\frac{(kr)^2}{\pi}\left(\gamma - 1 + \ln\frac{kr}{2}\right)}, \tag{10.20}$$

where γ = 0.577 is Euler's constant. The primary drawback of this result is that the compensator is non-causal (Miller *et al.*, 1990). Equation (10.20) can be further expanded into

$$\frac{f_{so}}{v_{so}} \cong \frac{1}{j\omega}\frac{2\pi\sqrt{Dm}\left(\omega r^2 - 4\sqrt{D/m}\right)}{r^2\left(\gamma - 1 + \ln\frac{kr}{2}\right)} = \frac{k_a}{j\omega}, \tag{10.21}$$

where the dependence on $\frac{1}{j\omega}$ has been made explicit in order to be able to express the remaining term as a stiffness coefficient k_a. The low frequency approximation of the stiffness coefficient k_a in equation (10.21) is given by

$$k_a \cong \frac{8\pi D}{r^2\left(1 - \ln\frac{kr}{2} - \gamma\right)}. \tag{10.22}$$

For very low frequencies and for separation distances $kr \cong 0.01$, in which case $\ln\frac{kr}{2} \cong -5$, equation (10.22) can be rewritten as

$$k_a \cong \frac{8\pi D}{r^2(6 - \gamma)}. \tag{10.23}$$

The full expression for the equivalent impedance, equation (10.19), is plotted in Figure 10.3, along with its passive approximation, given by a stiffness term $\frac{k_a}{j\omega}$, where k_a = $1.2 \cdot 10^6$ N/m, as computed from equation (10.23) for the 1.85 mm plate when the distance *r* between primary and secondary forces is 2 cm.

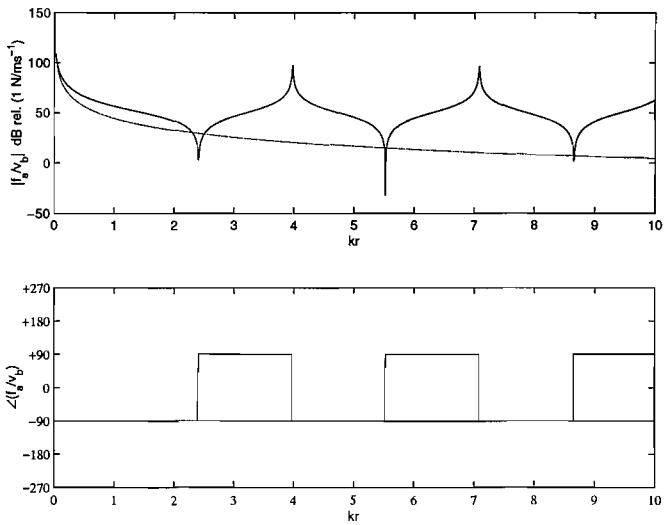

Figure 10.3 *Equivalent impedance due to the optimal solution (solid) and comparison with an impedance due to a spring whose stiffness is* $1.2 \cdot 10^6$ *N/m (faint).*

At low frequency, the equivalent impedance is very similar to the impedance given by a spring, whose stiffness is very large. When the above passive approximation is used instead of the optimal solution, the total power as a function of kr is shown as the dashed line in Figure 10.2. As expected, at low values of kr the performance of the passive solution is close to optimum. For values of kr between about 1 and 2, however, the performance of the passive solution is worse than applying no control at all. Appreciable reductions in total power can only be achieved if the secondary force is applied at a distance within $3\lambda_f / 8$ from the primary force (Jenkins *et al.* 1993), where λ_f is the frequency-dependent flexural wavelength in the receiving structure. When this distance is 2 cm on a 1.85 mm steel plate, reductions can be achieved up to 550 Hz, while when this distance is 20 cm, the optimal solution is effective only up to 60 Hz. When the value of the stiffness tends to infinity, the system behaves as an infinite plate pinned at the secondary location. In this case, attenuation in the total power for low values of kr is not as great as in the case when $k_a = 1.2 \cdot 10^6$ N/m. On the other hand, when kr assumes values between 0.5 and 1.5, the pinned case shows better results in terms of total power than the low kr approximation. One way to evaluate the performance of a passive control solution is the ratio of the frequency

averaged power values. This ratio is defined as $P = 10\log_{10}\frac{\langle P_c \rangle}{\langle P_u \rangle}$, where $\langle P_c \rangle$ and $\langle P_u \rangle$ represent, respectively, the power of the controlled and uncontrolled system, averaged over the frequency range 0 Hz to 200 Hz. As a function of the passive stiffness constant k_a , the frequency averaged power ratio reaches a minimum value when $k_a = 2 \cdot 10^8$ N/m, before it increases slightly and then it settles at the constant value of the averaged power ratio of –0.28 dB, which indicates that the plate is pinned and the system does not benefit from higher values of the stiffness. The choice of $k_a = 1.2 \cdot 10^6$ N/m is thus appropriate in order to achieve the best possible reduction at low kr, using only a stiffness term, but in order to minimize the averaged power ratio as defined above, it is better to pin the secondary location.

For $kr > 1$, the following Bessel's functions may be replaced with sufficient accuracy by their asymptotic representations (Skudrzyk, 1968), and in particular

$$J_0(kr) \cong \sqrt{\frac{2}{\pi kr}} \cos\left(kr - \frac{\pi}{4}\right) \tag{10.24}$$

$$Y_0(kr) \cong \sqrt{\frac{2\pi}{kr}} \sin\left(kr - \frac{\pi}{4}\right) \tag{10.25}$$

$$H_0^{(2)}(kr) \cong \sqrt{\frac{2}{\pi kr}} e^{-j\left(kr - \frac{\pi}{4}\right)}. \tag{10.26}$$

Equation (10.1), equation (10.2) and equation (10.3) describe the terms to be used in equation (10.19) to compute the high-kr approximation of the optimal impedance, which is found to oscillate about

$$Z_{opt} \cong 8\sqrt{Dm}\,, \tag{10.27}$$

which is equal to the infinite plate driving impedance obtained by the reciprocal of equation (10.1). Figure 10.3 shows that, after the stiffness-like behaviour for low values of *kr*, the optimal solution oscillates about an averaged value given by the driving point impedance of the infinite plate $Z_{00} = \frac{1}{Y_{00}}$, which is equal to 323 N/ms^{-1} for the plate considered above. The equivalent impedance, equation (10.19), is entirely reactive and the mechanism of control, for low *kr*, is one of loading the primary force, since no power can be absorbed by a reactive impedance. For larger values of *kr*, the reductions in total power output are far less and the main problem in generating a realisable approximation to the equivalent impedance is the increase in the total power output that occurs at about $kr = 1$ with the equivalent spring, as seen in Figure 10.2. It has been found that larger attenuations can be obtained for $kr \cong 1$ if a damper, of value Z_{00}, is connected in parallel with the spring. Figure 10.4 shows the total power transmitted to the infinite plate when the secondary force is given by such passive ideal impedance (whose impedance is shown in Figure 10.5) and its performance is compared to the optimal case. For values of *kr* between 3 and 5, the equivalent impedance is either mass or stiffness dominated, whereas this passive approximation to the equivalent impedance is damping dominated, but nevertheless the total power with the equivalent impedance is not very different from the optimal case. Comparing Figure 10.2 and Figure 10.4, the improved performance due to the new approximation to the equivalent impedance can be noticed. The frequency averaged power ratio between the controlled system, which uses the spring-damper impedance and the uncontrolled system, as a function of the passive stiffness constant k_a when the damper value is kept constant at 323 N/ms^{-1}, shows that the minimum of the curve occurs when $k_a = 1.2 \cdot 10^6$ N/m. For this configuration of the approximation to the equivalent impedance, the averaged power ratio is about –0.444 dB, and this value is less than the –0.3 dB, which was obtained when implementing a stiffness as an approximation to the equivalent impedance. For large values of the stiffness k_a, the ratio tends to –0.28 dB only, showing that for this value, the infinite plate is pinned at the secondary location.

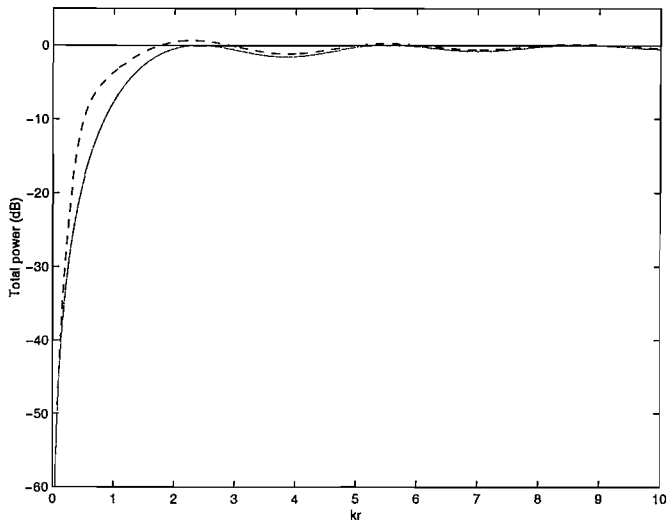

Figure 10.4 *Total power transmitted to an infinite plate, normalized to that due to the primary force only, when the primary and optimal secondary forces are applied (faint), and when the secondary force is replaced by a spring and a damper, whose stiffness and damping values are* $k_a = 1.2 \cdot 10^6$ *N/m and* $c_a = 1/Y_{00} = 323$ *N/ms*$^{-1}$ *(dashed).*

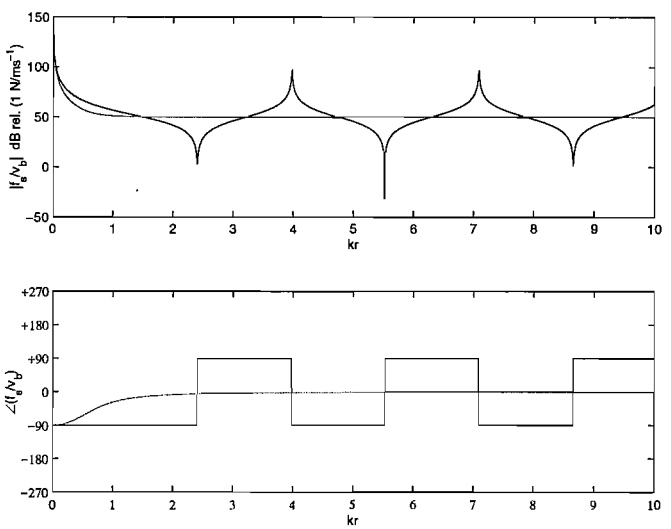

Figure 10.5 *Equivalent impedance due to the optimal solution (solid) and comparison with an impedance due to a spring and a damper whose stiffness and damping values are* $k_a = 1.2 \cdot 10^6$ *N/m and* $c_a = 1/Y_{00} = 323$ *N/ms*$^{-1}$ *(faint).*

In conclusion, when a secondary force is applied to an infinite plate to counteract the vibrations due to a primary force, the equivalent impedance of the optimal solution to the secondary force can be used to motivate a realisable passive approximation to the optimal active solution. This is given by the parallel combination of a spring and a damper. The stiffness approximates the behaviour of the optimal solution for small values of kr, while the damping approximates the frequency-averaged behaviour for greater values of kr, as shown in Figure 10.5. When the distance between primary and secondary forces is small compared with the flexural wavelength, the important part of the effective passive approximation to the optimal solution is thus the stiffness, while at greater distances, dissipating energy through a damper is the most effective way of controlling the power output. If calculations are performed with a number of primary forces having randomised phases, for which $kr > 1$ in each case, the optimal equivalent impedance, for minimum total power output, also tends to the driving point impedance of an infinite plate, Z_{00}. Since the equivalent impedance can no longer directly load the primary sources, its best strategy is to absorb power, and the impedance which absorbs the maximum power from a network is the conjugate of the network's driving point impedance (Elliott *et al.*, 1991). This is known as the matched load, and since Z_{00} is real in this case, the matched load is also equal to Z_{00}.

10.3 Equivalent impedance for global control of vibrating finite plates

In order to apply the optimal solution to a finite plate, we now examine a single point secondary force f_s acting in P_1 separated by a distance r from a point primary force acting in P_0, both forces being applied along the z-axis on a finite plate. This configuration is depicted in Figure 10.6. In the simulations it is assumed that the 700 x 500 x 1.85 mm (= l_x x l_y x h) plate is clamped on two opposite ends and free to move on the other two.

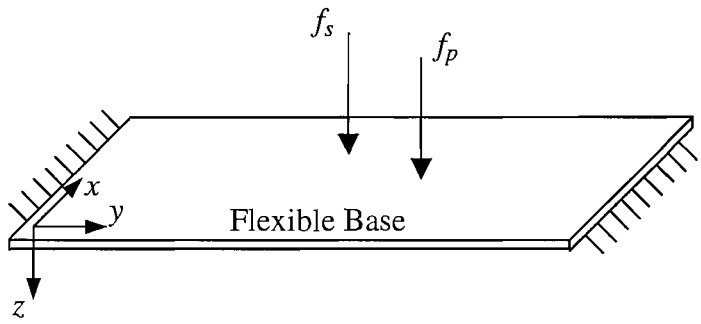

Figure 10.6 *A point primary force and a point secondary force applied to a finite 700 x 500 x 1.85 mm plate clamped on two opposite edges and free on the other two edges.*

These particular dimensions and boundary conditions were chosen to correspond to those of an experimental plate used in previous investigations (Benassi *et al.*, 2003a,b). Y_{00} is again the driving point mobility at $P_0 = (x_0, y_0)$, Y_{10} is the transfer mobility when the point of excitation is P_0 and the measurement occurs at $P_1 = (x_1, y_1)$, and Y_{11} is the driving point mobility at P_1. The driving point and transfer mobilities, relating the vertical velocity and the force excitation at the locations P_0 and P_1, can now be derived using a modal superposition approach (Soedel, 1993). The general expression for the mobility Y_{ij} when the force is applied in P_j and the velocity is measured in P_i is given by

$$Y_{ij} = \frac{j\omega}{M} \sum_{m=1}^{\infty} \sum_{n=1}^{\infty} \frac{\Phi_{mn}(P_i)\Phi_{mn}(P_j)}{\varepsilon_{mn}[\omega_{mn}^2(1+j\eta) - \omega^2]}, \tag{10.28}$$

where the indices m and n represent the number of half standing waves in the x and y directions for the natural mode Φ_{mn}. The term ε_{mn} is a normalising factor (Cremer *et al.*, 1988), M is the total mass of the plate, ω_{mn} is the m,n-th natural frequency of the flexural vibration and η is the hysteretic loss factor (Cremer *et al.*, 1988). The plate under study has two clamped edges and two free edges, therefore an exact solution of the wave equation and the boundary condition equations cannot be found. Thus an approximate solution must be used (Leissa, 1969). The expressions for the terms in equation (10.28) can be found in the work by Leissa (1969) and Bishop *et al.* (1960).

The cost function given by the sum of the power input due to the primary and secondary force, $\Pi = \Pi_p + \Pi_s$, can still be expressed in the quadratic form of equations (10.5) to (10.8) and thus be minimised with an optimum secondary force. The total power due to the primary force only, equation (10.9), is compared in Figure 10.7 with the total power described in equation (10.10) when the secondary force is given by the optimal solution described by equation (10.11). Figure 10.7 shows the power supplied to the finite plate due to the primary force only (solid line), applied at an arbitrary location P_0 = (0.32 m, 0.27 m), and due to the combination of the primary and optimal secondary force (faint line), applied at a distance r = 2 cm, at the location P_1 = (0.3059 m, 0.2841 m) from the primary. The reduction is substantial, with some of the modes being almost cancelled, while others are greatly reduced. This is due to the particular location that was chosen for the secondary force. At that location, the secondary force can couple into most modes, but this location is either on or close to the nodal lines of those modes that are not completely flattened out. The impedance that the secondary force has to present to the system in order to minimise the total power is obtained by computing the optimal secondary force per unit velocity at the secondary location, $\frac{f_{so}}{v_{so}}$. The velocity of the base v_{so} at P_1 when the optimal solution is implemented is given by

$$v_{so} = Y_{10} f_p + Y_{11} f_{so}. \tag{10.29}$$

Substituting equation (10.11) into equation (10.29), the equation becomes

$$v_{so} = Y_{10} f_p - Y_{11} \left(\frac{\mathrm{Re}(Y_{10})}{\mathrm{Re}(Y_{11})} \right) f_p, \tag{10.30}$$

which represents the velocity as a function of the primary force. Combining equations (10.11) and (10.30), the equivalent impedance when the optimal secondary force is implemented can be obtained. It is given by

$$Z_{opt} = \frac{f_{so}}{v_{so}} = \frac{\mathrm{Re}(Y_{10})}{\mathrm{Re}(Y_{10})Y_{11} - \mathrm{Re}(Y_{11})Y_{10}}. \tag{10.31}$$

This equivalent impedance, which is again entirely reactive, is shown in Figure 10.8, where it can be seen that sharp transactions occur between the stiffness dominated regions and the mass dominated regions. Between 0 and about 45 Hz, the impedance is stiffness dominated, as it is between about 60 Hz and 120 Hz, and between 155 Hz and 175 Hz. In the remaining intervals within the 0~200 Hz window, the impedance is mass dominated. As for the infinite plate case, this impedance is non-causal (Miller *et al.*, 1990) as it can be verified by computing the FFT of the result shown in Figure 8. Equation (10.31) can be rewritten as

$$Z_{opt} = \frac{1}{Y_{11} - \dfrac{\mathrm{Re}(Y_{11})}{\mathrm{Re}(Y_{10})}Y_{10}}, \tag{10.32}$$

where, from equation (10.28),

$$\mathrm{Re}(Y_{11}) = \sum_{m=1}^{\infty}\sum_{n=1}^{\infty} \frac{\Phi_{mn}^2(P_1)\omega\omega_{mn}^2\eta}{\Lambda_{mn}[(\omega_{mn}^2 - \omega^2)^2 + \eta\omega_{mn}^4]} \tag{10.33}$$

and

$$\mathrm{Re}(Y_{10}) = \sum_{m=1}^{\infty}\sum_{n=1}^{\infty} \frac{\Phi_{mn}(P_1)\Phi_{mn}(P_0)\omega\omega_{mn}^2\eta}{\Lambda_{mn}[(\omega_{mn}^2 - \omega^2)^2 + \eta\omega_{mn}^4]}. \tag{10.34}$$

At very low frequency the ratio between the real parts in equation (10.32) can be approximated by taking only the first modal term, in which case

$$\frac{\mathrm{Re}(Y_{11})}{\mathrm{Re}(Y_{10})} \cong \frac{\Phi_{11}(P_1)}{\Phi_{11}(P_0)}. \tag{10.35}$$

The mode shape of the first mode can be found in the work by Bishop and Johnson (1960), and at low frequency, for the chosen locations, from equation (10.35), then $\frac{\mathrm{Re}(Y_{11})}{\mathrm{Re}(Y_{10})} \cong 0.84$. At very low frequencies the driving point mobility Y_{11} can also be approximated by

$$Y_{11} \cong j\omega \frac{\Phi_{mn}^2(P_1)}{M\varepsilon_{mn}\omega_{mn}^2}, \tag{10.36}$$

where

$$\omega_{11} = \sqrt{\frac{Eh^2}{12\rho(1-\upsilon^2)}}\left(\frac{\pi}{l_x}\right)^2 q_{22}. \tag{10.37}$$

The expression for the coefficient q_{22} is provided by Bishop and Johnson (1960) and the normalising factor ε_{11} can be approximated using the factor for the free-free boundary condition, which is given by $\varepsilon_{11} \cong \frac{1}{4}$. Substituting the appropriate values in the above equations, a low frequency approximation to the equivalent impedance Z_{opt} in equation (10.32) is given by

$$Z_{opt} \cong \frac{\pi^4 Eh^3 l_y q_{22}^2}{j\omega 48(1-\upsilon^2) l_x^3 \Phi_{11}(P_1)\left[\Phi_{11}(P_1) - 0.84\Phi_{11}(P_0)\right]} \cong \frac{9\cdot 10^6}{j\omega}. \tag{10.38}$$

As well as the equivalent impedance in the optimal case, Figure 10.8 also shows the low-frequency approximation to the impedance given by a spring, whose stiffness is $k_a = 9\cdot 10^6$ N/m.

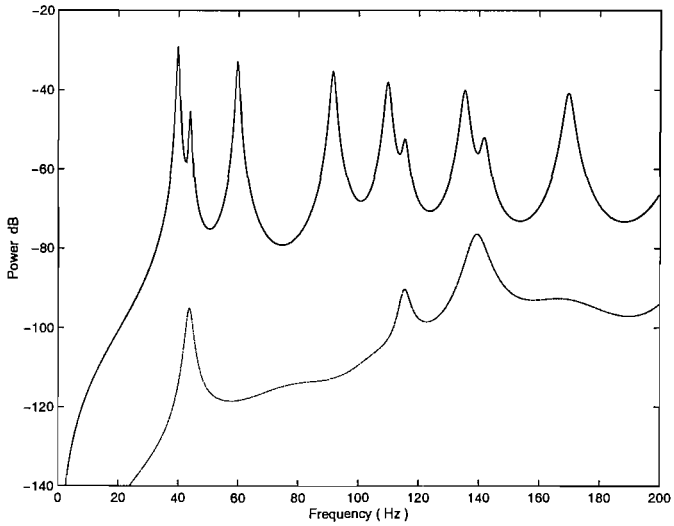

Figure 10.7 *Total power transmitted to the finite plate due to the primary force only (solid) and due to the primary and secondary forces when the optimal feedforward solution is applied and the distance between primary and secondary force is 2 cm (faint).*

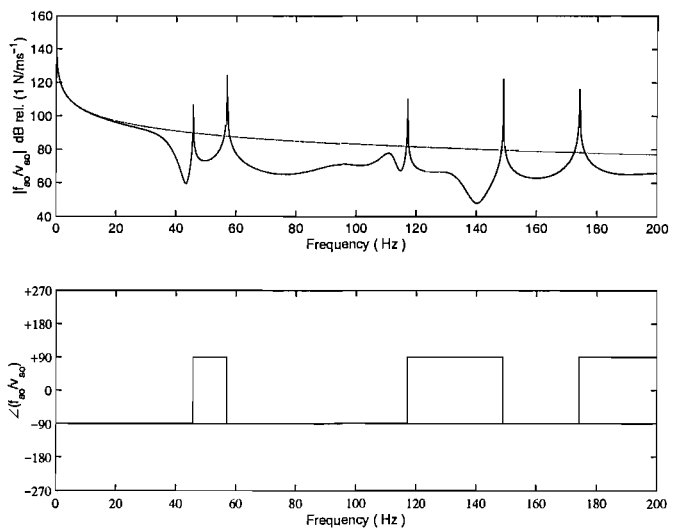

Figure 10.8 *Equivalent impedance due to the optimal secondary force (solid) and the impedance of an ideal stiffness whose value is* $k_a = 9 \cdot 10^6$ *N/m (faint). The distance between primary and secondary force is 2 cm and the plate is finite. It can be noted that the real part of the impedance is zero.*

When the distance r is equal to 20 cm, not as much attenuation in the total power is obtained, as shown in Figure 10.9, which is calculated for the case where P_0 = (0.32 m, 0.27 m) and P_1 = (0.179 m, 0.411 m). The optimal impedance also has lower average values, compared to the case when r = 2, as shown in Figure 10.10, which also shows the impedance of a spring, whose stiffness is $k_a = 2.5 \cdot 10^5$ N/m, that has been computed in an analogous way to that above.

When the relative distance between primary and secondary forces is large and at low frequency, the driving point mobility dominates the transfer mobility in equation (10.32). Hence, when $|Y_{11}| >> |Y_{10}|$ then $Z_{opt} \cong Z_{11} = \frac{1}{Y_{11}}$. Equation (10.36) provides the approximation of the expression for the driving point mobility at low frequency and it is equivalent to a stiffness of about $7 \cdot 10^4$ N/m. In the simulations, this is the value of the stiffness that approximates the low frequency behaviour when the relative distance r = 80 cm.

At high frequency or large relative distances r, the characteristic driving point or transfer mobility are equal to the driving point or transfer mobility of an infinite plate (Skudrzyk, 1968). Consequently, equation (10.12) and equation (10.13) describe the real part of the driving point and transfer mobility for an infinite plate, while equation (10.1), equation (10.2) and equation (10.3) describe the remaining terms to be used in equation (10.32) to compute the high-kr approximation to the equivalent impedance, which is found to oscillate about a value which is equal to the infinite plate driving impedance. Assuming a constant location of the secondary force, and varying the location of the primary force on the plate, it is found that for small relative distances between the primary and secondary forces, the average of the optimal equivalent impedance above 40 Hz can be approximated using a larger damper, whose maximum damping value was found to be about c_a = 4,000 N/ms^{-1} when the distance r = 2 cm. For large distances between primary and secondary forces the averaged equivalent impedance can be approximated using lower values of the damping. The minimum value that was found is about c_a = 323 N/ms^{-1} when the distance r = 80 cm, as expected from the above discussion. This indicates that even for finite plates, a simplified approximation to the equivalent impedance is given by the parallel of a spring and a damper.

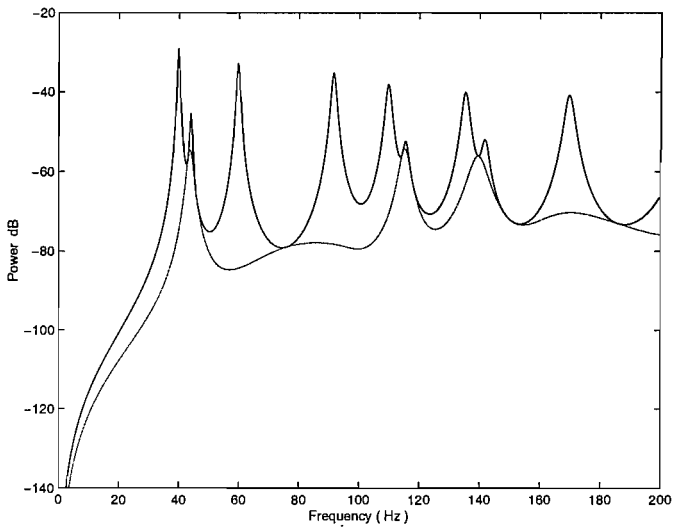

Figure 10.9 *Total power transmitted to the finite plate due to the primary force only (solid) and due to the primary and secondary forces when the optimal feedforward solution is applied and the distance between primary and secondary force is 20 cm (faint).*

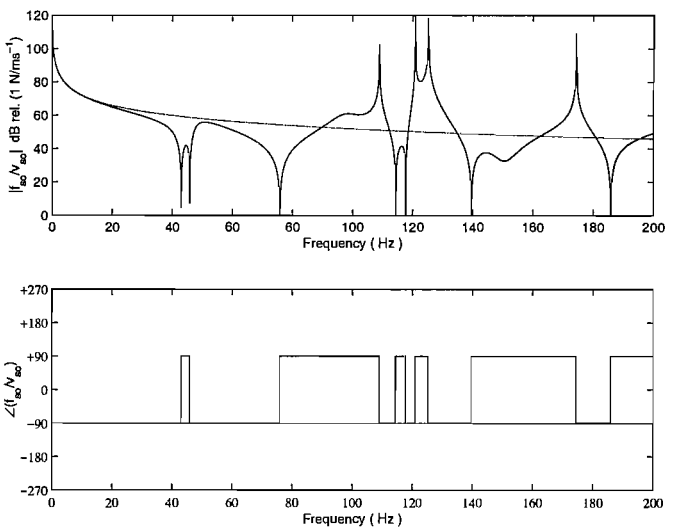

Figure 10.10 *Equivalent impedance due to the optimal secondary force (solid) and the ideal stiffness whose value is* $k_a = 2.5 \cdot 10^5$ *N/m. The distance between primary and secondary force is 20 cm and the plate is finite. It can be noted that the real part of the impedance is zero.*

10.4 Optimising the spring/damper approximation to the equivalent impedance

The primary drawback of the optimal equivalent impedance shown in Figure 10.8 and Figure 10.10 is that it is non-causal and so cannot be implemented with broadband random excitations. Therefore, other solutions have been investigated even though their performance will be worse than that one provided by the optimal solution. In this section, the combination of an optimum stiffness and a damper will be analysed. Firstly, the two solutions are investigated independently, then they will be considered together, acting in parallel on the finite plate (Benassi and Elliott, 2003c). The relative distance, r, between primary and secondary forces is assumed to be 2 cm for these simulations.

10.4.1 Control with a spring

Figure 10.11 shows the ratio of the frequency-averaged power P, as defined above, as a function of stiffness. The function descends monotonically until it flattens off at about $k_a = 9 \cdot 10^6$ N/m, which indicates the minimum value of stiffness that provides the greatest attenuation in power (about 14 dB). At low values of the stiffness, the ratio of the frequency averaged power is very steep. Figure 10.12 shows the total power when the stiffness is chosen to be $k_a = 9 \cdot 10^6$ N/m (dashed line), compared to the optimal solution (faint line) and the uncontrolled case (solid line). It can be noted that high attenuations can be achieved at low frequency due to the similarity between optimal solution and passive equivalent approximation. Although $k_a = 9 \cdot 10^6$ N/m seems to be a good choice at low frequency, as discussed above, at higher frequency its effect is merely to pin the structure at the secondary location and therefore only a redistribution of the resonances is experienced.

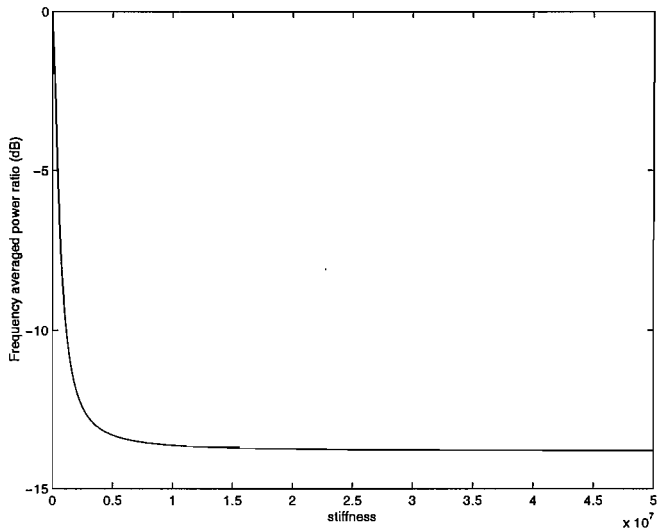

Figure 10.11 *Ratio of the frequency averaged power between power of the uncontrolled and controlled plate, as a function of the stiffness value* k_a. *After about* $k_a = 9 \cdot 10^6$ *N/m, the average power ratio does not improve much. The distance between primary and secondary forces is 2 cm.*

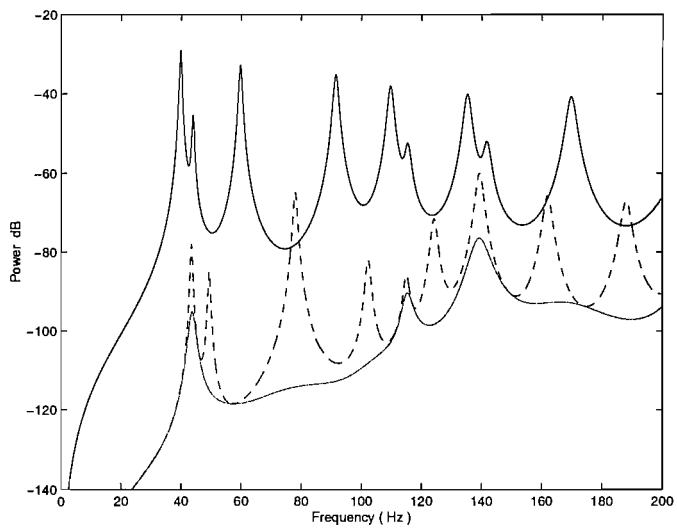

Figure 10.12 *Total power transmitted to the finite plate due to the primary force only (solid), the primary and secondary forces when the optimal feedforward solution (faint), and the primary and secondary forces when the ideal displacement feedback is implemented and the stiffness is* $k_a = 9 \cdot 10^6$ *N/m (dashed). The distance between primary and secondary force is 2 cm.*

10.4.2 Control with a damper

Figure 10.13 shows the ratio of the frequency averaged power as a function of damping c_a introduced at P_1. The minimum of the function at about c_a = 4,000 N/ms^{-1} is –14.5 dB, and it indicates the value of damping that provides the greater attenuation in terms of power. At low gains, the frequency averaged power is very steep then, after reaching a minimum value, it settles towards the constant value –14 dB, which indicates that the system is pinned and it does not benefit from higher damping values. This limiting value is the same as that in Figure 10.11. Figure 10.14 shows the total power when c_a = 4,000 N/m (dashed line), compared to the optimal solution (faint line) and the uncontrolled case (solid line). Compared to Figure 10.12, lower attenuations are experienced below the first plate resonance and higher attenuations can be achieved at high frequency.

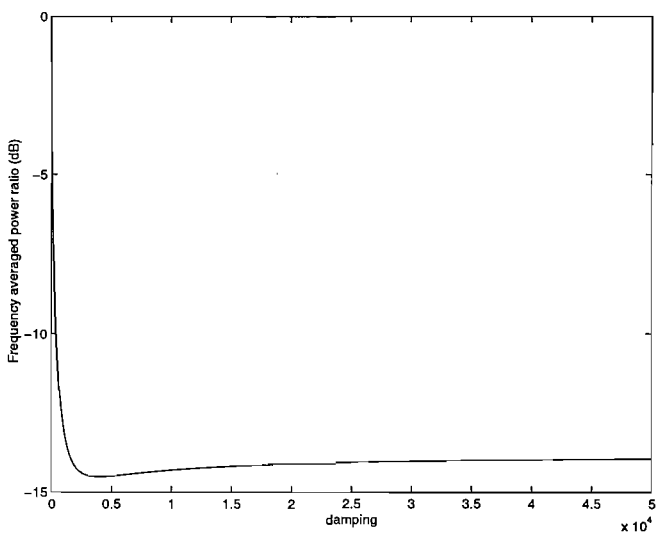

Figure 10.13 *Ratio of the frequency averaged power between power of the uncontrolled and controlled plate, as a function of the damping value c_a. The minimum of the function at about c_a = 4,000 N/ms^{-1} indicates the value of the gain that provides the greater attenuation in terms of power. The distance between primary and secondary forces is 2 cm.*

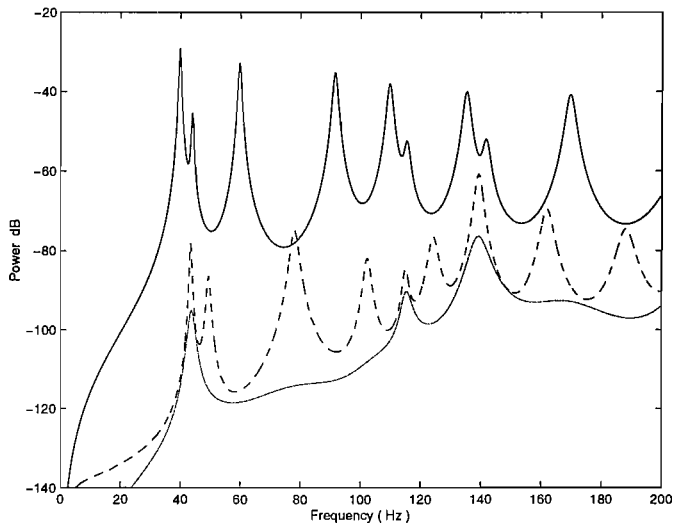

Figure 10.14 *Total power transmitted to the finite plate due to the primary force only (solid), the primary and secondary forces when the optimal feedforward solution is applied (faint), and the primary and secondary forces when the ideal velocity feedback is applied and the damping value* c_a *= 4,000 N/ms*$^{-1}$ *(dashed). The distance between primary and secondary force is 2 cm.*

10.4.3 Control with a spring and a damper

We now assume that the secondary force is generated by a spring and a damper, whose values are chosen by a joint optimisation. Figure 10.15 shows the contour plot of the ratio of the frequency-averaged power as a function of damping and stiffness. The ratio is maximum at the origin, after which it descends. The minimum of the function (about –14.62 dB) occurs when the damping value $c_a = 4{,}000$ N/ms^{-1}, which coincides with the minimum of the curve in Figure 10.13, and the stiffness value $k_a = 5.5 \cdot 10^5$ N/m. Figure 10.16 shows both the equivalent impedance of the optimal solution and the impedance of the chosen spring-damper system. In particular, the passive approximation does not match the equivalent impedance at low frequency, and this is due to the particular choice made for the stiffness, which minimises the frequency averaged power. Figure 10.17 shows the total power when the chosen spring-damper system is applied (dashed line). Compared to Figure 10.14, the system clearly benefits at low frequency from the stiffness, and above the first plate resonance, it benefits from the energy that has been taken away by the damper. Compared to Figure 10.12 and Figure 10.14, this case provides a better performance.

In summary, although the power reduction due to the parallel of a stiffness term and a damping term is greater than the results obtained by using either a spring or a damper, the difference in frequency averaged power between the parallel case and the single cases is not substantial. This result holds for the case where the relative distance between primary and secondary forces is relatively small and the frequency band of interest includes low and higher frequency components. These conditions are often met in practical vibration attenuation problems, while for limit cases, at very low or very high frequency, or very short or very long relative distances, as discussed above, the equations derived previously are valid.

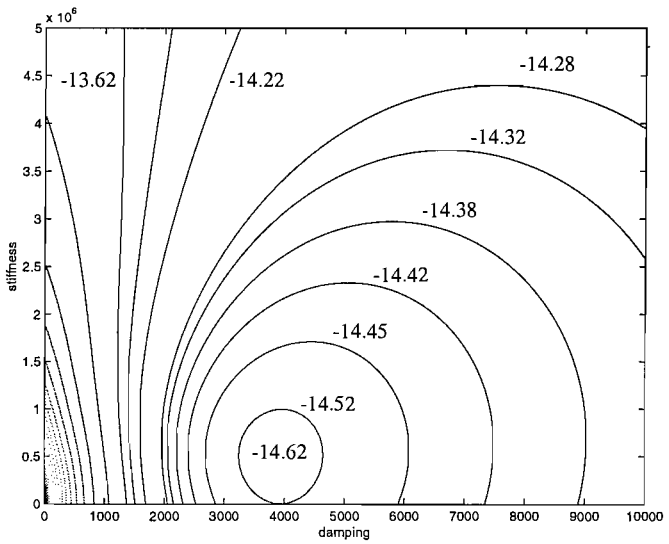

Figure 10.15 *Contour plot of the ratio of the frequency averaged power between power of the uncontrolled and controlled plate, as a function of the damping value c_a and the stiffness value k_a . The minimum of the function at –14.62 dB occurs when c_a = 4,000 N/ms^{-1} and k_a = $5.5 \cdot 10^5$ N/m. The distance between primary and secondary forces is 2 cm.*

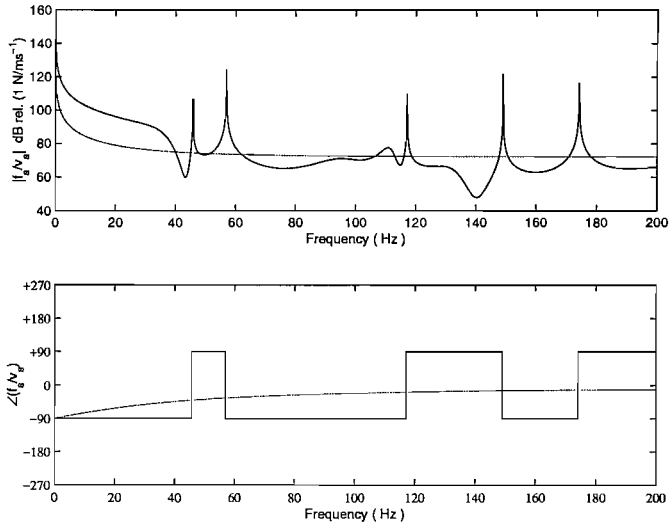

Figure 10.16 *Equivalent impedance due to the optimal secondary force (solid) and the ideal displacement and velocity feedback control, where the stiffness value* $k_a = 5.5 \cdot 10^5$ *N/m and the damping value* c_a = *4,000 N/ms*$^{-1}$ *(dashed). The distance between primary and secondary force is 2 cm.*

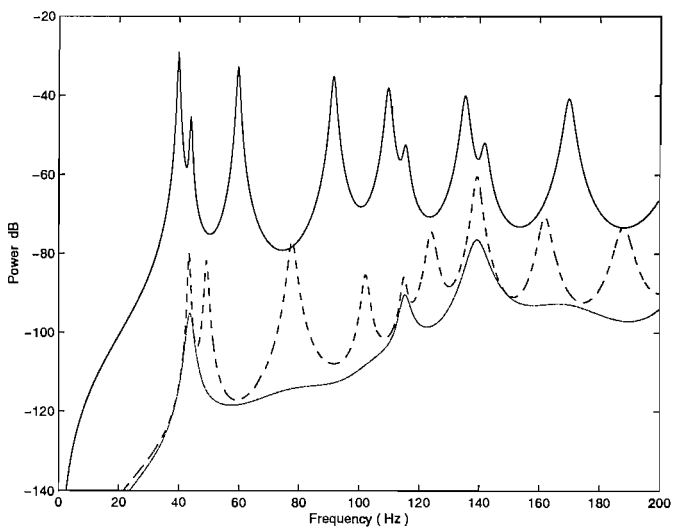

Figure 10.17 *Total power transmitted to the finite plate due to the primary force only (solid), the primary and secondary forces when the optimal feedforward solution is applied (faint), and the primary and secondary forces when the ideal displacement and velocity feedback is applied, where the stiffness value* $k_a = 5.5 \cdot 10^5$ *N/m and the damping value* c_a = *4,000 N/ms*$^{-1}$ *(dashed). The distance between primary and secondary force is 2 cm.*

10.5 Conclusions

In this study the total power supplied to the structure by a primary and secondary force was chosen to be the cost function to be minimised. In particular, the effect of the distance between primary and secondary excitations was taken into account and simulated for both infinite and finite plates.

The core of this study was the comparison between optimal solutions and the performance of idealised passive control treatments. In particular, the optimised equivalent impedance for global control was compared with its passive approximation. It was found that, although the equivalent impedance is able to provide a substantial total power reduction compared to the other treatments, ideal passive solutions, based on the parallel configuration of a spring and a damper, can guarantee a good power reduction. The locations of the primary and secondary excitations and their relative distance may become an important aspect of the design of the panel vibration controller. In fact, depending on the location of the primary force with respect to the nodal lines, the power distribution of the uncontrolled system changes and, depending on the location of the secondary force with respect to the nodal lines, the optimal solution turns out to be more or less effective. Unfortunately, in many practical applications a rigid ground is not available and therefore these solutions cannot be implemented. The use of inertial actuators to provide substantial attenuation in panel vibration is analysed in the next chapter.

Chapter 11

Global control of a vibrating plate using an inertial actuator

11.1 Introduction

The objective of this chapter is to compare the results obtained in the previous chapter with solutions obtained using inertial actuators for active vibration control. In order to understand the implications and the consequences of using inertial actuators, in this study we will be limited to using only one device.

11.2 Approximated equivalent impedance for global control of vibrating finite plates

11.2.1 Mass-spring-damper system on flexible plate

Figure 11.1 shows the case where a passive system, comprising a mass, spring and a damper, is installed upon the plate at P_1 = (0.3059 m, 0.2841 m), 2 cm from the primary force at P_0 = (0.32 m, 0.27 m). The values that were used in the simulations for the passive system corresponded to those of the modified ULTRA actuator and were m_a = 0.24 Kg, c_a = 18 N/ms^{-1} and k_a = 2000 N/m, where m_a is the proof-mass, c_a is the damping of the passive system and k_a is its stiffness.

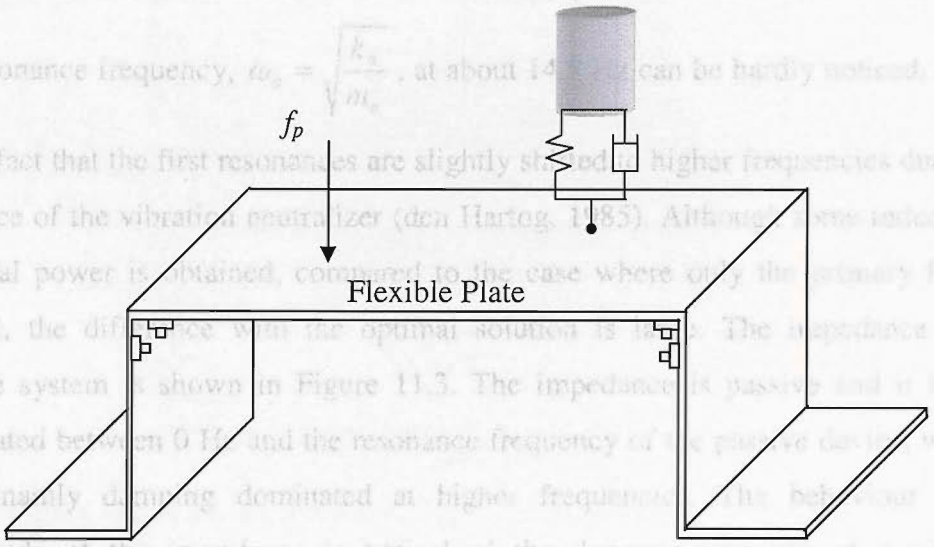

Figure 11.1 *A point primary force and a point secondary force, obtained through a mass-spring-damper system, applied to a finite 700 x 500 x 1.85 mm plate. The plate is clamped on two opposite edges and free on the other two edges.*

The transmitted force, f_t , exerted by a mass-spring-damper system is equal to the secondary force f_s and it is given by equation (2.6)

$$f_s = f_t = -\frac{j\omega m_a k_a - \omega^2 m_a c_a}{k_a + j\omega c_a - \omega^2 m_a} v_b = -Z_{open} v_b \ . \tag{11.1}$$

The velocity, v_b , of the base at P_1 is given by

$$v_b = Y_{10} f_p + Y_{11} f_t = Y_{10} f_p - Y_{11} Z_{open} v_b \ , \tag{11.2}$$

which can be rewritten as

$$v_b = \frac{Y_{10}}{1 + Y_{11} Z_{open}} f_p \ . \tag{11.3}$$

The total power Π, described by equation (10.4), is shown in Figure 11.2 and in particular the dashed line shows the effect of the passive controller. The addition of the resonance frequency, $\omega_a = \sqrt{\frac{k_a}{m_a}}$, at about 14.5 Hz can be hardly noticed, as well as the fact that the first resonances are slightly shifted to higher frequencies due to the presence of the vibration neutralizer (den Hartog, 1985). Although some reduction in the total power is obtained, compared to the case where only the primary force is present, the difference with the optimal solution is large. The impedance of the passive system is shown in Figure 11.3. The impedance is passive and it is mass dominated between 0 Hz and the resonance frequency of the passive device, whereas it is mainly damping dominated at higher frequencies. The behaviour of the magnitude of the impedance is typical of the dynamic response of a vibration neutralizer, which is quite different from the optimal solution in Figure 10.7. This difference in the impedance presented to the system explains the considerable difference in performance, together with the fact that the damping value of the actuator is 18 N/ms^{-1}, which is much less than that calculated in Section 10.4.3 that is required for optimal control (4000 N/ms^{-1}).

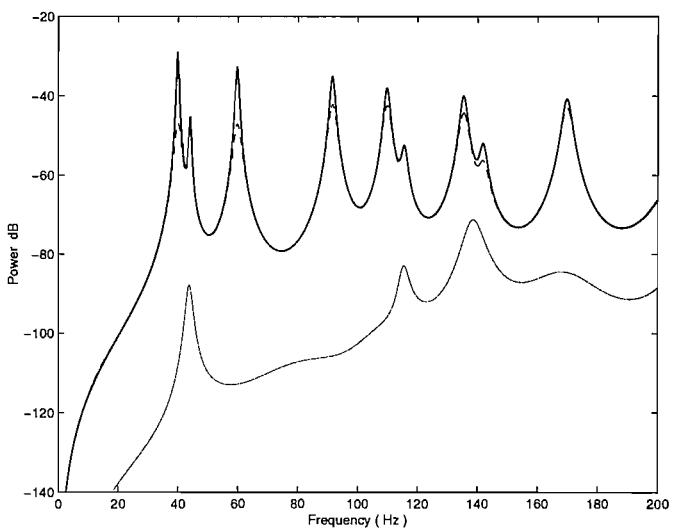

Figure 11.2 *Total power transmitted to the finite plate due to the primary force only (solid), the primary and secondary forces with the optimal feedforward solution (faint), and the primary and secondary forces when the mass-spring-dashpot system with no other inner loop is applied (dashed). The distance between primary and secondary force is 2 cm.*

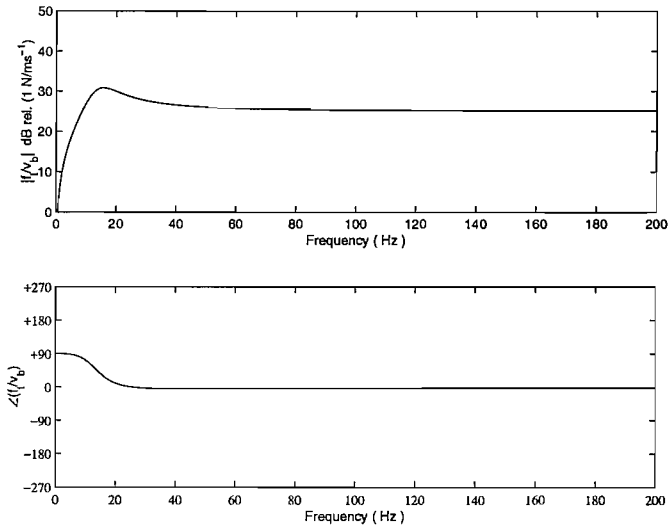

Figure 11.3 *Mechanical impedance of the mass-spring-dashpot system.*

11.2.2 Inertial actuator with inner actuator displacement feedback and outer equipment velocity feedback

Figure 11.4 illustrates the case where a modified inertial actuator, based on an inertial actuator with inner displacement feedback, described in Chapter 4, is installed on the plate at a distance from the primary force of 2 cm. The measurement of the displacement of the proof-mass relative to the inertial actuator's base is connected to the usual PID controller, which modifies the frequency response of the actuator. The values within the PID controller that were used in the simulations are: proportional gain g_P = -1000, integral gain g_I = 10,000, and differential gain g_V = 18.

The secondary force f_s is equal to the transmitted force f_t exerted by the device and its equation, as a function of the command signal, f_c, and the plate velocity at P_1, v_b, is given by equation (4.12)

$$f_s = f_t = \frac{-\omega^2 m_a}{-\omega^2 m_a + j\omega c_a + k_a + g_P + \frac{g_I}{j\omega} + j\omega g_V} f_c - \frac{\left(j\omega m_a k_a - \omega^2 m_a c_a\right)\cdot\left(g_P + \frac{g_I}{j\omega} + j\omega(g_V + Z_a)\right)}{\left(-\omega^2 m_a + j\omega c_a + k_a + g_P + \frac{g_I}{j\omega} + j\omega g_V\right) j\omega Z_a} v_b \quad , \tag{11.4}$$

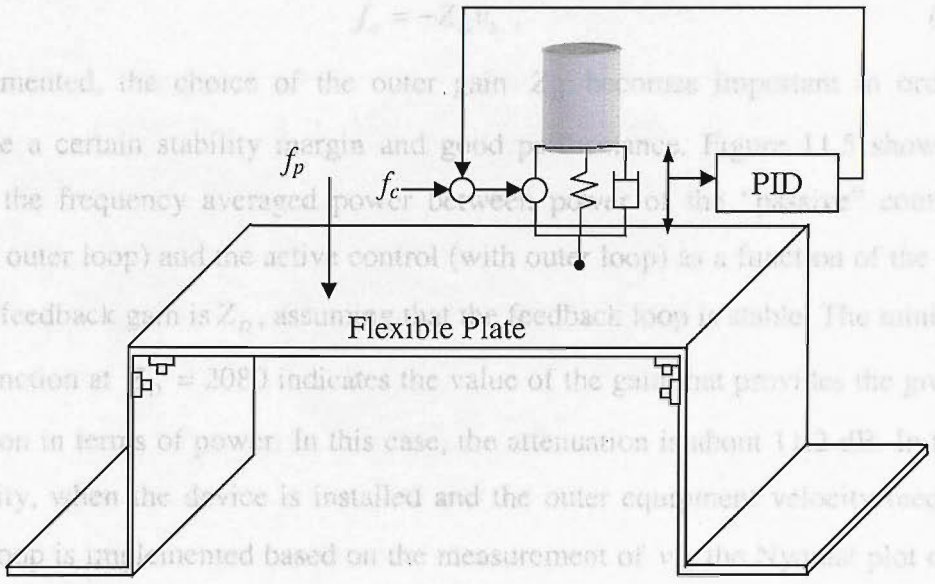

Figure 11.4 *A point primary force and a point secondary force, obtained through the modified inertial actuator, applied to a 700 x 500 x 1.85 mm plate. The plate is clamped on two opposite edges and free on the other two edges.*

where $Z_a = c_a + \frac{k_a}{j\omega}$. The command force, f_c, will be used to implement the outer velocity feedback control loop. Equation (11.4) can be grouped as

$$f_t = T_a^{'} f_c - Z_a^{'} v_b \ , \tag{11.5}$$

where $T_a^{'}$ and $Z_a^{'}$ are the blocked response and mechanical impedance of the actuator, as modified by the inner displacement feedback. The base velocity at P_1 is given by

$$v_b = Y_{10} f_p + Y_{11} f_t \ . \tag{11.6}$$

Substituting equation (11.5) into equation (11.6) the base velocity is computed as a function of the primary force f_p and the control command f_c

$$v_b = \frac{Y_{10}}{1 + Y_{11} Z_a^{'}} f_p + \frac{Y_{11} T_a^{'}}{1 + Y_{11} Z_a^{'}} f_c \ . \tag{11.7}$$

When the outer velocity feedback loop, described by

$$f_c = -Z_D v_b \ , \tag{11.8}$$

is implemented, the choice of the outer gain Z_D becomes important in order to guarantee a certain stability margin and good performance. Figure 11.5 shows the ratio of the frequency averaged power between power of the "passive" controller (without outer loop) and the active control (with outer loop) as a function of the outer velocity feedback gain is Z_D, assuming that the feedback loop is stable. The minimum of the function at $Z_D = 2080$ indicates the value of the gain that provides the greatest attenuation in terms of power. In this case, the attenuation is about 11.2 dB. In terms of stability, when the device is installed and the outer equipment velocity feedback control loop is implemented based on the measurement of v_b, the Nyquist plot of the second term of equation (11.7) provides the means to determine the stability of the closed loop system. The theoretical active controller becomes unstable when the outer velocity feedback gain is greater than 2410, as shown by the Nyquist plot in Figure 11.6. In the simulations, a velocity feedback gain of $Z_D = 150$ was chosen in order to guarantee a 6 dB stability margin when the additional phase shifts present in the experimental system are accounted for. This implies, from Figure 11.5, that an attenuation of about 4 dB is achieved.

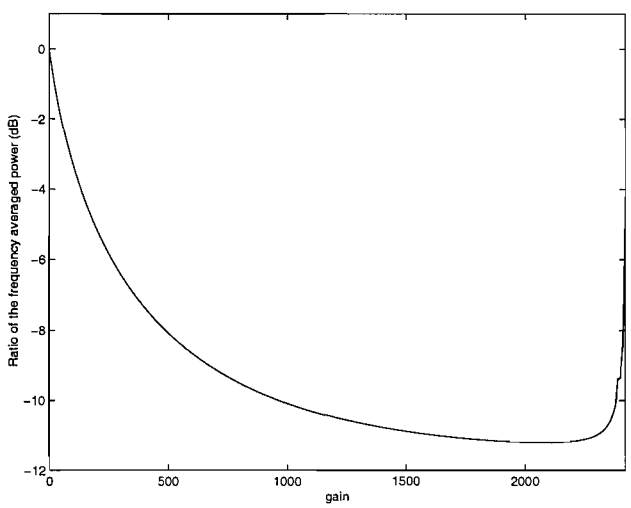

Figure 11.5 *Ratio of the frequency averaged total power transmitted to the plate with the modified actuator before and after the outer feedback loop is implemented, as a function of the outer velocity feedback gain Z_D. The minimum of the function at Z_D = 2080 indicates the value of the gain that provides the greatest attenuation (about 11.2 dB) in terms of power. The active controller becomes unstable for outer velocity gains Z_D > 2410. The distance between primary and secondary forces is 2 cm.*

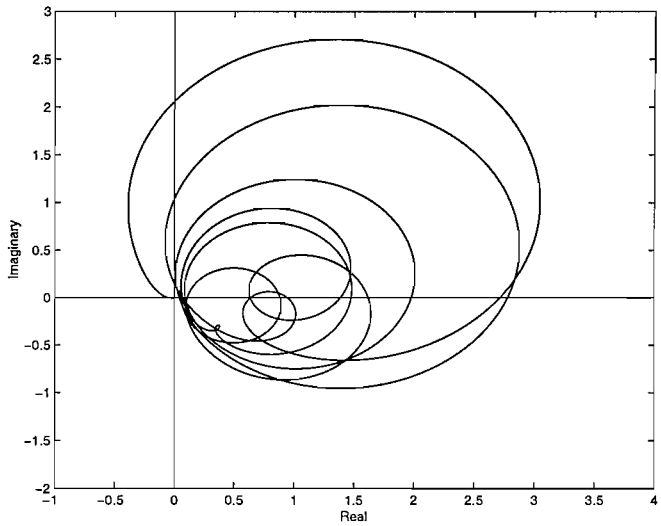

Figure 11.6 *Nyquist plot of the idealised open loop system when the modified inertial actuator is applied and an outer velocity feedback control loop is implemented. The distance between primary and secondary force is 2 cm and the plate is finite. The values within the PID controller that were used in the simulations are:* g_P *= -1,000,* g_I *= 10,000,* g_V *= 18, and the outer velocity feedback gain* Z_D *= 150.*

When the outer velocity feedback loop in equation (11.8) is implemented, the base velocity, described in equation (11.7), becomes

$$v_b = \frac{Y_{10}}{1 + Y_{11} Z_a^{'} + Y_{11} T_a^{'} Z_D} f_p \ . \tag{11.9}$$

Substituting equation (11.8) into equation (11.4), the transmitted force, f_t, as a function of the bas velocity, v_b, is given by

$$f_t = -\frac{\left(j\omega m_a k_a - \omega^2 m_a c_a\right)\cdot\left(g_P + \frac{g_I}{j\omega} + j\omega(g_V + Z_a)\right) - j\omega^3 Z_a Z_D}{\left(-\omega^2 m_a + j\omega c_a + k_a + g_P + \frac{g_I}{j\omega} + j\omega g_V\right) j\omega Z_a} v_b \ . \tag{11.10}$$

Once the base velocity in equation (11.9) is computed, then the transmitted force in equation (11.10) can be obtained and therefore the total power can be calculated. This

is plotted in Figure 11.7, where it can be noted that the reduction of the total power due to the modified inertial actuator (dashed line) is greater than the results obtained with the passive treatment, shown in Figure 11.2. Although the difference with the optimal solution is still large, useful reductions in power are predicted, which shows that the modified inertial actuator can be used effectively in reducing the vibration of panels. The impedance presented by the active mount to the system is given by equation (11.10), which is plotted in Figure 11.8. The impedance is not passive, unlike the previous case, and it is mainly damping dominated at frequencies greater than the inertial actuator's resonance frequency. As explained in Chapter 4, this is due to the choice of the inner feedback gains, and in particular the derivative term within the PID controller. In conclusion, the modified inertial actuator with outer velocity feedback loop is an effective way of adding damping to the system.

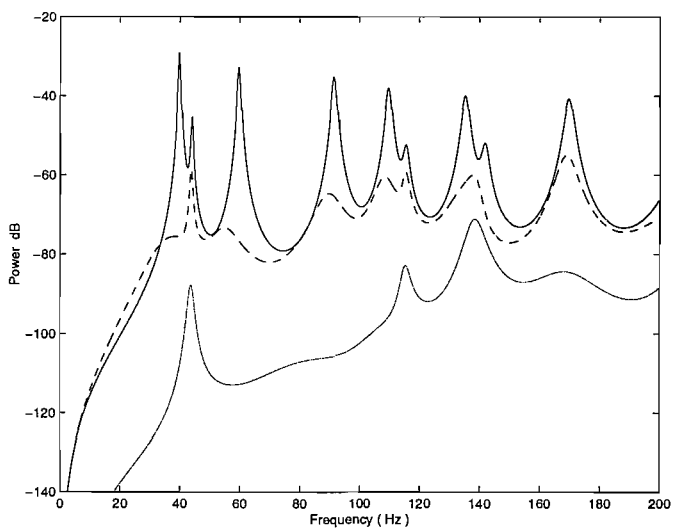

Figure 11.7 *Total power transmitted to the finite plate due to the primary force only (solid), the primary and secondary forces when the optimal feedforward solution is applied (faint), and when the feedback system, based on the modified inertial actuator and an outer feedback loop with* Z_D *= 150, is applied (dashed). The distance between primary and secondary force is 2 cm.*

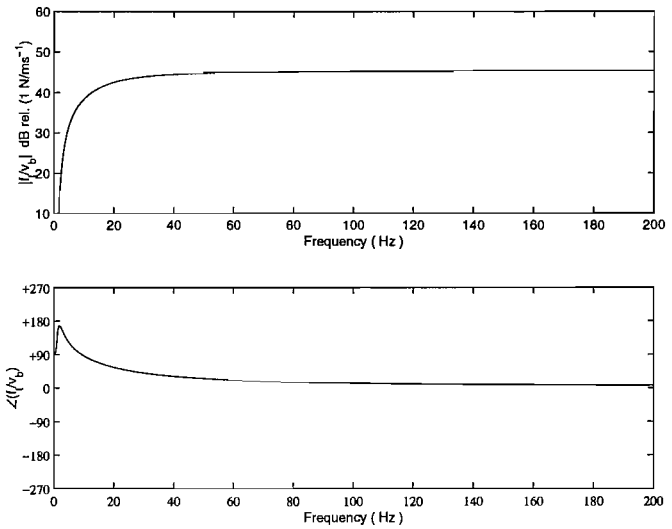

Figure 11.8 *Mechanical Impedance of the inertial actuator with inner and outer feedback loops when the inner displacement feedback control and the outer velocity feedback control are implemented. In particular,* g_P *= -1000,* g_I *= 10,000,* g_V *= 18 and* Z_D *= 150.*

When the outer control gain Z_D is chosen to be the equivalent impedance described in equation (10.31), the control system turns out to be unstable. If the outer feedback controller is an integrator of the form $Z_D = \frac{k_D}{j\omega}$, interesting results are obtained. Choosing such a control impedance implies that only the first part of the optimal impedance in equation (10.31) is considered. In other words, k_D is chosen to be the low frequency passive approximation of the optimal solution. In particular, when k_D = 550,000 N/m (the same value was chosen as the passive approximation for this system in the previous chapter), the closed loop system turns out to be conditionally stable, and a 6 dB stability margin is guaranteed. This is shown in the Nyquist plot in Figure 11.9, where the curve at low frequency intersects the real axis at about –0.5.

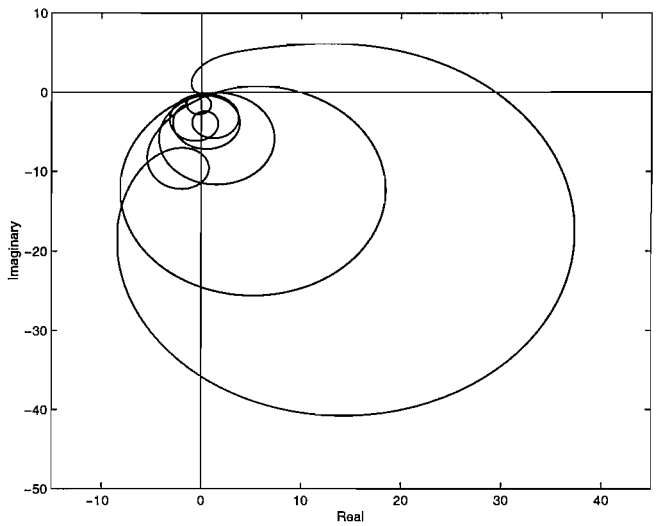

Figure 11.9 *Predicted Nyquist plot of the open loop system when the modified inertial actuator is applied and an outer feedback control loop, based on an integrator of the form $Z_D / j\omega$, is implemented. The distance between primary and secondary force is 2 cm and the plate is finite. The values within the PID controller that were used in the simulations are: g_P = -1,000, g_I = 10,000, g_V = 18, and the outer feedback gain $Z_D = \frac{k_D}{j\omega}$ whre $k_D = 550{,}000$.*

The total power for this case is plotted in Figure 11.10, where the reduction of the total power due to the modified inertial actuator and the outer controller, based on the passive approximation of the optimal solution, is quite outstanding and not very dissimilar from the optimal solution. At low frequency, attenuations of more than 40 dB can be obtained, which indicates that the panel vibrations are almost suppressed. Unfortunately in real systems, due to low frequency phase shifts of the electronic components (Brennan *et al.*, 2002), the stability margin of the system is greatly reduced and the performance of the closed loop system is not dissimilar to the outer velocity feedback case. By considering an outer feedback controller of the form $Z_D = \frac{k_D}{j\omega}$, stiffness is added to the system (also illustrated in the impedance plot in Figure 11.11) and this implies that the peaks in Figure 11.10 are moved to higher frequencies. This is beneficial in the low frequency range, but those peaks are not suppressed, they are simply moved to higher frequencies. Also, a portion of the inertial actuator resonance which occurs at low frequency is greatly amplified because of the integral velocity feedback control law. The impedance presented to the system is plotted in Figure 11.12. It is not passive, and it is mainly stiffness dominated,

except at very low frequency, where a phase shift occurs. The magnitude of the impedance is "that of the dynamic response of a vibration neutralizer", which is quite different from the optimal solution in Figure 10.7.

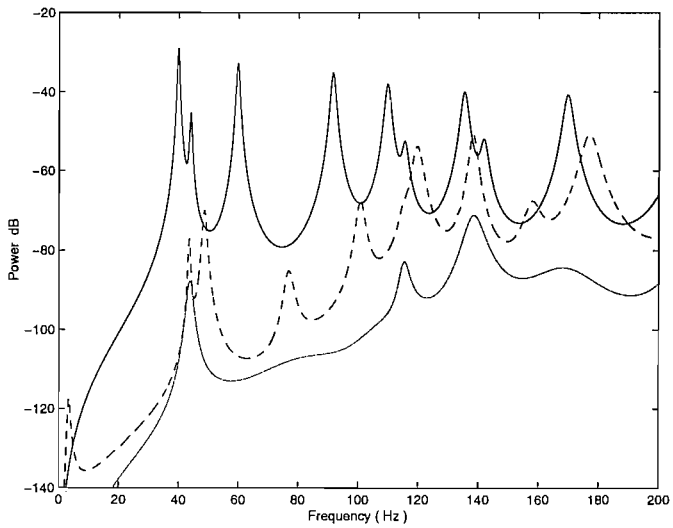

Figure 11.10 *Total power transmitted to the finite plate due to the primary force only (solid), the primary and secondary forces with the optimal feedforward solution (faint), and the primary and secondary forces when the modified inertial actuator and the outer feedback controller, based on a passive approximation of the optimal solution* $Z_D = k_D / (j\omega)$ *with* $k_D = 550{,}000$, *are applied (dashed). The distance between primary and secondary force is 2 cm.*

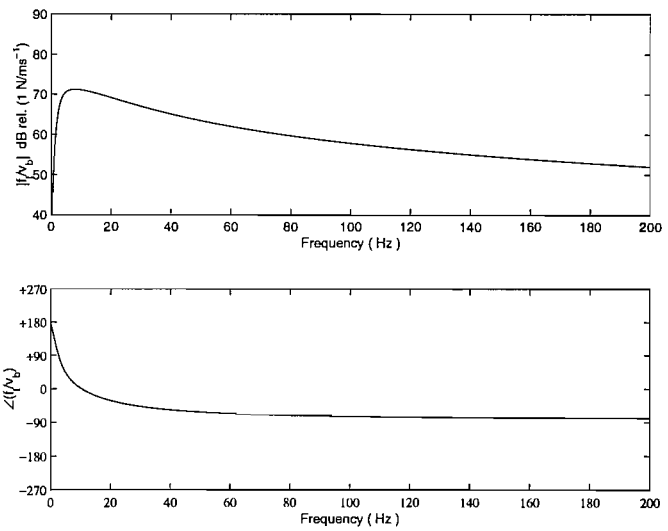

Figure 11.11 *Mechanical Impedance of the inertial actuator with inner and outer feedback loops when the inner displacement feedback control and the outer integral feedback control are implemented. In particular,* g_P = -1000, g_I = 10,000, g_V = 18 *and* $Z_D = k_D / (j\omega)$ *where* k_D = 550,000.

11.3 Experiments on active vibration suppression with the modified inertial actuator

In this section we consider the practical use of an inertial actuator with inner feedback for the active suppression of a vibrating flexible plate. The arrangement is illustrated in Figure 11.12. It consists of the flexible steel plate 700mm × 500mm × 1.85mm, clamped on the two longer sides, as described in Chapter 7 and Chapter 9, on which is mounted a modified inertial actuator. The primary force is provided by an LDS Ling 401 shaker, placed underneath the plate. The inertial actuator used for the experiments to produce the control force was a mechanically modified version of an active tuned vibration absorber (ATVA) manufactured by ULTRA Electronics, described in detail by Hinchliffe *et al.*, 2002 and shown in Figure 11.12, from which the internal springs were removed, leaving the proof-mass (m_a = 0.24 Kg) attached to the case by eight thin flexible supports. This modification in the stiffness (so that k_a = 2000 N/m) changed the actuator resonance frequency from 73.8 Hz to 14.5 Hz, as described in Chapter 4. The measured damping ratio was used to estimate the damping factor as c_a = 18 N/ms^{-1}. An inner displacement feedback loop is used to modify the response of the inertial actuator, as discussed above, and an outer velocity feedback system is used to provide active skyhook damping for the equipment. The values of the gains within the PID controller were chosen in order to provide a modified inertial actuator with the characteristics described in Section 3.2. In this experimental configuration, an outer velocity feedback control gain $Z_D = 150$ was chosen, which guarantees a 6 dB stability margin.

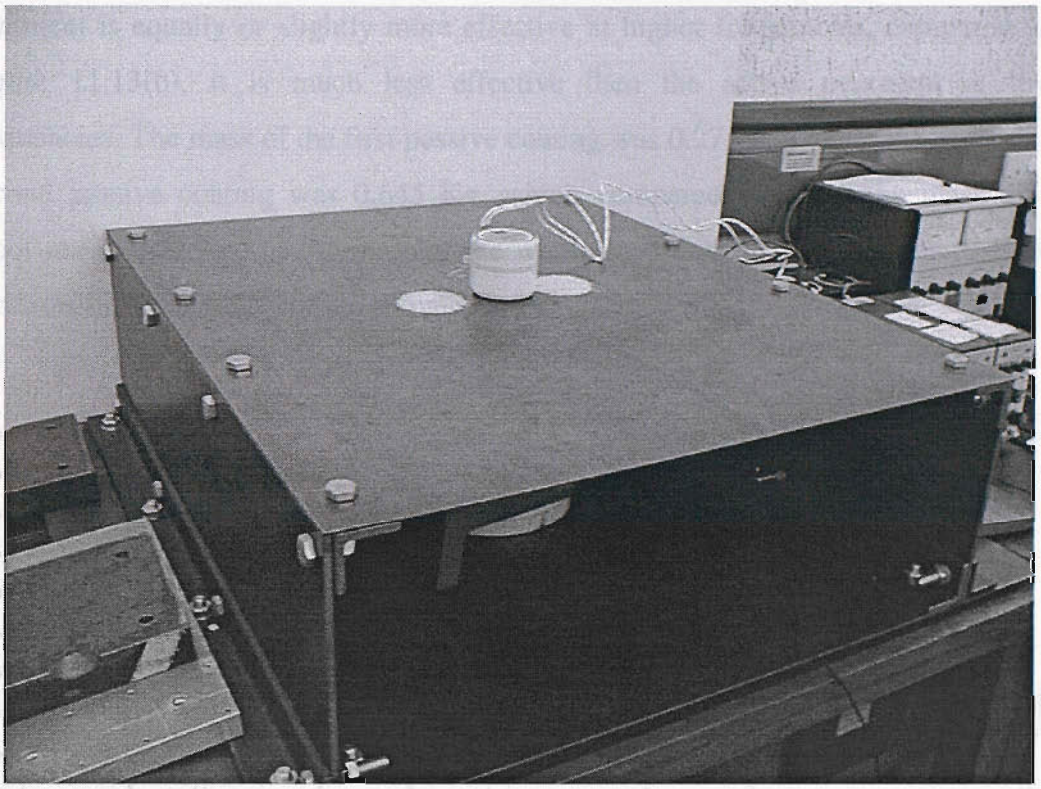

Figure 11.12 *The experimental arrangement, which consists of a finite flexible plate, driven by a primary force (shaker underneath), and controlled by a modified ULTRA Electronics inertial actuator placed on the flexible plate.*

Figure 11.13(a) shows the theoretical prediction of the equipment velocity per unit primary excitation for the uncontrolled and the control cases when the relative distance is 2 cm. Good vibration isolation conditions can be achieved by the modified inertial actuator and the outer velocity feedback loop. The outer loop, with response Z_D, improves the behaviour of the plate, but it also enhances its frequency response at low frequency, as predicted by the conditional stability of the closed loop system. The corresponding measured data is shown in Figure 11.13(b), where a 20 dB reduction at the first plate resonance frequencies was observed. The theoretical prediction and the experimental measurements agree well, demonstrating the effectiveness of the active control system based on a modified inertial actuator with inner displacement feedback control.

This result was compared with an entirely passive vibration control method, when the flexible plate was entirely covered by either a passive unconstrained viscoelastic layer, composed of foam, or a 2.5 cm thick passive constrained layered absorber, composed of the same viscoelastic material with layers of aluminium. Figure 11.14 shows the measured data, compared to the uncontrolled case. Although the passive

treatment is equally or slightly more effective at higher frequencies, compared with Figure 11.13(b), it is much less effective then the active treatment at lower frequencies. The mass of the first passive coating was 0.275 Kg, while the mass of the second passive coating was 0.645 Kg, which compared to either the mass of the proof-mass (0.24 Kg) or the mass of the whole modified inertial actuator (0.42 Kg) confirms the potentiality of the active solution.

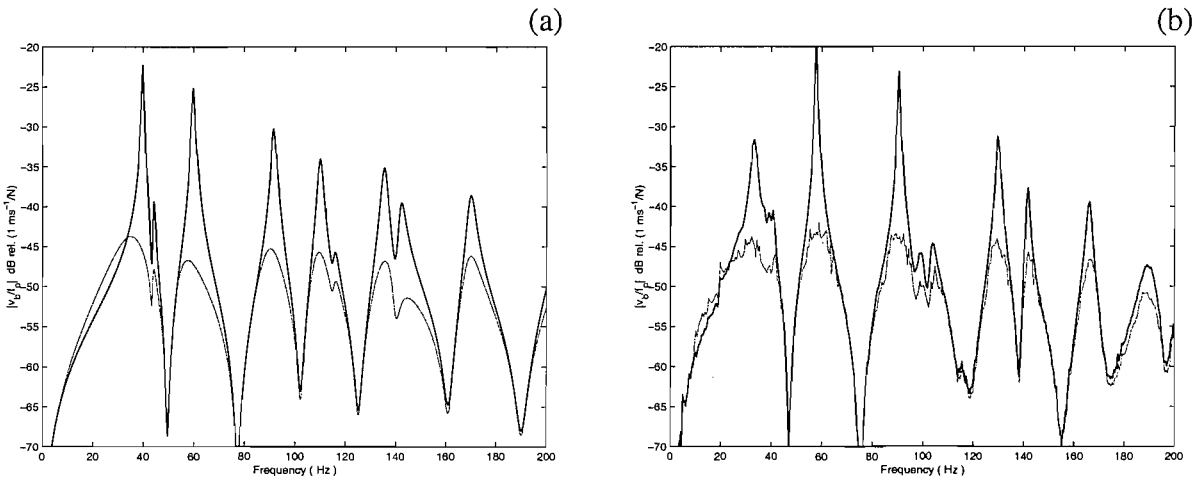

Figure 11.13 *Predicted (a) and measured (b) frequency response of the plate velocity at the secondary location per primary excitation when no control is implemented (solid), and when both the modified inertial actuator and the outer velocity feedback loop are implemented with Z_D = 150 (faint). Under experimental conditions, stability is guaranteed when Z_D < 300.*

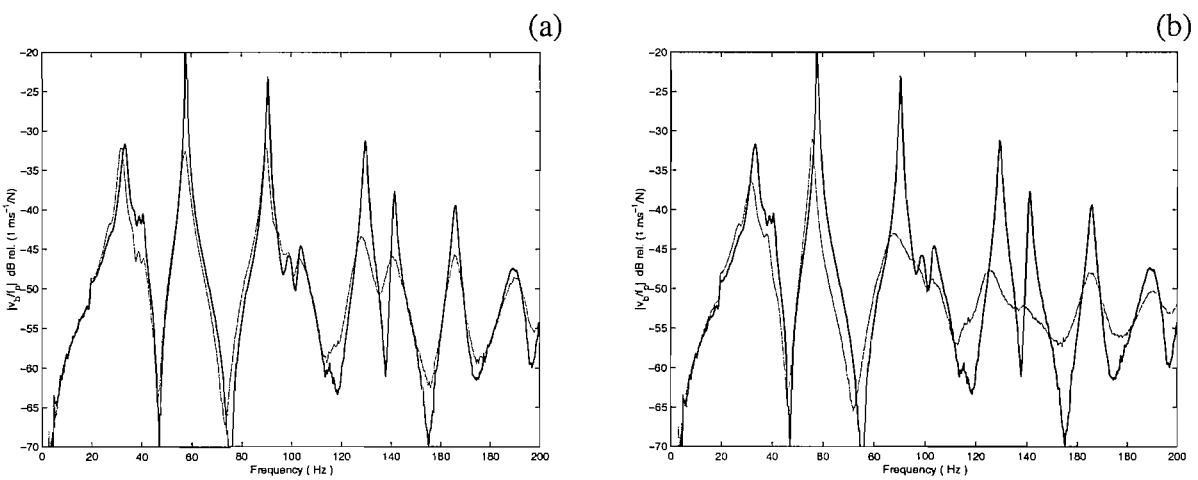

Figure 11.14 *Measured frequency response of the plate velocity at the secondary location per primary excitation when no control is implemented (solid), when a passive vibration absorber, based on foam, is installed and covers the whole plate (a, faint), and when a passive vibration absorber, based on foam and aluminium layers, is installed and covers the whole plate (b, faint).*

11.4 Kinetic energy analysis of the active vibration suppression system with the modified inertial actuator

The control performance of the active vibration suppression system with the modified inertial actuator has been re-examined based on the kinetic energy. To calculate the true kinetic energy of the system, the vibration of both the rigid body modes and the flexible body modes would have to be accounted for. In the experiments, however, only the plate velocities at 40 locations were measured, when the modified inertial actuator with outer velocity feedback loop was installed at the same location as described above. The sum of squared velocities at each location is therefore used to evaluate the control performance of the system. Figure 11.15 shows the predicted and experimental results, which lead to similar conclusions as those drawn in the previous section. Theory and measurements agree well, showing up to 20 dB reduction in the vibration level and demonstrating the effectiveness of the modified inertial actuator.

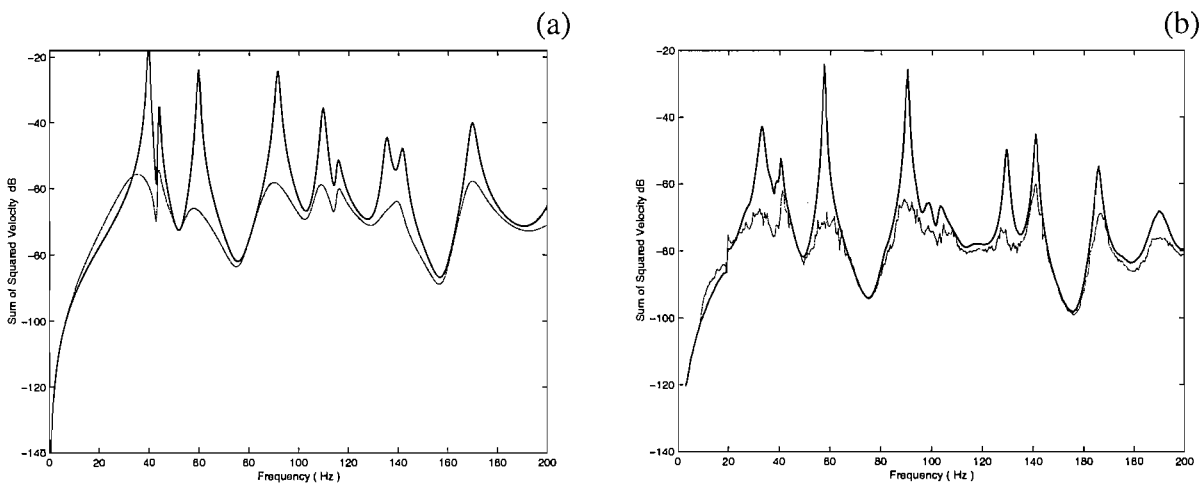

Figure 11.15 *Predicted (a) and measured (b) sum of square velocities of the plate when no control is implemented (solid), and when both the modified inertial actuator and the outer velocity feedback loop are implemented with* Z_D *= 150 (faint).*

11.5 Variation of performance with the location of the modified inertial actuator

The objective of this section is to compare the previous results with solutions obtained by placing the modified inertial actuator with outer velocity feedback loop in other locations on the flexible plate (Benassi and Elliott, 2003d). Figure 11.16 shows the total power transmitted to the finite plate due to the primary force only, and with the modified inertial actuator having only the inner feedback loop. The controller is installed on the plate at P_1 = (0.12 m, 0.27 m), 20 cm from the primary force, which is located at P_0 = (0.32 m, 0.27 m). The plate resonances are attenuated, and in particular the first resonance is reduced by about 20 dB.

When the outer velocity feedback loop is implemented, the choice of the outer gain Z_D becomes important in order to guarantee a certain stability margin and good performance. Figure 11.17 shows the ratio of the frequency averaged power between the "passive" controller (the inertial actuator without outer loop) and the active controller (with outer loop) as a function of the outer velocity feedback gain is Z_D . The minimum of the function at Z_D = 200 indicates the value of the gain that provides the greatest attenuation in terms of power. In this case, the attenuation is only 2.4 dB, but this depends on the location of the primary and secondary forces, as explained below. For outer loop gains greater than about 1400 the ratio is positive, which indicates that the "passive" controller performs better than the active solution. The active controller becomes unstable when the outer velocity feedback gain is greater than 2450, as shown in the Nyquist plot in Figure 11.18. The Nyquist plot shows that the stability margin is mainly affected by the modified inertial actuator's natural frequency and in real systems the margin is greatly reduced, as experienced above, due to low frequency phase lags, which are present in the electronic components (Brennan *et al.*, 2002).

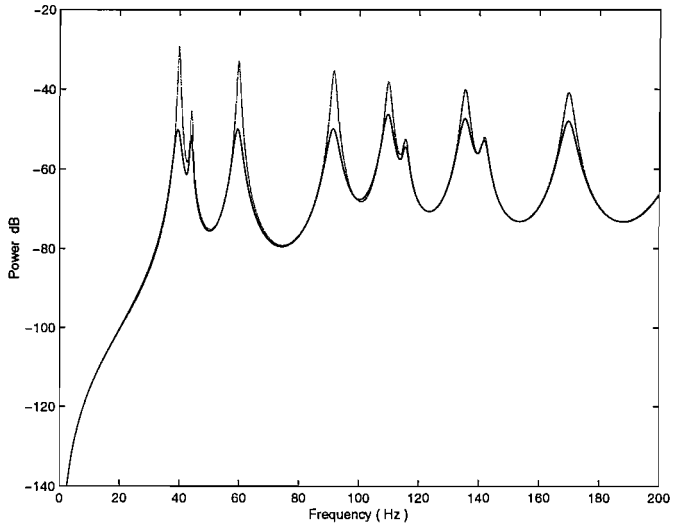

Figure 11.16 *Total power transmitted to the finite plate due to the primary force only with no actuator attached (solid), and with the modified inertial actuator ("passive" controller, faint). The distance between primary and secondary force is 20 cm.*

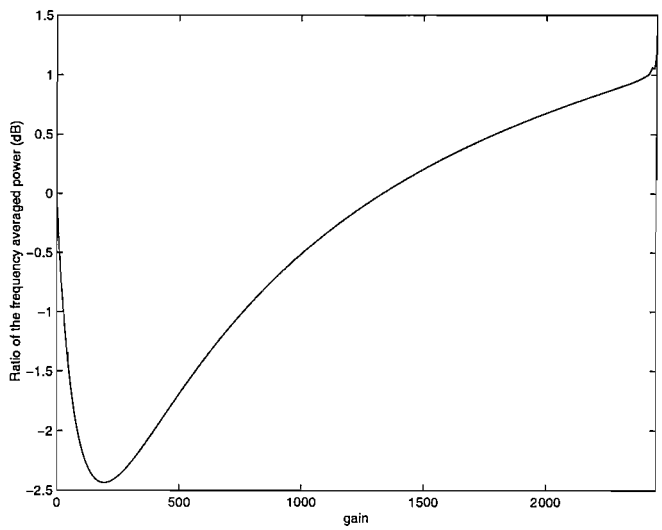

Figure 11.17 *Ratio of the frequency averaged total power transmitted to the plate with the modified actuator before and after the outer feedback loop is implemented, as a function of the outer velocity feedback gain Z_D. The minimum of the function at Z_D = 200 indicates the value of the gain that provides the greatest attenuation (about 2.4 dB) in terms of power. For gains greater than about 1400 the ratio is positive, indicating that the active controller is less effective than the "passive" controller. The active controller becomes unstable for outer velocity gains Z_D > 2450. The distance between primary and secondary forces is 20 cm.*

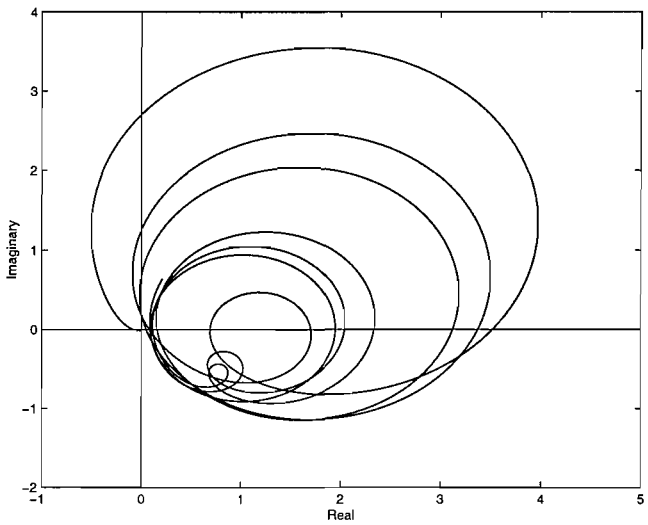

Figure 11.18 *Predicted Nyquist plot of the open loop system when the modified inertial actuator is applied and an outer feedback control loop, based on velocity feedback control, is implemented. The distance between primary and secondary force is 20 cm and the plate is finite. The outer feedback gain Z_D = 200 and this value minimises the function in Figure 11.17 and intersects the x-axis at (-0.081,0), indicating that a gain of 2450 would set the closed loop system unstable.*

The total power transmitted to the plate due to both the primary and the "passive" controller is shown as the solid line in Figure 11.19. This power is compared to the optimal solution, which defines the control target, since no other control can perform better. The dashed line in Figure 11.19 shows the total power due to the primary force and the active controller, whose outer feedback gain is Z_D = 200. Although the stability margin is quite big and therefore the gain could be safely increased, this value guarantees the largest attenuation over the selected frequency range between 0 Hz and 200 Hz. As predicted by the Nyquist plot, at some frequencies the total power due to the active control is greater than the power due to the "passive" control. At this particular location the vibration of only a few modes is reduced by more than 20 dB, while the total power of other modes is either unaffected or slightly enhanced. Figure 11.20 shows the equivalent impedance due to the optimal secondary force compared with the impedance due to the modified inertial actuator with the outer feedback control loop described above. The mismatch between the two curves is quite evident at low frequency, while at higher frequencies the impedance of the active controller, which is damping dominated, seems to match the average value of the equivalent impedance quite well.

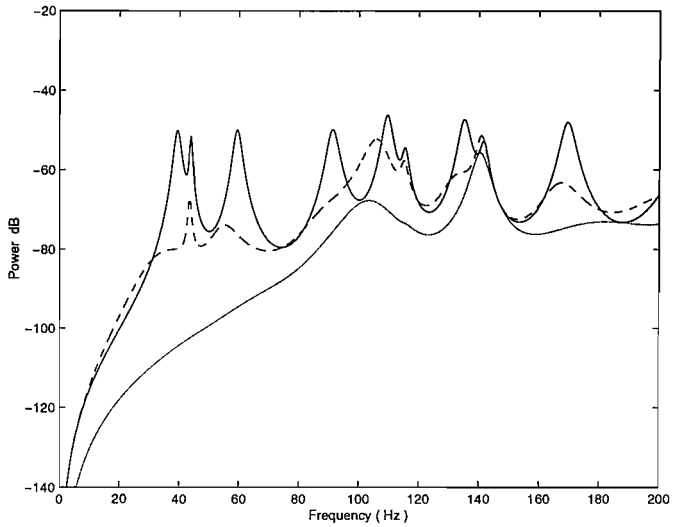

Figure 11.19 *Total power transmitted to the finite plate due to the primary and secondary forces when the "passive" controller is applied (solid), the primary and secondary forces with the optimal feedforward solution (faint), and the primary and secondary forces when the modified inertial actuator and the outer velocity feedback controller are applied (dashed). In this case, the distance between primary and secondary force is 20 cm and* $Z_D = 200$.

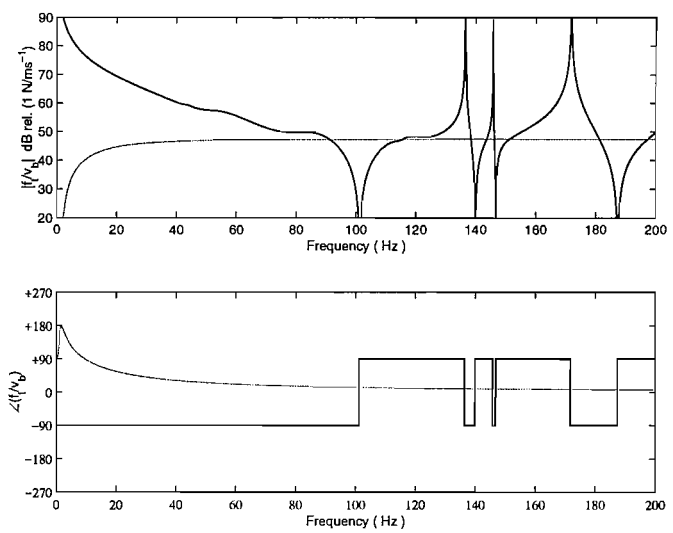

Figure 11.20 *Equivalent impedance due to the optimal secondary force (solid) and the impedance of the active controller, based on the modified inertial actuator and an outer velocity feedback loop whose gain* $Z_D = 200$ *(faint). The distance between primary and secondary forces is 20 cm.*

Figure 11.21 shows the contour plot of the ratio of the frequency averaged power between power of the uncontrolled plate and the "passively" controlled plate, as a function of the x and y positions of the actuator on the flexible plate. In other words, the primary force is assumed to be at a location P_0 = (0.32 m, 0.27 m) which guarantees that a sufficient number of modes are excited, while the "passive" controller, based on the modified inertial actuator, is assumed to be installed in turn on the plate at different locations. For this purpose, 500 potential locations were selected. Figure 11.21 shows that the "passive" controller achieves at least a 3 dB reduction in the ratio of the frequency averaged power not only around the location of the primary force, as expected, but also at symmetrical locations on the plate. This distribution obviously changes if the location of the primary force changes.

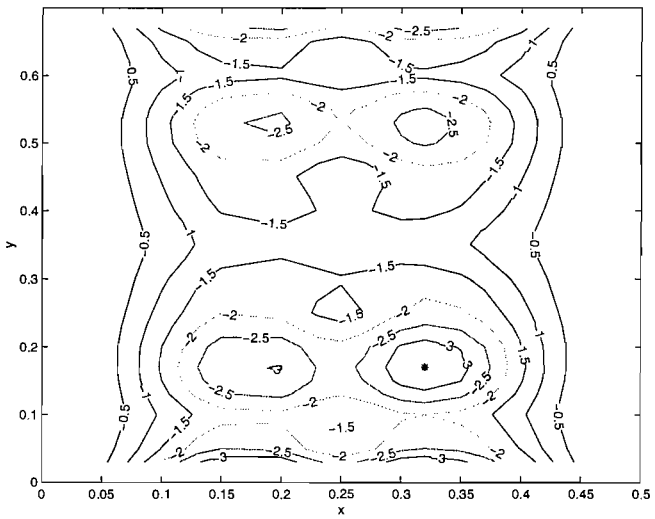

Figure 11.21 *Contour plot of the ratio of the frequency averaged power between power of the uncontrolled and the "passively" controlled plate with the modified inertial actuator, as a function of the x and y position of the controller on the flexible plate. The location of the primary force is indicated with a *.*

When the active control, based on the modified inertial actuator with outer velocity feedback loop, is implemented, the value of the feedback control gain Z_D that minimises the ratio of the frequency averaged power, can be computed at each of the 500 selected locations on the plate, and is shown in Figure 11.22. For each case, the stability of the closed loop system was guaranteed, although no specific stability

margin was set. Depending on the location, the maximum gain Z_D before instability can change considerably, but the gain which minimises the ratio of the frequency averaged power was always computed to be less or equal than the stability limit. In Figure 11.22 three main regions can be identified: around the location of the primary force high outer loop gains are needed in order to achieve the best attenuation possible with the active controller. High gains are also required close to the clamped edges. In the rest of the plate, although there are some differences, lower gains are needed. Figure 11.23 shows the contour plot of the ratio of the frequency averaged power when the gains in Figure 11.22 are used in the outer feedback loop control. In other words, Figure 11.23 shows the best attenuation that can be obtained with the active controller for that specific primary force location. If the active controller is placed near the primary force, average attenuations of up to 12.9 dB can be achieved within the selected frequency range between 0 Hz and 200 Hz, using the high outer gains shown in Figure 11.22. This attenuation is decreased to about 9 dB if the active controller is installed about 8 cm away from the primary force, where the x direction seems to be a little more privileged than the y direction in terms of attenuation. Although high gains are needed along the edges, as shown in Figure 11.22, the attenuation is not significant, while in the rest of the plate attenuations, which vary from 2.3 dB to 5.4 dB, can be obtained, depending on the location of the secondary force. In Figure 11.24 and Figure 11.25 the same kind of analysis is repeated, but the ratio of the frequency averaged power between power of the "passively" controlled plate and the actively controlled plate is plotted, which shows the incremental effect of the outer loop. The outer velocity feedback gains that minimise the above ratio are very similar to Figure 11.22, where the ratio of the frequency averaged power between power of the uncontrolled controlled plate and the actively controlled plate was used, indicating that the same values can be used to minimise both ratios. The attenuations in Figure 11.25 are smaller than the attenuations in Figure 11.23, as expected since some attenuation has already been achieved by the "passive" actuator, but the qualitative nature of the results is quite similar.

In summary, the performance of the control strategy, based on the modified inertial actuator with outer velocity feedback control, depends on both the relative distance between primary and secondary forces as well as their absolute location on the plate.

Ideally, the best solution would be to install the controller as close as possible to the primary disturbance.

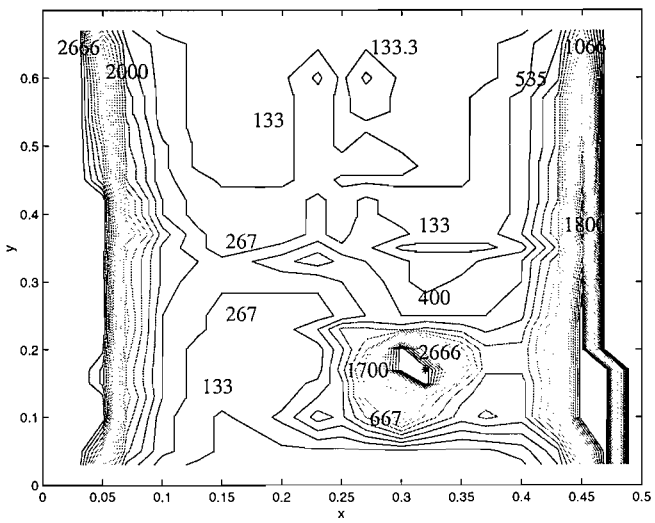

Figure 11.22 *Contour plot of the outer velocity feedback gain Z_D which, for a specific location, provides the minimum of the ratio of the frequency averaged power between power of the plate with no actuator and the plate with the modified inertial actuator and outer velocity feedback loop, as a function of the x and y position of the controller on the flexible plate. The location of the primary force is indicated with a *.*

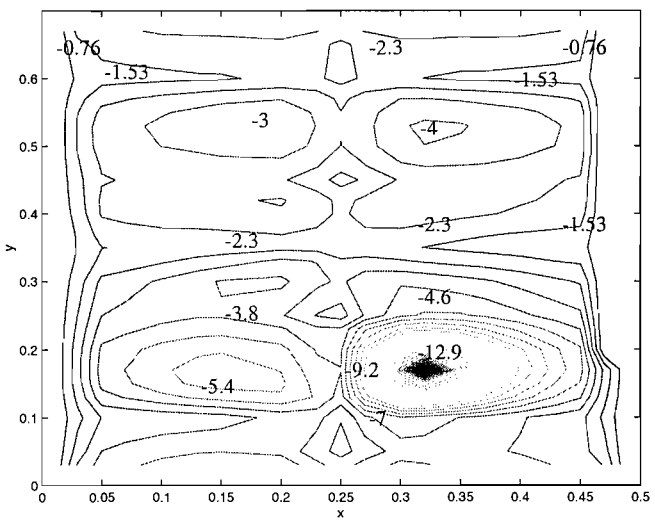

Figure 11.23 *Contour plot of the ratio of the frequency averaged power between power of the plate with no actuator and the plate with the modified inertial actuator and outer velocity feedback loop, as a function of the x and y position of the controller on the flexible plate. The controller is based on the modified inertial actuator with outer velocity feedback loop, whose gain Z_D for a specific location was chosen from the corresponding location in Figure 11.22. The location of the primary force is indicated with a *.*

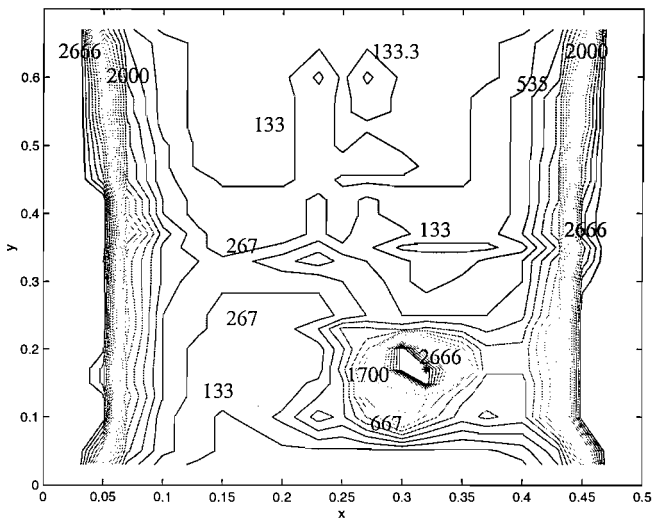

Figure 11.24 *Contour plot of the outer velocity feedback gain Z_D which, for a specific location, provides the minimum of the ratio of the frequency averaged power between power of the plate with no actuator and the plate with the modified inertial actuator and outer velocity feedback loop, as a function of the x and y dimensions of the flexible plate. The location of the primary force is indicated with a *.*

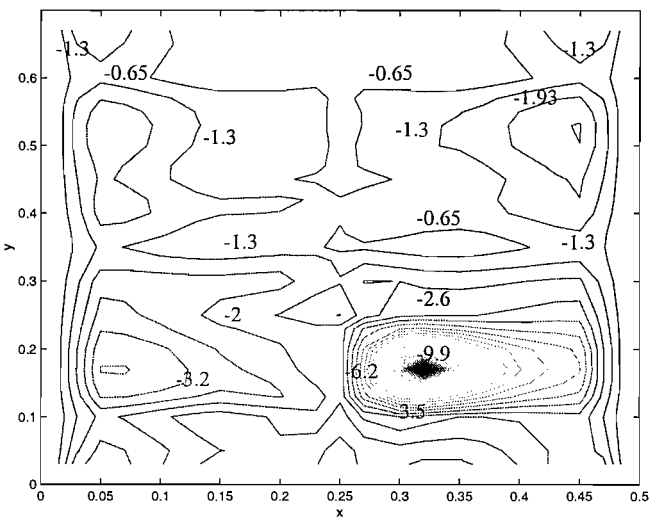

Figure 11.25 *Contour plot of the ratio of the frequency averaged power between power of the plate with modified inertial actuator and the plate with the modified inertial actuator and outer velocity feedback loop, as a function of the x and y dimensions of the flexible plate. The active controller is based on the modified inertial actuator with outer velocity feedback loop, whose gain Z_D for a specific location was chosen from the corresponding location in Figure 11.24. The location of the primary force is indicated with a *.*

11.6 Conclusions

In this chapter the total power of the forces exerting on a structure was minimised and a comparison was made between optimal solutions and the performance of various passive and active control treatments involving inertial actuators. In particular, the optimised impedance for global control was compared to the performance of a modified inertial actuator. It was found that, although the optimal impedance is able to provide a more substantial total power reduction than the other treatments, the modified inertial actuator can still guarantee a good power reduction, especially when combined with an outer velocity feedback controller. This seems to be a very promising solution to the vibration suppression problem, even though attention must be paid to the location of the secondary force in order to achieve the best possible attenuation.

As we have seen in Chapter 5, in using an inertial actuator for active vibration isolation, the resonance frequency should be lower than the first natural frequency of the system under control and it should be well damped. The modified inertial actuator can be effectively employed for this kind of applications, although the phase shifts due to transducer conditioning circuitry limit the maximum gain which can be achieved in the outer loop of the actuator before instability. In the current arrangement a maximum gain of only 150 N/ms^{-1} has been used, which only gives an impedance close to the optimal value when the actuator is positioned some distance from the primary source, as shown in Figure 11.22. Much larger reductions in power output from a single primary force are, in principle, possible if the destabilising phase shifts could be reduced and the inertial actuator was placed close to the primary excitation with a gain which was perhaps ten times that currently used.

Chapter 12

Conclusions and suggestions for future work

12.1 Conclusions

Vibration control systems can be classified as linear or non-linear (Kolovsky, 1999), depending on whether or not their dynamic response is governed by a set of linear differential equations. They can be further classified as active or passive, depending on whether or not external power is required. The principal vibration control techniques employ resilient load-supporting mechanisms and energy dissipating mechanisms. Typical passive control systems employ metallic springs, elastometers or other cushioning devices. Active vibration control systems comprise vibration sensors, controllers and actuators. The sensors provide signals proportional to the dynamic excitation or the structural response. The controllers then generate the command signals as a function of the sensor signals. The actuators finally apply these forces in response to the command signals.

This is the environment in which this thesis finds its place. In particular, during this thesis several methods have been investigated for active vibration control using an inertial actuator. Inertial actuators do not need to react off a base structure, so they can be used as modules that can be directly installed on a vibrating structure. This feature makes them very useful.

A review of different inner feedback loop strategies for active vibration control using an inertial actuator was presented. Feedback stability margins and performance were considered for each case. The main finding was that the use of a phase-lag compensator within the inner feedback loop provides good stability margins and good performance.

There is an overall requirement for the actuator's natural frequency to be below that of the first structural mode of the system under control. Further analysis on the active vibration control problem led to the development of a new device, based on an inertial actuator with very low stiffness and an inner displacement feedback control loop. In particular, the controller is a PID which uses the measurement of the relative displacement between the actuator reference base and the actuator moving mass. The control law is the sum of an integral term, which solves the sagging problem, a derivative term, which provides the device with sufficient initial damping to guarantee a very good stability margin, and a proportional term, which sets the actuator resonance frequency.

Then theoretical and experimental investigation of the active vibration isolation of a rigid piece of equipment structure from a vibrating base structure using an inertial actuator was carried out. The dynamics and control mechanisms of the mounted rigid equipment structure on a flexible base plate have been studied experimentally and the results have been compared with the theoretical findings. The equipment velocity responses, measured from the experiments, agree well with the predicted results, which demonstrates that the theoretical model can be used to help understand the dynamics of the overall system. It was found, from the simulations and the experiments, that from a stability point of view, the force and velocity feedback control scheme does not guarantee a good stability margin at low frequency. This is especially true when the outer velocity gain is increased. On the other hand, from a performance point of view, this scheme offers very good results using lower gains than the other schemes. When an integrator is added to the inner feedback controller, the overall system significantly improves its stability characteristics. On the other hand, if high performance is needed, very high gains are necessary. The results obtained by the implementation of a phase-lag compensator within the inner feedback loop and a velocity feedback outer loop seem to be very encouraging. In fact, simulations and experiments show that a strong reduction of the equipment resonance can be achieved, together with very good stability margins.

It was found from the simulations and the experiments that the new device is effective in actively isolating a piece of equipment from the vibrations of a base structure. Although the overall system is conditionally stable, very good performance can be achieved.

In the second part of the thesis the active control of a vibrating panel was investigated. The total power supplied to the plate by a primary and a secondary force was chosen to be the cost function to be minimised. In particular, the effect of the distance between primary and secondary excitations was investigated and simulations were carried out for both infinite and finite plates. The core of this study was the theoretical and experimental comparison between optimal solutions in terms of secondary force, and the performance of passive and active control treatments. In particular, the optimised impedance for global control was compared to the impedance that the new device is able to add to the system in order to achieve the goal of minimizing the cost function. It was found that, although the optimal impedance is able to provide an outstanding power reduction compared to the other treatments, the new device guarantees very good power reduction and seems to be a promising solution to the vibration reduction problem, especially if combined with an outer controller based on a passive approximation of the optimal solution.

12.2 Suggestions for future work

The vibration isolation of large pieces of equipment or the vibration suppression of large panels may require that more than one device is installed. The study carried out in this thesis considers the investigation of the stability and performance of one device only, so a natural extension to this research would be the theoretical and experimental investigation of the effect of having several devices, all trying to either minimize the equipment velocity or minimize the total power. Each device would have its own inner control scheme, so another result of this future study would be the analysis of the mechanisms behind the decentralized control of structures using several inertial actuators. By doing this kind of investigation, the transition from a single degree of freedom problem to a multi degree of freedom problem would be made.

The protection of structures from the damaging effects of vibration and shock that occur in dynamic environments is of prime consideration in the design of such structures. Depending on the particular application, the structure to be protected may contain mechanical, electrical or optical systems, humans, etc. Traditionally, the terms vibration absorber and shock absorber refer, respectively, to absorbers of oscillations due to harmonic or random excitation and absorbers that deal with oscillations due to shock excitations or transient vibration in terms of initial conditions. Therefore, in a practical application, it may be necessary to combine these absorbers together. However, an absorber that exhibits good vibration suppression does not necessarily provide adequate shock attenuation. A shock may be defined as "a transmission of kinetic energy to a system which takes place in a relatively short time compared with the natural period of oscillation of the system" (Broch, 1980). For example, an impulsive excitation of a structure implies that all the modes at all frequencies are excited. If a certain vibration control scheme is effective only within a limited frequency range, then problems may occur due to those excited modes outside the frequency range. In particular, if stiffness is added to a structure, then the modal peaks are moved to higher frequencies and the frequency range of interest results with a larger stiffness dominated region. Those peaks outside the range of interest are still present in the system and therefore an impulsive excitation may excite them and possibly damage the structure. On the other hand, "if the duration of the shock pulse is short in comparison with one half period of the isolation system resonant frequency, the response of the system may not have serious consequences" (Broch, 1980). In summary, even though the principles involved in shock isolation are similar to those involved in vibration isolation, some differences exist due to the transient nature of a shock. In particular, the reduction in shock severity results from the storage of the shock energy within the isolator and its subsequent release in a smoother form (i.e. over a much longer period of time). It would be interesting to assess whether the new device is a good shock absorber as well as being a very good vibration absorber.

References

Abramowitz, M., and Stegun, I. A., 1972, *Handbook of Mathematical Functions*, Dover Publications, Inc., New York.

Ahmadian, M., Miller, L. R., Southward, S. C., and Roemer, M. J., 1993, "Performance Analysis of Active Mounts for Structural Vibration Reduction," *Proceedings of the 2nd Conference on Recent Advances in active Control of Sound and Vibration*, Blacksburg, VA, April 28-30.

Althaus, J., Ulbrich, H., 1992, "A Fast Hydraulic Actuator for Active Vibration Control," *Proceedings of the Institute of Mechanical Engineers International Conference on Vibration in Rotating machinery*, Bath.

Alvarez-Salazar, O., Iliff, K. W., 1999, "Destabilizing Effects of Rate Feedback on Strain Actuated Beams," J. Sound and Vibration, **221**, No. 2, pp. 289-307.

Alvarez-Salazar, O. S., 2002, personal communication.

Anderson, E. H., Holcomb, M. D., and Leo, D. J., 2001, "Integrated Electromechanical Devices for Active Control of Vibration and Sound," CSA Engineering Inc. Technical Report.

Ananthaganeshan, K. A., Brennan, M. J., and Elliott, S. J., 2001, "Low and High Frequency Instabilities in Feedback Control of a Vibrating Single Degree of Freedom System," ISVR Technical Report No. 870.

Anthony, D. K, Elliott, S. J., and Keane, A. J., 2000, "Robustness of Optimal Design Solutions to Reduce Vibration Transmission in a Lightweight 2-D Structure, Part I: Geometric Design," J. Sound and Vibration, **229**, No. 3, pp. 505-528.

Anthony, D. K, Elliott, S. J., 2000a, "Robustness of Optimal Design Solutions to Reduce Vibration Transmission in a Lightweight 2-D Structure, Part II: Application of Active Vibration Control Techniques," J. Sound and Vibration, **229**, No. 3, pp. 529-548.

Anthony, D. K., Elliott, S. J., 2000b, "Comparison of the Effectiveness of Minimizing Cost Function Parameters for Active Control of Vibrational Energy Transmission in a Lightly Damped Structure," J. Sound and Vibration, **237**, No. 2, pp. 223-244.

Baek, K. H., Elliott, S. J., 2000, "The Effects of Plant and Disturbance Uncertainties in Active Control Systems on the Placement of Transducers," J. Sound and Vibration, **230**, No. 2, pp. 261-289.

Balakrishnan, A. V., 1993, "Explicit LQG Optimised Control Laws for Flexible Structures/Collocated Rate Sensors," *AIAA-93-1657 Adaptive Structures Forum*, La Jolla, CA, April 19-22, pp. 3108-3114.

Balakrishnan, A. V., 1999, "Damping Performance of Strain Actuated Beams," *Comp. Applied Mathematics*, Vol. 18, No. 1, pp. 31-86.

Balas, M. J., 1978, "Direct Velocity Feedback Control of Large Space Structures," J. Guidance and Control, Vol. 2, No. 3, pp. 252-253.

Bardou, O., Gardonio, P., Elliott, S. J., and Pinnington, R. J., 1997, "Active Power Minimization and Power Absorption in a Plate with Force and Moment Excitation," J. Sound and Vibration, **208**, No. 1, pp. 111-151.

Basak, A., 1996, *Permanent-Magnet DC Linear Motors*, Claredon Press.

Beard, A. M., von Flotow, A. H., and Schubert, D. W., 1994, "A Practical Product Implementation of an Active/Passive Vibration isolation System," *Proc. IUTAM Symposium on the Active Control of Vibration*, Bath, pp. 101-108.

Benassi, L., Gardonio, P., and Elliott, S.J., 2002a, "Equipment Isolation of a SDOF System with an Inertial Actuator using Feedback Control Strategies – Part I: Theory," ISVR Technical Memorandum No. 883, University of Southampton.

Benassi, L., Gardonio, P., and Elliott, S.J., 2002b, "Equipment Isolation of a SDOF System with an Inertial Actuator using Feedback Control Strategies", *Proceedings of the ACTIVE 2002Conference, Southampton, U.K.*, 15-17 July 2002.

Benassi, L., Gardonio, P., and Elliott, S.J., 2002c, "Equipment Isolation of a SDOF System with an Inertial Actuator using Double Feedback Control Strategies," ISVR Technical Memorandum No. 893, University of Southampton.

Benassi, L., Elliott, S.J., and Gardonio, P., 2002d, "Equipment Isolation of a SDOF System with an Inertial Actuator using Feedback Control Strategies – Part II: Experiment," ISVR Technical Memorandum No. 896, University of Southampton.

Benassi, L., Elliott, S.J., and Gardonio, P., 2003a, "Active Vibration Isolation using an Inertial Actuator with Local Force Feedback Control," Journal of Sound and Vibration. *Accepted for publication.*

Benassi, L., and Elliott, S.J., 2003b, "Active Vibration Isolation using an Inertial Actuator with Local Displacement Feedback Control," Journal of Sound and Vibration. *Accepted for publication.*

Benassi, L., and Elliott, S.J., 2003c, "The Equivalent Impedance of Power-Minimising Vibration Controllers on Plates," Journal of Sound and Vibration. *Submitted.*

Benassi, L., and Elliott, S.J., 2003d, "Global Control of a Vibrating Plate using a Feedback-Controlled Inertial Actuator," Journal of Sound and Vibration. *Submitted.*

Bhat, S P., Miu, D. K., 1991a, "Solutions to Point-to-Point Control Problems using Laplace Transform Techniques," Journal of Dynamic Systems, Measurement, and Control, Vol. 113, September, pp. 425-431.

Bhat, S P., Miu, D. K., 1991b, "Experiments on Point-to-Point Position Control of a Flexible Beam using Laplace Transform Technique - Part II: Closed-Loop," Journal of Dynamic Systems, Measurement, and Control, Vol. 113, September, pp. 438-443.

Bhat, S P., Tanake, M., and Miu, D. K., 1991c, "Experiments on Point-to-Point Position Control of a Flexible Beam using Laplace Transform Technique - Part I: Open-Loop," Journal of Dynamic Systems, Measurement, and Control, Vol. 113, September, pp. 432-437.

Bies, D. A., and Hansen, C. H., 1996, *Engineering Noise Control*, E&FN Spon.

Bishop, R. E. D., Johnson, D. C., 1960, *The Mechanics of Vibration*, Cambridge University Press.

Blackwood, G. H., and von Flotow, A. H., 1993, "Active Control for Vibration Isolation Despite Resonant Structural Dynamics: A Trade Study of Sensors, Actuators and Configurations," *Proc. 2nd VPI Conference on Recent Advances in the Active Control of Sound and Vibration*, pp. 482-494.

Boldea, I., 1997, *The Induction Machine Handbook*, CRC Press.

Brennan, M. J., Elliott, S. J., Pinnington, R. J., 1995, "Strategies for the Active Control of Flexural Vibration on a Beam," J. Sound and Vibration, **186**, No. 4, pp. 657-688.

Brennan, M. J., 1997, "Vibration Control Using a Tunable Vibration Neutralizer," *Proceedings of the Institute of Mechanical Engineers*, Vol. 211, Part C, pp. 91-108.

Brennan, M. J., 1998, "Control of Flexural Waves on a Beam using a Tunable Vibration Neutraliser, J. Sound and Vibration, **222**, No. 3, pp. 389-407.

Brennan, M. J. *et al*, 1999, "Experimental Investigation of Different Actuator Technologies for Active Vibration Control," Smart Mater. Struct., **8**, pp. 145-153.

Brennan, M. J., Dayou, J., 2000, "Global Control of Vibration using a Tunable Vibration Neutralizer," J. Sound and Vibration, **232**, No. 3, pp. 585-600.

Brennan, M. J., Ananthganeshan, K. A., and Elliott, S.J., 2002, "Low and High Frequency Instabilities in Feedback Control of vibrating single-degree-of-freedom Systems", *Proceedings of the ACTIVE 2002Conference, Southampton, U.K.*, 15-17 July 2002.

Brennan, M. J., 2003, personal communication.

Broch, J. T., 1980, *Mechanical Vibration and Shock Measurements*, Bruel & Kjaer.

Bryson, A. E., and Ho, Y.-C., 1975, *Applied Optimal Control*, Taylor&Francis.

Carabelli, S, Tonoli, A., 2000, "System Properties of Flexible Structures with Self-Sensing Piezoelectric Transducers," J. Sound and Vibration, **235**, No. 1, pp. 1-23.

Cazzolato, B. S., 2002, personal communication.

Chase, J. G, Yim, M., and Berlin, A. A., 1999, "Integrated Centering Control of Inertially Actuated Systems," Control Engineering Practice, No. 7, pp. 1079-1084.

Choi, S. B., Hwang, J. H., 2000, "Structural Vibration Control using Shape Memory Actuators," J. Sound and Vibration, **231**, No. 4, pp. 1168-1174.

Clark, R. L., Saunders, W. R., and Gibbs, G. P., 1998, *Adaptive Structures: Dynamics and Control*, John Wiley & Sons, Inc.

Crandall, S. H., Dahl, N. C., 1978, *An Introduction to the Mechanics of Solids*, McGraw-Hill.

Crede, C. E., and Ruzicka, J. E., 1996, "Theory of Vibration Isolation," Chapter 30, C. M. Harris, ed., *Shock and Vibration Handbook*, McGraw Hill, New York.

Cremer L., Heckl, M., and Ungar, E. E., 1988, *Structure-borne Sound*, Springer-Verlag.

CSA Engineering, 2002, www.csaengineering.com

Daley, S., Johnson, F. A., Pearson, J. B., and Dixon, R., 2002, "Active Vibration Control for Marine Applications," *Proceedings of Control 2002,* University of Sheffield, 17 September.

D'Cruz, J., 1998, "Active Suppression of Aircraft Panel Vibration with Piezoelectric Strain Actuators," Journal of Aircraft, Vol. 35, No. 1, January-February, pp. 139-144.

den Hartog, J. P., 1985, *Mechanical Vibrations*, Dover Publications, Inc., New York.

Dosch, J., Lesieutre, G., Koopman, F., and Davis, C., 1995, "Inertial Piezoceramic Actuators for Smart Structures," *Proceedings of the SPIE smart structures and materials conference*, San Diego, CA, pp. 14-25.

Doyle J. C. and Stein, G., 1979, "Robustness with Observers," IEEE Transactions on Automatic Control, **AC-24**, pp. 607-611.

Dunn, B., Garcia, E., 1997, "Optimal Sensor and Actuator Placement for Structural Control Based on output Controllability," *Proceedings of the 11th Conference on Structural Dynamics and Controls*, Blacksburg, VA, May 1997.

El-Beheiry, E. M., Karnopp, D. C., 1996, "Optimal Control of Vehicle Random Vibration with Constrained Suspension Deflection," J. Sound and Vibration, **189**, No. 5, pp. 547-564.

Elliott, S. J., Sothers, I. M., and Nelson, P. A., 1987, "A Multiple Error LMS Algorithm and Its Application to the Active Control of Sound and Vibration," *IEEE Transactions on Acoustics, Speech and Signal Processing*, Vol. ASSP-35, No. 10, October 1987, pp. 1423-1434.

Elliott, S. J., Joseph, P., Nelson, P. A., Johnson, M. E., 1991, "Power Output Minimizations and Power Absorption in the Active Control of Sound," J. Acoustic Society of America, **90**, No. 5, pp. 2501-2512.

Elliott, S. J., Boucher, C. C., 1994, "Interaction Between Multiple Feedforward Active Control Systems," *IEEE Transactions on Speech and Audio Processing*, Vol. 2, No. 4, October 1994, pp. 521-530.

Elliott, S. J., 1997, "The Control of Transmitted Power in an Active Isolation System," *ACTIVE 97, Budapest-Hungary*, August 21-23, pp. 93-103.

Elliott, S. J., Gardonio, P., and Rafaely, B., 1998, "Performance Evaluation of a Feedback Active Isolation System with Inertial Actuators," ISVR Technical Memorandum No. 832.

Elliott, S. J., 2000, "Active Isolation Systems: A State-of-the-Art Study," ISVR Contract Report No. 00/28.

Elliott, S. J., Serrand, M., and Gardonio, P., 2001a, "Feedback Stability Limits for Active Isolation Systems with Reactive and Inertial Actuators," J. Vibration and Acoustics, Vol. 123, April 2001, pp. 250-261.

Elliott, S. J., Gardonio, P., Sors, T. J., and Brennan, M. J., 2001b, "Active Vibro-Acoustic Control with Multiple Local Feedback Loops," *SPIE's 8th Annual International Symposium on Smart Structures and Materials*, 4-8 March 2001, Newport Beach, CA, USA.

Fang, K., Tang, C., and Tong, Z., 2001, "Theoretical and Experimental Research on New Type Distributed Vibration Damper," *Proceedings of the 8th International Congress on Sound and Vibration*, Hong Kong, China, July 2-6.

Flint, E., Evert, M., Anderson, E., and Flannely, P., 2000, "Active/Passive Counter-Force Vibration Control and Isolation Systems," CSA Engineering Inc. Technical Report.

Franklin, G. F., Powell, J. D., and Emani-Naeini, A., 1994, *Feedback Control of Dynamic Systems*, Third Edition, Addison-Wesley, Reading, MA.

Friswell, M. I., Inman, D. J., and Lam, M. J., 1997a, "On the Realisation of GHM Models in Viscoelasticity," Journal of Intelligent Material Systems and Structures, **8**, pp. 986-993.

Friswell, M. I., Penny, J. E. T., and Garvey, S. D., 1997b, "Parameter Subset Selection in Damage Location," Inverse Problems in Engineering, Vol. 5, No. 3, pp. 189-215.

Friswell, M. I., and Inman, D. J., 1999a, "The Relationship between Positive Position Feedback and Output Feedback Controllers," Smart Mater. Structures, **8**, pp. 285-291.

Friswell, M. I., and Inman, D. J., 1999b, "Sensor Validation for Smart Structures," Journal of Intelligent Material Systems and Structures, Vol. 10, pp. 973-982.

Friswell, M. I., 2001, "On the Design of Modal Actuators and Sensors," J. Sound and Vibration, **241**, No. 3, pp. 361-372.

Fuller, C. R., Elliott S. J., and Nelson, P. A., 1997, *Active Control of Vibration*, Academic Press.

Garcia, E., Webb, S., and Duke, J., 1995, "Passive and Active Control of a Complex Flexible Structure Using Reaction Mass Actuators," J. Vibration and Acoustics, **117**, pp. 116-122.

Garcia-Bonito, J. *et al*, 1998, "A Novel High-displacement Piezoelectric Actuator for Active Vibration Control," Smart Mater. Struct., **7**, pp. 31-42.

Gardonio, P., Elliott, S. J., and Pinnington, R. J., 1996, "User Manual for the ISVR Isolation System with Two Active Mounts for the ASPEN Final Project Experiment," ISVR Technical Memorandum No. 801.

Gardonio, P., Elliott, S. J., 1996, "Active Control of Waves on a One-Dimensional Structure with a Scattering Termination," J. Sound and Vibration, **192**, No. 3, pp. 701-730.

Gardonio, P., Elliott, S. J., Pinnington, R. J., 1997a, "Mobility Model for Active Isolator," *Proceedings of the 6th International Conference: Structural Dynamics Recent Advances*, University of Southampton, July 14-17, Volume 1, pp. 501-519.

Gardonio, P., Elliott, S. J., and Pinnington, R. J., 1997b, "Active Isolation of Structural Vibration on a Multiple-Degree-of-Freedom System, Part I: the Dynamics of the System," J. Sound and Vibration, **207**, No. 1, pp. 61-93.

Gardonio, P., Elliott, S. J., and Pinnington, R. J., 1997c, "Active Isolation of Structural Vibration on a Multiple-Degree-of-Freedom System, Part II: Effectiveness of Active Control Strategies," J. Sound and Vibration, **207**, No. 1, pp. 95-121.

Gardonio, P., Elliott, S. J., 1998, "Driving Point and Transfer Mobility Matrices for Thin Plates Excited in Flexure," ISVR Technical Report No. 227.

Gardonio, P., Elliott, S. J., 1999, "A Study of Control Strategies for the Reduction of Structural Vibration Transmission," J. Vibration and Acoustics, Vol. 121, October 1999, pp. 482-487.

Gardonio, P., Elliott, S. J., 2000, "Passive and Active Isolation of Structural Vibration Transmission between Two Plates Connected by a Set of Mounts," J. Sound and Vibration, **237**, No. 3, pp. 483-511.

Gennesseaux, A., 1997, "The Active Mount by Paulstra," *Proceedings of the Conference: Elastische Lagerungen im Automobilbau*, Essen, Germany.

Gawronski, W., 2000, "Modal Actuators and Sensors," J. Sound and Vibration, **229**, No. 4, pp. 1013-1022.

Gerhold, C. H., Rocha, R., 1987, "Active Vibration Control in Microgravity Environment," NASA-Johnson Technical Memorandum No. 870601.

Ghoshal, A. *et al.*, 2000, "Vibration Suppression using a Laser Vibrometer and Piezoceramic Patches," J. Sound and Vibration, **235**, No. 2, pp. 261-280.

Goh, C. J., and Caughey, T. K., 1985, "On the stability problem caused by finite actuator dynamics in the collocated control of large space structures," International Journal of Control, Vol. 41, No. 3, pp. 787-802.

Grewal, A., Zimcik, D. G., and Leigh, B., 2001, "Feedforward Piezoelectric Structural Control: an Application to Aircraft Cabin Noise Reduction," Journal of Aircraft, Vol. 38, No. 1, January-February, pp. 164-173.

Griffin, S., Gussy, J., Lane, S. A., Henderson, B. K., Sciulli, D., 2002, "Virtual Skyhook Vibration Isolation System," Journal of Vibration and Acoustics, Vol. 124, pp. 63-67.

Guicking, D., Melcher, J., Wimmel, R., 1989, "Active Impedance Control In Mechanical Structures," Acoustica, Vol. 69, pp. 39-52.

Guigou, C., Fuller, C. R., and Wagstaff, P. R., 1994, "Active Isolation of Vibration with Adaptive Structures," J. Acoustical Society of America, **96**, No. 1, pp. 294-299.

Hiramoto, K., Doki, H, and Obinata, G., 2000, "Optimal Sensor/Actuator Placement for Active Vibration Control using Explicit Solution of Algebraic Riccati Equation," J. Sound and Vibration, **229**, No. 5, pp. 1057-1075.

Hinchliffe, R., Scott, I., Purver, M., and Stothers, I., 2002, "Tonal Active Control in Production on a Large Turbo-Prop Aircraft", *Proceedings of the ACTIVE 2002Conference, Southampton, U.K.*, 15-17 July 2002.

Hodgson, D. A., 1991, "Frequency-Shaped Control of Active Isolators," Presented at AHS-RaeS Technical Specialist Meeting on Rotorcraft Acoustics and Rotor Fluid Dynamics, Philadelphia, PA, October 15-17.

Holloway, C. D., 1993, "Inertial Actuators for Active Control," ISVR Part III Project, University of Southampton.

Horodinca, M., Abu Hanieh, A., and Preumont, A., 2002, "A Soft Six Degrees of Freedom Active Vibration Isolator based on a Stewart Platform", *Proceedings of the ACTIVE 2002Conference, Southampton, U.K.*, 15-17 July 2002.

Horning, R. W., and Schubert, D. W., 1988, "Air Suspension and Active Vibration Isolation Systems," Chapter 33 of *Shock and Vibration Handbook*, McGraw-Hill.

Howard, C. Q., Hansen, C. H., 1997, "Active Isolation of a Vibrating Mass," Acoustics Australia, Vol. 25, No. 2, pp. 65-67.

Howard, C. Q., Hansen, C. H., 2000, "Active Vibration Isolation Using Force and Velocity as Cost Functions – Experimental Results," *Proceedings of the Seventh International Congress on Sound and Vibration*, 4-7 July 2000, Garmisch-Partenkirchen, Germany, pp. 435-442.

Howard, C. Q., Snyder, S. D., and Hansen, C. H., 2000, "Calculation of Vibratory Power Transmission for use in Active Vibration Control," J. Sound and Vibration, **233**, No. 4, pp. 573-585.

Huang, X., Elliott, S.J., and Brennan, M. J., 2001a, "Active Isolation of a Flexible Equipment Structure on a Rigid Base," ISVR Technical Memorandum No. 866, University of Southampton.

Huang, X., Elliott, S.J., and Brennan, M. J., 2001b, "Active Isolation of a Flexible Equipment Structure on a Flexible Base," ISVR Technical Memorandum No. 879, University of Southampton.

Ivers, D. E., Miller, L. R., 1991, "Semi-Active Suspension Technology: An Evolutionary View," The American Society of Mechanical Engineers, Book No. H00719, pp. 327-346.

Jenkins, M. D., Nelson, P. A., Pinnington, R. J., and Elliott, S. J., 1993, "Active Isolation of Periodic Machinery Vibrations," J. Sound and Vibration, **166**, No. 1, pp. 117-140.

Johnson, C. D., 1995, "Passive Damping," *Proceedings of the SPIE Smart Structures and Materials Conference*," 1-2 March 1995, San Diego, CA, Vol. 2445, No. 3, pp. 161-175.

Kaplow, C. E., Velman, J. R., 1980, "Active Local Vibration Isolation Applied to a Flexible Space Telescope," J. Guidance and Control, Vol. 3, No. 3, May-June, pp. 227-233.

Karnopp, D., 1995, "Active and Semi-active Vibration Isolation," ASME J. Mech. Des., **117**, pp. 177-185.

Kim, S. M., Elliott, S. J., and Brennan, M. J., 1999, "Active Vibration Isolation of a 3-Dimensional Structure using Velocity Feedback Control," ISVR Technical Memorandum No. 845.

Kim, S. M., Elliott, S. J., and Brennan, M. J., 2001, "Decentralized Control for Multichannel Active Vibration Isolation," *IEEE Transactions on Control Systems Technology*, Vol. 9, No. 1, January 2001, pp. 93-100.

Kolovsky, M. Z., 1999, *Nonlinear dynamics of active and passive systems of vibration protection.* Springer.

L.D.S., Installation and Operating Manual for the V100 Series Vibrators. Manual No. 899061, 2nd Edition.

L.D.S., Installation and Operating Manual for the V400 Series Vibrators. Manual No. 586441, 1st Edition.

Leissa, A. W., 1969, *Vibration of Plates*, Washington D.C. Office of Technology Utilization, NASA SP-160.

Li, X., Cordioli, J., Cazzolato, B. S., Qiu, X., and Hansen, C. H., 1999, "Tuneable Inertial Shakers for Active Control," technical report of the Department of Mechanical Engineering, University of Adelaide.

Li, W., Gibson, J. S., 1992, "Adaptive Identification and Disturbance Rejection for Flexible Structures," MAE Dept Technical Report No. 910016.

Liang, C., Sun, F. P., and Rogers, C. A., 1992, "An Impedance Method for Dynamic Analysis of Active Material Systems," J. Vibration and Acoustics, December 1992, pp. 500-527.

Lindner, D. K., Celano, T. P., and Ide, E. N., 1991, "Vibration Suppression Using a Proof-mass Actuator Operating in Stroke/Force Saturation," J. Vibration and Acoustics, **113**, pp. 423-433.

Lindner, D. K., Zvonar, G. A., and Borojevic, D., 1994, "Performance and Control of a Proof-Mass Actuator Accounting for Stroke Saturation," J. Guidance, Control, and Dynamics, **17**, No. 5, pp. 1103-1108.

Lindner, D. K., Zvonar, G. A., and Borojevic, D., 1997, "Nonlinear Control of a Proof-Mass Actuator," J. Guidance, Control, and Dynamics, **20**, No. 3, pp. 464-470.

Lyon, R H., Dejong, R. G., 1995, *Theory and Application of Statistical Energy Analysis*, Academic Press.

Lord Corporation, 2002, "Vibration and Shock Theory", www.lordmpd.com.

Marouze', J. P., Cheng, L., and Gauthier, P. A., 2001, "Hybrid Vibration Isolation with Thunder Actuators," *Proceedings of the 8th International Congress on Sound and Vibration*, Hong Kong, China, July 2-6.

McConnell, K. G., 1992, *Vibration Testing: Theory and Practice*, John Wiley & Sons, Inc.

Meirovitch, L., 1967, *Analytical Methods in Vibration*, MacMillan.

Meirovitch, L., 1990, *Dynamics and Control of Structures*, John Wiley & Sons, Inc.

Melcher, J., 1992, "Active Vibration Isolation using Multifunctional Interfaces and Adaptive Digital Controllers," *Proceedings of the 3rd International Conference on Adaptive Structure*, San Diego, CA, November 9-11.

Meng, G., and Wang, J. X., 2001, "Experimental Study on Vibration Control of Flexible Rotor System by Magnetorheological Fluid Damper," *Proceedings of the 8th International Congress on Sound and Vibration*, Hong Kong, China, July 2-6.

Mide' Technology (2002) www.mide.com

Miller, D. W, Hall, S. R., and von Flotow, A. H., 1990, "Optimal Control of Power Flow at Structural Junctions," J. Sound and Vibration, **140**, No. 3, pp. 475-497.

Miller, L. R., Ahmadian, M., and Nobles, C. M., 1992a, "Modelling and Performance of an Experimental Active Vibration Isolator," *ASME Transactions on Active Control of Noise and Vibration*, DSC-Vol. 38, pp. 157-163.

Miller, L. R., Ahmadian, M., 1992b, "Active Mounts – A discussion of Future Technological," *Proceedings of INTER-NOISE 92*, July 20-22, Toronto, Ontario, Canada.

Minus K Technologies (2002) www.minusk.com

Miu, D. K., 1991, "Physical Interpretation of Transfer Function Zeros for Simple Control Systems with Mechanical Flexibilities," Journal of Dynamic Systems, Measurement, and Control, Vol. 113, September, pp. 419-422.

Miu, D. K., 1993, *Mechatronics*, Springer-Verlag.

Morgan Electro Ceramics, 2001, "Introduction - Piezoelectric Ceramics," http://www.piezoceramics-philips.com/pdf/tech.pdf

Morgan Electro Ceramics, 2001, "Material grade specification – Piezoelectric Ceramics," http://www.piezoceramics-philips.com/pdf/mater.pdf

Morgan Electro Ceramics, 2001, "Product specification – Piezoelectric Ceramics," http://www.piezoceramics-philips.com/pdf/prod.pdf

Motran Inc. (2002) www.motran.com

Mottershead, J. E., and Friswell, M. I., 1993, "Model Updating in Structural Dynamics: a survey," J. Sound and Vibration, **167**, No. 2, pp. 347-375.

Nelson, P. A., and Elliott S. J., 1992, *Active Control of Sound*, Academic Press.

Nelson, P. A., Jenkins, M. D., and Elliott, S. J., 1987, "Active Isolation of Periodic Vibration," *NOISE-CON 87*, The Pennsylvania State University, State College, PA, June 8-10, pp. 425-430.

Ohayon, R., Soize, C., 1998, *Structural Acoustics and Vibration*, Academic Press.

Owen, R. G., Lorenz, M. H., and Jones, D. I., 1992, "A Comparison of Control Schemes for the Microgravity Isolation Mount," *ASME Transactions on Active Control of Noise and Vibration*, DSC-Vol. 38, pp. 319-326.

Petyt, M., 1998, *Introduction to Finite Element Vibration Analysis*, CUP.

Politansky, H., Pilkey, W. D., 1989, "Suboptimal Feedback Vibration Control of a Beam wth a Proof-Mass Actuator," J. Guidance, Control, and Dynamics, **12**, No. 5, pp. 691-697.

Preumont, A., Loix, N., Malaise, D., and Lecrenier, O., 1993, "Active Damping of Optical Test Benches with Acceleration Feedback," Machine Vibration, No. 2, pp. 119-124.

Preumont, A., 1997, *Vibration Control of Active Structures*, Kluwer Academic Publishers.

Preumont, A., 2001, *Responsive Systems for Active Vibration Control*, NATO Science Series, Kluwer Academic Publishers.

Procopio, G. M., 1986, "Active Damping of a Bernoulli-Euler Beam via End Point Impedance Control Using Distributed Parameter Techniques," Combined Bachelor's and Master's thesis, Massachusetts Institute of Technology. Also Draper Laboratory Report CSDL-T-929.

Ren, M. Z., Seto, K., and Doi, F., 1997, "Feedback Structure-Borne Sound Control of a Flexible Plate with an Electromagnetic Actuator: the Phase Lag Problem," *Journal of Sound and Vibration,* Vol. 205, pp 57-80..

Ryaboy, V. M., 1995, "Limiting Performance Estimates for the Active Vibration Isolation in Multi-degree-of-freedom Mechanical System," J. Sound and Vibration, **186**, No. 1, pp. 1-21.

Scheuren, J. *et al.*, 1995, "Experiments with Active Vibration Isolation," *ACTIVE 95*, Newport Beach, CA, July 6-8, pp. 79-88.

Senior, S. L., 2002, personal communication.

Serrand, M., 1998, "Active Isolation of Base Vibration," MSc thesis, University of Southampton.

Serrand, M., and Elliott, S. J., 2000, "Multichannel Feedback Control for the Isolation of Base-Excited Vibration," J. Sound and Vibration, **234**, No. 4, pp. 681-704.

Sharp, S. J., Nelson, P. A., Koopman, G. H., 2002, "A Theoretical Investigation of Optimal Power Absorption as a Noise Control Technique," J. Sound and Vibration, **251**, No. 5, pp. 927-935.

Skogestad, S., Postlethwaite, I., 1996, *Multivariable Feedback Control: Analysis and Design*, John Wiley & Sons, Inc.

Skudrzyk, E., 1968, *Simple and Complex Vibratory Systems*, The Pennsylvania State University Press.

Soedel, W., 1993, *Vibration of Shells and Plates*, Marcel Dekker Inc. New York.

Sommerfeldt, S. D., Tichy, J, 1990, "Adaptive Control of a Two-stage Vibration Isolation Mount," J. Acoustical Society of America, **88**, No. 2, pp. 938-944.

Spanos, J., Rahman, Z., and Blackwood, G., 1995, "A Soft 6-axis Active Vibration Isolator", *Proceedings of the American Control Conference,* pp. 412-416.

Su, J. H., Ruckman, C. E., 1996, "Mechanisms of Localized Vibration Control in Complex Structures," Journal of Vibration and Acoustics, Vol. 118, January, pp. 135-139.

Sun, D. C., Tong, L, 2001, "Sensor/Actuator Equations for Curved Piezoelectric Fibers and Vibration Control of Composite Beams using Fiber Modal Actuators/Sensors," J. Sound and Vibration, **241**, No. 2, pp. 297-314.

Sun, J. Q., 1996, "Some Observations on Physical Duality and Collocation of Structural Control Sensors and Actuators," J. Sound and Vibration, **194**, No. 3, pp. 765-770.

Sun, J. Q., Jolly, M. R., and Norris, M. A., 1995, "Passive, Adaptive and Active Tuned Vibration Absorbers – A Survey," Transactions of the ASME, Vol. 117, pp. 234-242.

Sutton, T. J., Elliott, S. J., Brennan, M. J., Heron, K. H., and Jessop, D. A.C., 1997, "Active Isolation of Multiple Structural Waves on a Helicopter Gearbox Support Strut," J. Sound and Vibration, **205**, No. 1, pp. 81-101.

Swanson, D. A., Miller, L. R., 1993, "Design and Effectiveness Evaluation of an Active Vibration Isolation System for a Commercial Jet Aircraft," *Proceedings of the AIAA Aerospace Design* Conference, AIAA 93-1145, Irvine, CA, February 16-19.

Szefer, G., 2001, "Optimal Control of Vibration Systems," *Proceedings of the 8th International Congress on Sound and Vibration*, Hong Kong, China, July 2-6.

Tanaka, N., Kikushima, Y., 1988, "Rigid Support Active Vibration Isolation," J. Sound and Vibration, **125**, No. 3, pp. 539-553.

Titterton, P. J., 1999, "Synthesis of Optimal, Single-Frequency, Passive Control Laws, with Applications to Reducing the Acoustic Radiation from a Submerged Spherical Shell," J. Acoustic Society of America, **105**, No. 4, pp. 2261-2268.

Tzou, H. S., Ye, R, and Ding, J. H., 2001, "A New X-Actuator Design for DualBending/Twisting Control of Wings," J. Sound and Vibration, **241**, No. 2, pp. 271-281.

Ungar, E. E., 1992, "Vibration Isolation," Chapter 11, *Noise and Vibration Control Engineering*, L. Beranek and I. L. Ver, eds., Wiley, Chichester.

von Flotow, A. H., 1988, "An Expository Overview of Active Control of Machinery Mounts," *Proceedings of the 27th Conference on Decision and Control*, Austin, TX, December 1988, pp. 2029-2032.

von Flotow, A. H., Vos, D. W., 1990, "The Need for Passive Damping in Feedback Controlled Flexible Structures," *Proceedings of the 61st Shock and Vibration Symposium*, October, Pasadena, CA, pp. 593-603.

von Flotow, 1994a, "Isolation at Machinery Mounts," Short Course Notes.

von Flotow, A. H., Beard, A., and Bailey, D., 1994b, "Adaptive Tuned Vibration Absorbers: Tuning Laws, Tracking Agility, Sizing, and Physical Implementations," *NOISE-CON 94*, Ft. Lauderdale, FL, May 1-4, pp. 437-454.

von Flotow, A. H., Mercadal, M., Maggi, L., and Adams, N., 1997, "Vibration and Sound in Aircraft Cabins; A Comparison of Active/Passive and Active Control," *Proceedings of the SAE Conference*, Wichita, KS, May 1997.

Wang, Q., Wang, C. M., 2001, "A Controllability Index for Optimal Design of Piezoelectric Actuators in Vibration Control of Beam Structures," J. Sound and Vibration, **242**, No. 3, pp. 507-518.

Yousefi-Koma, A., Vukovich, G., 2000, "Vibration Suppression of Flexible Beams with Bonded Piezotransducers using Wave-Absorbing Controllers," J. Guidance, Control, and Dynamics, Vol. 23, No. 2, March-April 2000, pp. 347-354.

Yuan, J., 2002, "Global Damping of Noise or Vibration Fields with Locally Synthesized Controllers," J. Acoustic Society of America, **111**, No. 4, pp. 1726-1733.

Zhou, K., Glover, K., and Doyle, J., *Robust and Optimal Control*, 1998.

Zimmerman, D. C., Hornar, G. C., and Inman, D. J., 1988, "Microprocessor Controlled Force Actuator," J. Guidance, Control, and Dynamics, **11**, No. 3, pp. 230-236.

Appendix A

Equipment isolation of a SDOF system with an inertial actuator using a linear quadratic regulator

Optimal control can be employed to reduce the vibration transmission in structures, and in particular, lightweight structures with optimal controllers have been analysed by Politansky *et al.* (1989), Balakrishnan (1993) and Anthony *et al.* (2000a,b).

In this appendix the performance of a full state feedback controller designed using optimal control theory will be investigated to compare with the performance obtained from the inertial actuator with inner force and outer velocity feedback. The response of the base plate is approximated by that of a single mass spring damper system, as shown in Figure A.1, in order to keep the state-space model simple. The parameters of this model of the base structure were chosen to best approximate the first mode of the base plate. The internal states of the system are given by the displacements of the base mass, equipment mass and actuator mass, γ_1, γ_2, γ_3 and their velocities $\dot{\gamma}_1$, $\dot{\gamma}_2$, $\dot{\gamma}_3$ and the system is driven by the forces f_1, f_2 and f_3 .

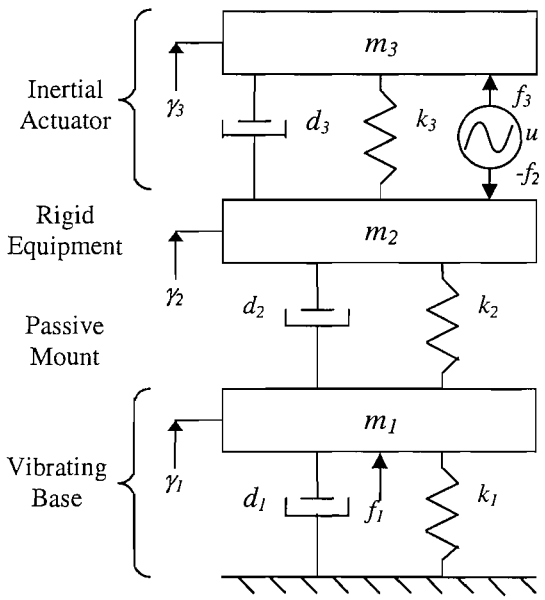

n_g = Number of degrees of freedom = 3
m_3 = 0.91 Kg
m_2 = 1.08 Kg
m_1 = 2 Kg
k_3 = 3900 N/m
k_2 = 20000 N/m
k_1 = 146000 N/m
d_3 = 5.8 N/ms^{-1}
d_2 = 18 N/ms^{-1}
d_1 = 36 N/ms^{-1}

Figure A.1 *Schematic of the plant and numerical values used in the simulations of a vibration isolation system with full state feedback control.*

The model of the plant in generalized coordinates in Figure A.1 is given by

$$m_1\ddot{\gamma}_1 = f_1 + k_2(\gamma_2 - \gamma_1) - k_1\gamma_1 + d_2(\dot{\gamma}_2 - \dot{\gamma}_1) - d_1\dot{\gamma}_1 \tag{A.1}$$

$$m_2\ddot{\gamma}_2 = f_2 + k_3(\gamma_3 - \gamma_2) - k_2(\gamma_2 - \gamma_1) + d_3(\dot{\gamma}_2 - \dot{\gamma}_1) - d_2(\dot{\gamma}_2 - \dot{\gamma}_1) \tag{A.2}$$

$$m_3\ddot{\gamma}_3 = f_3 - k_3(\gamma_3 - \gamma_2) - d_3(\dot{\gamma}_3 - \dot{\gamma}_2) \tag{A.3}$$

which can be written as

$$\mathbf{M}\ddot{\boldsymbol{\gamma}}(t) + \mathbf{D}\dot{\boldsymbol{\gamma}}(t) + \mathbf{K}\boldsymbol{\gamma}(t) = \mathbf{f}(t) \tag{A.4}$$

where

$$\mathbf{M} = diag\{m_1 \quad m_2 \quad m_3\} \tag{A.5}$$

$$\mathbf{K}=\begin{bmatrix}(k_1+k_2) & -k_2 & 0\\ -k_2 & (k_2+k_3) & -k_3\\ 0 & -k_3 & k_3\end{bmatrix},\ \mathbf{D}=\begin{bmatrix}(d_1+d_2) & -d_2 & 0\\ -d_2 & (d_2+d_3) & -d_3\\ 0 & -d_3 & d_3\end{bmatrix} \tag{A.6}$$

and

$$\boldsymbol{\gamma}(t)=\begin{bmatrix}\gamma_1(t)\\ \gamma_2(t)\\ \gamma_3(t)\end{bmatrix},\ \mathbf{f}(t)=\begin{bmatrix}f_1(t)\\ f_2(t)\\ f_3(t)\end{bmatrix}. \tag{A.7}$$

Multiplying both sides of equation (A.4) by $\mathbf{M}^{-1}$, the following equation is obtained:

$$\ddot{\boldsymbol{\gamma}}(t)+\mathbf{M}^{-1}\mathbf{D}\dot{\boldsymbol{\gamma}}(t)+\mathbf{M}^{-1}\mathbf{K}\boldsymbol{\gamma}(t)=\mathbf{M}^{-1}\mathbf{f}(t). \tag{A.8}$$

The equivalent model in modal coordinates is given by

$$\ddot{\boldsymbol{\eta}}(t)+\mathbf{D}_m\dot{\boldsymbol{\eta}}(t)+\boldsymbol{\Omega}^2\boldsymbol{\eta}(t)=\mathbf{V}^T\mathbf{f}(t) \tag{A.9}$$

where $\boldsymbol{\gamma}=\mathbf{V}\boldsymbol{\eta}$ and $\mathbf{V}$ is computed using $\mathbf{V}^T\mathbf{M}_g\mathbf{V}=\mathbf{I}_{ng}$. Also, $\mathbf{D}_m=\mathbf{V}^T\mathbf{D}_g\mathbf{V}$ and $\boldsymbol{\Omega}$ is the resonance matrix. For each mode, the damping is given by $\frac{1}{2}\mathbf{D}_m\boldsymbol{\Omega}^{-1}$. A more detailed study on the implications of using a model in modal coordinates is given by Benassi *et al.* (2002c).

Returning to the model in generalized coordinated, the state-space model (Zhou *et al.*, 1998), assuming that the system is driven by a disturbance $f_1=f_p$, controlled by an input u, where $f_2=u$ and $f_3=-u$, and the output of the system is given by the equipment velocity $\dot{\gamma}_2=v_e$, can be written as

$$\begin{aligned}\dot{\mathbf{x}}(t)&=\mathbf{A}\mathbf{x}(t)+\mathbf{B}u(t)+\mathbf{R}f_p(t)\\ \mathbf{y}(t)&=\mathbf{C}\mathbf{x}(t)\end{aligned} \tag{A.10}$$

where

$$\mathbf{x}(t)=\begin{Bmatrix}\gamma_1(t)\\ \gamma_2(t)\\ \gamma_3(t)\\ \dot{\gamma}_1(t)\\ \dot{\gamma}_2(t)\\ \dot{\gamma}_3(t)\end{Bmatrix},\ \mathbf{A}=\begin{bmatrix}\mathbf{0}_{n_g} & \mathbf{I}_{n_g}\\ -\mathbf{M}^{-1}\mathbf{K} & -\mathbf{M}^{-1}\mathbf{D}\end{bmatrix},\ \mathbf{B}=\begin{Bmatrix}0\\ 0\\ 0\\ 0\\ -1/m_2\\ 1/m_3\end{Bmatrix} \tag{A.11}$$

$$\mathbf{C}=\begin{bmatrix}0 & 0 & 0 & 0 & 1 & 0\end{bmatrix},\ \mathbf{R}=\begin{Bmatrix}0\\ 0\\ 0\\ 1/m_1\\ 0\\ 0\end{Bmatrix}. \tag{A.12}$$

When the disturbance input is assumed to be white noise and the final time of the simulation is assumed to be infinity, the LQG regulator can be obtained by minimising the cost function

$$J=\min\int_{t_0}^{\infty}\left[\mathbf{y}^T(t)\alpha\mathbf{y}(t)+u^T(t)u(t)\right]dt \tag{A.13}$$

where changing α provides a family of results depending on the relative importance of reducing the equipment velocity and reducing the control effort. The solution of the LQG problem (Zhou *et al.*, 1998) is given by

$$u(t)=\mathbf{K}\mathbf{x}(t) \tag{A.14}$$

where $\mathbf{K}=-\mathbf{R}^{-1}\mathbf{B}^T\mathbf{S}$ and $\mathbf{S}$ is the unique positive definite solution of the Algebraic Riccati Equation (ARE)

$$\mathbf{SA} + \mathbf{A}^T\mathbf{S} - \mathbf{SBR}^{-1}\mathbf{B}^T\mathbf{S} + \mathbf{C}^T\mathbf{QC} = \mathbf{0} \tag{A.15}$$

If the instabilities are in the controllable part of (**A**,**B**) and the non-observable modes of (**A**,**C**) are stable, then $u(t) = \mathbf{K}\mathbf{x}(t)$ ensures that the system is stable and minimizes the cost function *J*. In the cases presented below, the non-controllable or non-observable parts of the system are related to the behaviour of the base, which is stable because it is "passive".

It can be noted that **K** in equation (A.14) is a 1x6 matrix, which assumes that the state vector **x***(t)* is known at all times. Full state feedback would either require the use of many more than two sensors, or the implementation of a Kalman filter, or state observer, with a very detailed model of the system under control, which makes the stability of the overall feedback system very sensitive to changes in the response of the system (Doyle *et al.*, 1979, and Szefer, 2001).

Figure A.2 shows the spectrum of the equipment velocity before any control and with full state feedback calculated to minimise equation (A.13) with $\alpha = 30$ and $\alpha = 100$, where the former seems to be a choice that is comparable to the classical solution with direct velocity feedback control ($h_v = 15$) which guarantees a 6 dB stability margin. In the optimal control case, **K** = [-96.6 –413.7 347 4.56 –23.3 –0.53] when $\alpha = 30$. Figure A.2 also shows the spectrum of the equipment velocity with full state feedback calculated with $\alpha = 100$. This can be compared to the performance in Figure 6.14, where an inner phase-lag compensator and an outer equipment velocity feedback loop were implemented. This value of α for the optimal controller was chosen so that the control effort was similar to that required for $Z_D = 100$ in Figure 6.14. In the optimal control case with $\alpha = 100$, **K** = [-604.3 –2567.1 1694.8 13.03 –73.79 –4.62]. Although the LQ regulator may potentially perform better if α is increased, thanks to the fact that the control force is based on more information, a more complex controller and higher gains are needed to implement such a solution. In conclusion, classical methods based on an inner and an outer loop are not only robust, but they also perform well compared to an optimal LQ regulator, requiring a similar control effort.

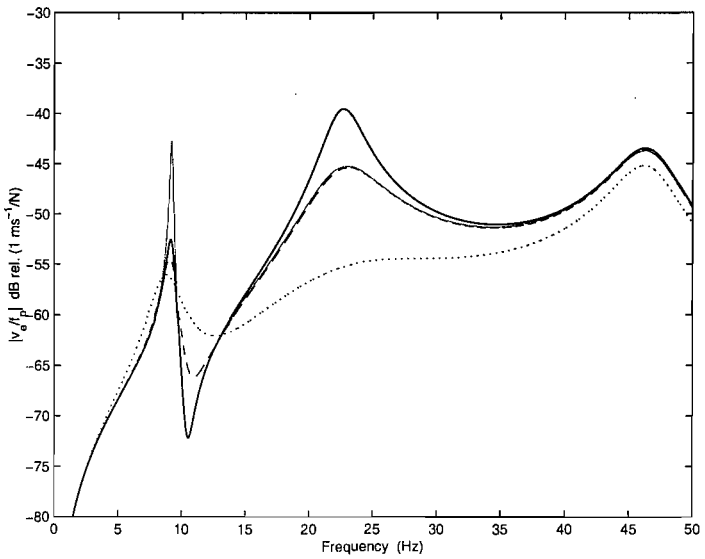

Figure A.2 *Bode plot of the equipment velocity per unit primary force when no control is implemented (solid), when direct velocity feedback control (faint) and when the full state feedback are implemented for* α *= 30 (dashed) and* α *= 100 (dotted).In the full state feedback cases, the controller has been optimised using LQG control theory.*

The control effort in the simulation in Figure A.2 (dotted line) was adjusted to be similar to that used by the dual-loop controller, as shown in Figure A.3. In particular, equation (6.12) was used to compute the actuator requirement, the inertial actuator force per unit primary excitation, when the inner force feedback control and outer equipment velocity feedback control are implemented.

In order to compare the magnitude of the required control effort in Figure A.3, the transmitted force that would guarantee zero equipment velocity was computed. From equation (6.1), if the equipment velocity v_e is imposed to be zero, follows that

$$\frac{f_t}{f_p} = -\frac{Z_m Y_b}{1 + Z_m Y_b} \tag{A.16}$$

which is plotted in Figure A.4 along with the case where the LQG regulator is implemented, but no control effort is present in the cost function J. If u is allowed to assume any value, at low frequencies, a very large control effort is needed.

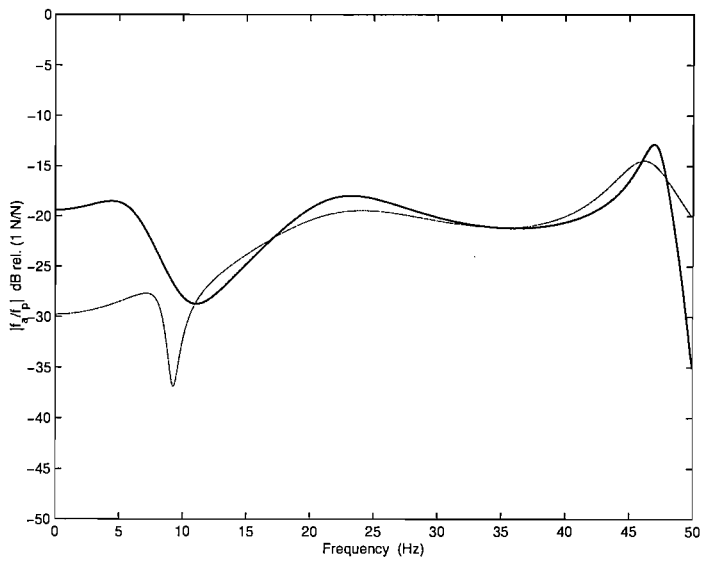

Figure A.3 *Actuator requirement, inertial actuator force per unit primary excitation, when (solid) an inner phase-lag compensator with h_{pl} = 100 and an outer feedback control with Z_D = 100 are implemented, and when (faint) an LQG regulator with α = 100 is implemented.*

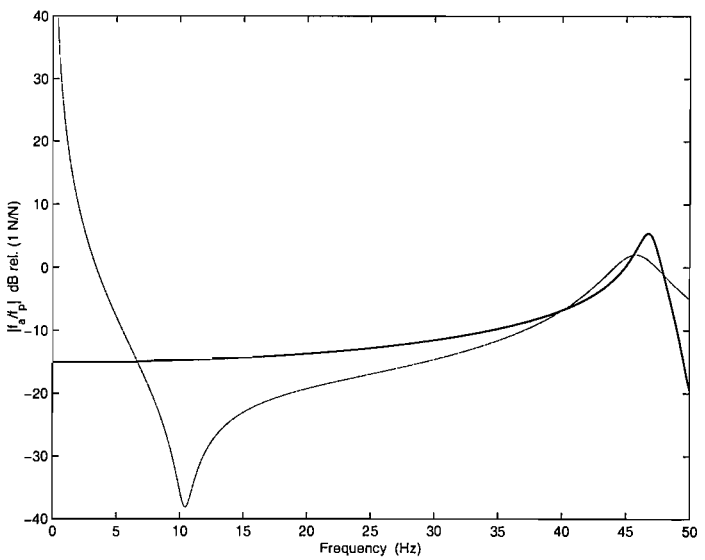

Figure A.4 *Transmitted force per unit primary excitation necessary to obtain an equipment velocity equal to zero (solid), and actuator requirement when no control effort u is present in the cost function J (faint).*

One way to overcome the problem of having to implement a state observer is to define the control force as $u(t) = \mathbf{K}\mathbf{y}(t)$. In this case only the outputs are fed back and no knowledge on the internal states is needed. However, this solution does not offer any improvement compared to the analogue solutions. In fact, it can be shown (Benassi *et al.*, 2002a) that when the equipment velocity $\dot{\gamma}_2$ is the only output and the feedback gain K varies from zero to infinity, the squared equipment velocity has its minimum when $K = K_{opt}$, where $K_{opt} = K_{velocity\ fb}$ (the optimal gain equals the largest gain before instability obtained when direct velocity feedback control is implemented). It can also be shown that the same applies when other classical control strategies are implemented. For example, if $y(t) = m_a \ddot{\gamma}_3 = f_t$ and $u(t) = Ky(t)$ then $K_{opt} = K_{force\ fb}$. In light of these results, it is pointless to analyse optimal control strategies based on $u(t) = \mathbf{K}\mathbf{y}(t)$ because we are after optimal controllers that perform better than classical techniques. To achieve this goal the constraint $u(t) = \mathbf{K}\mathbf{y}(t)$ has been relaxed to $u(t) = \mathbf{K}\mathbf{x}(t)$ and so far it has been assumed $\mathbf{x}(t)$ somehow known, therefore allowing $\mathbf{K}$ to be 1x6 matrix.

If the state vector $\mathbf{x}(t)$ is not known, then an observer can be implemented, as shown in Figure A.5, in order to estimate the state vector from the knowledge of the outputs of the plant $\mathbf{y}$(t) and the control effort u, which is obtained from the output of the LQG regulator. The model of the complete system is given by equation (A.10), equation (A.14) and the state-space model of the state observer, which is given by

$$\dot{\hat{\mathbf{x}}} = (\mathbf{A} - \mathbf{K}_o\mathbf{C})\hat{\mathbf{x}} + \mathbf{B}u + \mathbf{K}_o\mathbf{y} \tag{A.17}$$

where $\mathbf{A}$, $\mathbf{B}$, $\mathbf{C}$, $\mathbf{y}$ and u are described above. $\hat{\mathbf{x}}$ is the vector of the estimated states and $\mathbf{K}_o$ is the vector of the observation gains, which were chosen to guarantee that

$$\max_{i=1}^{n_g} \mathrm{Re}[\lambda_i(\mathbf{A} - \mathbf{K}_o\mathbf{C})] << \min_{i=1}^{n_g} \mathrm{Re}[\lambda_i(\mathbf{A} + \mathbf{B}\mathbf{K})] \tag{A.18}$$

where $\lambda_i(\cdot)$ indicates the i-th eigenvalue, and $(\mathbf{A}-\mathbf{K}_o\mathbf{C})$ and $(\mathbf{A}+\mathbf{BK})$ describe the dynamics of the of the estimation error $\mathbf{x}(t)-\hat{\mathbf{x}}(t)$ and the dynamics of the plant with full state LQG feedback, respectively.

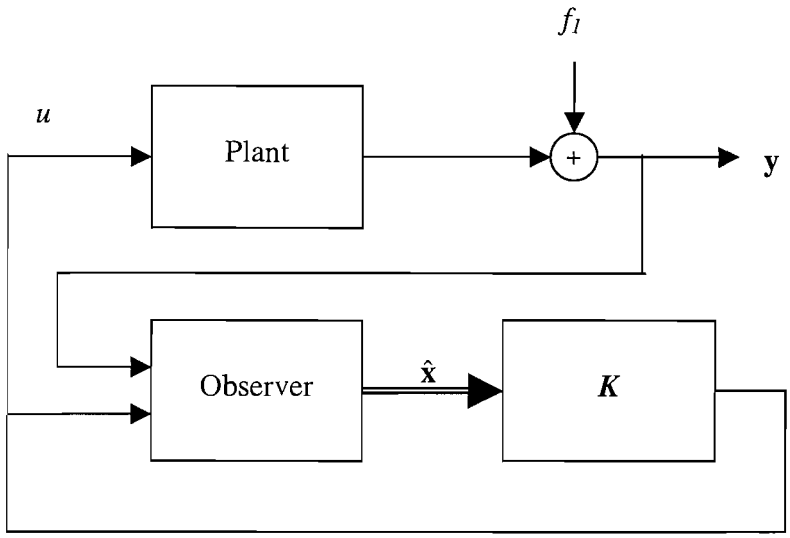

Figure A.5 *Block diagram of a closed-loop system, whose plant is composed of an active vibration isolation with an inertial actuator installed on a vibrating base, as described in Figure A.1. A full state feedback controller, optimised using LQG control theory, is implemented and the states of the plant are estimated through an observer, whose inputs are the outputs of the plant and the control effort u.*

If $y=\dot{\gamma}_2=v_e$ then the output matrix $\mathbf{C}$ is given by equation (A.12). However, in this case the rank of the observability matrix $(\mathbf{A},\mathbf{C})$ is equal to 5, which means that the system is not completely observable and therefore a full state observer cannot be implemented. On the other hand, if $\mathbf{y}(t)=\begin{Bmatrix}\dot{\gamma}_2(t)\\ m_3\ddot{\gamma}_3(t)\end{Bmatrix}=\begin{Bmatrix}v_e(t)\\ f_t(t)\end{Bmatrix}$ then

$$\mathbf{C}=\begin{bmatrix}0 & 0 & 0 & 0 & 1 & 0\\ 0 & k_3 & -k_3 & 0 & d_3 & -d_3\end{bmatrix},\ \mathbf{D}=\begin{bmatrix}0 & 0\\ 0 & 1\end{bmatrix} \tag{A.19}$$

and given the model of the controlled variable $z = \mathbf{Hx} = v_e$ to be used in the modified cost function

$$J = \min \int_{t0}^{\infty} \left[z^T(t) \alpha z(t) + u^T(t) u(t) \right] dt \tag{A.20}$$

then $(\mathbf{A}, \mathbf{C})$ turns out to be completely observable, and $(\mathbf{A}, \mathbf{B})$ is completely controllable, which is in reality a stronger condition of what it is actually required. Also, $(\mathbf{A}, \mathbf{H})$ is detectable, which means that the modes that are not observable by $(\mathbf{A}, \mathbf{H})$ are stable and in our case the flexible base is "passive" and therefore stable. Given the above satisfied conditions, there is a unique solution, which is given by equations (A.10), (A.14), (A.15), (A.17) and (A.18), to the estimation and the LQG regulation problem. Figure A.6 shows the performance of the LQG regulator obtained through the estimation of the states (dashed line) compared to the case (faint line) where the states are known. Although the performance of the regulator with observer is generally worse than the performance of the full state regulator, the attenuation that can be achieved compared to the uncontrolled case is quite good.

Returning to the case where the equipment velocity is the only output of the system, $y = \dot{\gamma}_2 = v_e$, since the rank of the observability matrix is 5, then a full state observer cannot be constructed, even though a reduced order observer can be implemented. In this case, the plant was decomposed in its observable and non-observable parts, which in practice implied that the states γ_1 and $\dot{\gamma}_1$ (base displacement and its velocity) were non estimated. The rank of both the observability and controllability matrices of the reduced system is 4 and Figure A.7 shows the comparison between the performance of the LQR regulator obtained using a reduced order observer and the case where the states are known. It can be noted that the performance of the former is worse than what it was obtained in Figure A.6 and in particular the regulator cannot do much to reduce the magnitude of the first base mode (in fact, there is enhancement), whose dynamics is not estimated by the observer.

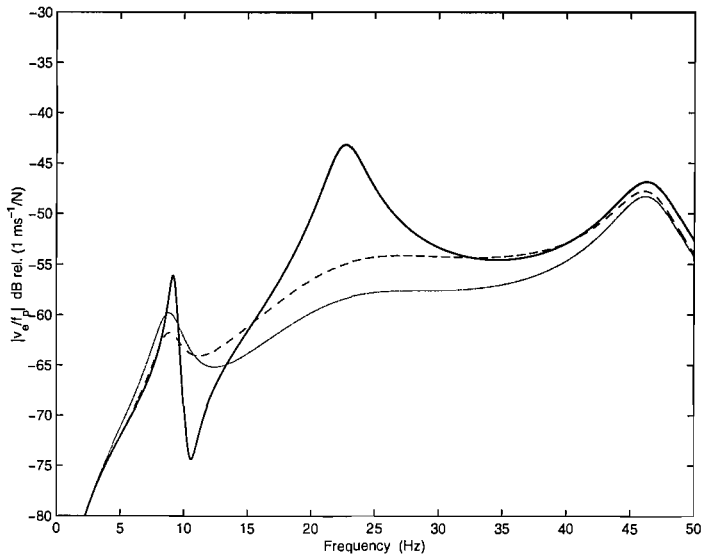

Figure A.6 *Bode plot of the equipment velocity per unit primary force when no control is implemented (solid), when the full state feedback, optimised using LQG control theory, is implemented for* $\alpha = 100$ *(faint), and when full state feedback, obtained through a full state observer and an LQG regulator, is implemented for* $\alpha = 100$ *(dashed).*

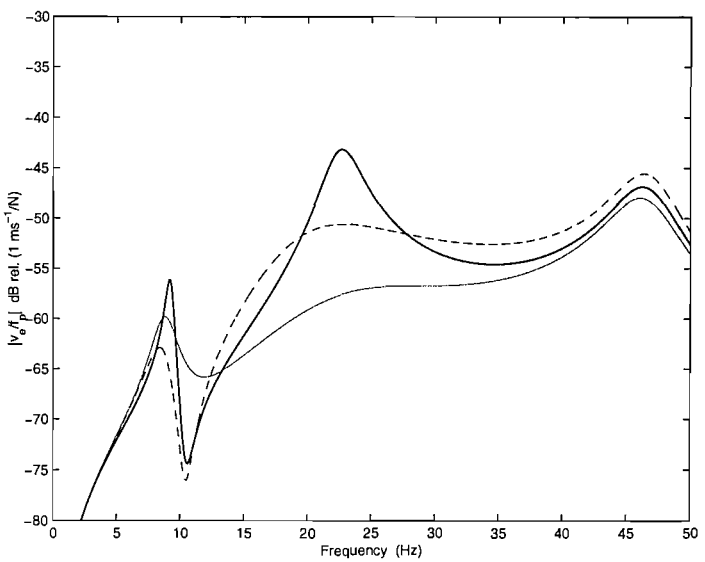

Figure A.7 *Bode plot of the equipment velocity per unit primary force when no control is implemented (solid), when the full state feedback, optimised using LQG control theory, is implemented for* $\alpha = 100$ *(faint), and when full state feedback, obtained through a reduced observer and an LQG regulator, is implemented for* $\alpha = 100$ *(dashed).*

In conclusion, an LQG regulator may perform better than the classical strategies thanks to the fact that the control force is based on more information. However, the difference between the LQG regulator and some classical schemes is not significant, leading to the conclusion that the optimal control may not be worth the implementation because the difference in the performance is not massive and its actual realization would require a lot of extra effort in terms of electronic components and in general the accurate knowledge of the plant model is needed.

Appendix B

PID schematic

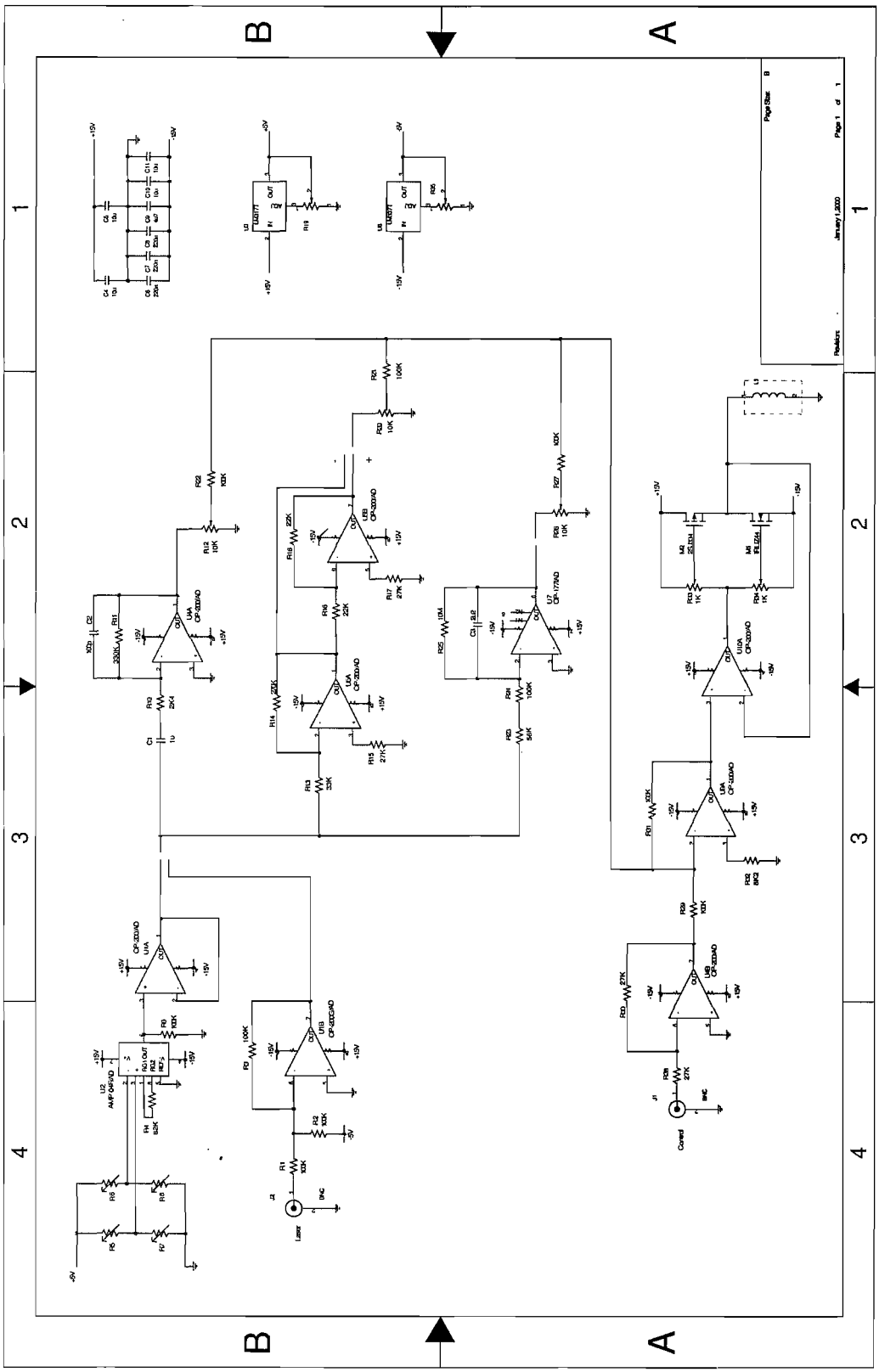

Appendix C

Geometrical and physical characteristics of the experimental set-up

This appendix contains the geometrical and physical characteristics of the equipment used during the experimentation work presented in Chapter 7.

Parameter	Value
Material	Aluminium
Plate dimensions	0.2 x 0.1 x 0.018 m
Density	2700 kg/m^3
Young's modulus of elasticity	7.1e10 N/m^2
Shear modulus of elasticity	2.4e10 N/m^2
Poisson's ratio	0.33
Mass of the plate	1.08 kg
Moment of inertia of the receiver	1.4e-2 kgm^2

Table C.1 *Geometrical and physical characteristics of the receiver.*

Parameter	Ring of rubber
External diameter	60 mm
Internal diameter	40 mm
Height	60 mm
Area	1.57e-3 m^2
Moment of inertia	5.1e-7 m^4
Density	909 kg/m^3
Young's modulus of elasticity	8e5 N/m^2
Shear modulus of elasticity	2.7e5 N/m^2
Poisson's ratio	0.3

Table C.2 *Main characteristics of the rubber mounts.*

Parameter	Value
Moment of inertia	$1.4e10^{-2}$ kgm^2
Total stiffness of each mount	24093 N/m
Total viscous damping for each mount	17.94 Ns/m
Effective mount damping ratio	4.8 %
Distance between mounts	134 mm

Table C.3 *Summary of the passive properties of the isolators (mounts).*

Specification	Value
Moving mass	0.91 kg
Maximum sine force – peak	8.9 N
Max displacement pk-pk (DC)	2.5 mm
Max sine velocity – peak	1.31 m/s
Max sine acceleration – pk	1373 m/s^2
Suspension axial stiffness	3.15 N/mm
Electrical requirement – Amplifier	0.09 kVA
Impedance at 500 Hz	4 Ω

Table C.4 *Specifications for a single control shaker LDS type V101.*

Parameter	Value
Material	steel
Dimensions	700 x 500 x 1.85 (mm)
Damping ratio	0.01

Table C.5 *Summary of the physical and geometrical properties of the base.*

Mode	Experimental frequency (Hz)	Calculated frequency (Hz)
(2,0)	32.6	44.8
(2,1)	37.7	49.0
(2,2)	58.8	65.4
(2,3)	91.1	98.8
(3,0)	100.0	123.3
(3,1)	105.0	129.2
(3,2)	128.0	149.8
(2,4)	139.0	151.8
(3,3)	166.2	186.0

Table C.6 *First 9 modes of the base supporting plate.*

Specification	Value
Maximum sine force – peak	196 N
Useful frequency range	DC to 9 kHz
Maximum displacement	±8.8 mm
Maximum acceleration	981 m/s^2
Maximum input power	100 VA
Maximum working current	9 A

Table C.7 *Specifications for a single control shaker LDS type V403.*

Equipment	Type
Accelerometer	B&K 4375
Force gauge	B&K 8200
Charge amplifier	B&K 2635
Power amplifier	HH Electronics MOS-FET
Integrator	ISVR designed
FFT Servo Analyzer/Generator	Advantest R9211B/C
Primary Shaker	LDS 403
Secondary shaker	LDS 101
Current meter	3 A and 5 A
Summing Box	ISVR designed

Table C.8 *List of the equipment.*

	Measurements		Model	
Modes	Without Isolator	With Isolator	Without Isolator	With Isolator
(2,0)	32.6	37.2	44.8	47.5
(2,2)	58.8	63.1	65.4	70.4
(2,4)	139.0	145.2	151.8	153.5
(4,0)	225.9	226.0	241.7	241.9

Table C.9 *Base plate modes observed by measurements and by simulations with and without the effect of the active isolator system.*